Sant'Anna
School of Advanced Studies – Pisa

**Academic Year 2017/2018**

Ph.D. Course in BioRobotics
XXX Cycle

# Engineering bio/non-bio interfaces for biomedical applications


## Author
Alice Rita Salgarella

## Supervisor
Prof. Leonardo Ricotti

## Tutor
Prof. Arianna Menciassi

## Co-tutors
Dr. Calogero Maria Oddo
Dr. Guido Giudetti

# Table of contents

# Abstract

Together with the rapid development of several bioengineering fields, among which those related to implantable medical devices, bio/non-bio interfaces have become of primary interest. In fact, in all those situations in which a biological component is in contact with an artificial one, a considerable number of mechanisms and pathways establish and lead to a biological response that may cause effects also on the artificial counterpart. This is the principle exploited in bio-hybrid sensors, for example, whose measures derive from sensing some changes in the properties of the biological elements. This bio/non-bio response is also a key aspect that boosts the integration between an implanted device and the host's organism, or to promote specific tissue responses (*e.g*. regeneration). Hence bio/non-bio interfaces are crucial for a considerable number of applications, in fields such as implantable biomedical devices, biomechatronics, tissue engineering and regenerative medicine. The aim of this research study was investigating bio/non-bio interfaces, engineering their bidirectional responsivity and exploiting them for applications in different bioengineering fields. In the introduction we will identify the three main players in a bio/non-bio interface that are (1) the biological component the material is in contact with, (2) the man-made material/biomaterial and (3) the external environment/stimuli. The mail goal of this thesis is the attempt to face different aspects of bio/non-bio interfaces. In particular, applications concern bio-hybrid tactile sensors and derived tools, interfaces with peripheral nerves, remote cell/material stimulation by means of ultrasound and triggerable drug delivery system. Considering the bio-hybrid sensing approach, the exploitation of a kidney derived cell line to achieve a mechanotransduction system will be presented, laying the foundation for an ever deeper interaction between artifacts and biocomponents. From this developed technology, we will present a fluidic mechanotransducer following the recent trend of creating flexible force sensors by using non toxic filling material, normally employed for cell culture routines. Then the thesis will focus on the direct stimulation that can be provided to the biological component by a bio/non-bio interface, in particular by the chemical and physical properties of a hydrogel soft coating designed for peripheral nerve interfaces, or by one of the most attractive external stimuli, i.e ultrasound, applied in this case directly to

muscle cells. Finally an ultrasound triggered drug release system, *i.e.* poly(2-oxazoline) micelles, will be analyzed for the dexamethasone administration with possible future application inside anti-inflammatory matrix. Although the presented research will differ in the topic treated and the application, the common scope is to find novel solutions going beyond the state-of-the-art, providing as much as possible a systematic investigation.

# 1. Introduction

Nowadays, as the population ages and the life expectancy rises, there is a growing need to replace and repair soft and hard tissues or even entire organs, as well as to develop advanced therapeutic strategies for age-related chronic illness such as heart diseases, cancer, diabetes or neurologic disorders. This led to a huge development of the biomedical devices and biomaterials markets; a report from the BCC research group[1] estimated that the global market for medical device technologies reached $458.3 billion in 2015. The market should reach $483.5 billion in 2016 and $634.5 billion by 2021, growing at a compound annual growth rate (CAGR) of 5.6% from 2016 to 2021, while the biomaterials market is expected to reach $149.17 billion by 2021 from $70.90 billion in 2016, at a CAGR of 16.0% from 2016 to 2021, according to a report of Markets and Markets group[2, 3]. Biomaterials and medical devices undoubtedly improve the quality of life of an increasing number of people each year; one of the key factors in their success is their ability to optimize the so called “bio/non-bio interfaces”, which namely are constituted by the intimate contact and interaction between artifacts (biomaterials, devices such as sensor or actuators) and biological components (tissues, cells, biomolecules such as protein). Engineering the biological environment with synthetic materials has been a long-standing challenge for biomedical research.[4] In fact, in all those situations in which a biological component is in contact with an artificial one, a considerable number of mechanisms and pathways establish, leading to a biological response that may cause effects also on the artificial counterpart. Engineering new tissue in the lab, encouraging self-regeneration of damaged tissues, replacing damaged tissues with synthetic materials or understanding unknown aspects of cell adhesion on surfaces or similar biological processes, all involve the interaction of biological components with artificial materials such as implants, scaffolds, biomedical devices and sensors, cell culture surfaces, etc.[5]

Hence bio/non-bio interfaces are crucial for a considerable number of applications, in fields such as implantable biomedical devices, biomechatronics, tissue engineering and regenerative medicine. The term "Tissue Engineering" was firstly introduced in 1988 in USA,

by attendees of the first National Science Foundation sponsored meeting, referring to as "the application of the principles and methods of engineering and life sciences towards fundamental understanding of structure–function relationship in normal and pathological mammalian tissues and the development of biological substitutes for the repair or regeneration of tissue or organ function".[6, 7] Then Langer and Vacanti[8] defined tissue engineering as "an interdisciplinary field that applies the principles of engineering and life sciences towards the development of biological substitutes that restore, maintain, or improve tissue or organ function. It means that this field involves multi-disciplinary knowledge between life science, biological cells, engineering biomaterials, biomedical factors and biotechnology".

At present, this commixture of different knowhow is considered as the strategic solution not only for tissues engineering but also in approaching all the emerging fields in which bio/non-bio interfaces are considered as crucial, especially with the advent of nanotechnologies and nanomaterials. They can provide a "smart" interface between biological and non-biological environments, even at a cellular level.[9] Hence bio/non-bio interaction must be considered at a multiscale level, opening different issues whether it is a micro- or a nano-scale, with correlated dynamic pathways that can be exploited to obtain high performance interfaces.[10]

The definition and classification of biomaterials and bio/non-bio interfaces is a process which is still ongoing.[5, 11] As far as biomaterials are concerned, for examples, the ones that are used clinically for biomedical applications can be roughly grouped into three main types described by the evoked tissue response: "nearly" inert (since every biomaterial provokes an initial immune response), bioactive and biodegradable (see Figure 1). Inert biomaterials elicit no or minimal tissue response, whereas bioactive materials enhance the material's integration by stimulating new tissue growth. Biodegradable (or bioresorbable) materials are engineered so to be initially incorporated into the surrounding tissue and then to completely dissolve in a time-dependent way. If we consider the classical metal implants such as cobalt–chromium alloys, for example, they are typically classified as inert. Ceramic materials can be inert, active or resorbable, while polymers can be inert or resorbable. The first generation of biomaterials was developed for routine use as medical implants and devices in the ‘60s and

'70s. Afterwards, over the '80s and '90s, the field started to shift towards the development of bioactive components in order to elicit a specific biological response at the bio/non-bio interface, also taking advantage from a better understanding of the mechanisms on which foreign body response relies.[12-14] The continuous advances in the cellular and molecular knowledge laid the scientific foundation for the development of the third-generation biomaterials, the bioresorbable ones. Nowadays we are facing the development of a fourth generation of biomaterials, the so-called smart or biomimetic biomaterials, providing the fundaments for increasingly advanced bio/non-bio interfaces (see Figure 1).[11]

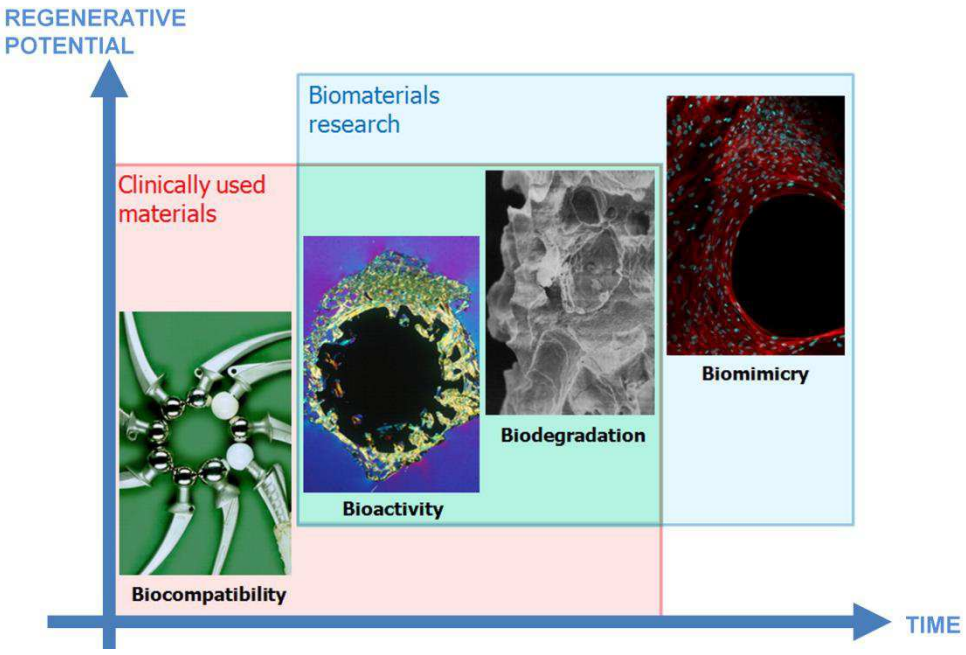


**Figure 1. Biomaterials present in literature in terms of their regenerative potential with respect to the time they were developed. (derived from Holzapfel et al. 2013 11).**

Smart bio/non bio interfaces are featured by their instructive/inductive or triggering/stimulating effects on the cells and tissues they are in contact with. Such effects are obtained through material responsiveness to internal stimuli (within the body), such as such as pH, temperature, ionic strength, etc. or external stimuli (out from the body) such as magnetic fields, ultrasound, light waves, etc.[11] This is often done with bioinspired multiscale structured materials[15], thus developing novel functional materials[10], *e.g.* bio-inorganic

materials[16], bio-nanomaterials[17], hybrid organic/inorganic implant materials[18], and other smart biomaterials[19, 20].

Biocompatibility is only one critical requirement for a smart bio/non bio interface. The old concept of biomaterials, for which the ideal implant must be biocompatible, not inducing any inflammatory response, extreme immunogenicity or cytotoxicity to native cells, tissues or organs *in vivo*, with its degradation products not being harmful, is becoming obsolete.[7] The boosting of fields, such as the bionics one, opened new frontiers that will bring towards new classes of interfaces, "cyborg" tissues[21], addressing a wide range of unmet needs. Here engineered tissues could include integrated circuits, which might provide real-time feedback relating to electrical and/or chemical activity within the tissue. Bionic interfaces could be established thanks also to advances in conformal device arrays, which have enabled, for example, technologies that can be grafted onto myocardium or blood vessels. for continuously monitoring catastrophic events, such as a heart attack or blood clot. Sensors coupled with stimulating electrodes could enable closed-loop systems that intervene immediately. High-resolution device arrays could also have substantial applications in prosthetics, enabling the patient to control artificial limbs with far greater fidelity than possible with current technology. Integrated biocompatible systems containing electronic interfaces, power sources, and supporting electronics have been developed.[22] The limitations of traditional silicon-based electronic devices which are rigid and not suitable to directly interface with tissues, have been addressed by recent advances in soft organic electronics, solid-state materials, and lithography techniques. Devices have been assembled on soft, biocompatible substrates, enabling tissue interfaces.[22]

In all these new applications that require materials to interface with cells, tissues or biomolecules, polymers constitute the fundament for a smart approach towards bio/non-bio interfaces, due to their tunable properties and different techniques for production and for their surface modification ("graſting from", "graſting to" and "blending" techniques).[23] The specific interactions (or lack thereof) between proteins and interfaces are essential for creating biosensors or in the field of antifouling materials (for antibacterial purposes, modulation of inflammatory reaction to implants, etc.). Proteins also mediate interactions

between cells and surfaces; the type of proteins, their orientation and their conformation are central in these interactions. Polymeric material properties and their modulation are crucial for providing temporal control over cell-surface interaction, such as mechanical properties and degradation rate, porosity, surface chemistry and topography, the display of signals to cells (through proteins or peptides), or electrical/optical properties in the case of conducting polymers.[24] Moreover, synthetic polymers are studied in order to be employed as therapeutic agents.[25] In fact polymers can be "activated" at the nano–bio interface to work as drugs, no matter how active or inert their constituents are, and may offer unique advantages over smaller compounds. They can also form higher-order structures, such as complex 3D nanostructures that may endow the polymer with unforeseen biological activities, as well as going through bioconjugation, which is the modification of polymer backbones with bioactive small molecules.[26]

These are just few of the possible strategies for obtaining advanced bio-non bio interfaces, and listing all the biomaterials used and applied in this field is far beyond the scope of this work. What is needed is to provide an attempt of classification of these interfaces so to contextualize the work (see Figure 2). Dhowre *et al.*[5] tried to classify the different interactions the biomaterials undergo with cells and external environments. The three main constituents of a bio/non-bio interface are (1) the biological component (this could be cells, tissues, bacteria, biomolecules such as proteins) with which the material is in contact, (2) the man-made material/biomaterial, and finally (3) the external environment/stimuli. These three elements must be considered deeply in order to design and engineer the desired bio/non-bio interface. Moreover they can or cannot play their fundamental role in the bio/non-bio interfaces, thus providing a classification.

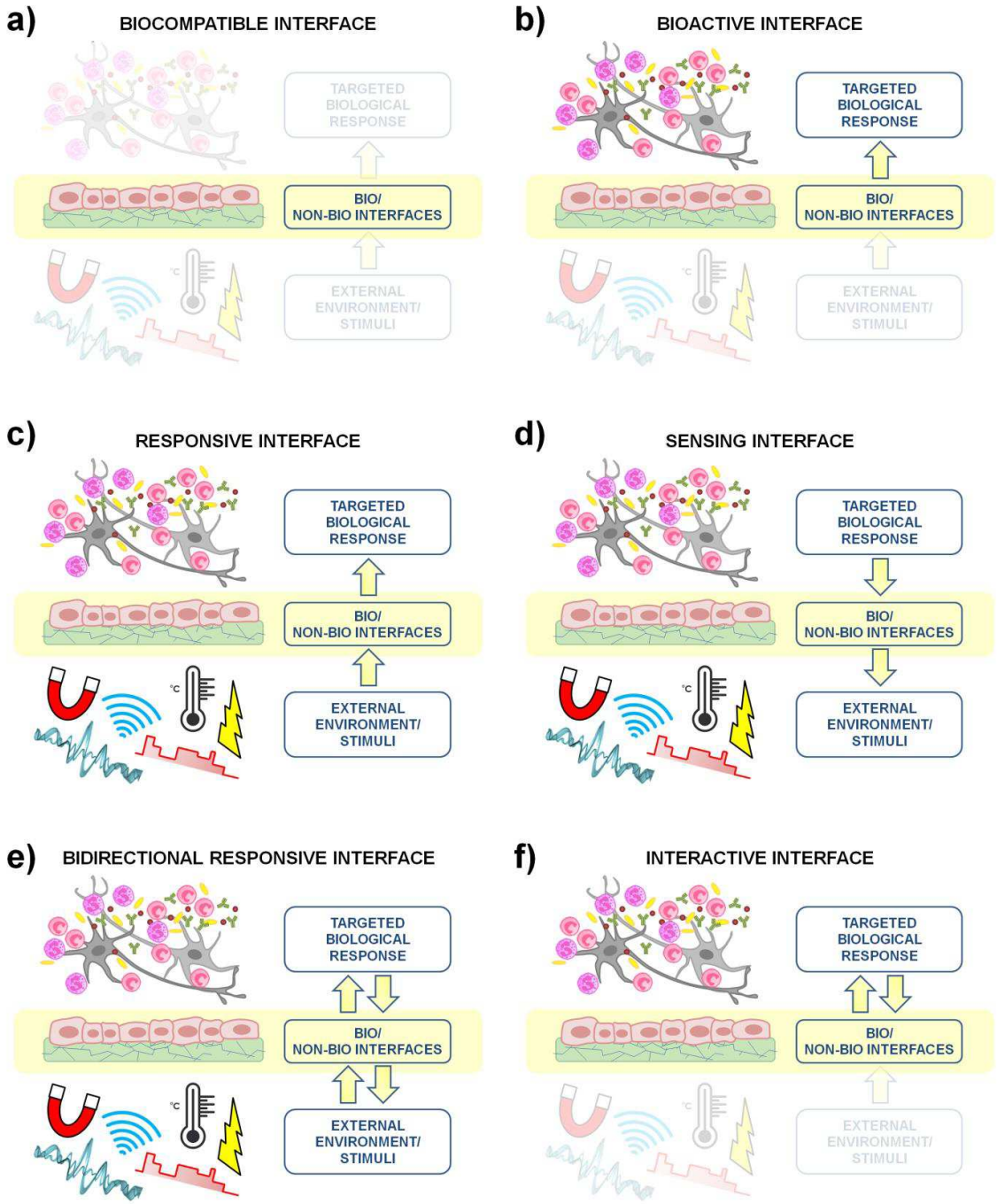


**Figure 2. Classification of the different types of bio/non-bio interfaces with respect of the three main components that play a role: (1) the biological component the material is in contact with, (2) the man-made material/biomaterial and (3) the external environment/stimuli.**

The **first type of interfaces** that can be identified are the **biocompatible** ones (Figure 2a). As previously mentioned, the initial focus in biomaterial selection was on biocompatibility, with the goal to suppress or reduce as much as possible cell–material interactions, thus to minimize undesired responses of cells or tissues to the implanted material.[27] This is also a property that has been pursued for obtaining reliable bio-sensors, so not to alter the sample to be analyzed.

Figure 2b depicts the class of **bioactive interfaces**, also named "instructive", in the Dhowre *et al.*[5] classification. They are designed to elicit a specific desired response from the cells with the aim to control cellular processes. They engage with the host tissue and positively enhance material integration,[28, 29] without the intervention of the external environment/stimuli. Hence, in this case it is very important to know which is the desired body/biological response and to understand the interaction of the artificial materials with its local environment. In some cases it is desirable to repel the protein interaction with the surface (this applies *e.g.* in the case of antifouling interfaces, for antibacterial purposes), while in others mimicking the dynamic processes within the extracellular cell matrix (ECM) is the main goal.[5] In fact it is well known that ECM goes through changes of its chemical and physical properties (such as mechanical and topographical ones), both spatially and temporally.[30] This dynamic behavior is an integral part of a functioning biological system and underlies essential biological processes, including stem cell differentiation, cell adhesion and migration[31, 32], as well as the development of diseases. Cells do not only respond to cues presented by their ECM, they also actively remodel it.[30] Through exocytosis and other pathways, cells secrete molecules that reshape the ECM and interact with other cells. Prominent examples are matrix metalloproteinases, cell secreted enzymes that degrade the ECM through proteolysis.[33] Other cell-secreted proteins such as collagen and fibronectin contribute to the construction of the ECM and thus influence the ECM structure and composition.[34] The first event after an implant is the protein adsorption to the biomaterial,[3, 35] thus modification of the substrate surface properties can affect the nature of the protein layer and thus provides control over the response of cells to the biomaterial.[36-38] Three surface properties have been identified as main determinants of cell behavior and cell fate: surface chemistry, surface topography and surface elasticity or stiffness.[39]

An ongoing need to improve the performance of bio/non-bio interfaces, led to the development of another class of interfaces in which also the external environment/stimuli play a fundamental role, namely **responsive interfaces** (Figure 2c).[5] These are able to change their properties dynamically and in some cases reversibly, in the presence of an external stimulus or multiple stimuli.[11, 40] In this case, the information flow is from the external environment to the biological component, through the material. Hence, it is necessary to control not only the way a material surface responds to stimuli, but also the mechanism of the stimulus action has to be carefully designed and incorporated into the interface, or externally provided. The choice of an appropriate stimulus depends on the application requirements. From a technical viewpoint, the stimuli must reach the interface and interact with it. This may not be so critical for *in vitro* applications as for *in vivo*, where the tissues between the stimulus and the target may not provide easy access to the interface, for externally controlled stimulation.[41] From a biological perspective instead, the stimuli have to be tolerated by the cells and must not trigger a negative cell response. In some cases it is also desirable that the stimulus contributes to the desired body response, so to provide an augmented beneficial effect to the regeneration process (as happens for example in the case of ultrasound). Preferred choices for stimuli are light, electrical potentials, small pH or temperature changes and mechanical stress or magnetic fields.[42]

Light responsive molecules can cause photoresponsive reorientation of chemical functionalities at the surface, or a reversibly attachment of chemical functionalities as in the case of azobenzene.[43-45] Electrical potentials have been used to alter biointerface properties, by reorganizing the surface molecular conformation,[46-48] or inducing chemical reactions that modulate the presence of certain surface chemical groups.[49-51] pH-responsive biointerfaces are mainly based on poly(acrylic acid) and poly(methacrylic acid) and can undergo changes in surface topographical features and water content, thus controlling surface swelling which induce bending and mechanical forces.[52-54] Thermoresponsive materials used for biointerfaces are typically polymers in which a change in temperature results in a change in the hydration state of the material,[55, 56] affecting the wettability and the morphology of the polymer film. A well-known example of temperature responsive materials is the poly(N-isopropylacrylamide).[57] Magnetoresponsive materials have been employed to modify cell–

surface interaction through the incorporation of magnetic nanoparticles into a polymeric matrix. An application of a magnetic field can cause distortion of the material, resulting in an alteration of the mechanical properties and also an increase of temperature.[58, 59] Finally mechanoresponsive biointerfaces can be prepares with polymer films that alter physical properties such as porosity and topography of the surface,[60, 61] as well as producing local electrical field by means of piezoelectricity exploitation and a remote mechanical stimulation by ultrasound.[62]

According to the classification provided by Dhowre *et al.*,[5] the inverse process, through which information about the biological component is collected by the material and transduced to an external processing unit, is typical of **sensing interfaces** (Figure 2d). There are several applications for such interfaces; one of the most known is a reliable glucose sensing to maintain the normoglycemia in diabetic patients.[63, 64] This requires regular and in some cases, continuous monitoring because major fluctuations can occur in a very short time. Moreover, implantable biosensor platforms have been developed for the detection of cancer biomarkers and lately some suggestions have been made on implantable systems for disease control and monitoring.[65] In fact there are several approaches for detecting viruses in patient samples, ranging from detecting the virus itself to the antibodies that are developed in the immune response to the virus. This is the case of the so called Point of Care devices, such as lateral flow assays and dipstick immunoassays, that allow diagnosis with specificity and sensitivity.[66]

Furthermore there are some cases in which these two latter classes of bio/non-bio interfaces, the responsive and the sensing ones, combine together so to form what it is usually identified as **bidirectional responsive interfaces** (Figure 2e), in which the flux of information/interaction can move from the external environment to the biological component and vice versa. This is the case of bioreactors[67, 68], organ-on-chip systems[69-71], neural interfaces[72], which are special electrodes that interface with the nervous system and allow a bidirectional communication with it, or bio-hybrid sensors[73]. Bidirectional responsive interfaces have a great potential in the field of regenerative medicine. Dynamic tissue culture platforms based on such interfaces would allow a finer control, respect to traditional

tools, over *in vitro* cell cultures, enabling the fabrication of artificial tissues with high complexity and proper functionality. Bi-responsive surfaces can be used to monitor biological processes either to design sensors or to gain an improved understanding of how cells interact with their environment and/or each other.

To target an ever more profound interaction between the biological environment and artifacts, another class of interfaces can be identified, namely **interactive interfaces** (Figure 2f). They are autonomous and often included biomolecules with the aim of developing cell-responsive materials that do not require the addition of external stimuli. Differently from externally controlled interfaces, autonomous ones are able to perform their function completely self-sustained and independent from external factors. It is becoming clear that the next generation of biomaterials should include significant elements of interactivity with the surrounding tissues to provide increased biomaterial functionality through a more seamless integration with the surrounding biological environment. This advancement of the field envisions the advent of the so called "living" bio/non-bio interfaces,[74] constituted of biomaterials that are indistinguishable in form and function from the biological matter. The aim is to design materials that provide cues dynamically and in a responsive manner to cells and nascent tissues as they develop, without external intervention. New hints have been provided by the fields of regenerative medicine, drug delivery, soft bioelectronics and artificial life.[74] A responsive scaffold for three-dimensional culture of mesenchymal stem cells has been designed to present an adhesive peptide while the stem cell remains latent but to release a ligand in response to protease expression as the stem cell becomes activated and differentiates towards a chondrocyte lineage.[75] A microneedle-based, transdermal patch has been engineered to sense and respond to local glucose concentration, releasing insulin only when needed, during hyperglycemia.[76] An advanced artificial skin has been fabricated so to convert mechanical force into electrical signal, which may be transmitted to biological organs.[77] Moreover protocells have been synthesized from lipid vesicles and RNA molecules, that will show basic functions of living cells, such as autonomous protein production and self-replication.[78]

# General aim of the thesis

The aim of this PhD thesis is to devise new bio/non-bio interfaces, engineering their bidirectional responsivity and identifying innovative solutions for each of their key components, exploiting them for applications in different biomedical fields.

Different aspects of systems pertaining to the classes described in the previous paragraphs have been examined, with the scope to find novel solutions going beyond the state-of-the-art. In particular, the thesis contributes to the fields of interfaces with peripheral nerves, bio-hybrid tactile sensors, triggerable drug delivery system and remote cell/tissue stimulation by means of ultrasound.

In particular the research work that was done in this direction during the PhD program of the candidate, is presented in this thesis dividing it in two main topics concerning bio-non-bio interfaces, that will be treated in the following Sections: the process of sensing from the biological components and the stimulation of the biological components (see Figure 3). In particular, the first process is exploited in the field of bio-hydrid sensors and peripheral nerve interfaces, where the signal flow can proceeds from the external environment towards the inner bio-response and vice versa. The stimulation instead, will be discussed in two different ways, directly and indirectly. In the first case, the external stimuli, *i.e.* ultrasound, will be applied to target a specific bioeffect on muscle cells or the physical and chemical surface properties of the bio/non-bio interfaces will be modified in order to modulate the adhesion of cell line involved in the foreign body reaction.

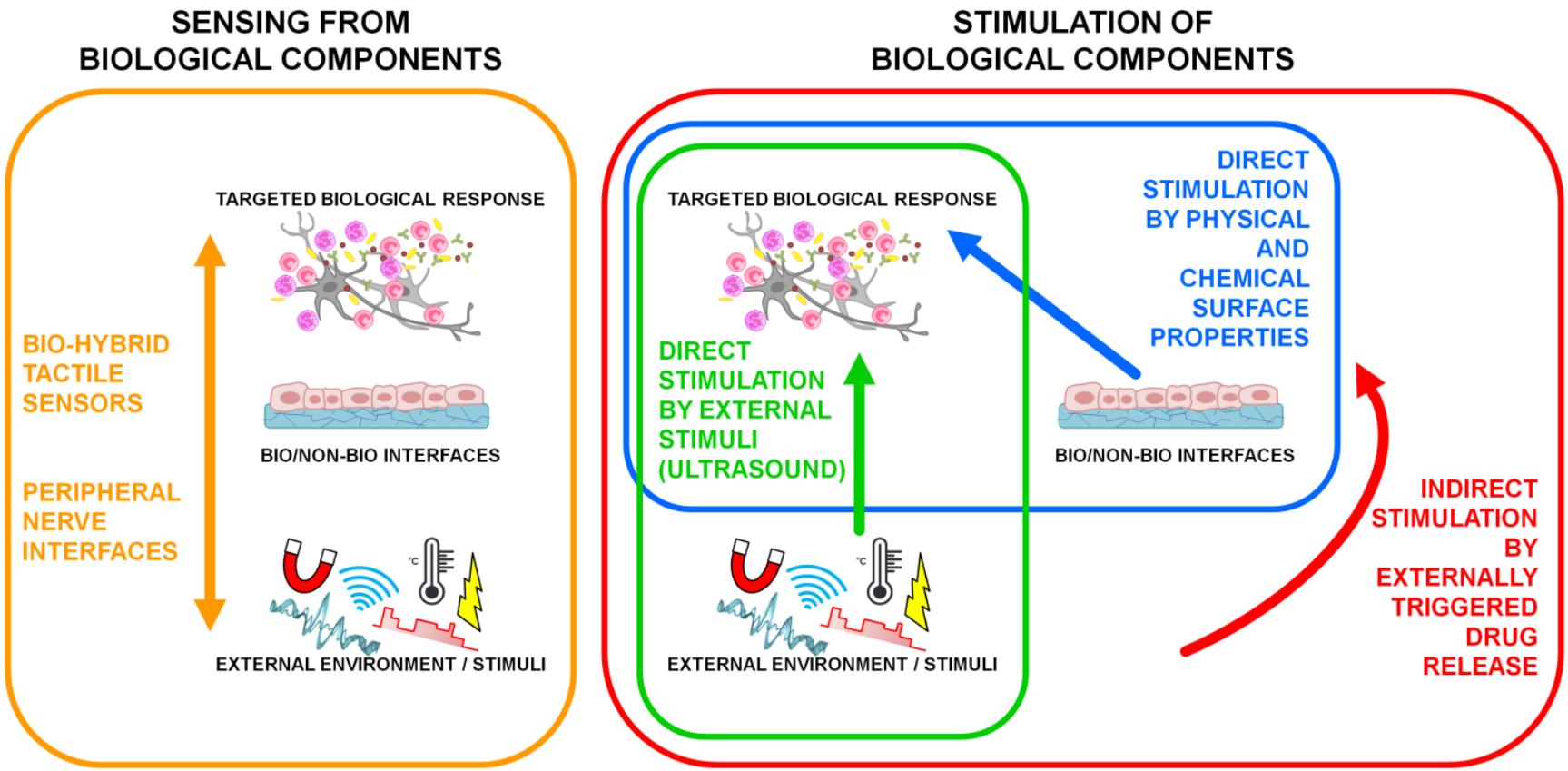


**Figure 3. The study of bio/non-bio interfaces that will be presented in this thesis.**

A detailed description of the content of each paragraph as well as an organizational workflow is provided below (see Figure 4).

We mentioned the opportunity of exploiting bio/non-bio interfaces for sensing applications from biological components and that such sensing properties could be combined with responsive ones in order to achieve a desired body response. Section 2 focuses on this topic. In particular, Section 2.1 concerns the design of an innovative bio-hybrid mechanotransduction system based on the mechanotransduction provided by kidney ciliate cells, for tactile sensing applications. Section 2.2 treats the development and the characterization of a mechanotransducer filled with different biocompatible ionic fluids, exploited also for *in vitro* cell culture. Finally, Section 2.3 presents the vision conceived in the frame of the European project M2Neural, towards the development of bidirectional responsive peripheral neural interfaces, able to provide sensing and stimulation of peripheral nerves.

Bio/non-bio interfaces can also provide stimulation of the biological component in a direct way, through the specific combination of interface properties (chemical and physical) as in the case of bioactive interfaces, or indirectly by interface modification provided with external stimuli, as in the case of responsive interfaces. We highlighted that it is crucial to study the external stimuli themselves and their engineering process as well as their bioeffects, which can determine a desired body response. Section 3 focuses on these topics and is divided in two parts: one concerning the direct stimulation of biological components and the other treating indirect stimulation. More precisely, Section 3.1.1 describes the design and the production of soft hydrogel coatings for polyimide-based neural interfaces. Such coatings were made of zwitterionic copolymers endowed with antifouling properties and low stiffness values. In Section 3.1.2 a deep analysis of the bioeffects triggered by ultrasound is reported, focusing especially on skeletal muscle cells and tissue. Finally, Section 3.2 focuses on the indirect stimulation (mediated by ultrasound) of poly(2-oxazoline) micelles, for drug delivery applications. Here, the possibility to modulate dexamethasone release from micellar carriers through ultrasonic stimulation is described.

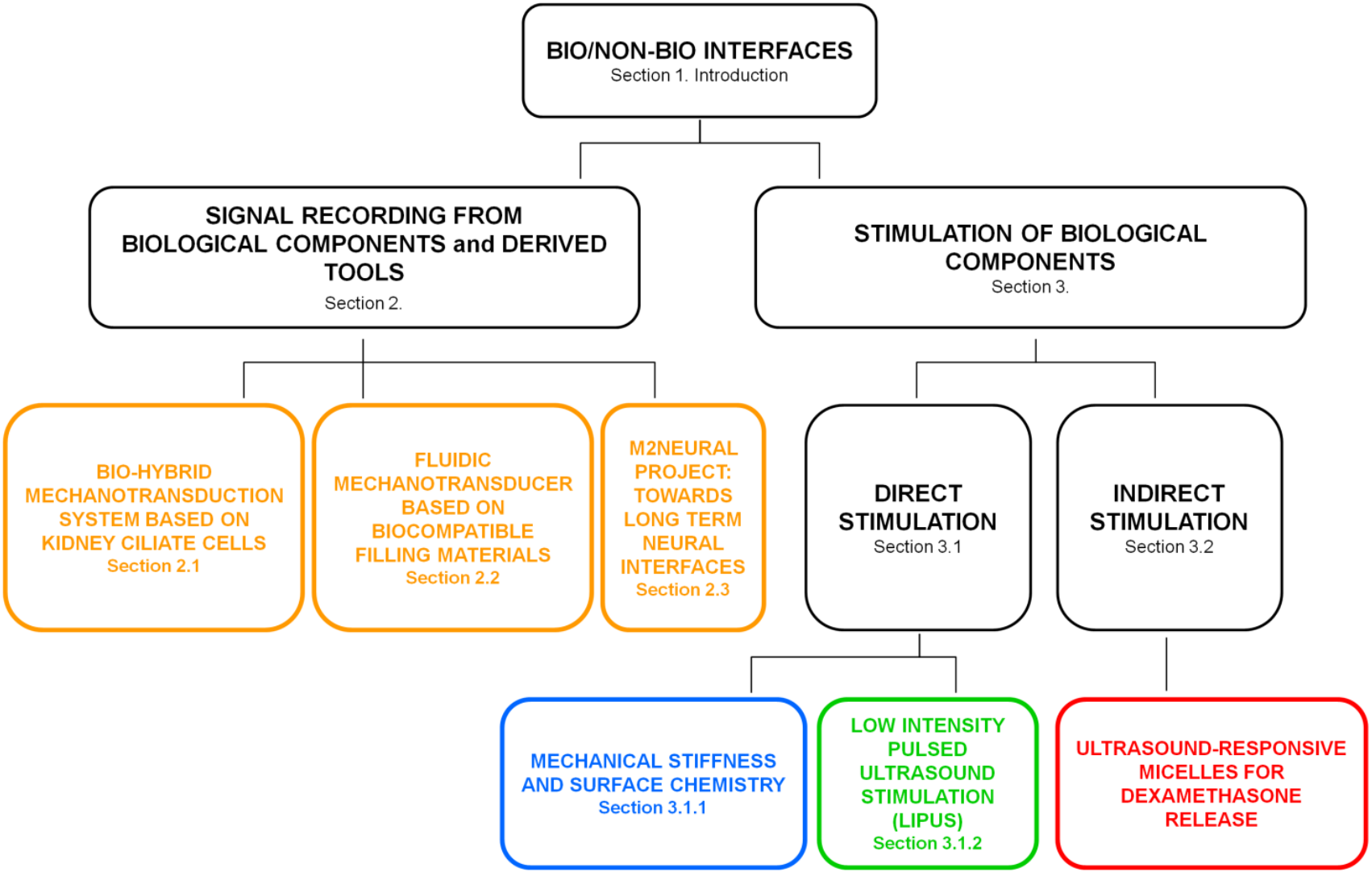


**Figure 4. Organizational workflow of the thesis work.**

# 2. Signal recording from biological components and derived tools

This Section focuses on the opportunity to exploit bio/non-bio interfaces for sensing applications from biological components, and on the fact that such sensing properties can be combined with responsive ones, thus to achieve a desired body response. In particular the mechanotransduction properties of a specific cell line are exploited in Section 2.1 in order to obtain a bio-hybrid mechanotransduction system. From this proof-of-concept, another device, not based on living cells, was derived, namely a biocompatible fluidic mechanotransducer (Section 2.2). Finally, Section 2.3 describes research efforts aimed at obtaining an advanced bi-directional interface, more precisely an advanced peripheral nerve electrode, in the framework of the M2Neural project.

# 2.1 Bio-hybrid mechanotransduction system based on kidney ciliate cells

## *Framework*

Bio-hybrid systems are emerging technological tools that integrate artificial components with living bio-systems to exploit the evolutionarily optimized, unique features of living cells/tissues for a wide range of applications.[79] Bio-hybrid retinal implants, bacteria-based chemical sensors, plasmodium-based controllers and muscle cell-based actuators are only few examples of the solutions proposed to date, whose technical feasibility is also being allowed by the advances in micro and nano-technologies. Conversely, the use of bio-hybrid systems raises some open problems such as long-term maintenance to assure stability and functionality.[80] Developing skin-like sensory systems capable to reproduce the human tactile sense is essential for applications such as neuro-prostheses[81], humanoid robotics and assistive technologies[82]. Using a bio-hybrid technological solution instead of a fully synthetic one is indeed a recent and less established trend in the design of tactile sensing systems: in the long term, such an approach could enable the development of sensors with self-healing properties, allowing regeneration and repair thanks to the embedded cells, not mentioning that these sensors may show biomimetic compliance if compared to synthetic ones[83]. Although consolidated tactile sensing technologies are based on synthetic sensors, mainly by integrating Micro Electro Mechanical Systems (MEMS) in polymeric packaging materials with soft and compliant properties[84], advancements have been achieved towards biomimetic designs of artificial skin with embedded sensors and hybrid artificial-biological microstructures[85]. BioMEMS and artificial skins can be fabricated with different classes of materials, such as artificial soft matrices, soft bio-derived structures and also biological components such as cells, tissues and proteins. Both synthetic and bio-hybrid sensing systems show an outer interface layer, mimicking the skin, and encapsulated mechanotransduction units. Considering the class of bio-hybrid tactile sensors, one of the first proposed systems consisted of a tissue engineered epidermis based on keratinocytes.

These cells were used as a covering layer for a MEMS-based capacitive tactile sensor[86]; further works exploited the mechanotransduction properties of the biological component, such as a system measuring the changes in conductivity due to fibroblast intracellular ions concentration variations by stretch-activated ion channels,[87, 88] or a prototype of a slime mould-based tactile sensor, based on *Physarum polycephalum*[89]. Such previous studies demonstrate an emerging trend towards exploiting the mechanotransduction and mechanotransmission properties of the biological component, considering it as the signalling unit of the sensor and not only as an engineered tissue-based cover/packaging. Recent results show the possibility to integrate fibroblasts as sensing elements of a bio-hybrid tactile sensor filled with an agar-based hydrogel.[73]

Along such trend, this Section reports the design and a preliminary experimental evaluation of a new bio-hybrid mechanotransduction system based on kidney epithelial cells, a cell population which demonstrates high responsiveness to mechanical stimuli due to their role of sensing elements within the organism and also to the presence of apical cilia.[90]

The work reported in this Section is published in:

**Salgarella A.R.**, Giudetti G., Ricotti L., Camboni D., Puleo G.L., Ruini F., Tonda-Turo C., Chiono V., Ciardelli G., Micera S., Menciassi A., Oddo C.M. (2015). "A bio-hybrid mechanotransduction system based on ciliate cells". Microelectronic Engineering, 144, pp.51-56.[91]

Several studies demonstrated that mechanical stimulation of these kidney epithelial cells, *i.e.* bending the mechanosensitive element as well as applying urine flow changes or hydrostatic pressure variations, ultimately causes an increase of intracellular $Ca^{2+}$ levels[92-94] also due to nucleotides release[94-96]. Much is still lacking to be understood about how the primary cilium senses flow[97] or shear stresses, some group even affirmed that primary cilia are not calcium-responsive mechanosensors [98], after changing their own previous statements[99]. A mechanism that has been proposed shows that cilium mechanotransduction response in kidney cells is mediated by interactions between members of the transient receptor potential TRP family of mechano-regulated ion channels, namely polycystin proteins: Polycystin-1 (PC1) and Polycystin-2 (PC2) as well as PKD1L1 and PKD2L1 co-localize with microtubules within the primary cilium and are shown to co-assemble and form

macromolecular complexes that act either as a $Ca^{2+}$-permeable channel[90, 100] or as a G protein-coupled receptor[101], hence allowing the initial $Ca^{2+}$ influx in the cells. It has also been proposed that this influx leads to the so called "calcium induced calcium release" from internal stores, although in a cell line-dependent way[97]. Regarding the pressure-induced $Ca^{2+}$ response, it always results in a cytosol concentration increase of these ions probably due to nucleotide release, namely adenosine triphosphate (ATP), produced by stress onto the plasma membrane[94, 97].

In this study, Madin Darby Canine Kidney (MDCK) cells were selected for integration in the system, since they constitute a robust mechanosensitive cell line characterized by a rapid growth rate [102]. The bio-hybrid sensor working principle is based on the detection of system impedance variations (implemented as voltage stimulation and current measurement). These variations are due to cellular mechanotransduction and, as stated before, this is likely caused by $Ca^{2+}$ ion concentration changes that occur both in the filler material of the sensor and within the cellular cytosol. The detection was achieved by means of a patterned gold electrode on which cells were seeded. The electrode was integrated within a custom self-contained cell culture well, sealed with a polydimethylsiloxane (PDMS) cap (Figure 5), and filled either with cell culture medium (test filling material) or with a soft agar-gelatin-genipin-based hydrogel (control filling material) [103] in order to assess sensor performance with materials showing different mechanotransmission properties (Figure 7).

# *Methods*

***Device Fabrication and cell culture set-up***

The bio-hybrid sensor was designed as a multilayered structure that is schematically represented in Figure 5a. Sensing electrodes had a geometry with central symmetry as in several state-of-the-art technologies[104, 105] and were prepared as follows: first, to improve electrode adhesion, a layer of titanium was sputtered on a cell culture grade polystyrene support (Fisherbrand™ - Fisher Scientific, USA) *via* DC magnetron sputtering (RF/DC magnetron sputtering, Kenosistec S.r.l., Italy, with sputtering parameters: 120 W, 1 min, argon atmosphere at a pressure of $10^{-5}$ bar) through a 0.5 mm wide shadow mask fabricated by wire cut electrical discharge machining (AP200L CNC Micro WEDM machine, Sodick, USA). Second, a gold layer was sputtered on the titanium one, using the same mask (sputtering parameters: 70 W, 2 min, argon atmosphere at a pressure of $10^{-5}$ bars). The sensor basement on which the electrode was placed and the well (volume 850 µL) for the cell culture were fabricated from polycarbonate and Teflon, respectively, by traditional machining techniques, and assembled by means of nylon screws. The assembly was covered with a PDMS cap (Sylgard 184, Dow Corning, USA; 2 mm thickness) and blocked with an aluminium frame. The cap was fabricated by casting PDMS (10:1 monomer/curing agent ratio) within a 3D-Printed mold (Projet HD 3000, 3D Systems, USA).

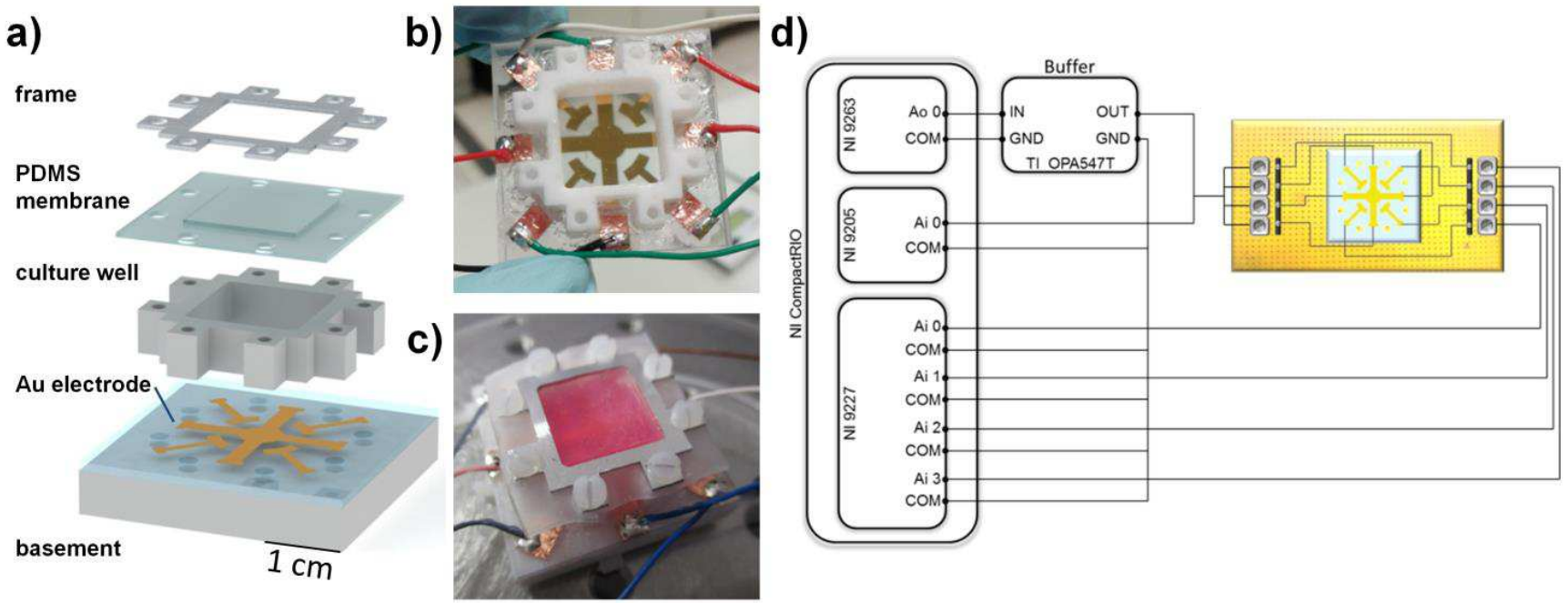


**Figure 5. Bio-hybrid mechanotransduction system. a) Exploded representation of the sensing system. b) The Au-Ti electrode sputtered on polystyrene substrate, integrated in the sensing system. c) Fully assembled sensing system filled with cell culture medium. d) Schematic diagram of sensor connections to the readout electronics. (from Salgarella *et al.*, 2015 [91])**

The parental line MDCK NBL-2 (ATCC®, USA) was selected as living transduction element, since it is characterized by a pronounced mechanotransduction activity and the presence of a consistent apical cilium, although in a heterogeneous way [102] (see Figure 6).

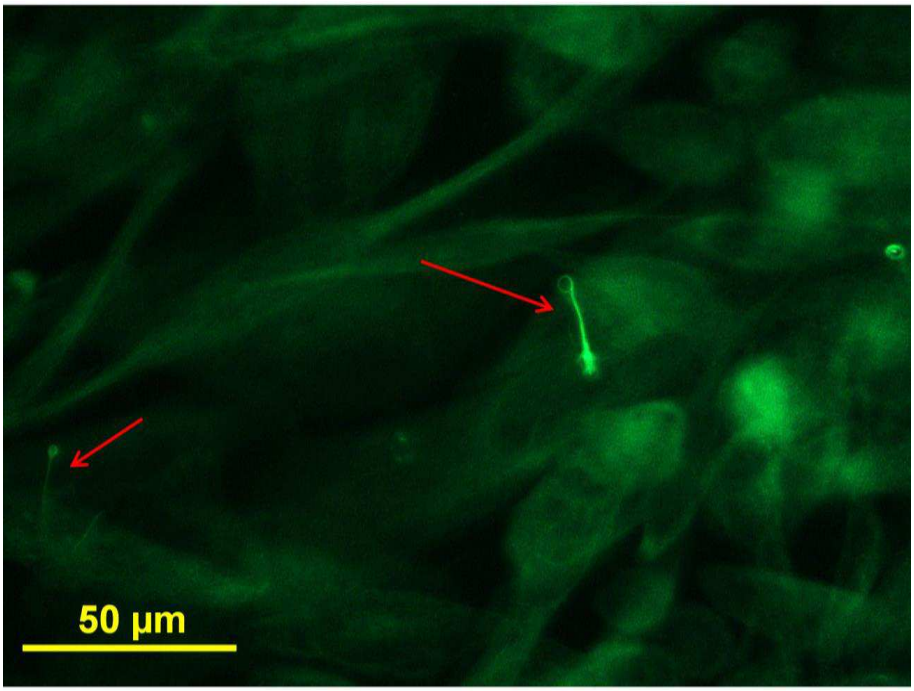


**Figure 6. MDCK cells cultured on polystyrene substrate and stained in green with immunofluorescence technique to detect α-Tubulin protein. In this image two apical cilia are showed.**

Cells were cultured in high-glucose Dulbecco's Modified Eagle's Medium (DMEM, EuroClone® S.p.a., Italy), added with Fetal Bovine Serum (FBS, Gibco® - Life Technologies, USA) to a final concentration of 10%, and Penicillin/Streptomycin (PEN/STREP, Gibco® - Life Technologies, USA) to a final concentration of 1%. In order to perform the tests, MDCK cells were propagated in a vented flask near to confluence; to harvest cells, the medium was removed and the cells were washed twice with PBS and trypsinized at 37 °C (trypsin solution: 0.25% w/v Trypsin - 0.53 mM EDTA, Gibco® - Life Technologies, USA). Trypsin activity was inhibited by adding complete medium, then cells were centrifuged (2500 rpm, 7 min, by means of an EBA 20 centrifuge, Hettich Lab Technology, Germany), re-suspended and seeded for experiments at a suitable density (118,000 cells/cm$^2$) in the sensor well (area: 1.69 cm$^2$). Cells were grown within a controlled environment (incubator, 37 °C and 5% of

$CO_2$) as a monolayer until confluence. In order to assess cellular viability on the electrode surface, a LIVE/DEAD® Viability/Cytotoxicity Assay (Molecular Probes® - Life Technologies, USA) was performed, by following the manufacturer directions.

Different cell culture set-ups were evaluated, either with hydrogel (control, Figure 7 left) or growth medium (test, Figure 7 right) used as filler of the sensor, without (control, Figure 7 up) or with (test, Figure 7 down) cells. In order to experiment the control filling material, cells were grown to confluence, then the medium was removed from the well and the hydrogel was injected over the cell layer. The hydrogel was obtained with an agar/gelatin mix at 20:80% (w/w) and cross-linked with genipin (2.5% w/w). This hydrogel has been proposed in the literature as an injectable drug delivery system and three-dimensional scaffold for peripheral nerve tissue engineering [103, 106], hence it shows good biocompatibility and good handling properties, which allow to easily fill the sensor. Moreover it has a Young's modulus of 66 kPa, which is in the range of human skin mechanical properties [107]. In particular, agar (Sigma Aldrich® Corporation, USA) and gelatin (type A from porcine skin, Sigma Aldrich® Corporation, USA) were dissolved in complete cell medium to obtain a solution at a concentration of 2% (w/v). For instance, in order to prepare a solution of 5 mL, 0.02 g of agar were dissolved in 4.2 mL of DMEM at 90 °C for 1 h. The agar solution was kept stirring in a heated bath at 50 °C, thus stabilizing the solution temperature. Then 0.08 g of gelatin were added and the resulting solution was kept stirring at 50 °C for 1 h. 50 µL of 5% w/v genipin-DMSO solution (Sigma Aldrich® Corporation, USA) were diluted in DMEM (1:4 dilution rate) and added to the agar-gelatin solution, thus obtaining a final concentration of 0.05% w/v of genipin. The resulting mix was kept stirring at 50 °C until a colour change to deep violet occurred, indicative of the first phase of the crosslinking process (genipin grafting to the gelatin chains and its partial polymerisation). Afterwards, the temperature was decreased to 37 °C, which is in the range of agar gelling temperature, still keeping stirring, and 0.5 mL of FBS and 0.05 mL of PEN/STREP were added. The mixture was transferred into a syringe where both gelatin crosslinking and agar sol-to-gel transitions were completed, leading to the formation of the hydrogel in complete growth medium ready for injection. In order to experiment the test filling material, cells were grown to confluence and the medium was replaced with fresh one, just before the experimental session.

***Sensor testing and data analysis***

A programmable automation controller (CompactRIO, National Instruments, USA) with graphical software design (Labview 2013, National Instruments, USA) was used to provide voltage stimulation and to record current signals in order to detect ions concentration variations within the well environment. Three modules were used (Figure 5d): an analog voltage output module to provide the voltage stimulation (NI 9263, 4-channel, ±10 V, 16-bit) followed by a buffer (OPA547T, Texas Instruments, USA), an analog voltage input module (NI 9205, 8-channel, ±20 mA, 16-bit) to read the voltage provided by the first module to verify lack of voltage drop along the connection wires and a simultaneous, channel-to-channel isolated analog current input module (NI 9227, 4-channel, 5 Arms, 24-bit) to read the current flowing through the sensor.

Sensor readout was implemented *via* electric stimulation provided by using a sinusoidal wave voltage with amplitude of 2 $V_p$ and a frequency of 20 Hz. For the frequency selection of the electrical signal provided to the electrodes interfaces, a preliminary assessment was performed. Firstly, it must be considered that this technology was inspired by the Electric Cell-substrate Impedance Sensing[108] (ECIS®) technique, that is a real-time, label-free, impedance-based method, used to study the activities of cells grown in tissue culture, developed by Applied BioPhysics Inc. (please refer to http://www.biophysics.com/ecis-theory.php). Differently to our system, in this technique the total current is maintained constant, voltage changes are measured and the frequency of the current is changed, depending on which is the assay to be performed. In particular "high frequency" impedance (*i.e.* higher than 2 kHz) is more affected by cell-coverage of the surface, whereas the "low frequency" responds more strongly to changes in the spaces either under or between the cells. For this reason lower frequencies were selected for cell stimulation. Moreover, a multi-frequency voltage signal was provided in order to understand which was the proper frequency to optimize the sensor functioning. This signal was constituted by a sum of 5 cosine waves each with the same amplitude of 0.5 V and with different frequencies (4, 8, 12, 16, 20 Hz). After the analysis of the sensor output signal, 20 Hz was chosen as the frequency component that provided the highest sensor output in terms of signal power. Although our

developed sensor differs a lot respect to the ECIS® one, the current that is provided to the MDCK cells (in the mA range) is lower than the one used for this impedance measurement technique, namely 1 μA, which is considered non-invasive.[109] The following experimental set-ups were tested (detailed in Figure 7): (1) Electrode without cells (control), using hydrogel as filling material (control); (2) Electrode without cells (control), using culture growth medium as filling material (test); (3) Electrode with a monolayer of MDCK cells (test), using hydrogel as filling material (control); (4) Electrode with a monolayer of MDCK cells (test), using culture growth medium as filling material (test).

In the devices integrating cells, the seeding was with the same density (118,000 cells/$cm^2$) to allow a comparative evaluation in similar conditions. The experimental sessions were performed at room temperature and they lasted a few minutes each so to avoid cellular degeneration.

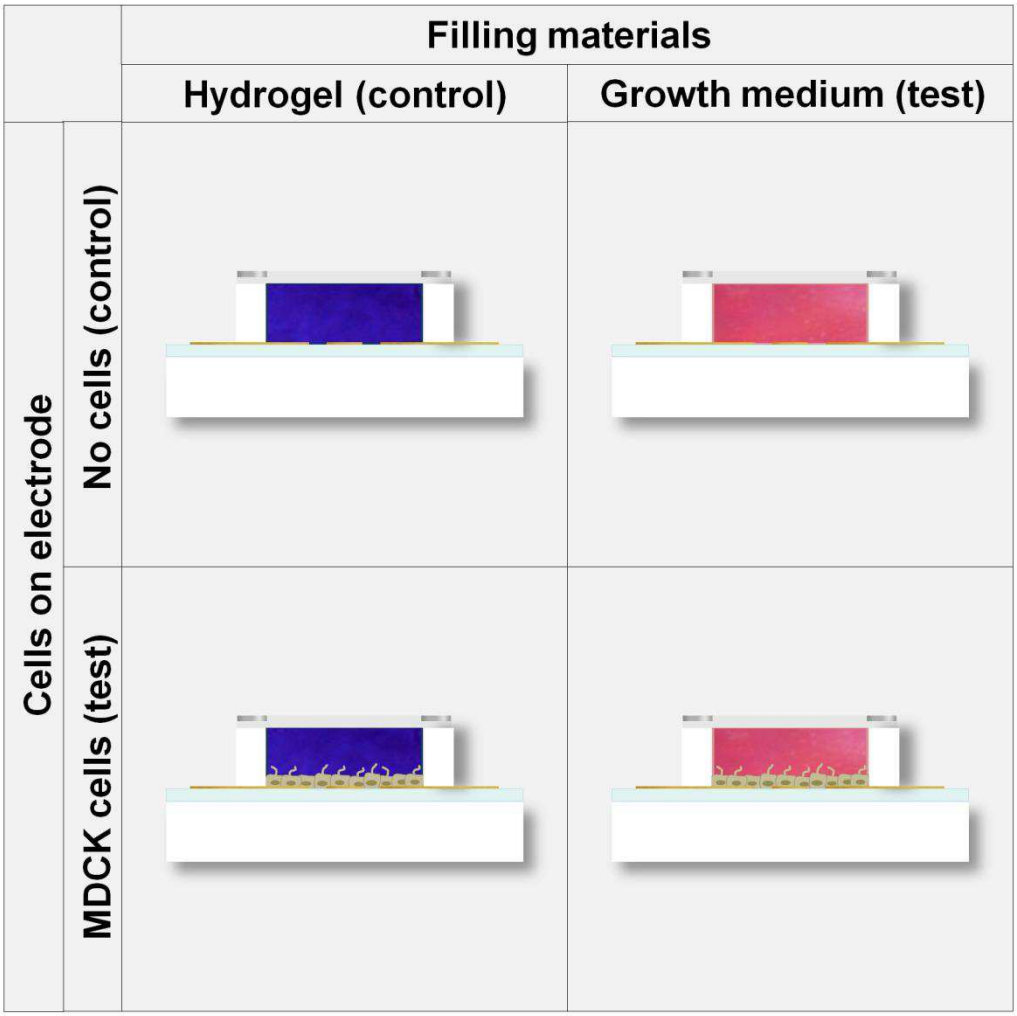


**Figure 7. Experimental set-up details. Schematic representation (not in scale) of the four experimental set-ups: electrodes without (control) or with (test) MDCK cells, and covered with hydrogel (control) or complete growth medium (test) as filling materials. (from Salgarella *et al.*, 2015 [91])**

Initially all the four set-ups were experimented with manual mechanical stimulation with a pipette tip, applying a single load. Then, all the previous set-ups were evaluated with a rectangular probe mounted on a mechatronic indenter (C-863 Mercury 1-axis DC-servo-motor controller, PI, Germany) to allow a higher degree of controllability in the mechanical stimulation and to measure (Nano 17 load cell, ATI, USA) the contact force arising while probing the sensory system.

During data analysis (Matlab 2013b, MathWorks, USA) the mean current was removed in the recorded sensor measurements, and the signals were normalized by dividing by the maximum current value. For each signal the normalized wavelet power was computed as:

$$Normalized\ wavelet\ power = \frac{|W_n^{\boldsymbol{X}}(s)|^2}{\max(|W_n^{\boldsymbol{X}}(s)|^2)}$$

where $W_n^{\boldsymbol{X}}$ is the continuous wavelet transform of the signal computed using the Wavelet Coherence Package [110]. In the case of the mechatronic indenter probing, the $R^2$ determination coefficients were computed between the forces applied and the envelope of the current signals modulating around the 20 Hz carrier frequency. To extract the envelope, the current signals were squared and filtered with a low pass Butterworth filter ($15^{th}$ order, cut-off frequency 4 Hz).

## *Results and discussion*

The cultured cells were observed to reach confluence in a monolayer, adhering promptly on the electrode surface and forming a uniform population (Figure 8a). Cellular viability assays on the electrode surface clearly showed a green fluorescent layer of healthy cells and a negligible number of dead red cells (Figure 8b).

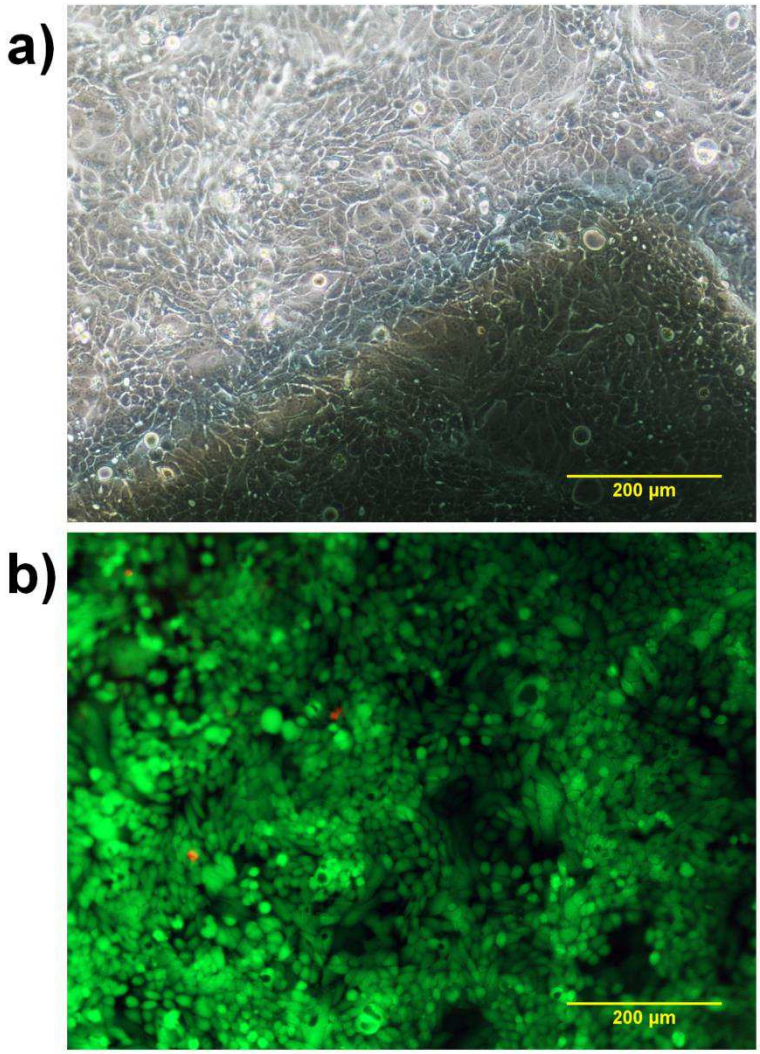


**Figure 8. MDCK cell cultures on electrode surface imaged *via* UV-VIS microscopy analysis (ECLIPSE Ti-E, Nikon Corporation, Japan). a) Bright field image (10x magnification) of MDCK cells cultured on the Au-Ti polystyrene electrode, which is visible as a shadowed region at the bottom of the picture. b) Fluorescence image (10x magnification) showing alive MDCK cells in green and dead/necrotic cells in red. (from Salgarella *et al.*, 2015 [91])**

Experiments under manual mechanical probing with a pipette tip were first carried out, in order to preliminary assess the sensor response. Results showed a limited response, consisting in a slight enhancement in the wavelet power of the signal, in the case of the electrode without cells and covered with hydrogel (Figure 9a), whereas no response could be qualitatively associated to the load stimulus in the case of the electrode without cells and filled with complete growth medium (Figure 9b). Considering the test sensors with cultured MDCK cells, different results were observed depending on the filling medium. In particular, in the set-up with MDCK cells covered by hydrogel (Figure 9c), the response was qualitatively comparable to that with hydrogel without cells. Instead, in the set-up with cells covered by complete culture medium, a pronounced response was appreciated with an inverted trend compared to the hydrogel-covered set-up, that consisted in an amplitude reduction of the current signal and the wavelet power (Figure 9d). A possible explanation is that MDCK cells respond to a mechanical load by opening membrane channels, thus producing an ion inflow in the cytoplasm as well as by the release of ATP which itself produces a transient increase in $Ca^{2+}$ intracellular levels. This possibly leads to positive charge carriers depletion within the sensor cell environment, with a consequential increment of the system impedance and reduction of measured current. The transient increase in $Ca^{2+}$ intracellular levels of MDCK cells upon mechanical stimulation (both hydrostatic pressures and fluid shear stresses) has already been demonstrated in the literature by several groups, using techniques such as real time calcium imaging (with fluorescent probes such as Fluo-4-AM[94, 96] or Fura-2[95]). This is the main reason why this cell line was selected among others, together with its robustness and easy culture routines.

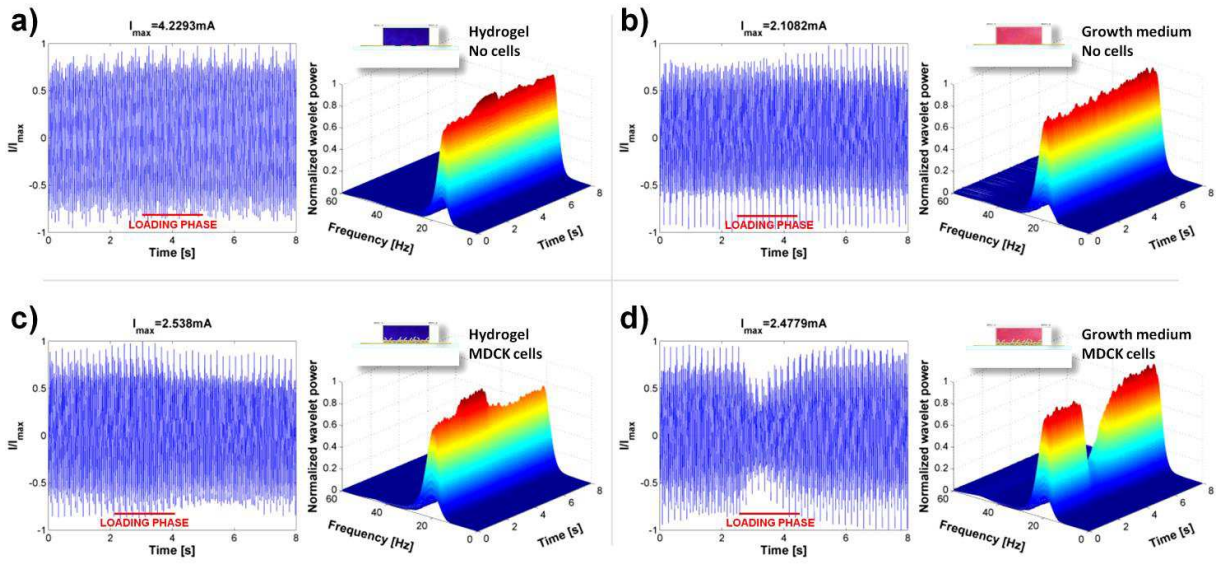


**Figure 9. Single manual mechanical stimulation. Each panel shows results for the 4 experimental set-ups in response to single manual load application: a) hydrogel without cells, b) culture medium without cells, c) monolayer of MDCK cells covered with hydrogel and d) monolayer of MDCK cells covered with culture medium. Each panel displays, on the left, the normalized current signal $I/I_{max}$, recorded from the sensor while providing a sinusoidal voltage (2 $V_p$, 20 Hz), and, on the right, the normalized wavelet power of sensor current. (from Salgarella *et al.*, 2015 [91])**

More quantitative outcomes were obtained by applying loads on the experimental set-ups by means of a servo-controlled indenter. A slight/non significant enhancement in the wavelet power of the signal in the case of sensor filled with hydrogel is shown (Figure 10a) while no significant response can be appreciated in the case of the sensor filled with growth medium (Figure 10b), thus confirming manual stimulation results. Experiments under servo-controlled application of multiple loads showed a tonic response as well as a dynamic tracking of stimulus changes in both set-ups with test MDCK cells (Figure 10c-d). A greater current modulation was systematically observed in the set-up with MDCK cells covered with complete growth medium, as observed in the previous experiments under manual probing. This could be associated with a better response of MDCK cells in the liquid environment of the culture medium, compared to the viscous environment provided by the hydrogel, since their specific function *in vivo* is to sense flow changes and hydrostatic pressure provided by urine in the kidney tubules. The determination coefficients $R^2$ (Table 1) provide evidence that for the test-device a simple linear function could model (explaining more than 60% of

the signal power) the relationship between the input load force and the envelope of sensor outputs. In fact, the fraction of explained variance $R^2$ has the highest value in the case of the sensor with a layer of MDCK cells and filled with growth medium whereas the lowest value is for the device filled with growth medium but without MDCK cells. Therefore, in the mechanotransduction process with MDCK cells a quite high input-output correlation was achieved, whereas in a previous study with fibroblasts the determination coefficient was used only to assess repeatability of the bio-hybrid sensor readouts[73].

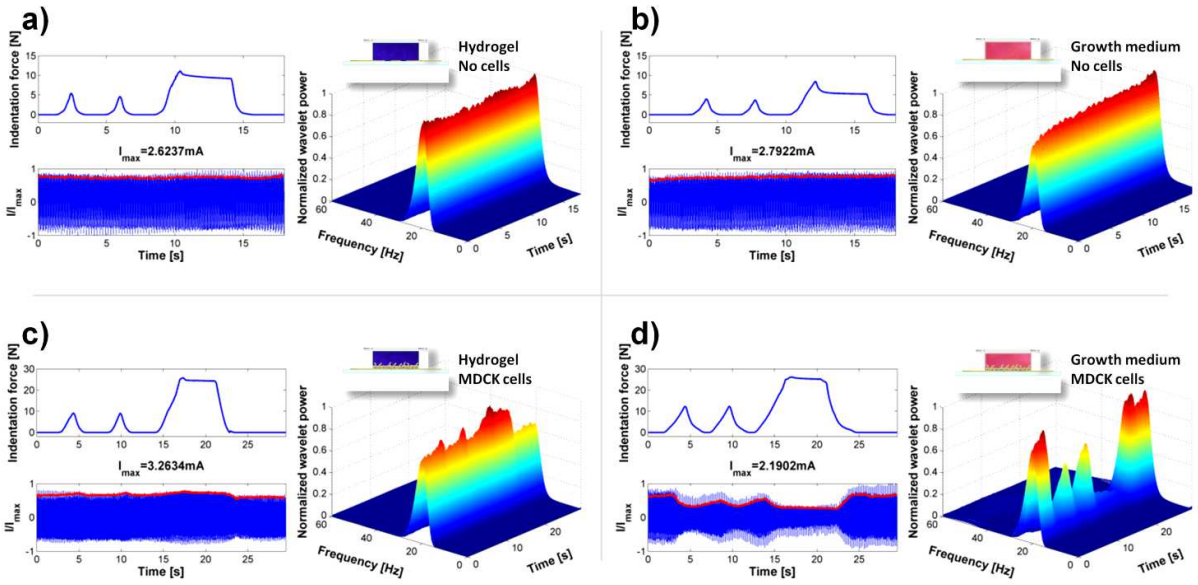


**Figure 10. Multiple load stimulation with a servo-controlled indenter. Each panel shows results for the 4 experimental set-ups in response to a multiple mechanical stimulation applied by the servo-controlled indenter: a) hydrogel without cells, b) culture medium without cells, c) monolayer of MDCK cells covered with hydrogel and d) monolayer of MDCK cells covered with culture medium. Each panel displays, on the left, time-plots of the indentation force and the normalized current signal $I/I_{max}$ (blue) and its envelope (red), recorded from the sensor while providing a sinusoidal voltage (2 $V_p$, 20 Hz), and, on the right, the normalized wavelet power of sensor current. (from Salgarella *et al.*, 2015 [91])**

| Experimental set-up | Determination coefficient ($R^2$) |
|---|---|
| Hydrogel without cells | 0.36 |
| Growth medium without cells | 0.30 |
| Hydrogel and MDCK cells | 0.59 |
| Growth medium and MDCK cells | 0.62 |

**Table 1. $R^2$ determination coefficients for the 4 experimental set-ups and testing with the mechatronic indenter.**

There are two different aspects that show promise for possible future application in the tactile field, such as for artificial prosthesis covering and skin. Firstly, the fact that the bio-hybrid transducer showed a tonic response as well as a dynamic tracking of the provided mechanical stimulus. Secondly the fact that the experimented dynamic load force range was up to about 30 N (even over the one that is typically targeted in tactile sensing for robotic hand manipulation applications[82, 111], which is up to about 10 N).

***In summary***

The developed system and its preliminary experimental evaluation demonstrate the possibility to integrate Madin Darby Canine Kidney cells as the core sensing element of a bio-hybrid mechanotransduction system. In particular, it has been shown that MDCK cells can implement mechanotransduction in an integrated sensing system. As a matter of fact, the readout system was implemented providing a voltage stimulation, and the response was recorded via measurement of current modulation. Several set-ups were evaluated, to compare the sensing system response in a liquid (cell culture medium) and viscous (hydrogel) environment. In particular, no significant response of the sensing system was observed with cell culture medium only, while a limited but observable response was qualitatively appreciated while testing the hydrogel without cells (probably because of

increase of density of charge carriers as a consequence of the mechanical compression of the hydrogel [112]). The highest sensitivity to stimulation was observed in the set-up with the monolayer of cells covered by the cell culture medium. This could be explained by the consideration that MDCK is a cell line derived from kidney, so that such cells naturally respond to fluid flow changes and hydrostatic pressure applications. Moreover, the system showed a tonic response when a continuous stimulus was provided. Recent successful tactile sensing technologies were based on fluid-filled devices with synthetic transducers [113, 114], whereas the novel technology presented in this study integrates fluidic filling material and living cellular transducers with promising future applications in prosthetics and other bio-applied domains. A thorough comparison of metrological characteristics between synthetic and bio-hybrid sensors will be targeted in the upcoming studies. Future developments will also approach system homeostasis and long-term cell viability, allowing the sensing system to become enduring and potentially usable for long periods. This would allow to fully exploit the intriguing advantages of the bio-hybrid paradigm with respect to synthetic one, such as intrinsic compliance and self-healing capabilities, with the future aim of achieving an ever deeper contact between artificial and biological components, in the field of tactile sensing

# 2.2 Fluidic mechanotransducer based on biocompatible filling materials

## *Framework*

Many fluidic force sensors have been proposed in the literature, but most of them are using non biocompatible fluids, like conductive liquid eutectic gallium-indium[115] or galistan[116-118] (a liquid metal alloy composed by gallium-indium-tin), sodium bromide[119], 1-ethyl-3-methylimidazolium tricyanomethanide[120]. Hence, a fully exploitation of these sensors is hampered in applications such as tactile feedback for minimally invasive surgery[121], delicate surgical procedures in the eye[122] and brain[123] for example, as well as tissue health diagnostics[124]. This is due to the toxicity these fluids could provide if liquid leakage occurs. For this reason, there is a trend towards the development of sensors whose working principle is based on the electrochemical impedance change measurements using simple biocompatible liquids such as deionised water[125, 126] or buffer such as Phosphate-Buffered Saline[127].

Along this trend, in this Section we present the electrical and mechanotransduction characterization of a fluidic mechanotransducer filled with different biocompatible materials.

Starting from the structure of the bio-hybrid sensor described in the above Section, a fluidic mechanotransducer was developed. The electrode shape was maintained the same one, while the well was changed (better described in the Methods subsection), thus obtaining a single soft polymeric structure made of PDMS. In this way the number of layers was reduced in order to provide an improved leakproof. As for the bio-hybrid sensor, the working principle of this transducer is based on the detection of system impedance variations (implemented as voltage stimulation and current measurement), but differently to that, these variations are due not to cellular mechanotransduction, but to the change in the cross sectional area between the electrodes, which is filled with different electrolyte materials.

This change of cross sectional area is due to the deformation of the filled PDMS well under the application of external forces, thus providing mechanotransduction. Eight different filling materials were tested, among them some were selected for their low conductivity. The mechatronic platform for fluidic transducer stimulation and the readout system were improved respect to the version used for bio-hybrid sensing in order to provide a force-controlled platform, and to allow for a precise synchronization between the recordings of the provided force and the transducers' output.

# *Methods*

***Fluidic mechanotransducer fabrication***

The fluidic mechanotransducer was designed as a multilayered structure that is schematically represented in Figure 11a. It is based on a sensing electrode covered with a soft polymeric well in which several fluid filling materials have been inserted. The electrode has the same geometry exploited in the previous work for bio-hybrid sensing[91], which was described in the previous Section. It has a central symmetry as in several state-of-the-art technologies[104, 105] thus allowing for further scalability and increase of sensing channel number. The electrodes were prepared on square polystyrene support (36 mm, Fisherbrand™ - Fisher Scientific, USA) via DC magnetron sputtering of both titanium and gold (RF/DC magnetron sputtering, Kenosistec S.r.l., Italy). Titanium was used for improving electrode adhesion, it was sputtered for 2 min on the polystyrene surface, in argon atmosphere at a pressure of $10^{-5}$ bar, at 120 W through a 0.5 mm wide shadow mask fabricated by wire cut electrical discharge machining (AP200L CNC Micro WEDM machine, Sodick, USA). Second, a gold layer was sputtered on the titanium one, using the same mask (sputtering parameters: 75 W, 2 min, argon atmosphere at a pressure of $10^{-5}$ bars). The electrode is placed on a polycarbonate basement and covered by the polymeric well. The polymeric well is blocked to the assembly by means of a polycarbonate frame and 8 nylon screws. All polycarbonate pieces were fabricated by traditional machining techniques, while the soft well was fabricated by casting polydimethilsiloxane (PDMS, Sylgard 184, Dow Corning, USA; 2 mm thickness) with a monomer/curing agent ratio of 10:1, within an aluminium mold.

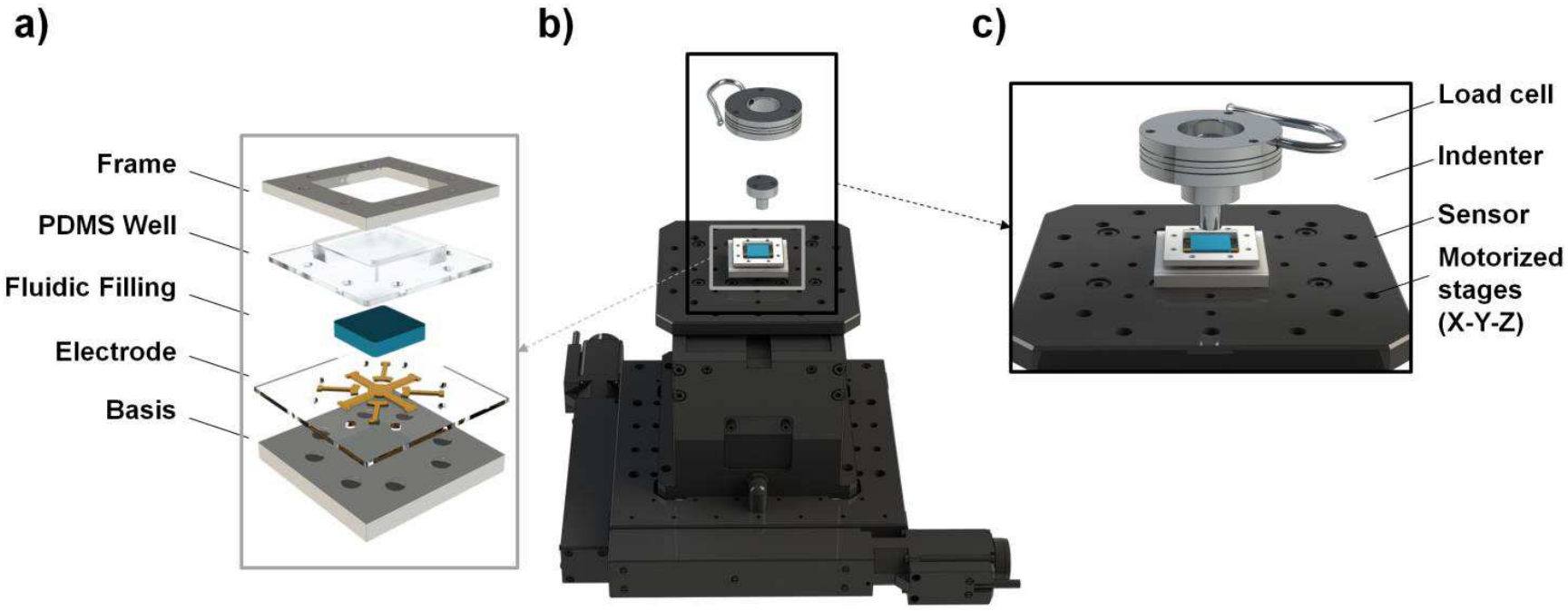


**Figure 11. Fluidic mechanotransduction system and its mechatronic stimulation platform. a) Exploded representation of the sensing system. b) and c) 3D-rendering of the stimulation platform and a zoom in on its components: the motorized translational stages (3 degrees of freedom, DOFs), a fixed indenter and a load cell.**

***Mechatronic platform for fluidic transducer stimulation and readout system***

The mechanical stimulation was provided by means of a force controlled mechatronic platform constituted of two motorized translational stages (3 degrees of freedom, DOFs), a fixed indenter and a load cell (see Figure 11b and c).

One stage was used to provide lateral motion on x and y axes (8MTF-102LS05, STANDA, Vilnius, Lithuania), while the other, mounted on top of the lateral stage, was used for vertical motion on the z axis (8MVT120-25-4247, STANDA, Vilnius, Lithuania). Both stages were characterized by a high precision positioning and smooth travel. Their motion was provided step by step with a tunable speed and different resolutions, respectively 2.5 µm for the xy stage, and 5 µm for the z one. The two stages were linked each other within a rigid frame and the sensor was blocked on top of the z stage. In order to provide mechanical stimulation, the sensor was moved towards a fixed cylindrical indenter, mounted facing the upper face of the z stage and made of aluminium (with a diameter of 6 mm). The indenter was coupled to the lower face of a 6 axis load cell (Nano 43, ATI Industrial Automation, Apex, NC, USA) able to measure the forces provided to the sensor during the indentation. The measured normal forces (due to the contact between the sensor and the indenter) enabled the control of the stages motion, hence providing precise mechanical stimulation protocols.

A programmable automation controller (CompactRIO 9114, National Instruments, USA) was used to provide voltage stimulation, sensor signal readout and synchronization between data acquisitions (see Figure 12). It was equipped with an analog voltage output module (NI 9263, 4-channel, ±10 V, 16-bit), an analog voltage input module (NI 9205, 8-channel, ±20 mA, 16-bit) and a digital I/O module (NI 9401, 8-channel, 5V/TTL, 100µs, bidirectional).

In particular the sensor was provided with a voltage stimulation by means of NI 9263 module, followed by a buffer (OPA547T, Texas Instruments, USA). The buffer allowed to provide a stable output stimulation voltage despite system impedance changes. A sinusoidal wave voltage $V_{IN}$ with amplitude of 0.5 $V_p$ and a frequency ranging between 10 to 100 Hz was provided to the central part of the electrode (cross shape). The current flowing through the sensor was collected by the four slanting electrode channels (I0-I3) and converted to voltage thanks to a TIA (transimpedance amplifier), made with Texas Instrument© OPA 4277

configured as a TIA with a gain of 22 kΩ. The four converted voltage signals (V0-V3) were read by NI 9205 module. Please refer to Figure 12b and c.

The load cell was connected to a data acquisition card (Ni DAQ PCIe 6259) for signal conditioning and data recording. A main clock of 800 Hz was generated from the DAQ card and shared with the CompactRIO (through NI 9401 module) in order to synchronize the data acquired from the load cell and from the different modules of the CompactRIO. The DAQ card and the CompactRIO were connected to the same computer while the controller of the translational stages was connected to another computer. The two computer shares the data of the forces and the position of the translational stages through an Ethernet connection in order to implement the force closed loop control. Both the computer and the CompactRIO were equipped with a graphical programming software (Labview 2017, National Instruments, USA), Please refer to Figure 12a for block diagram of the system.

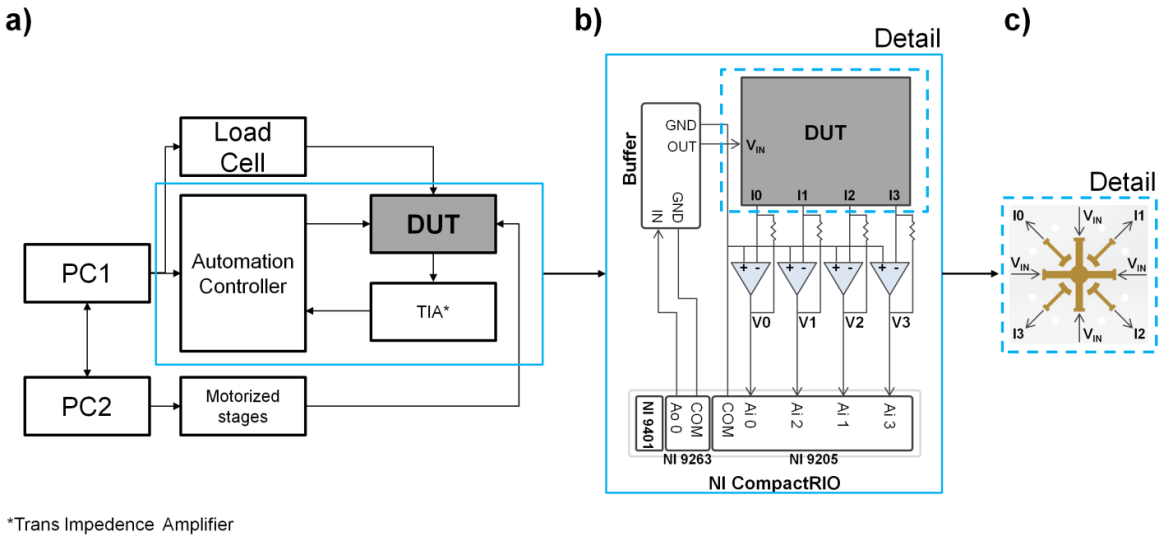


**Figure 12. Mechanotransducer readout system and force closed loop control. a) Block diagram of the force closed loop control implementation and signals synchronization. b) and c) Schematic diagram of sensor connections to the readout electronics, including the amplification stage.**

***Sensor testing and data analysis***

Different biocompatible and non toxic filling materials were used to fill the soft polymeric well of the sensor, prior to its assembly. Namely they are: (1) ultrapure MilliQ water, (2) saline solution (NaCl 0.9% wt/vol in water) (3) Dulbecco's Phosphate-Buffered Saline (DPBS), (4) high-glucose Dulbecco's Modified Eagle's Medium (DMEM), (5) complete cell growth medium composed by high-glucose DMEM, added with Fetal Bovine Serum (FBS) to a final concentration of 10%, and Penicillin/Streptomycin (PEN/STREP) to a final concentration of 1%, (6) FBS in deionized water to a final concentration of 10% v/v (FBS is a mixture of plasmatic proteins like albumin, growth factors, salts, vitamins and electrolytes used to sustain *in vitro* cell culture), (7) silk fibroin solution 5% wt/vol in deionized water, extracted from *Bombyx mori* cocoons by the team of Professor Silvestro Micera, following the protocols described in [128], (8) silk fibroin gel prepared from the previous solution following the procedure explained in [129]. In particular (1), (7) and (8) were selected for their expected low conductivity.

The sensor with each filling material was electrically and mechanically tested.

In the first case, the $V_{in}$ provided was a sinusoidal wave voltage with amplitude of 0.5 $V_p$ and a set of frequencies, chosen from 10 to 100 Hz with a 10 Hz step. For each frequency the stimulation duration was of 10 s and sensor readouts were collected. The complex impedance of the system, Z, was computed as

$$Z = I_{out}/V_{in}$$

being $I_{out}$ = I0-I3 the sensors readouts, and provided as module, $|Z|$,

$$|Z| = |I_{out}|/|V_{in}|$$

and phase, $\Phi_Z$,

$$\Phi_Z = \Phi_{Iout} - \Phi_{Vin}$$

as a function of the frequency in Figure 14. The obtained system impedance Z was then fitted by means of MATLAB® software (MathWorks, Massachussets, USA) and its function for

non linear regression, *nlinfit*, using the equation of an electrical equivalent circuit impedance proposed by Gutierrez *et al.* [125] as the model function (Figure 15a). The equation is as follow:

$$Z_{fit}(\omega) = R_s + 2\,R_{ct}/(1 + j\omega R_{ct} C_{dl})$$

were $R_s$ is the electrolyte/filling material resistance, while $R_{ct}$ and $C_{dl}$ describe phenomenon at each electrode interfaces, which in this case are the cross shaped central electrode and one of the four slanting electrode channels. The goodness of the fitting (expressed as *R* coefficient) and the parameters found for each filling material are reported in Table 2.

Considering the mechanical stimulation, the sensor filled with the different materials was provided with a sinusoidal voltage $V_{in}$ of 0.5 $V_p$, at 20 Hz and with five consecutive normal indentations with different forces (range: 1 - 5 N, step:1 N). The stimulation was applied in the centre of the sensor, thanks to the movement of the z stage at a speed of 0.125 mm/s. The modulating sensor readouts from each channel ($I_{out}$ = I0-I3) were normalized by dividing for the maximum current values and the mean value was subtracted. To extract their envelope ($\Delta I_{out}$ due to mechanical load application), the signals were time-aligned with the normalized $V_{in}$ voltage and multiplied by it, then filtered with a low pass Butterworth filter ($5^{th}$ order, cut-off frequency 10 Hz), as shown Figure 13. $R^2$ determination coefficients were computed between the normalized forces applied and the $\Delta I_{out}$ of each channel. The $\Delta I_{out}$ of the channel which gave the highest $R^2$ value and the respective normalized forces applied to the transducer are reported in the graphs of Figure 16 for each filling material tested.

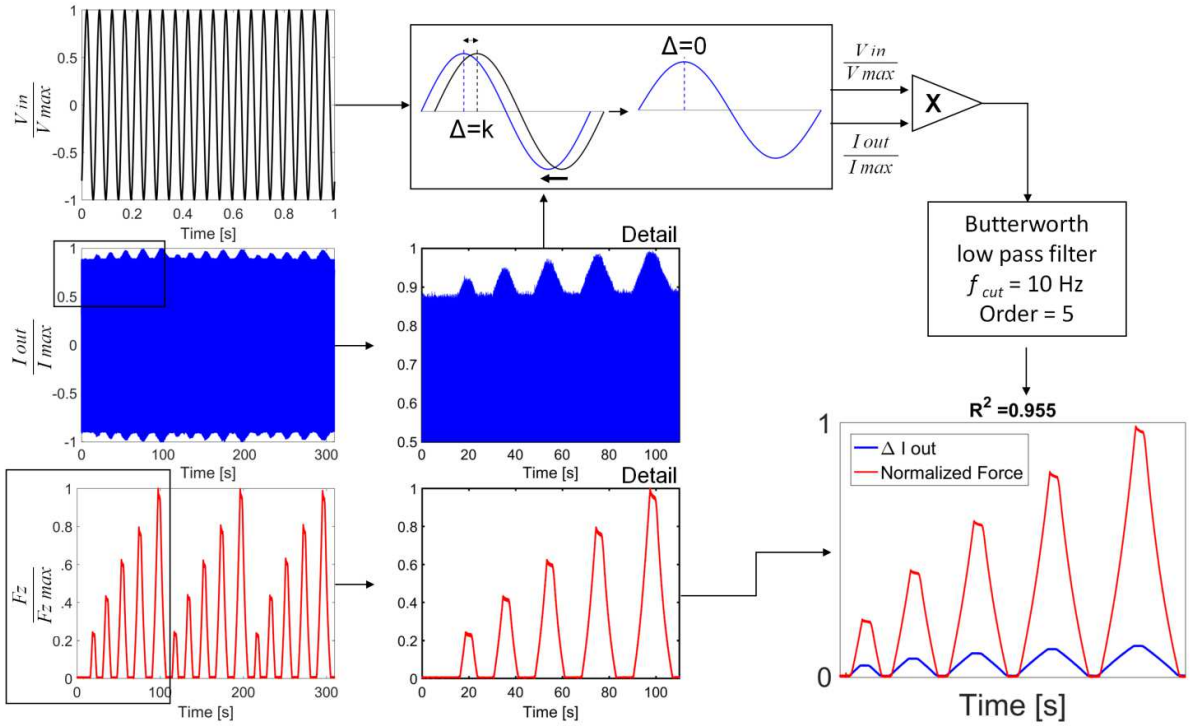


**Figure 13. Signal processing to obtain the current modulation due to the mechanotransduction, $\Delta I_{out}$. The normalized stimulation voltage $V_{out}$ is represented in black color, the normalized transducer output $I_{out}$ in blue and the normalized applied force $F_z$ in red**

## *Results and discussion*

The electrical characterization of the transducer filled with different materials is depicted in Figure 14. In particular Figure 14a and Figure 14b show respectively the module, $|Z|$, and the phase, $\Phi_Z$, of the complex impedance of the system, Z, as a function of the frequency. For all the materials a preliminary reduction of the $|Z|$ in the range of 10-20 Hz was seen, reaching then a plateaux for the following tested frequencies, while an almost linear increment of $\Phi_Z$ with the frequency was appreciated for all the material except for the MilliQ water, Silk fibroin solution and gel.

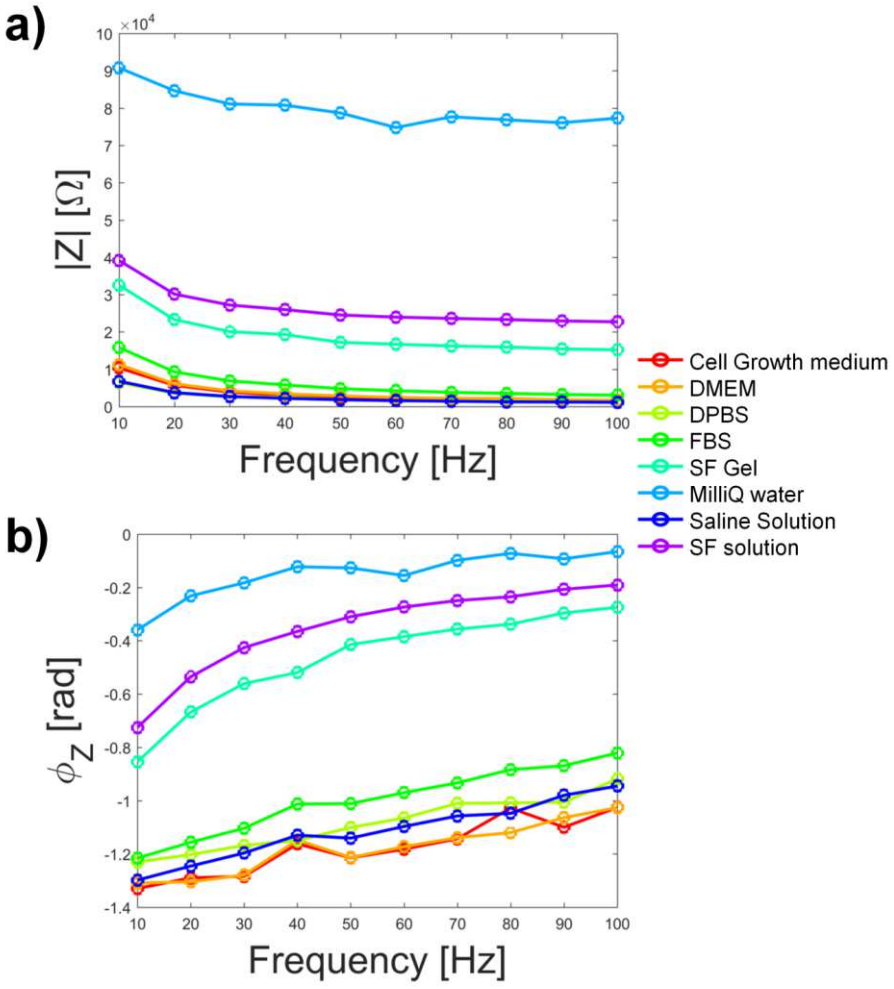


**Figure 14. Module a) and phase b) of the complex electrical impedance of the mechanotransduction system (*Z*) filled with eight different materials, as a function of the frequency.**

As already stated in the Methods subsection, the obtained system impedance Z was then fitted by non linear regression analysis using, as model equation, the one of an electrical equivalent circuit impedance proposed by Gutierrez *et al.* [125] (showed in Figure 15a). A representative graph of both experimental (in red) and fitted (in blue) $|Z|$ and $\Phi_Z$ is shown in Figure 15b. The parameters obtained by the non linear regression are reported in Table 2 as well as the goodness of the fitting expressed as R coefficient values for both module and phase of the complex system impedance, *Z*.

The fitting achieved with this model was almost very good for all the filling materials and for all the four recorded channels (all R coefficients were > 0.9, except for the fitting of $|Z|$, in case of channel I2 of the sensor filled with MilliQ water).

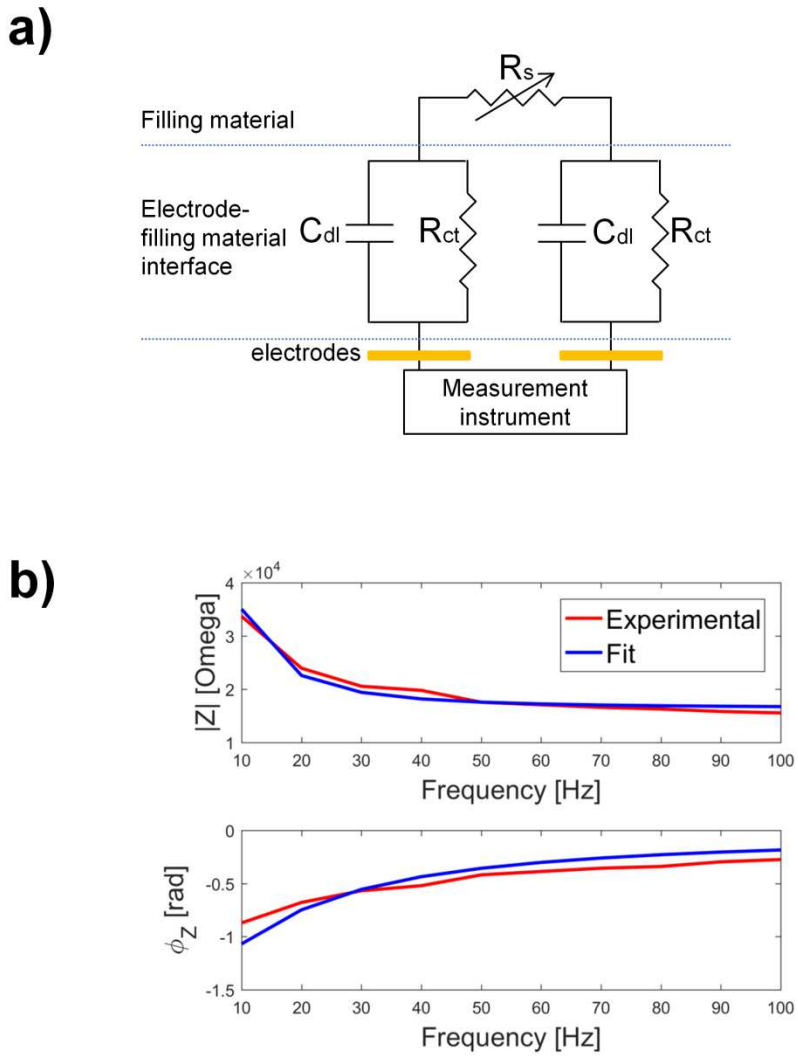


**Figure 15. a) Equivalent electrical circuit used to model the electrical behavior of the mechanotransducer. b) Example of the experimental (red) and fitted (blue) module and phase of the sensor electrical impedance obtained by linear regression. The model parameters and the R coefficients for both module and phase are reported in Table 2.**

| Filling Material | Channel | $R_s$ [kΩ] | $R_{ct}$ [MΩ] | $C_{dl}$ [μF] | R ( \|Z\| ) | R ( $\Phi_Z$ ) |
|---|---|---|---|---|---|---|
| MilliQ water | I0 | 73.93 | 0.90 | 0.66 | 0.970 | 0.981 |
| | I1 | 77.58 | 1.00 | 0.62 | 0.912 | 0.974 |
| | I2 | 92.33 | 6.06 | 0.55 | 0.872 | 0.983 |
| | I3 | 108.28 | 0.95 | 0.53 | 0.910 | 0.971 |
| Saline solution | I0 | 1.07 | 0.58 | 5.17 | 0.996 | 0.969 |
| | I1 | 1.08 | 0.60 | 4.63 | 0.997 | 0.981 |
| | I2 | 1.28 | 0.65 | 3.61 | 0.996 | 0.946 |
| | I3 | 1.18 | 0.64 | 3.75 | 0.997 | 0.981 |
| DPBS | I0 | 1.14 | 0.57 | 5.32 | 0.997 | 0.970 |
| | I1 | 1.20 | 0.58 | 4.88 | 0.992 | 0.964 |
| | I2 | 1.22 | 0.64 | 3.74 | 0.997 | 0.915 |
| | I3 | 1.07 | 0.63 | 3.91 | 0.998 | 0.942 |
| DMEM | I0 | 1.46 | 0.65 | 3.52 | 0.997 | 0.951 |
| | I1 | 1.55 | 0.72 | 2.80 | 0.998 | 0.941 |
| | I2 | 1.45 | 0.79 | 2.37 | 0.998 | 0.966 |
| | I3 | 1.48 | 0.82 | 2.25 | 0.997 | 0.926 |
| Cell growth medium | I0 | 1.64 | 0.70 | 2.95 | 0.996 | 0.965 |
| | I1 | 1.38 | 0.70 | 3.03 | 0.998 | 0.934 |
| | I2 | 1.32 | 0.73 | 2.75 | 0.997 | 0.940 |
| | I3 | 1.64 | 0.83 | 2.19 | 0.995 | 0.929 |
| FBS | I0 | 3.27 | 0.88 | 1.88 | 0.992 | 0.990 |
| | I1 | 3.19 | 0.85 | 1.97 | 0.992 | 0.990 |
| | I2 | 3.55 | 0.96 | 1.68 | 0.994 | 0.993 |
| | I3 | 3.77 | 1.00 | 1.61 | 0.993 | 0.991 |
| Silk Fibroin solution | I0 | 24.63 | 1.08 | 0.93 | 0.981 | 0.995 |
| | I1 | 23.57 | 1.03 | 0.97 | 0.982 | 0.996 |
| | I2 | 24.62 | 1.07 | 0.93 | 0.981 | 0.995 |
| | I3 | 25.01 | 1.07 | 0.93 | 0.982 | 0.995 |
| Silk Fibroin gel | I0 | 15.46 | 1.10 | 1.08 | 0.981 | 0.992 |
| | I1 | 16.13 | 1.08 | 1.08 | 0.980 | 0.992 |
| | I2 | 17.73 | 1.12 | 1.01 | 0.980 | 0.992 |
| | I3 | 16.45 | 1.12 | 1.04 | 0.982 | 0.993 |

**Table 2. Model parameters estimated by non linear regression and R coefficients for the fitting of both impendance module and phase.**

The values obtained for $R_s$, which in the model represents the electrolyte/filling material resistance, is in the range of few kΩ, except for MilliQ water (from 73.93 to 108.28 kΩ), Silk Fibroin solution (from 23.57 to 25.01 kΩ) and Silk Fibroin gel (from 15.46 to 17.73 kΩ). This is

in accordance with the fact that these materials were chosen for their low electric conductivity. $R_{ct}$ and $C_{dl}$, which in the model describe phenomena at the electrode/electrolyte interfaces, were respectively in the range of MΩ and µF.

The fact that different model parameters values were found for the different channels can be partially explained by the "handicraft" production procedure of electrodes and overall transducers; this could be improved by using engineered and automated microfabrication techniques.

Concerning the mechanical stimulation of the fluidic transducer, the results obtained are shown in Figure 16. Experiments under servo-controlled application of multiple loads showed current modulation in terms of amplitude increase for all the tested filling materials, except for MilliQ water, that did not provide mechanotransduction. In particular Figure 16 shows the graph of the simultaneous normalized force and the current modulation, $\Delta I_{out}$, recorded for each filling material and for the channel that provided the highest determination coefficient between these two signals.

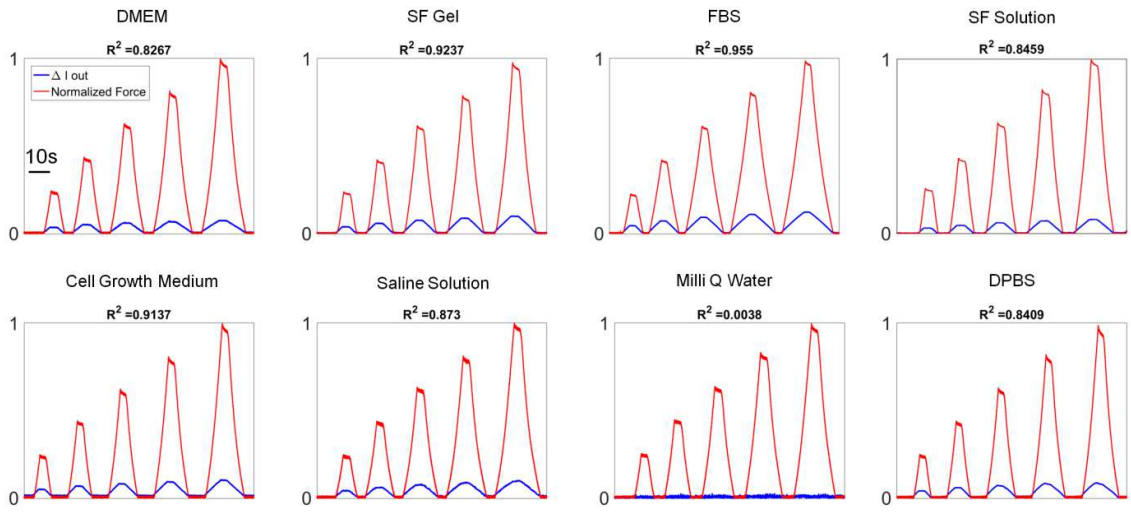


**Figure 16. Graphs representing the force applied to the sensor and the respective current modulation $\Delta I_{out}$. The determination coefficients $R^2$ reported on top of the graphs for each filling material, are the highest ones obtained among the four sensor output channels.**

The determination coefficients $R^2$ provide evidence that for all the filling materials, except MilliQ water, a simple linear function could model the relationship between the input load force and current modulation of sensor outputs, explaining more than 90% of the signal power, in some cases. In fact, the fraction of explained variance $R^2$ showed that a high input-output correlation was achieved, reaching the highest value for the sensor filled with FBS in deionized water to a final concentration of 10% v/v.

***In summary***

We developed and tested a fluidic mechanotransducer filled with different materials, usually used for cell culture routines, starting from an electrode system used for bio-hydrid sensing. The working principle of such device is the measurement of electrochemical impedance changes due to mechanical stimulation. This approach follows the recent trend of creating flexible force sensors by using non toxic filling material such as deionised water and PBS, like the ones proposed by Gutierrez *et al.*[125-127]. The aim of this trend is to provide reliable and high sensitive sensors for delicate applications involving minimally invasive surgery, where "less biocompatible" solutions could provoke tissues damages in case of breakage. The solutions proposed by Gutierrez *et al.*[125-127] allowed for the detection of forces from 0 up to 79 mN. This very low range is far below the one usually targeted by fluidic sensors systems, filled with toxic fluids (few N [117, 120]) which are geared towards general surgical gripping and grasping tasks (from 0.1 up to 10 N [130]).In our system, we tested, both electrically and mechanically, eight different filling material which are often used in cell culture laboratories, from simple ultrapure water to complete cell growth medium. Except for the case of MilliQ ultrapure water, all tested materials provided very good mechanotransduction, confirmed by the high determination coefficients, $R^2$, we found also in the case of the silk fibroin solution and gel, which are characterized by lower conductivity.

Our tested forces are in the range of those used to characterize other fluidic sensors [117, 120], but the fact that a dynamic tracking of the force stimulus was achieved by the mechanotransducer, lead us to think that a deeper characterization will disclose if a lower sensitivity is achievable with the different filled materials. This was done and will be deepen

in the future thanks to the proper readout system and force-controlled platform which allowed for a precise correlation between the force applied to the transducer and its output signals. This platform can be used also for the validation of other sensing system and mechanotransducers. Our system is far away from being considered a fully functioning force sensor, but thanks to its tunable and flexible characteristic and to the developed stimulation structure, it can be used as a platform for the test of different filling materials and their application for electrochemical impedance based force sensing.

# 2.3 M2Neural project vision: toward long term neural interfaces

## *Framework*

Neural interfaces are active medical devices aimed at restoring nervous system functions in case of impairments. Peripheral nerve interfaces, in particular, can provide a direct connection between the peripheral nervous system (PNS) and an external artificial device. They can be used to control limb prostheses bidirectionally, that means both recording the signals from the PNS to control the artificial devices and stimulating nerves to restore afferent pathways, *e.g.* the sense of touch in hand prostheses.[81] Neural interfaces in general can also be used to face other diseases/injuries in which the peripheral nerve function is compromised, such as neuropathies, spinal cord injury, deafness, blindness, stroke, urinary incontinence, epilepsy, chronic pain, neurological disorders, and psychiatric disorders. The latest ones are further pathologies that can be treated by electrically stimulating the nervous system by means of active implantable medical devices.[131]

Neurotechnology has grown and matured as an industry thanks to the advances in several fields of science and technology, including neuroscience, biomaterials and microelectronics. MEMS technology had a positive impact on the development of neurotechnology devices. Moreover these products and services will experience considerable growth in the worldwide healthcare market, in large part because of the continued growth and identification of neurological disorders and conditions. Many of these disorders and conditions will become even more pronounced as the demographic shift in the aging of the population will exert its effects, as well as the life expectancy and demand for a higher quality of life by senior citizens. Neurotech Reports projected, in their Market Research Report 2016-2020, that the overall worldwide market for neurotechnology products was $7.6 billion in 2016 and will reach $12.0 billion in 2020.[132] Neurotech Reports divides the market for neurotechnology into four segments: neuroprosthetics, neuromodulation, neurorehabilitation and neurosensing. The largest segment of the market for neurotechnology is currently

neuromodulation, followed by neural prostheses, and neurosensing. Today hardware market is just the tip of the iceberg, as illustrated by an analysis of more than 10,000 IP filings worldwide by a market research firm, SharpBrains[133]. Therefore, innovative products based on novel advanced materials could drive and increase the estimated market annual growth rate. Also, successful neuroprosthetics have been shown to be cost-effective because of the reduction in ongoing costs for healthcare and assistive services. Some studies have shown that these devices pay for themselves with five to seven years.

The bottleneck of this approach remains biocompatibility and long-term implant stability/functionality. An improved interface based on advanced multifunctional materials has the potential to revolutionize invasive nerve interfaces, and thus neuroprosthetic technologies. Such technological advancement would provide enormous benefits for people with neurological disorders or amputations. In addition, it could be also exploited in other health conditions, as stated before, normally treated by stimulation of the peripheral nervous system (PNS) by using active implantable medical devices (AIMDs), *e.g.* chronic pain and incontinence.

Chronic implant of electrodes in the PNS leads to the formation of scar-like fibrotic tissue and low axonal health, determining a loss of functionality after few months from the implant[134], thus strongly limiting their clinical use. In fact both the insertion of the electrode and its permanence in the body cause peripheral nerve injury and lead to responses such as neuropathic pain and fibrosis. This determines the replacement of active tissues with passive ones, bringing to a consequent loss of electrode's functionality.[135] This non-desired host response is mostly due to the mismatch of both biochemical and mechanical properties between the electrode surface and the nerve tissue.[136] Recent strategies to partly overcome these problems focused on polyimide surface functionalization, for example with amino acids or peptides[137] and on engineered coatings, *e.g.* based on poly(ethylene glycol) (PEG)[35, 138].

## *M2Neural focus*

The focus of M2Neural project, funded in the FP7 M-ERA.NET Transnational framework, is the development of an advanced novel multifunctional polymeric coating for polyimide based peripheral nerve interfaces. In particular M2Neural project focuses on the surface modification of a particular type of polyimide-based electrode used for interfacing the PNS, called SELINE[139] (SELf-opening Intrafascicular NEural interface), which is commercialized by SMANIA S.r.l.

A scheme of the overall concept is represented in Figure 17.

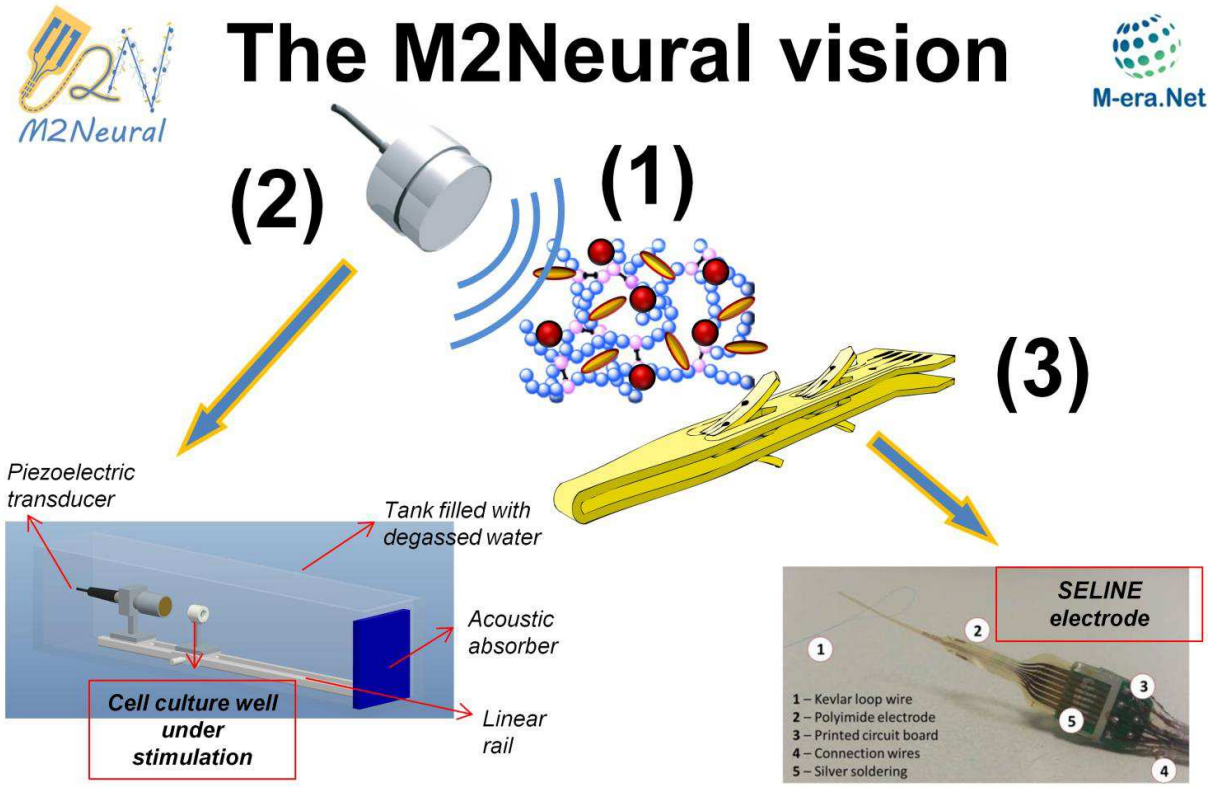


**Figure 17. Concept representation of M2Neural project and its main elements. (1) Biocompatible and nondegradable soft polymeric coating doped with anti-inflammatory/neurotrophic factors and piezoelectric nanoparticles to reduce inflammation and promote neural health. (2) Tunable external ultrasound stimulation system to cause local mild hyperthermia and to activate piezoelectric nanoparticles. (3) Coating of a polyimide-based electrode used for interfacing the PNS, SELINE (SELf-opening Intrafascicular NEural interface) commercialized by SMANIA S.r.l.**

The desired multifunctional polymeric coating should be able to:

minimize the mechanical mismatch between the implanted device and the tissue by means of a soft coating made of a biocompatible synthetic polymer. The target is a biocompatible and non-degradable hydrogel with a thickness in the micrometer range, capable to minimize both the mechanical and chemical mismatches between the implanted electrodes and the peripheral nerves. This can be achieved with a tuned Young's modulus mimicking the one of neural tissues (~ 1 kPa);

promote neural health by means of embedded piezoelectric nanoparticles such as in the hydrogel layer, able to provide neurons with indirect electrical stimuli when activated by external mechanical stimulations, *i.e.* ultrasound. In the literature, an enhancement of neurite outgrowth in neuronal-like cells following piezoelectric particles-mediated stimulation has been demonstrated using boron nitride nanotubes (BNNT)[140] as well as significantly increase of the intracellular calcium concentration using barium titanate nanoparticles (BTNP)[141]. Hence, we envision a tunable external ultrasound stimulation causing local mild hyperthermia and activating piezoelectric nanoparticles during few weeks after the implant would dramatically improve neural health;

further increase the level of electrode performance in terms of biocompatibility and axonal health by means of neurotrophic factors and anti-inflammatory factors, embedded in the hydrogel layer and gradually released.

Along point 1. of M2Neural focus, preliminary work has been done on the production and the characterization of an hydrogel coating for polyimide substrate. The results obtained and the methods used are proposed in Section 3.1.1. The sole hydrogel was designed to provide by itself direct stimuli of the biological component, both chemical and physical. In fact the hydrogel was produced with zwitterionic copolymers thus exploiting their non-biofouling properties and achieving low Young's modulus values, in the range of the neural tissue (in our case from 2 to 19 kPa). The hydrogel was covalently attached to the PI surface and crosslinked with photoactivated groups. This work is still going on, and further work has to be done to load nanoparticles, drug and anti-inflammatory factors.

Considering instead the stimulation by means of ultrasound (point 2.), we already stated that in general it is also desirable that the external stimulus contributes itself also to the desired body response, providing an augmented beneficial effect to the process of regeneration. Moreover it is fundamental to control precisely the external stimulus and to know its bioeffects. For this purpose a proper fully tunable stimulation system with an ultrasound-transparent cell culture well was developed, thus enabling correlation between the ultrasound delivered and the triggered bioeffects. This cell culture well, as well as the platform, were validated on mouse myoblast cell line. The detailed description of the system and the *in vitro* systematic investigation of the bioeffects on muscle cells of low intensities ultrasound exposures (LIPUS) at different frequencies and intensities are reported in Section 3.1.2.

Considering instead a strategy for obtaining a controlled drug delivery of neurotrophic and anti-inflammatory factors from the polymeric matrix (point 3.), a pilot study on the possibility to achieve ultrasound mediated dexamethasone release form poly(2-oxazolines) micelles is presented in Section 3.2. These structures could be exploited in the future with hydrogel matrices further modulating (*e.g.* slowing down) the release rate.

## *The neural interface*

Neural interfaces have been recently successfully used for the bidirectional control of limb prostheses and in brain-computer interfaces [142-144]. In this field, polyimide (PI) has been identified as a good candidate material for the development of advanced neural interfaces.

Different PI-based interfaces have been developed, for interfacing with central nervous system as in the case of intracortical neural activity recordings [145, 146] or cortical surface field potential recordings [147] and for interfacing with peripheral nerves.

One of the main challenges of these neural interfaces is to achieve the best tradeoff between recording/stimulation selectivity and invasiveness. In fact the alteration of action potentials recording and stimulation thresholds is mainly due to the formation of fibrotic capsule. The injury due to the invasive procedures of implantation leads to an acute inflammation, characterized by leucocytes accumulation at the site of injury; then the inflammation becomes chronic and granulation tissue is produced by fibroblast and the foreign body reaction proceeds with the accumulation of giant cells (fusion of macrophages) and fibrosis [148, 149]. Please see Figure 18 for the representation of the possible host response mechanisms in case of a peripheral nerve interface (namely SELINE interface). Moreover this is worsened in the central nervous system, where gliosis establishes due to microglia activation and consequent implant encapsulation by means of astrocytes [135]. In peripheral nervous system a damage to the nerve during insertion or after extended time in the body can also provoke the so called "Wallerian degeneration" which is the breakdown of the distal stump of a severed nerve, that can cause signal loss if the distal nerve is close to an electrode, as this nerve will no longer convey signals to the device. [135]

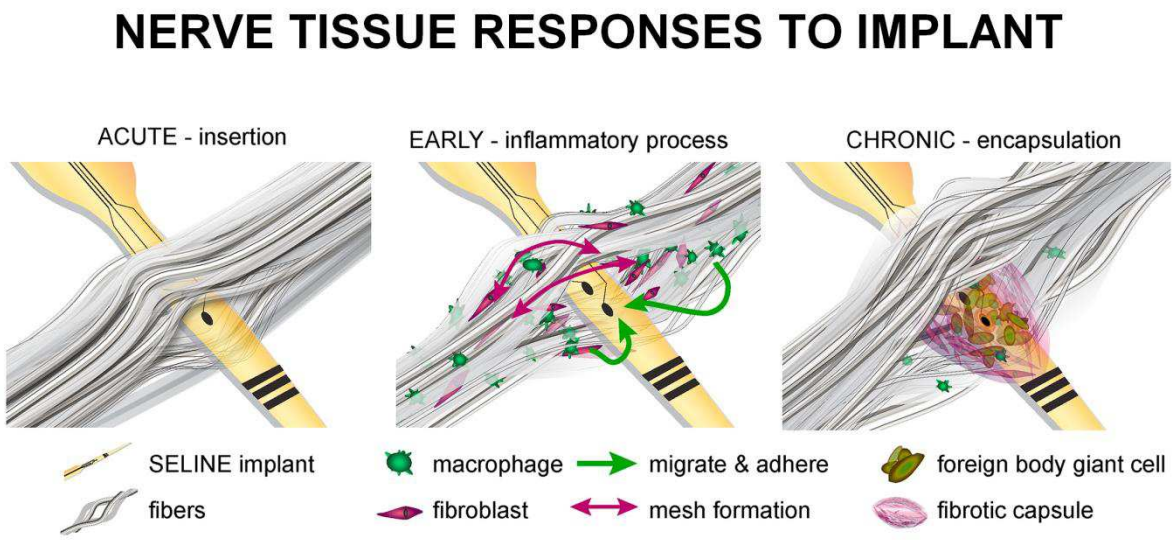


**Figure 18. Schematic representation of possible mechanisms of peripheral nerve tissue response to insertion and chronic implantation of polyimide-based intra-neural implant. (from Wurth *et al.*, 2017[150])**

In particular, considering peripheral neural system interfaces they can be classified depending on nerve invasiveness as extraneural, interfascicular, intraneural, or regenerative. Extraneural interfaces such as cuff electrodes [151] are implanted around a peripheral nerve to stimulate or record large groups of axons at a time, thus resulting in poor selectivity, while interfascicular solutions tried to improve selectivity by means of perpendicular contacts that can provide electrical access to the different fascicles of the nerve[152]. Intraneural electrodes are implanted within a nerve; the intimate contact with different fascicles provides a lower threshold for axonal stimulation, the improvement of selectivity and a higher signal-to-noise ratio of recordings. In this case both longitudinal (LIFE [153]) and transversal (TIME [154] and SELINE [139]) solutions have been proposed. Regenerative interfaces are implanted in a sectioned nerve forced to grow through them.[155] (See Figure 19).

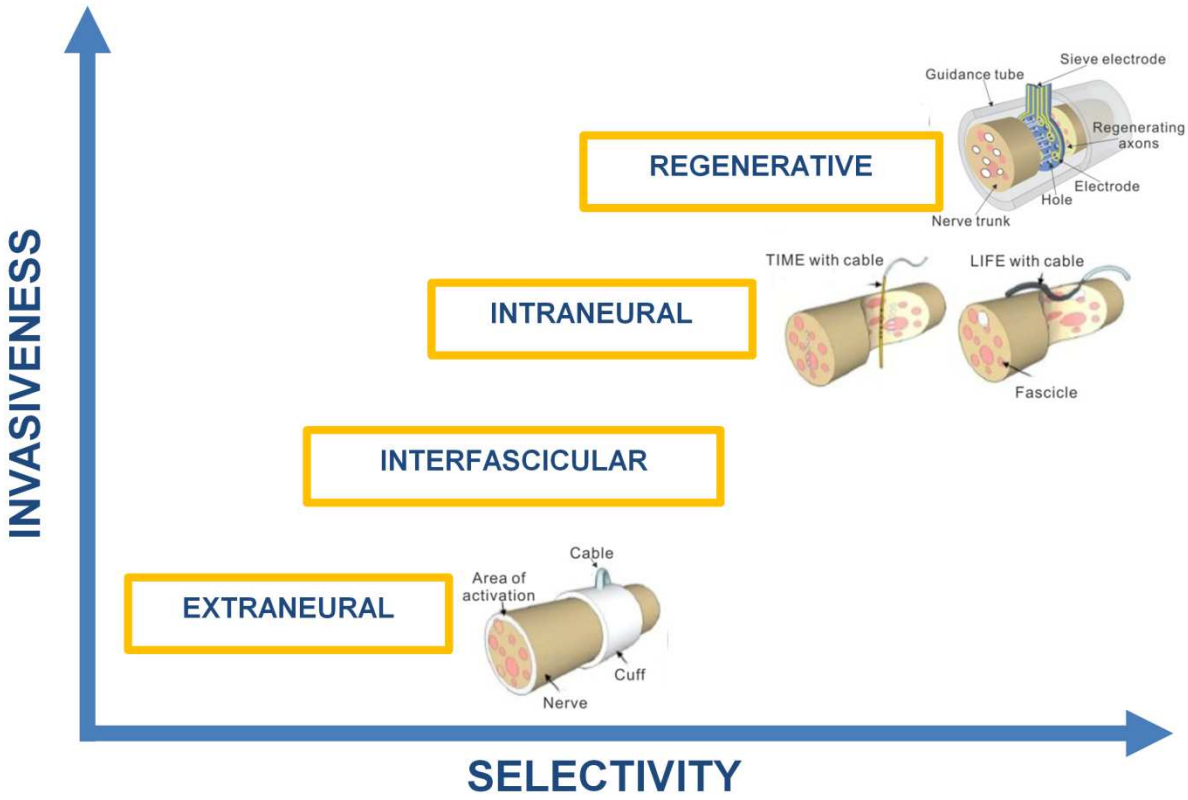


**Figure 19. Peripheral nerve interface classification in terms of their invasiveness *vs* selectivity.**

Despite a good compromise between selectivity and invasiveness, and a proper biocompatibility showed by TIME and LIFE interfaces, some problems remained. The SELINE interface, the target of the M2Neural project, was developed for this purpose. In fact movements of the limbs where the electrode is implanted can produce changes in the position of the active sites within the nerve, with a decrease in the signal-to-noise ratio of recorded signal when the distance between the electrode and the axons increases. For this reason a SELf-opening Intrafascicular NEural interface was designed. The innovative aspect of this neural interface is its three-dimensional geometry conferred to the electrode by means of polyimide plastic deformation: the electrode has a main body and two lateral "wings" on each side, provided with active sites. Each device has a total of ten active sites. The structure is inserted into the nerve and then gently pulled back, allowing the transversal opening of the wings. Thanks to this working principle, wings can open through the tissue and remain anchored to it. Furthermore, the three-dimensional geometry offers a second

dimension for contacting more axons from different sub-fascicles.[139] See Figure 20 for SELINE structure.

Recently the selectivity, stability, functionality, and biocompatibility of the SELINE polyimide-based intra-neural implant have been tested.[150] They were inserted into the sciatic nerve of 28 healthy rats for durations of up to 6 months. SELINE electrodes exhibited remarkably stable responses to charge delivery that supported robust stimulation selectivity over extended periods of time, despite the development of an encapsulating layer around the implant, in particular during the first month after insertion. A tight relationship was found between the thickness of the encapsulating layer around the implant and the increases in stimulation thresholds and electrode impedance. The fibrotic network and sustained foreign body reaction triggered by the implant did not prevent regenerative sprouting of peripheral nerve axons, suggesting a potential for long-term clinical applications. The development of a multifunctional coating could enhance this already promising features. The procedure for the coating needs to be engineered and optimized with the aim of adapting it to the industrial production pipeline of the interface.

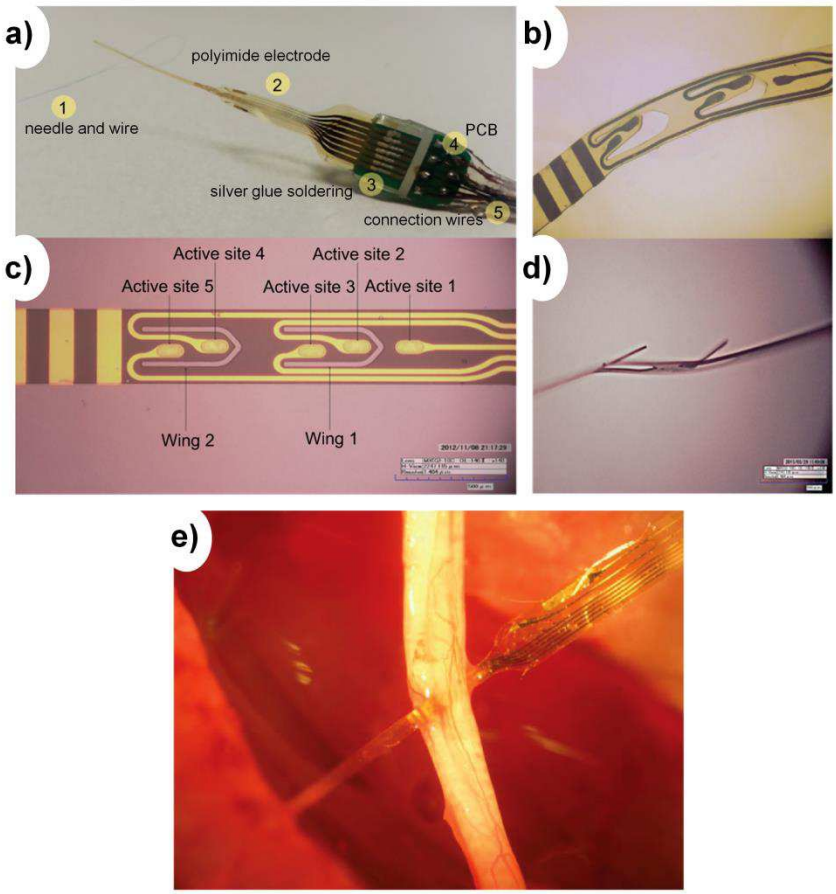


**Figure 20. SELf-opening Intrafascicular NEural interface (SELINE) produced by SMANIA srl spin-off company. a)-d) different views of the peripheral nerve interface and its details as well as its 3D structures, namely the " wings". e) SELINE implanted in a rat sciatic nerve. (from Cutrone *et al.*, 2015[139])**

# 3. Stimulation of biological components to achieve targeted response

Bio/non-bio interfaces can be exploited to promote/inhibit a specific body response, through a modulation of certain biological effects. This can be achieved by devising a proper stimulation. Such stimulation can be provided directly to the biological component by chemical or physical means (*e.g.* by functionalizing the material surface, by varying its stiffness, by providing ultrasound stimulation, etc.). It can be also provided indirectly, *e.g.* by means of externally triggered drug release systems.

## 3.1 Direct stimulation

This Section addresses the direct stimulation of biological components. In particular, in Section 3.1.1. the production and the *in vitro* characterization of soft coatings for polyimide substrate is presented. The coatings are based on zwitterionic hydrogels covalently attached to polyimide via a photolabile group. They show non-biofouling properties and low stiffness, approaching the one of nervous tissues. In this way a direct physical and chemical stimulation to cells is provided, in order to be exploited in the future as coatings for polyimide neural interfaces, with the aim to reduce foreign body reaction. Section 3.1.2 focuses on the investigation of the bioeffects triggered on muscle cells by ultrasound stimulation. To this purpose, a tunable and repeatable ultrasonic stimulation system and an ultrasound-transparent cell culture well are described to provide a controlled and well known dose to the biological component.

### 3.1.1 Mechanical stiffness and surface chemistry

## *Framework*

Implantable devices are gaining an increasing relevance in the biomedical engineering field. This is due to their high potential to restore the body functions after impairments and, generally, to improve the patients' quality of life.[156] To address these clinical goals, it is desirable to achieve a long-term functionality of implanted systems keeping them stable within the body environment and avoiding undesired biological processes.

The implant long-term functionality is particularly important in the case of neural interfaces. As stated in Section 2.3, these systems are active implanted medical devices aimed at restoring a connection with the central and peripheral nervous system after pathological conditions, such as neuropathies, multiple sclerosis, amyotrophic lateral sclerosis or spinal cord injuries and limb amputations.[135, 157] Exciting results have been recently achieved, which demonstrated the potential of this implantable technology.[142-144] As mentioned, among the different options, polyimide (PI) has been identified as a promising candidate material for the development of advanced neural interfaces. Indeed, it is a biocompatible and flexible polymer featured by proper dielectric properties, thermal stability, resistance to solvents and strong adhesion to metals and metal oxides. Moreover, it can be easily patterned with lithographic and dry etching techniques and produced in the form of thin layers by spinning deposition.[158-160] Different PI-based interface designs have been developed in the last years for selectively interfacing with the central nervous system for intracortical neural activity recordings,[145, 146] cortical surface field potential recordings[147] as well as for intraneural interfacing with peripheral nerves.[139, 151, 153, 154]

Currently, a full medical and commercial exploitation of neural interfaces is hampered by a limited long-term implant stability. Intraneural implants are highly demanding since they provide an intimate contact with axons, and trigger foreign body response and molecular cascades related to chronic inflammation. This leads to the formation of a scar-like fibrotic tissue that engulfs and electrically insulates the neural interface, thus altering the recording

of nerve action potentials and stimulation thresholds.[135, 150, 153] This process starts already with the injury produced by the invasive implantation procedure, which results in an acute inflammation and leucocytes accumulation at the site of injury. Afterwards, the inflammation becomes chronic, granulation tissue is produced by fibroblasts, and the foreign body reaction proceeds with the accumulation of giant cells and fibrosis.[149, 161]

Several strategies have been proposed to overcome the foreign body and inflammatory reactions stimulated by implanted neural electrodes. In some cases the material surface was functionalized with the aim of improving tissue integration within the implant. To this purpose, adhesion molecules,[162] specific peptides,[163-165] and whole engineered proteins[166] have been proposed. Another strategy was based on the physical modification of the implant surface, *e.g.* by providing it with proper patterns.[167-169] A further option was to suppress adverse local reactions by means of polymeric coatings exhibiting advanced features, such as controlled release of bioactive molecules and/or non-biofouling surface properties.[35, 170-172] The undesired host response to implants is due not only to their surface chemical properties, but it is also determined by the mechanical mismatch between the implant and the surrounding tissue.[136, 158, 173] The use of PI-based interfaces reduces this mismatch compared to silicon- and glass-based interfaces. Nevertheless, the PI Young's modulus of a few GPa is significantly higher than the Young's modulus of neural tissue, which ranges between 0.1 and 10 kPa.[174] Moreover, it is known that the substrate stiffness influences the behavior of a wide variety of cells, including macrophages, which are directly and primarily involved in the body reaction to implants. Indeed, Blakney *et al.* demonstrated that macrophage activation is reduced on softer poly(ethylene glycol)-based hydrogels exhibiting the elastic modulus in the range from 130 to 840 kPa.[175] Softer hydrogels also induced a lower expression level of genes involved in the production of inflammatory cytokines and showed a less severe foreign body reaction *in vivo*. Hydrogel-based coatings can thus be considered a promising solution to minimize the mechanical mismatch between implanted devices and tissues. These hydrogel coatings can be produced in a wide range of Young's moduli (even a few kPa)[176] and made of polymers exhibiting non-biofouling properties.

Most of the polymeric layers proposed so far as neural interface coatings were based on poly(ethylene glycol) (PEG) and PEG-based copolymers utilizing the PEG non-biofouling properties.[35, 138, 171, 177] However, the role of stiffness was not investigated in these studies. Spencer *et al.* recently reported PEG-based hydrogels with controllable elastic moduli as scarring-reducing coatings on neural probes.[178] However, PEG is known to produce undesired effects *in vivo*, *e.g.* oxidative damage in biological fluids, bioaccumulation in cell lysosomes and generation of anti-PEG antibodies that may lead to a severe immune response.[179-181] Therefore, the exploration of other types of non-biofouling polymers for a functional protective coating of neural electrodes represents an ongoing challenge.

Zwitterionic polymers, including poly(carboxybetaines), poly(sulfobetaines) and poly(phosphobetaines), are non-toxic materials with a high hemocompatibility and ultralow non-specific protein and cell adhesion.[182-184] The mechanism behind this behavior was ascribed to the formation of a hydration layer,[185] which prevents hydrophobic interactions of proteins and lipidic membranes of cells with the polymer surface. It was recently demonstrated that surfaces decorated with zwitterionic molecules bind water molecules more strongly than PEG due to electrostatically induced hydration.[186] Strategies for surface attachment of zwitterion-based compounds can be divided into “grafting from” and “grafting to” methods. In the first case, methacrylates and methacrylamides containing zwitterionic moieties in a side chain are polymerized via surface-initiated controlled radical polymerizations.[187] The “grafting to” method typically involves chemically induced attachment of zwitterionic polymers, containing suitable chemical moieties, to the surface of other materials.[188]

Recently, zwitterionic polymers bearing photoactivated groups were used for the preparation of covalently attached coatings via a photochemically controlled process. The overall benefits of a photochemical surface modification are *(i)* formation of a stable bond with hydrocarbon groups on various polymer substrates, *(ii)* simple manufacturing in dry state, and *(iii)* possibility of micropatterning. Photoreactive copolymers bearing zwitterionic phosphorylcholine and benzophenone units were used for modification of a commercial cyclic polyolefine.[189] Similarly, photoreactive poly(sulfobetaines) and poly(carboxybetaines)

bearing photolabile arylazide groups were applied for modification of various polymeric substrates.[188, 190-192] However, to the best of our knowledge, zwitterionic polymers have never been photochemically coupled with PI substrates in view of a future use in the domain of neural interfaces.

Hence, zwitterionic hydrogel coatings of PI substrates are proposed in this Section. The hydrogels are based on poly(carboxybetaine methacrylamide) and the coatings are obtained through a photoactivated process enabled by a photolabile azidophenyl group. The aim is to exploite the non-biofouling properties of zwitterionic hydrogels and achieve low Young's modulus values in the range of the neural tissue. The hydrogel layers were characterized to verify the presence of hydrogel attached to the PI surface, hydrogel thickness and Young's modulus. *In vitro* tests with fibroblasts and macrophages were carried out to evaluate the adhesion of these cells on the hydrogel-modified PI surfaces and to correlate these results with hydrogel stiffness. In addition, the coatings were tested for cytotoxicity and macrophages activation. Preliminary work has been done for engineering the hydrogel deposition methods in order to include it in the electrode production process and some insertion tests have been carried out to prove coating stability, thus contributing to create a strategy for PI based devices coatings, *e.g.* neural interfaces, and envisioning future applications of these materials *in vivo*.

This work has been done in strict collaboration with the Department for Biomaterials Research of the Polymer Institute of the Slovak Academy of Sciences, in Bratislava (Slovakia). Thanks to their specialized skills in chemistry, polymer synthesis and characterization, and their deep knowledge on zwitterions, we were able to obtain the hydrogel coatings and a detailed chemical analysis.

# *Methods*

## ***Materials***

*N*-[3-(dimethylamino)propyl]methacrylamide, ethyl bromoacetate, 4-azidoaniline hydrochloride, methacryloyl chloride, 2,2'-azobis(2-methylpropionamidine) dihydrochloride (AIBA), amberlite IRA 400 chloride, and Pluronic F-127 were purchased from Sigma Aldrich (Steinheim, Germany) and used as received. Sodium hydroxide, sodium carbonate, and dioxane were purchased from Lachema (Brno, Czech Republic). Acetone, ethanol, and dichloromethane were purchased from CentralChem (Slovakia) and distilled prior to use.

## ***Preparation of 2-{dimethyl[3-(2-methylprop-2-enamido)propyl]ammonio}acetate (M1)***

Monomer **M1** was prepared by adapting the procedure described by Abraham and Unsworth[193] (see Figure 21). *N*-(3-(dimethylamino)propyl)methacrylamide (5 g, 29 mmol) was diluted in 20 mL of acetone. Then ethyl bromoacetate (3.1 mL, 28 mmol) was added dropwise into the reaction mixture under an argon atmosphere. The reaction mixture was stirred overnight at room temperature. The white precipitate was filtered off, washed with acetone and dried under reduced pressure. The resulting white powder was dissolved in distilled water and applied onto a column filled with basic ionic exchange resin (Amberlite IRA 400) activated for 30 min with 1 M aq. NaOH. After ion exchange, the solvent was evaporated and the product was dried under reduced pressure. The resulting product was obtained as a colorless viscous compound with a yield of 7 g (~ 100%). For $^1$H NMR spectrum of **M1**, see Figure 22.

$^1$H NMR (400 MHz, $D_2O$, $\delta$, ppm): 1.79 (s, $CH_3$-C=$CH_2$, 3H), 1.88 (m, -$CH_2$-, 2H), 3.07 (s, $(CH_3)_2$-$N^+$, 6H), 3.22 (t, NH-$CH_2$-, 2H), 3.43-3.47 (m, -$CH_2$-$N^+$, 2H), 3.72 (s, $N^+$-$CH_2$-$COO^-$, 2H), 5.33 (s, $CH_2$=, 1H), 5.59 (s, $CH_2$=, 1H).

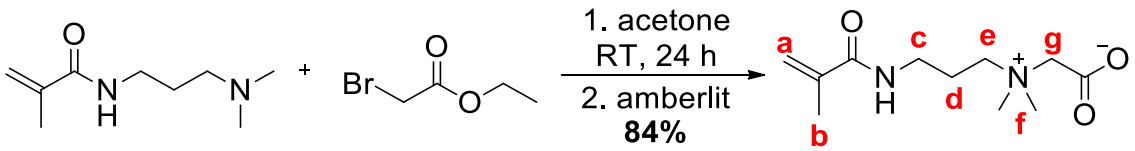


**Figure 21. Synthesis of 2-{dimethyl[3-(2-methylprop-2-enamido)propyl]ammonio}acetate (M1).**

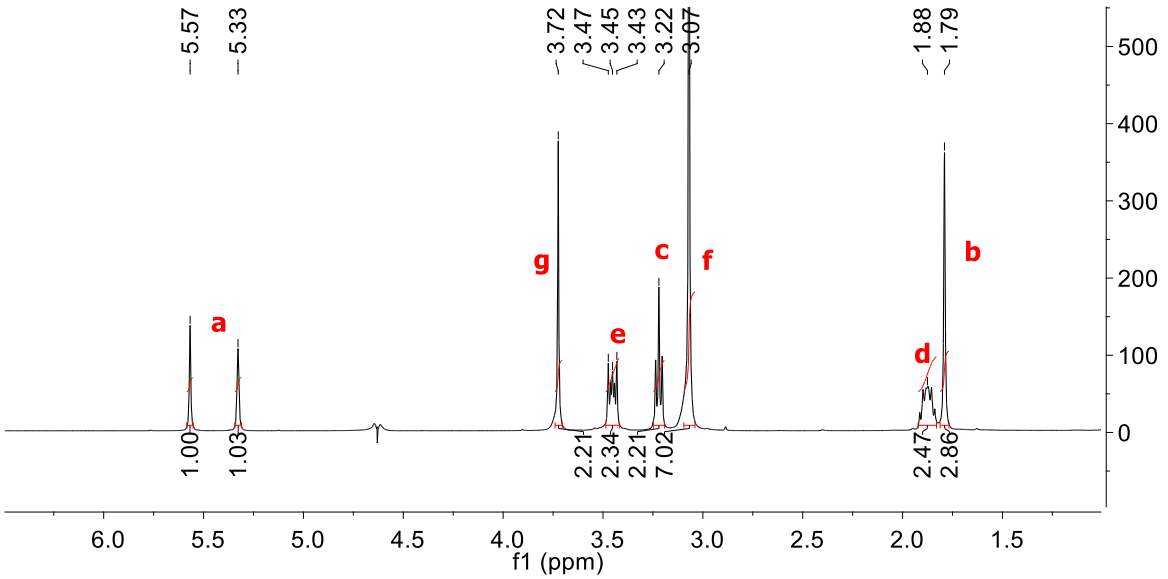


**Figure 22. $^{1}$H NMR spectrum of 2-{dimethyl[3-(2-methylprop-2 enamido)propyl]ammonio}acetate (M1).**

***Preparation of N-(4-azidophenyl)-2-methylprop-2-enamide (M2)***

Monomer **M2** was prepared according to the procedure described by Ito *et al* (see Figure 23).[194] Azidoaniline hydrochloride (501 mg, 2.9 mmol) was dissolved in 60 mL distilled water containing sodium carbonate (933 mg, 8.8 mmol), and cooled down to 4 °C by using an ice bath. Then, methacryloyl chloride (492 µL, 5.0 mmol) in 10 mL of dioxane was added dropwise and the reaction mixture was stirred for 3 h in dark. The obtained precipitate was filtered off, washed with distilled water and dried under reduced pressure. The resulting product was obtained as a grey powder with a yield of 0.64 g (~ 100%). For $^{1}$H NMR spectrum of **M2**, see Figure 24.

$^{1}$H NMR (400 MHz, $CDCl_3$, $\delta$, ppm): 2.05 (s, 3H, $CH_3$), 5.45 (s, 1H, $=CH_2$), 5.77 (s, 1H, $=CH_2$), 6.97-6.99 (dd, 2H, NH-Ar-H), 7.53-7.56 (dd, 2H, $N_3$-Ar-H).

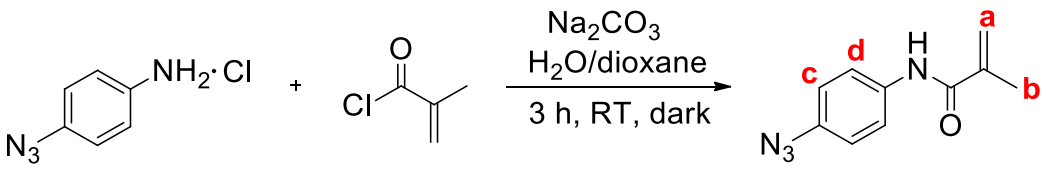


**Figure 23. Synthesis of *N*-(4-azidophenyl)-2-methylprop-2-enamide (M2).**

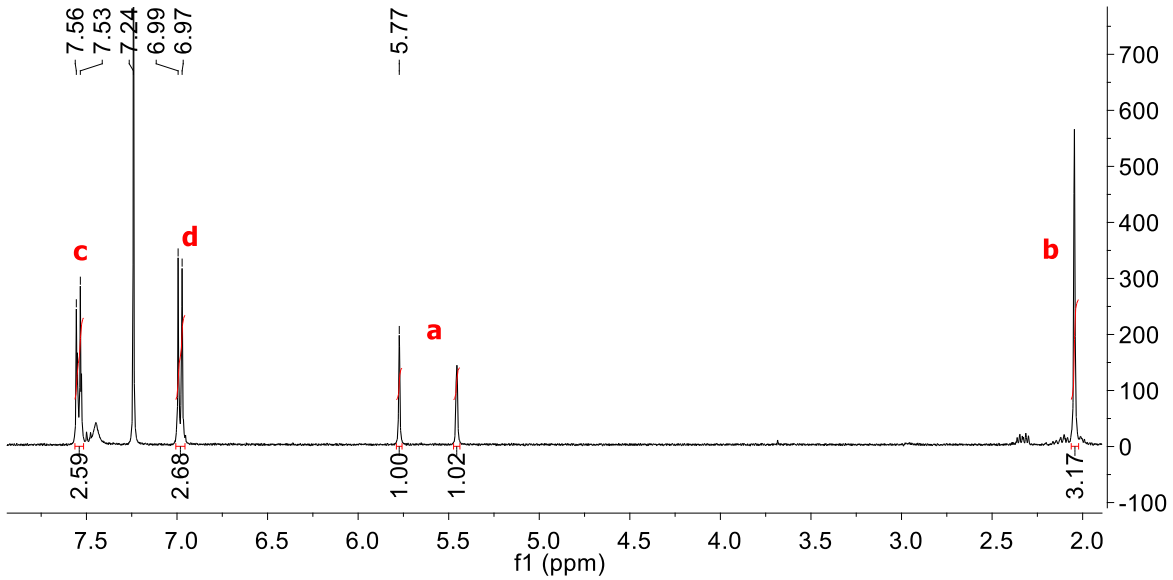


**Figure 24. $^{1}$H NMR spectrum of N-(4-azidophenyl)-2-methylprop-2-enamide (M2).**

***Copolymerization of M1 and M2***

For the preparation of copolymers, two feeding molar ratios of **M1/M2** were selected, namely 97.8/2.2 (copolymer **C1**) and 96.6/3.4 (copolymer **C2**). **C1** was prepared as follows: **M1** (320 mg, 1.4 mmol) was first dissolved in 3 mL of water/ethanol mixture (1:1 v/v), then **M2** (6.2 mg, 0.031 mmol) and AIBA (8.2 mg, 0.03 mmol) were added. Three freeze-pump-thaw cycles were applied and the reaction flask was filled with argon. The reaction mixture was stirred for 4 h at 60 °C in dark. After cooling down, the reaction mixture was dialyzed against a water/ethanol mixture (1:1 v:v, 3x) and distilled water (2x) using a Spectra/Por® dialyzing tubing (MWCO 3.5 kDa, Spectrum Laboratories, Inc., CA, USA). After freeze-drying, 195 mg (yield 60%) of white powder were obtained. **C2** was prepared with a similar procedure in a yield of 287 mg (yield 71%). The dialysis steps as well as all subsequent manipulation with copolymers **C1** and **C2** in either powder or solution forms were performed in dark.

$^{1}$H NMR (400 MHz, $D_2O$, $\delta$, ppm): 3.76 (s, $N^+$-$CH_2$-$COO^-$, 2H), 3.50 (m, -$CH_2$-$N^+$, 2H), 3.10 (m, $(CH_3)_2N^+$ and NH-$CH_2$-, 8H), 1.85 (s, -$CH_2$-, 2H), 0.97-0.84 (m, $CH_3$, 3H).

***Preparation of polyimide covered silicon wafers and round glass coverslips***

Two different types of PI plates were prepared on different substrates, namely *(i)* round glass coverslips (diameter: 6 mm), and *(ii)* square silicon (Si) wafers (2 x 2 $cm^2$). Si wafers are typically used as substrate for the preparation of PI based neural interfaces, by lithographic and dry etching techniques, while for *in vitro* experiments glass coverslips were identified as a more appropriate solution, so not to provide undesired biological response and to have rather transparent substrates. Anyhow, on both substrate types a uniform PI layer was achieved. For *(i)*, a layer of PI resin (PI2610, HD Microsystems, Germany) was spun at 10,000 rpm for 30 s onto the polished glass coverslips. Samples were then cured at 130 °C for 120 s and subsequently hard baked in oven with nitrogen flux at 350 °C for 1 h (Carbolite, UK). Finally, PI samples were washed twice with a liquid detergent (RBS 35 Concentrate, Belgium) in order to eliminate contaminants and dust. For *(ii)*, Si wafers (Si-Mat, Germany) were cut into square samples (2 x 2 $cm^2$) by using a diamond tip. Samples were cleaned in acetone for 10 min, rinsed with deionized water, cleaned with isopropanol for 10 min, and dried. Two layers of PI resin were subsequently spin-coated at 2,000 rpm for 30 s. Samples were cured at 130 °C for 120 s and hard baked in oven with nitrogen flux at 350 °C for 1 h.

***Deposition of copolymers C1 and C2 onto polyimide plates***

Both types of PI plates were coated with the **C1** and **C2** copolymers. PI plates were first washed in distilled water (3 min), ethanol (3 min), and dichloromethane (10 min) and subsequently dried at room temperature and atmospheric pressure. Dry plates were then uniformly covered with an aqueous solution of Pluronic F-127 (average molecular weight 12.6 kDa) with a concentration of 0.1 and 0.5 wt.%, respectively, using the solution volumes of 20 µL, in the case of *(i)* plates, and 283 µL, in the case of *(ii)* plates. Plates were dried overnight at room temperature and atmospheric pressure. Aqueous solutions of **C1** and **C2** with a concentration of 0.5 and 1.0 wt.%, respectively, were subsequently pipetted and homogeneously spread on the plate surface (20 µL in the case of *(i)* plates and 283 µL in the case of *(ii)* plates) to create a uniform layer of a copolymer solution. Plates were dried overnight at room temperature and atmospheric pressure in dark. Then they were irradiated by UV light for 20 min (UV Black Ray B100-A, 100 Watt, 365 nm, distance 5 cm) with a light

intensity of 20-24 mW/cm$^2$. After irradiation, the samples were washed in distilled water for 5 min and dried overnight at room temperature and atmospheric pressure prior to characterization. The procedure used for formation of zwitterionic hydrogel layers attached to PI surfaces is illustrated in Figure 25. The long-term storage conditions were room temperature and protection from dust and light.

The experimental conditions used for hydrogel fabrication, such as distance between the UV lamp and the surface, irradiation time, copolymer concentration and concentration of surfactant, were optimized to obtain hydrogel layers stably bound to the surface. Based on these data, we selected the irradiation conditions, which were kept constant for all experiments. Additionally, we selected combinations of two copolymer types differing in the content of 4-azidophenyl group, two different copolymer concentrations and two different surfactant concentrations, which all were expected to affect the thickness and mechanical properties of resulting hydrogel layers. In summary, six different protocols for fabricating polyzwitterionic hydrogel layers covalently attached to the PI plates were selected using the experimental conditions listed in Table 3 The hydrogel layers formed at the surface of PI plates were characterized by attenuated total reflectance Fourier-transform infrared spectroscopy, white light interferometry, confocal laser scanning microscopy, water contact angle measurements, and nanoindentation (details given below).

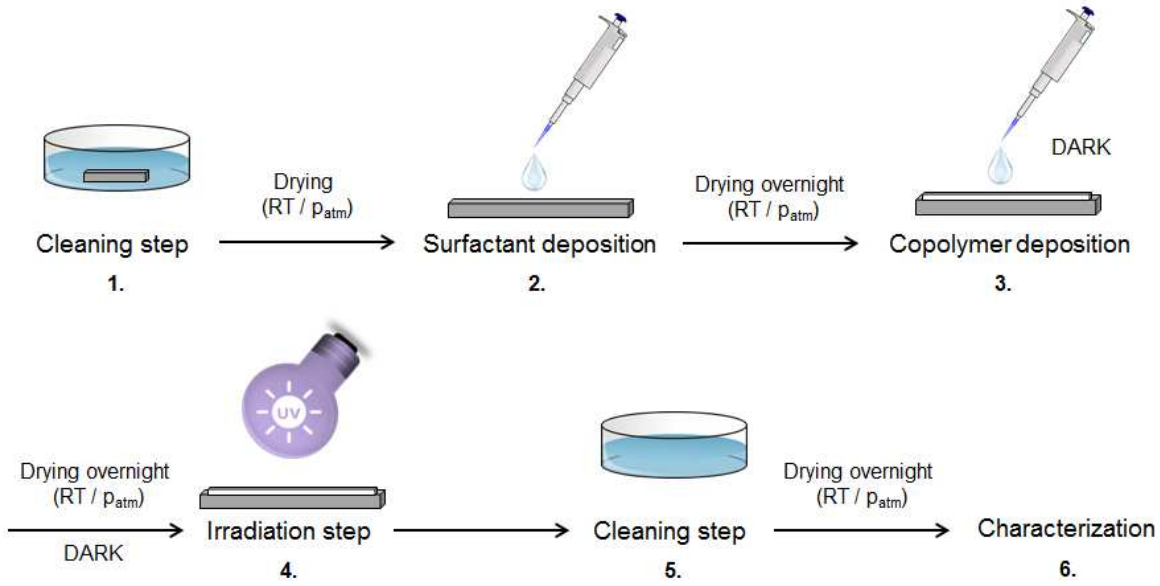


**Figure 25. Procedure for covalent modification of PI plates by zwitterionic hydrogel layer: 1.) cleaning (in distilled water for 3 min, in ethanol for 3 min, and in dichloromethane for 10 min); 2.) deposition of the surfactant solution; 3.) deposition of the copolymer solution; 4.) irradiation step; 5.) cleaning (in distilled water for 5 min); 6.) characterization.**

***Nuclear magnetic resonance spectroscopy***

Nuclear magnetic resonance spectroscopy (NMR) measurements were used to characterize the structure of monomers and copolymers. $^{1}H$ NMR spectra were measured at room temperature in deuterated solvents ($D_2O$, $CDCl_3$) using a Varian 400-MR spectrometer (Varian, USA) and tetramethylsilane (TMS) as an internal standard.

***Attenuated total reflectance Fourier-transform infrared spectroscopy***

Attenuated total reflectance Fourier-transform infrared spectroscopy (ATR-FTIR) spectra of monomers, copolymers and hydrogel layers deposited on *(ii)* were measured by means of a Nicolet 8700 FT-IR spectrometer (Thermo Scientific, USA) equipped with a Nicolet Continuum Microscope and a germanium ATR crystal. Spectra were collected with a resolution of 4 $cm^{-1}$ using 128 scans. A software Omnic 8 (Thermo Scientific, USA) was used for spectra evaluation.

***UV/Vis absorbance spectroscopy***

UV/Vis absorbance spectroscopy was used to determine the amount of **M2** (N-(4-azidophenyl)-2-methylprop-2-enamide) in **C1** and **C2** copolymers using a Shimadzu 1650 PC spectrometer (Kyoto, Japan). A calibration curve was prepared from UV/Vis data for monomer **M2** dissolved in distilled water at the concentrations ranging from 0.01563 to 0.00125 g·L$^{-1}$ (6.2 x 10$^{-6}$ to 7.7 x 10$^{-5}$ mol·L$^{-1}$) and plotting the absorbance maxima at 273 nm against concentration (Figure 26). Then the absorption spectra of **C1** and **C2** copolymers in 1 g·L$^{-1}$ aqueous solutions were measured and molar content of **M2** ($c_{M2}$) in copolymers was calculated from the following equation:

$$c_{M2}\ (\text{mol}\%) = \frac{n_{M2}}{n_{M2}+n_{M1}} \cdot 100 = \frac{\frac{A_{273}}{\varepsilon}}{\frac{A_{273}}{\varepsilon} + \frac{1-\frac{A_{273}}{\varepsilon} * M_{M2}}{M_{M1}}} \cdot 100$$

where $A_{273}$ is the absorbance at 273 nm, $M_{M1}$ and $M_{M2}$ are the molar masses of the corresponding monomers ($M_{M1}$ = 228.29 g·mol$^{-1}$, $M_{M2}$ = 202.21 g·mol$^{-1}$), $n_{M1}$ and $n_{M2}$ are the molar fractions of monomers and $\varepsilon$ is the extinction coefficient of monomer **M2** (equivalent to 4-azidophenyl group), equal to 10 680 L·mol$^{-1}$·cm$^{-1}$.

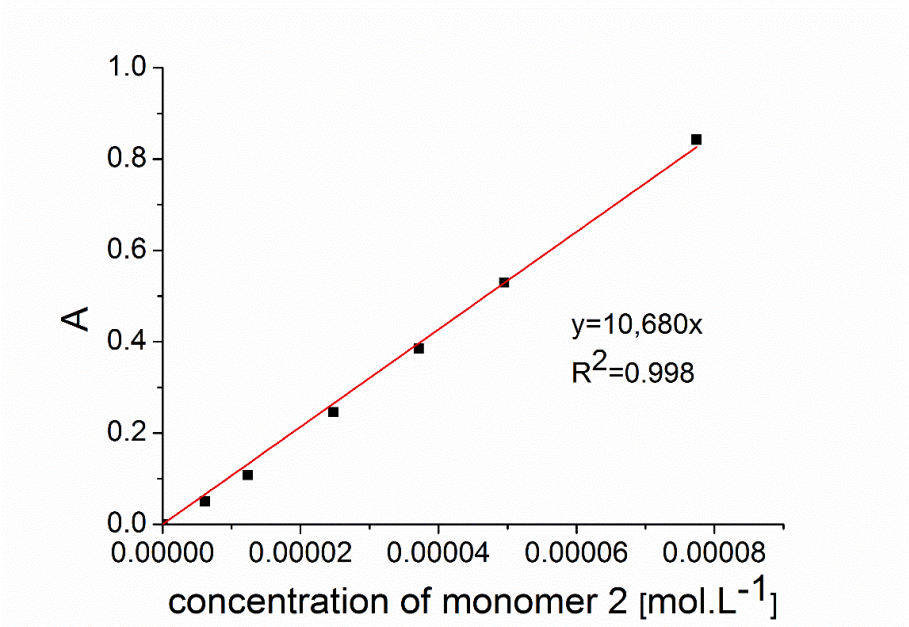


**Figure 26. Calibration curve for absorbance of azide monomer M2 at 273 nm as a function of concentration.**

***Water contact angle***

The hydrogel water contact angle was measured using the sessile drop technique with a Surface Energy Evaluation system (SEE system with CCD camera, Advex Instruments, Czech Republic). Dried hydrogel surfaces were wetted with a 3 μL water drop. For each sample, six independent measurements were performed.

***White light interferometry (WLI)***

Topography, surface roughness and thickness of hydrogel layers deposited on *(ii)* in their dry state were assessed by white light interferometry (WLI). A GT-K1 interferometer (Bruker, USA) in vertical scanning interferometry mode, using a broad-band white light source, was employed. Data were acquired and evaluated using a dedicated control and an analysis software package, Vision 64. The topography was analyzed at the sample center, in order to capture the topography of a continuous hydrogel layer, and at the edge, in order to capture the topography of the layer and the PI substrate simultaneously. The surface area of approximately 4.5 x 3.5 $\mu m^2$ was assessed for seven different positions of each hydrogel. A dry hydrogel layer thickness was determined from controllably scratched layers in a swollen state (in distilled water) using a scalpel to remove hydrogel and uncover the PI substrate. Subsequently, the samples were washed with distilled water and dried for 24 h at room temperature and atmospheric pressure prior to the WLI analysis (see Figure 27 for a depiction of the procedure). The reported thickness values represent the average of six independent measurements made for each hydrogel type.

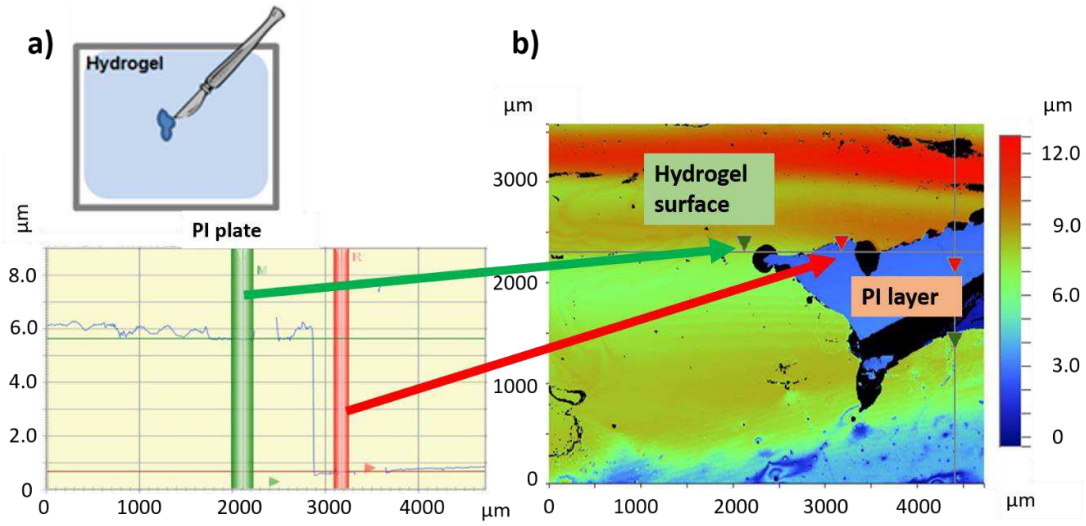


**Figure 27. Determination of hydrogel layer thickness in a dry state using a WLI method: a) Illustration of manual scratching of the hydrogel layer in a swollen state by a scalpel. b) Evaluation of the hydrogel thickness as a difference between hydrogel surface and PI plate surface based on the WLI 2D scan. The green arrow is positioned at the layer surface while the red arrow is positioned at the bare PI plate level. The left bottom image shows the line scan through these two regions of the sample.**

***Confocal laser scanning microscopy***

Confocal laser scanning microscopy (CLSM) in reflection and fluorescence modes was used to determine the thickness of hydrogels deposited on *(ii)* in a swollen state. A LSM 510 META scanning confocal microscope head on Axiovert 200M inverted microscope (Zeiss, Germany) was used with a 488 nm line of Ar ion laser for sample excitation. Fluorescence emission was detected through a 500-550 nm bandpass emission filter, the reflected laser light was detected through a 435-485 nm bandpass filter and both channels were featured by a pinhole setting of 1 Airy unit. Samples for CLSM measurements were prepared by careful peeling off the PI layer with deposited hydrogel coating from the wafer surface. These samples were placed on a microscope glass coverslip; a glass spacer was put around the samples to provide a chamber. Then the chamber was closed with another glass coverslip. Before closing, the chamber was filled with a solution of immunoglobulins G (IgG) labelled with Alexa Fluor® 488 (goat anti-human IgG, ThermoFisher Scientific, USA) in PBS (concentration of 0.5 mg/mL) for 10 min prior to a measurement. All measurements were done at room temperature. Images were obtained by scanning in the transversal XZ plane

with a 16x line-averaging protocol using either PlanApochromat 20x/0.75 or C-Apochromat 40x/1.2W Corr objectives. This method was used to visualize the swollen hydrogel, overcoming the influence of strong fluorescence emission of the PI layer. In fact the labeled IgG did not significantly penetrate inside the hydrogel volume within the time-scale of CLSM analysis, and the hydrogel layer was seen as a dark object well-visible between the fluorescent IgG solution and the fluorescent PI layer. Please refer to Figure 28 for the process. At least five independent images were acquired, with a total number of 15 measured height values determined for each hydrogel type, and averaged.

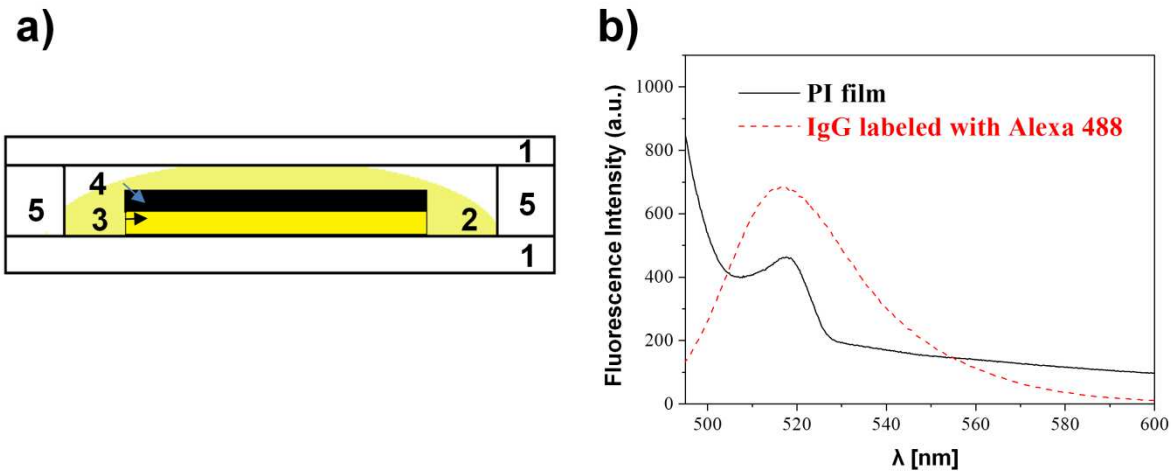


**Figure 28. Determination of the thickness of hydrogel layers swollen in PBS by CLSM. a) Schematic illustration of experiment arrangement for CLSM measurement: 1. Glass coverslip, 2. Solution of Alexa 488-labeled IgG in PBS (c = 0.5 mg/mL), 3. PI layer, 4. Hydrogel layer, 5. Glass spacer, b) comparison of fluorescence spectra of PI layer and solution of Alexa 488-labeled IgG in PBS.**

***Nanoindentation via atomic force microscopy***

Atomic force microscopy (AFM) in force spectroscopy mode[195, 196] was carried out by a collegue from the Department of Physics of University of Genova to determine the Young's modulus of hydrogels deposited on *(ii)* by using a Nanowizard III (JPK Instruments, Germany) set-up. A Si nitride cantilever (DNP, Bruker, USA) with a nominal spring constant of 0.24 $N \cdot m^{-1}$ was used. The tip shape was pyramidal and the nominal radius at the tip apex was 20 nm. The actual spring constant of each cantilever was determined by using the *in situ* thermal

noise method.[197] All measurements were performed in a liquid environment (PBS, Sigma-Aldrich, USA) at room temperature. The maximum force applied on the samples was 2 nN. The velocity of the piezo-scanner was maintained constant at 3 $\mu m \cdot s^{-1}$. Force curves were corrected for the cantilever bending[198] to calculate the tip-sample separation and to build force *vs* indentation (F-I) curves. The Young's modulus of the sample was calculated by fitting the corresponding F-I curves with the Bilodeau model for a pyramidal indenter.[199] A proper fitting of the F-I curves was performed by means of a dedicated data processing software provided by JPK Instruments. Five independent samples were analyzed for each hydrogel type and each sample was indented at least in 50 different points, randomly selected over the entire surface area.

***Cell cultures and in vitro characterization: Fibroblast culture, adhesion and cytotoxicity tests***

Normal human dermal fibroblasts, nHDFs (Cat. # CC-2511, Lonza, Basel, Switzerland) were cultured using a complete growth medium composed of high-glucose Dulbecco's Modified Eagle's Medium (DMEM, Gibco™ - Thermo Fisher Scientific, Waltham, Massachusetts, USA) with phenol-red supplemented with Fetal Bovine Serum (FBS, Gibco™-Thermo Fisher Scientific, Waltham, Massachusetts, USA) to a final concentration of 10%, and with Penicillin/Streptomycin (PEN/STREP, Gibco™-Thermo Fisher Scientific, Waltham, Massachusetts, USA) to a final concentration of 1%.

For adhesion tests, round glass coverslips (6 mm diameter) covered with PI *(i)* (control samples) and with PI further coated with selected zwitterionic hydrogels were used. Briefly, the samples were placed in 48-well plates, washed once with PBS and then incubated for 1 h in PBS, in order to let hydrogels swell. Then, samples were washed again with PBS supplemented with PEN/STREP (1%) and conditioned with the complete growth medium for 5 h. nHDFs were then seeded on the samples at a density of 15,000 cells/$cm^2$ and cultured for 24 h. To evaluate cell adhesion on the different substrates, cells were stained for nuclei with Hoechst 33342 (Molecular Probes™-Thermo Fisher Scientific, Waltham, Massachusetts, USA). Hoechst 33342 was diluted to a final concentration of 10 $\mu g \cdot mL^{-1}$ in Dulbecco's PBS (DPBS, Gibco™-Thermo Fisher Scientific, Waltham, Massachusetts, USA), added to cells and

kept for 5 min at room temperature. Glass plates were then turned upside down to bypass PI autofluorescence and imaged by means of a UV/Vis microscope (ECLIPSE Ti-E, Nikon Corporation, Minato-ku, Tokyo, Japan). Images of the blue channel (stained nuclei, bandpass filter value equal to 461 nm) were acquired at 10x magnification and the number of nuclei per image was quantified through the ImageJ® software (National Institutes of Health, Bethesda, Maryland, USA; available at https://imagej.nih.gov/ij/). Three independent plates were analyzed for each sample type, including the control, to quantitatively evaluate cell adhesion. Three images on different areas were acquired for each sample.

Whole cell morphology was also qualitatively assessed. To this purpose, at the same time-point (24 h) cells were fixed with a paraformaldehyde (Sigma Aldrich® Corporation, St. Louis, Missouri, USA) solution in PBS (4% w/v) for 15 min, then permeabilized with 0.1% Triton X-100 (Sigma Aldrich® Corporation, St. Louis, Missouri, USA) in PBS for 15 min and finally co-stained for 15 min for actin fibers with tetramethylrhodamine B isothiocyanate labeled Phalloidin (Sigma Aldrich® Corporation, St. Louis, Missouri, USA) as well as for nuclei with Hoechst (as described above). Fluorescence images (blue and red channels, bandpass filter values equal to 461 and 570 nm) were acquired at 10x magnification.

For cytotoxicity tests, a Pierce LDH Cytotoxicity Assay kit (Thermo Fisher Scientific, Waltham, Massachusetts, USA) was used. Lactate dehydrogenase (LDH) is a cytosolic enzyme that is released in the cell culture medium after the cell plasma membrane is damaged. LDH can be quantified spectrophotometrically by means of a coupled enzymatic reaction that leads to the formation of red insoluble formazan, which is directly proportional to the amount of LDH released. To perform this experiment, round glass coverslips (6 mm diameter) covered with PI *(i)* (control samples) and with PI further coated with selected zwitterionic hydrogels were placed into 96-well plates, pretreated with PBS and complete growth medium as described above. nHDFs were then seeded at a density of 25,000 cells/cm$^2$ (200 µL of cells suspension in complete growth medium, without phenol red that would interfere with the measurements, per each well) both on covered round glass coverslips (3 coverslips per sample type) to assess substrate-induced LDH activity, and on polystyrene wells to assess spontaneous and maximum LDH activity (3 wells per type). Cells were cultured for 24 h, then

treated according to the LDH kit manufacturer's instructions properly adapted to the samples. Absorbance at 490 nm (related to LDH amount) was measured (3 replicates for each sample) with a plate reader (Victor X3, Perkin Elmer, Waltham, Massachusetts, USA). Background was removed and the cytotoxicity was computed for each hydrogel and for PI as:

$$\%\ Cytotoxicity = \frac{substrate\ induced\ LDH\ activity - spontaneous\ LDH\ activity}{maximum\ LDH\ activity - spontaneous\ LDH\ activity}$$

***Cell cultures and in vitro characterization: Macrophage culture, adhesion and activation tests***

The murine RAW 264.7 macrophage cell line (ATCC® TIB-71™, ATCC®, Manassas, Virginia, USA) was cultured in the same complete growth medium used for nHDFs.

For adhesion tests, round glass coverslips covered with PI *(i)* (control samples) and with PI coated with selected zwitterionic hydrogels were placed in 48-well plates and pretreated similarly to fibroblasts (see above). RAW 264.7 cells were then seeded at a density of 30,000 cells/cm$^2$ and cultured for 24 h. The cell nuclei were stained with Hoechst 33342 and imaged, similarly to nHDFs. Three independent plates were analyzed for each sample type, including the control, and three images were acquired for each sample on different areas.

Similarly to nHDFs, qualitative cell imaging was also performed through tetramethylrhodamine B isothiocyanate labeled Phalloidin and Hoechst. In order to compare macrophage morphology changes due to activation, the same cell density was seeded on polystyrene wells and left to attach for 4 h. Then, lipopolysaccharide (LPS) from Escherichia coli 055:B5 (Sigma Aldrich® Corporation, St. Louis, Missouri, USA) was added to a concentration of 1 µg·mL$^{-1}$ and incubated for 24 h, to provide a positive control for activation. Then, cells underwent fixation, permeabilization and staining as described above.

Macrophage activation was evaluated through the assessment of nitric oxide production. Nitrite ($NO_2$-), a stable breakdown product of NO, was measured by means of a Griess Reagent system (Promega Corporation, Madison, Wisconsin, USA). Round glass coverslips (6

mm diameter) covered with PI *(i)* (control samples) and with PI further coated with selected zwitterionic hydrogels were placed in 96-well plates and pretreated as described above. RAW 264.7 were seeded at a density of 80,000 cells/$cm^2$ (150 µL of cells suspension in a complete growth medium without phenol red per each well) both on samples and on bare polystyrene. The latter samples were used as positive controls to assess nitrite release from activated macrophages: the cells were cultured for 4 h, then 50 µL of complete growth medium supplemented with LPS to a final concentration of 1 $\mu g \cdot mL^{-1}$ were added to induce macrophage activation, while all other PI samples were only provided with complete growth medium in order to compensate for volume increase. Cells were exposed to the different substrates or to LPS for 24 h, then the Griess assay was performed, according to the manufacturer's instructions. The absorbance at 560 nm for each sample was measured with a plate reader (Victor X3, Perkin Elmer, Waltham, Massachusetts, USA). Three independent samples were analyzed for each sample type and three absorbance reading replicates were measured for each sample.

***Data analyses***

Data underwent a non-parametric statistical analysis using a Kruskal-Wallis post-hoc test and a Dunn's multiple comparison test in order to evaluate significant differences among the samples. Results were considered statistically different for $p$-values $\leq 0.05$.

***Preliminary optimization of electrodes coverage and ex vivo insertion tests***

After the achievement of a zwitterionic hydrogel based PI coating with the young modulus in the range of neural tissue one, and after having understood their *in vitro* response, we started to optimize the hydrogel integration in the electrodes production process. Several drawbacks were found, since the hydrogel layer must be deposited on top of the electrodes which are fabricated by lithography technique, and be patterned prior to their peel off from Si wafers. For these reasons the photolabile azidophenyl group content in the poly(carboxybetaine methacrylamide) was modified (3.3 mol.%) and optimized as well as the coating deposition method in order to be included in the production process of thin film PI intraneural interfaces. This work has just started and is in progress. A water solution of Pluronic F-127 0.5 wt.% and NaCl 0.3 M was used to dissolve the modified zwitterionic

copolymer to a concentration of 8 wt%. This solution was spin-coated at 1000 rpm for 40 s on the electrodes prior to their peel off from the silicon wafer and then irradiated for 180 s with a UV mask aligner (Karl Suss, Germany). The coated interfaces were stained with a red liquid food dye (E122). This dye was able to penetrate into the hydrogel without colouring the PI interface and was used to check for coating integrity. Then the coated intraneural interface was inserted in dry state in both calf and pig sciatic nerve. After insertion the coating was washed with PBS in order to remove possible residues of the tissues and then again immersed in the liquid dye to prove the coating stability during the insertion procedure. Both manually insertion in calf nerve and controlled insertion in pig nerve were performed. In particular the second one was done thanks to a mechanical testing equipment, namely Instron 4464 (Instron, Norwood, Massachusetts, USA), that allowed for a controlled insertion velocity of 15 mm/min. Six different electrode were tested with this procedure.

# *Results and discussion*

***Preparation and photoimmobilization of zwitterionic copolymers***

Two photoreactive zwitterionic copolymers **C1** and **C2,** differing in the content of photolabile 4-azidophenyl groups, were prepared by the radical copolymerization of 2-{dimethyl[3-(2-methylprop-2-enamido)propyl]ammonio}acetate (**M1**) with N-(4-azidophenyl)-2-methylprop-2-enamide (**M2**) bearing photoreactive 4-azidophenyl unit (Figure 29). The chemical structure of monomers and copolymers was determined by NMR and ATR-FTIR spectroscopies. The presence of small broad signals in the range from 7 to 7.5 ppm in $^{1}H$ NMR spectrum revealed the presence of 4-azidophenyl group in the structure of both copolymers (Figure 30 and Figure 31).

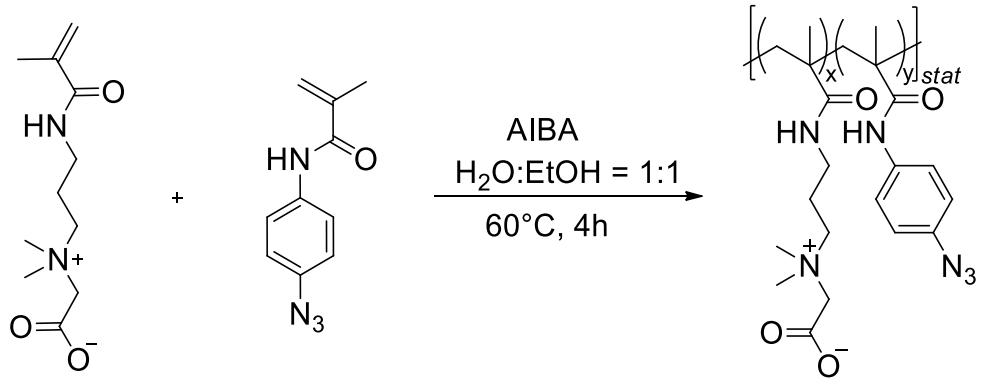


**Figure 29. Scheme of the synthesis of zwitterionic copolymers C1 and C2 containing photolabile 4-azidophenyl groups.**

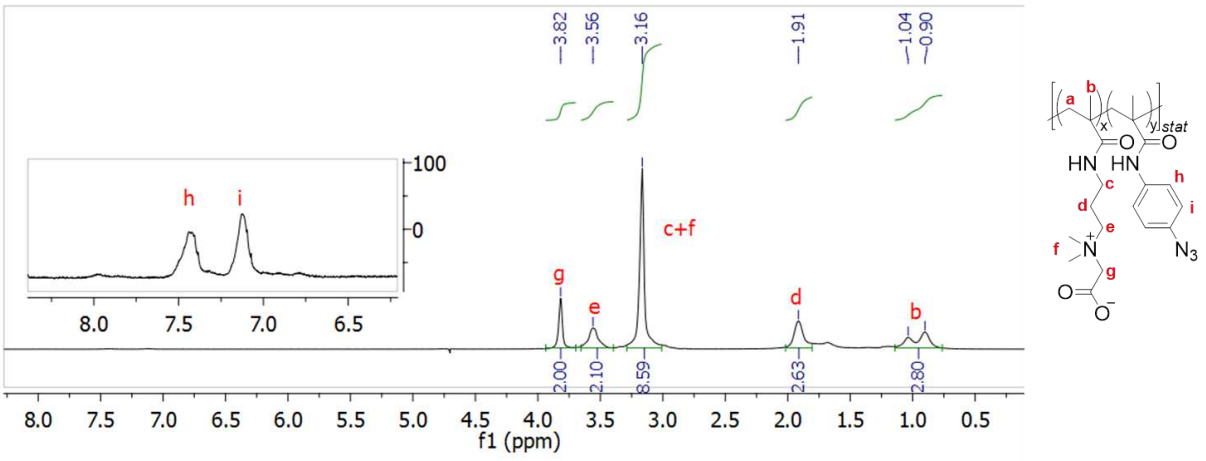


**Figure 30. $^{1}$H NMR spectrum of copolymer C1.**

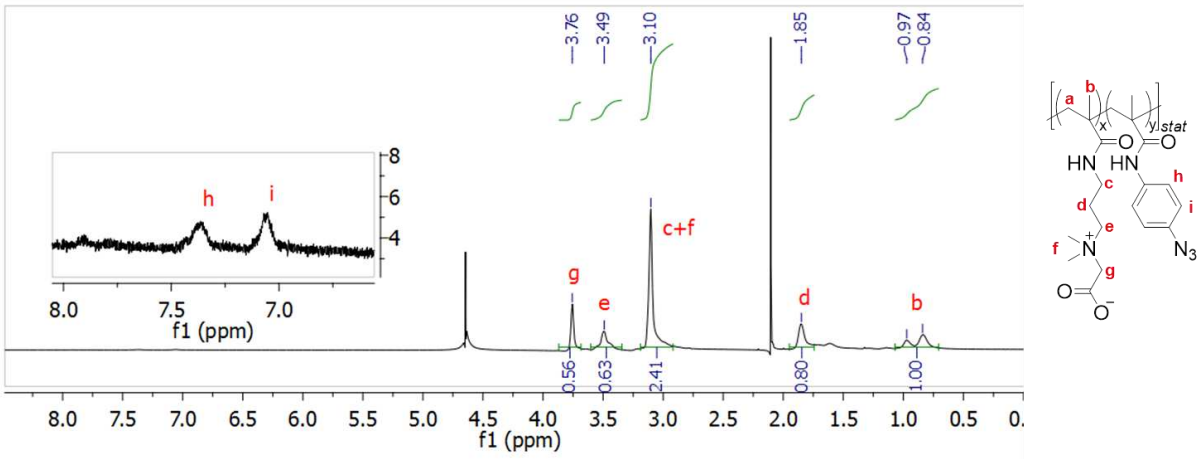


**Figure 31. $^{1}$H NMR spectrum of copolymer C2.**

In the ATR-FTIR spectra of **C1** and **C2**, a small vibration band of the azide group was observed at 2119 $cm^{-1}$ (Figure 32). Asymmetric and symmetric stretching vibrations of carboxylate group of zwitterionic unit were present at 1630 and 1380 $cm^{-1}$. Vibration bands connected to N-H bond of zwitterionic unit were also visible at 1529 and 1483 $cm^{-1}$. All signals were in accordance with results published recently by Sobolčiak *et al.*[192]

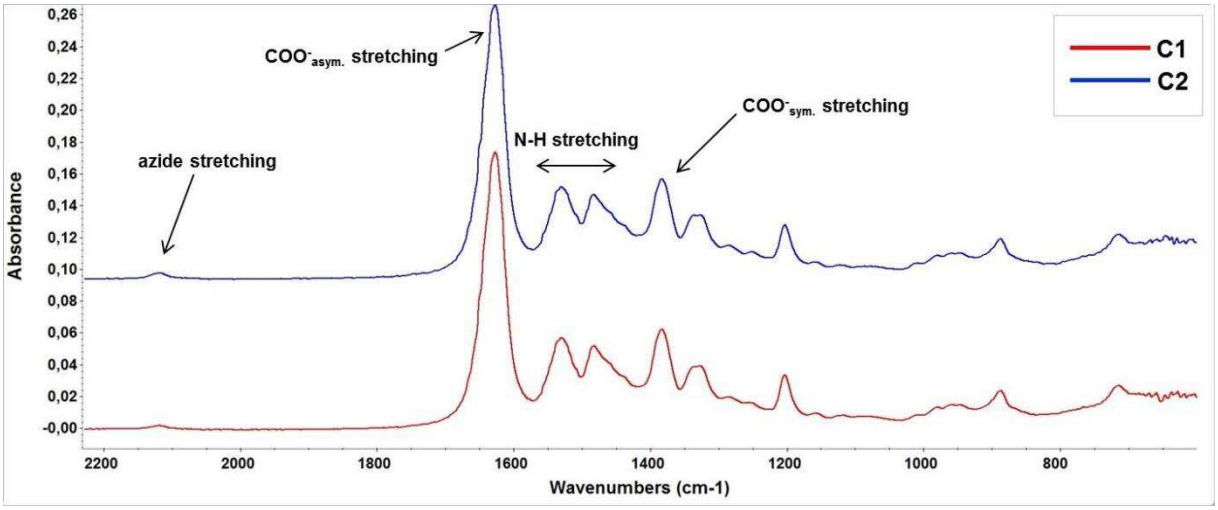


**Figure 32. ATR-FTIR spectra of C1 and C2 copolymers in the region from 2200 to 600 $cm^{-1}$.**

Molar percentages of 4-azidophenyl groups in copolymers **C1** and **C2** of 1.6 and 3.1 mol.%, respectively, were calculated from UV/Vis absorbance spectra of copolymers in water using the calibration curve for **M2** (Figure 26). These values were slightly lower compared to feeding **M2** comonomer content equal to 2.2 and 3.4 mol.% for **C1** and **C2**, respectively, probably due to an incomplete conversion and a minor compositional drift in favor to consumption of **M1** comonomer.

***Characterization of PI plates modified by polyzwitterionic layers***

The aim of this study was to identify the conditions for a covalent attachment of soft zwitterionic hydrogel layers (with a thickness in the micrometer range) to the PI surface. In order to achieve this goal, we adapted principles that employ a photoactivated attachment of zwitterionic polymers via a C-H insertion reaction using 4-azidophenyl groups.[188, 192] The characterization of polyzwitterionic hydrogel layers on PI substrates included surface chemical analysis and measurement of wettability, thickness, surface roughness and mechanical properties. These data are summarized in Table 3, together with the conditions used for fabricating the six representative hydrogel types (**H1** - **H6**).

| Sample | M2 in copolymer [mol.%] | Copolymer [wt.%] | Pluronic F-127 [wt.%] | Contact angle [a)] [°] | $h_{dry}$ [b,c)] [μm] | $R_a$ [b)] [μm] | $h_{wet}$ [d)] [μm] | Young's modulus [e)] [kPa] |
|---|---|---|---|---|---|---|---|---|
| **H1** | 1.6 | 1.0 (C1) | 0.1 | 59 ± 3 | 5.1 ± 0.3 | 0.16 ± 0.06 | 13 ± 2 | 2.7 ± 0.2 |
| **H2** | | 1.0 (C1) | 0.5 | 66 ± 9 | 6.4 ± 0.4 | 0.10 ± 0.03 | 32 ± 5 | 2.0 ± 0.2 |
| **H3** | 3.1 | 0.5 (C2) | 0.1 | 33 ± 6 | 4.6 ± 0.6 | 0.13 ± 0.05 | 28 ± 6 | 12 ± 3 |
| **H4** | | 1.0 (C2) | 0.1 | 45 ± 4 | 5.2 ± 0.2 | 0.30 ± 0.10 | 24 ± 6 | 15 ± 2 |
| **H5** | | 0.5 (C2) | 0.5 | 34 ± 6 | 4.8 ± 0.9 | 0.14 ± 0.02 | 14 ± 3 | 5.2 ± 0.8 |
| **H6** | | 1.0 (C2) | 0.5 | 39 ±4 | 3.1 ± 0.4 | 0.12 ± 0.05 | 24 ± 4 | 19 ± 4 |

**Table 3. Preparation conditions and properties of zwitterionic hydrogel coatings covalently attached to PI substrates. Water contact angles, dry ($h_{dry}$) and wet ($h_{wet}$) thickness, surface roughness ($R_a$) in a dry state, and Young's moduli are expressed as the mean value ± standard deviation.**

**[a)] the measured water contact angle for PI plate was 75°**

**[b)] determined by white light interferometry for dried hydrogels**

**[c)] $h_{dry}$ theoretical values are 3.5 and 7.0 μm for coatings using 0.5 and 1.0 wt.% of copolymer, respectively, assuming Pluronic F-127 does not take part in the layer formation and the copolymer density is 1 g·cm$^{-3}$**

**[d)] determined by confocal laser scanning microscopy for wet hydrogels in PBS**

**[e)] determined by AFM nanoindentation for wet hydrogels in PBS**

In the absence of alternative surface analytical techniques such as X-ray photoelectron spectroscopy, the modification of PI substrates by hydrogel layers was characterized by ATR-FTIR, shown in Figure 33, using non-modified PI substrate and **C1** and **C2** copolymers as controls. In agreement with previously published data,[200] the spectrum of non-modified PI consists of peaks, which can be assigned to the asymmetric stretching vibration of C=O group at 1773 $cm^{-1}$, the symmetric stretching vibration of C=O group at 1708 $cm^{-1}$, C-N stretching vibration at 1352 $cm^{-1}$ and imide five-ring deformation vibration at 734 $cm^{-1}$ (Figure 34a).

The PI and copolymer vibration peaks in the ATR-FTIR spectra of hydrogel layer-coated PI plates were present at different intensities depending on the sample type (Figure 33). The layers prepared of lower 0.5 wt.% copolymer concentration (**H3** and **H5**, Figure 33b) showed a significant presence of PI vibrations in the spectra compared to the layers prepared of 1.0 wt.% copolymer concentration. This observation did not correlate with the WLI analysis. In fact this analysis shows, in Figure 35, a complete coverage of PI plates with an hydrogel thickness, $h_{dry}$, in the range from 3 to 6 µm (Table 3). Considering that the ATR-FTIR has a penetration depth of the infrared beam of approximately 1 µm for Ge crystal[201], we propose that the presence of the PI in the FTIR spectra was rather due to the use of ATR mode for these very soft hydrogel layers, featured by a thickness of few micrometers. During the analysis, the hydrogel layers were likely compressed by the ATR crystal towards the hard substrate (PI on silicon wafer, *(ii)*) resulting in an analytical thickness that was within the infrared beam penetration depth.

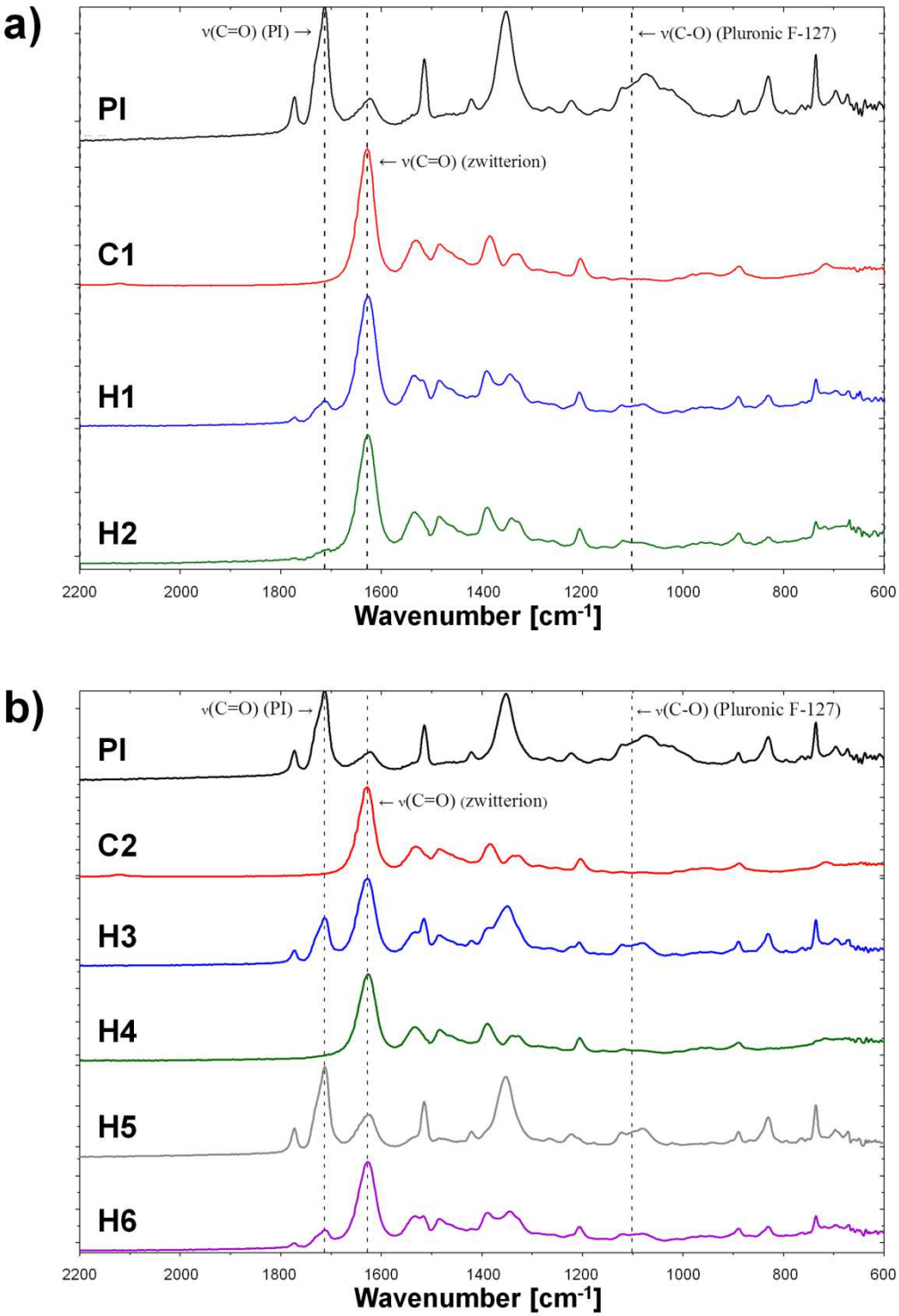


**Figure 33. ATR-FTIR spectra of a) H1 and H2 hydrogel layers compared to PI surface and copolymer C1 and b) H3-H6 hydrogel layers compared to PI surface and copolymer C2, in a wavenumber region from 2200 to 600 $cm^{-1}$. Dashed lines depict the characteristic bands for PI, copolymers and Pluronic F-127.**

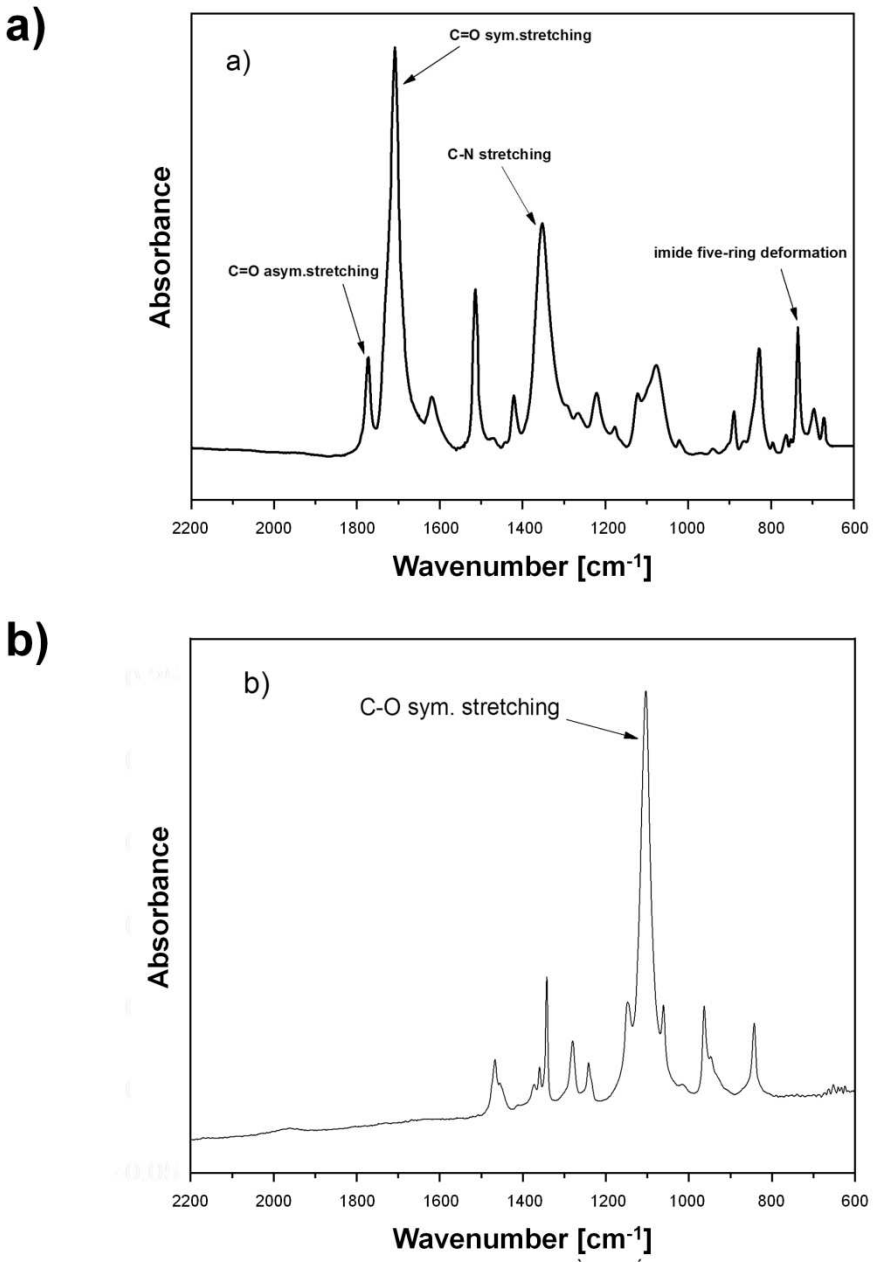


**Figure 34. ATR-FTIR spectrum of a) non-modified polyimide and b) Pluronic F-127 in the region from 2200 to 600 cm$^{-1}$.**

As stated before, Figure 35 shows the WLI images for hydrogel layers in their centers, verifying a complete PI surface coverage and a high degree of layer smoothness, which was quantitatively expressed by the surface roughness values, $R_a$, ranged from 0.1 to 0.3 µm (Table 3). Figure 35 also reveals the images of the plate edges to visualize the situation for imperfect PI surface coverage that is in contrast to complete coverage of the sample central

areas. The $R_a$ values resulted less than 10% of the thickness values for the dry layers, determined as the height difference between the surface of hydrogel and the PI surface obtained after careful removal of the hydrogel layers by a scalpel, in a swollen state.

Overall, the ATR-FTIR and WLI data show that the PI vibration peaks in the ATR-FTIR spectra displayed in Figure 33 could not result from a non-coated PI surface or from the extensive surface roughness, but rather due to the aforementioned compression of the soft hydrogel layer during ATR-FTIR measures.

The ATR-FTIR spectra for all hydrogel layers in Figure 33 highlighted also the position of the high intensity C-O stretching vibration at 1102 $cm^{-1}$ for Pluronic F-127 (the individual ATR-FTIR spectra for Pluronic F-127 are shown in Figure 34b). Pluronic F-127 was used as a surfactant during the hydrogel fabrication, for wetting the PI hydrophobic surface prior to deposition of the copolymer solution. Its presence in the hydrogel layer was assumed since the C-H insertion reaction may proceed also with the alkyleneoxy units of Pluronic F-127 molecule. The Pluronic F-127 concentration is in the range of copolymer concentration (0.1 and 0.5 wt.%, Table 3); therefore, its high intensity vibration at around 1100 $cm^{-1}$ was expected to be detected. However, this was not the case (Figure 33) and it is not trivial to understand whether this behavior corresponds with a negligible incorporation of this surfactant into the hydrogel layer followed by its gradual washing from the hydrogel, or with the overlap of PI and Pluronic F-127 bands in this region of FTIR spectra. The high hydrophobicity of PI surface required as the key factor using of a surfactant (Pluronic F-127 in our case) in order to achieve uniform wetting of the PI surface for deposition of the copolymer solution. We selected this surfactant in order to avoid any toxic effect on cells in case that it would contribute to the composition of the hydrogel layer. In fact, Pluronic F127 has been approved by Food and Drug Administration[202, 203] for use as food additives and pharmaceutical ingredients. Future work will be done in order to better understand the structure of the hydrogel, for example by using Confocal Raman microscopy.

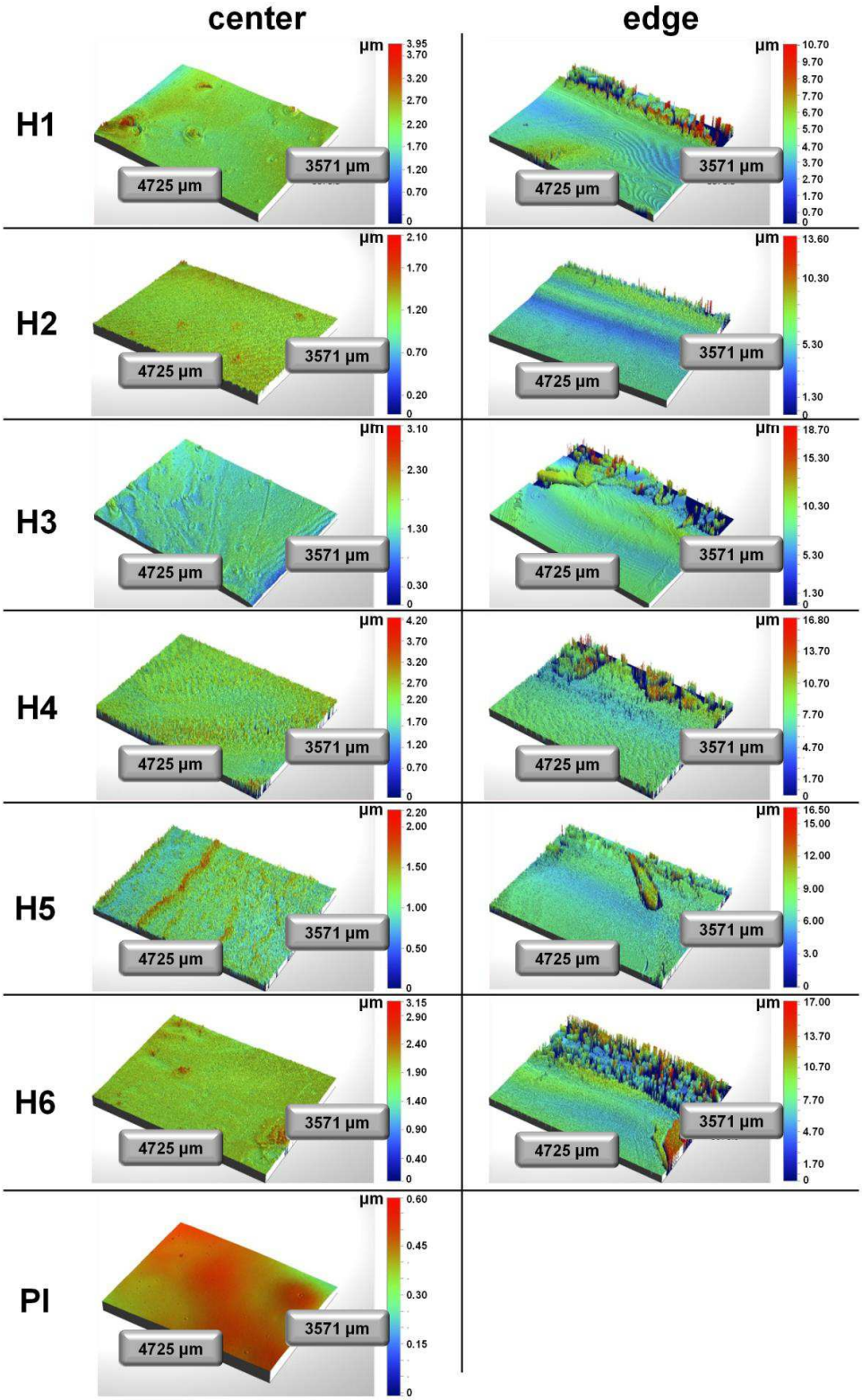


**Figure 35. White light interferometry visualization of hydrogel coatings on a PI substrate in the sample center and edge, respectively, for selected samples H1-H2 (made of the copolymer C1), H3-H6 (made of the copolymer C2). The main preparation conditions of hydrogels are given in Table 3.**

The hydrogel layer deposited on PI substrates modified the surface wettability. The contact angle determined for a non-modified PI plate was 75°, a value close to the one reported in the literature (72°).[66] The coating of PI plates by zwitterionic hydrogels reduced this contact angle to values included in the range between 33° and 66°, as reported in Table 3.

These values are in the same range as previously reported for other zwitterionic polymer layers, with a thickness typically in the sub-micrometer range.[188, 191, 192, 204-206] A higher contact angle and, hence, a slightly more hydrophobic surface, was observed for layers formed from **C1** copolymer of lower 4-azidophenyl content compared to the layers based on **C2** copolymer, especially at the lower **C2** content of 0.5 wt.%. During the formation of these hydrogel layers, two competing C-H insertion reactions of nitrene radicals proceed concurrently, *i.e.*, with the PI surface and within the copolymer chains, resulting in the attachment of the hydrogel layer to the surface and the intra- and intermolecular crosslinking of **C1** and **C2** copolymer chains. The competition between these two pathways was suggested to control the water contact angle for poly(carboxybetaine) layers deposited by photoactuation to various polymer substrates.[192] In our case, the obtained water contact angle data provide no clear reason why the hydrogels made of **C1** copolymer would experience a higher intra- and intermolecular crosslinking compared to hydrogels made of **C2** copolymer with a slightly higher content of 4-azidophenyl group. This issue remains open also in view of the Young's modulus data (reported in Table 3 and discussed below), showing that the hydrogel layers based on **C2** copolymer are stiffer than those based on **C1** copolymer, under identical conditions.

Hydrogel thickness values in a swollen state, $h_{wet}$, ranged between 13 and 32 µm (Table 3). They were determined by a CLSM technique, as shown in Figure 36. This is an important feature of the layers, for their future deposition on the surface of real neural electrodes. This method enabled to precisely visualize the swollen layer as a dark object well-visible in the PBS solution containing the IgG labeled with Alexa 488 (Figure 36). The labeled IgG did not significantly penetrate inside the hydrogel volume within the time-scale of CLSM analysis. This arrangement eliminated the influence of strong fluorescence emission of the PI layer compared to Alexa 488-labeled IgG. The CLSM images of hydrogels **H2, H5** and **H6** (*i.e.*, the

samples used for the *in vitro* experiments discussed further below) are shown in Figure 36. The $h_{wet}$ values did not correlate with either preparation conditions or $h_{dry}$ values. In addition, the thickness of individual swollen hydrogels exhibited a significant variation that was not expected from the low $R_a$ values obtained for the dry layers (Table 3)

This suggests that the uneven swelling of hydrogel layers may be caused by a crosslinking reaction that did not proceed homogeneously within the entire hydrogel volume irradiated in the dry state.

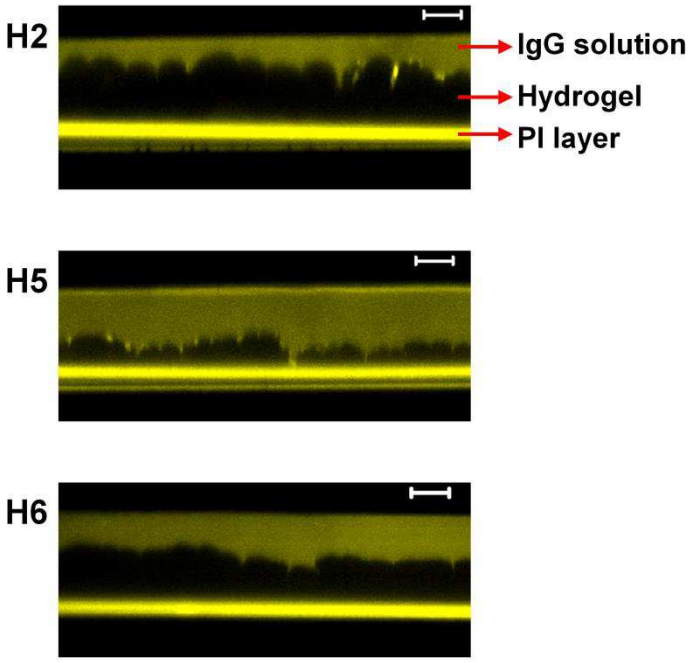


**Figure 36. CLSM images of H2, H5 and H6 in solution of Alexa 488-labeled IgG in PBS (scale bar is 20 µm).**

The hydrogel Young's moduli, determined in a PBS liquid environment by AFM measurements are reported in Table 3 and plotted in Figure 37. The layers made of **C1** copolymer with a lower 4-azidophenyl content exhibited Young's modulus of around 2 kPa. A higher content of 4-azidophenyl groups in the **C2** copolymer resulted in a Young's modulus increase up to 20 kPa depending on the copolymer concentration. Young's modulus data do not correlate with the content of Pluronic F-127. Rather, they are associated to the network density, which is in turn proportional to the 4-azidophenyl content and to the polymer concentration. Note that the higher network density for **C2** copolymer was not demonstrated by the $h_{wet}$ with expected lower thickness in the swollen state than for **C1**

copolymer due to lower swelling. Neither the higher network density for **C2** copolymer resulted in a higher water contact angle compared to hydrogels made of **C1** copolymer. Even though some of the obtained data would require further understanding, the employed strategy successfully served the primary aim of this study that was to covalently coat stiff PI plates by zwitterionic hydrogels of low stiffness, thus approaching the stiffness of neural tissues.

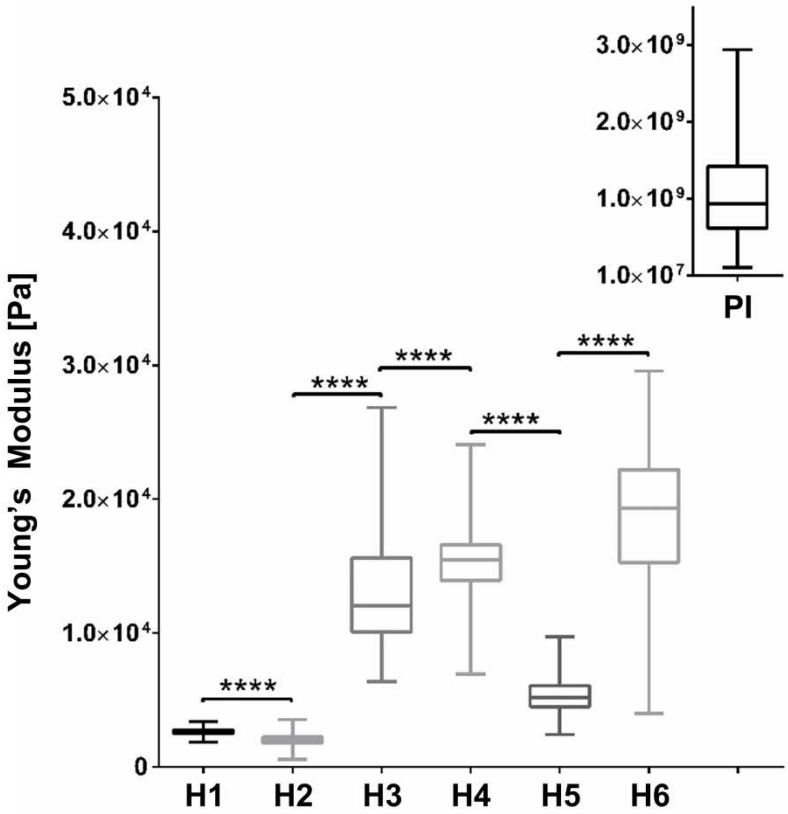


**Figure 37. Young's moduli of zwitterionic hydrogels H1-H6 deposited on PI plates, and of the PI plate assessed by AFM nanoindenting in PBS. Box and whisker plots show the median values and interquartile ranges (whisker represent the maximum and minimum values obtained). **** = $p < 0.0001$.**

***In vitro experiments***

*In vitro* tests were performed on three hydrogel types coated on the PI plates *(i)*: **H2**, **H5** and **H6**. These were selected based on their Young's modulus and chemical composition. In particular, we selected the hydrogels with the lowest and the highest Young's modulus, respectively, **H2** and **H6**, which featured the same amount of copolymer and Pluronic F-127, but different content of 4-azidophenyl groups. As a third sample type, we selected the **H5** hydrogel, which showed an intermediate value of Young's modulus and the same Pluronic F-127 content as **H2** and **H6** samples (see Table 3).

Fibroblast adhesion and morphology were evaluated by fluorescence imaging of living and fixed nHDF cells cultured on **H2**, **H5** and **H6** hydrogels and on PI controls. Figure 38a shows the fluorescence patterns of actin (stained in red) and nuclei (stained in blue) in cells attached on the different substrates. In particular, almost no adhesion was found on **H2** samples, while cells formed few clusters in scattered areas of the **H5** and **H6** samples. In contrast, cells on PI samples were well spread on the entire sample surface and there was no cluster formation. The cell density (in terms of cells/cm$^2$) was evaluated by counting the stained nuclei of living nHDFs attached on the different substrates; the results are reported in Figure 38b. Overall, a strong reduction of cell adhesion was observed for the samples covered with zwitterionic hydrogels compared to PI samples (median value reduction: **H2** = 97.4%, **H5** = 79.4% and **H6** = 72.6%). Comparing the fibroblast adhesion on the three different hydrogels, a statistical difference was found between sample **H2** and **H5** ($p$ = 0.0087) and between **H2** and **H6** ($p$ = 0.0003), which suggests that the lowest Young's modulus of **H2** hydrogel reduces the cell adhesion in a higher degree than for hydrogels **H5** and **H6** of somewhat higher Young's modulus.

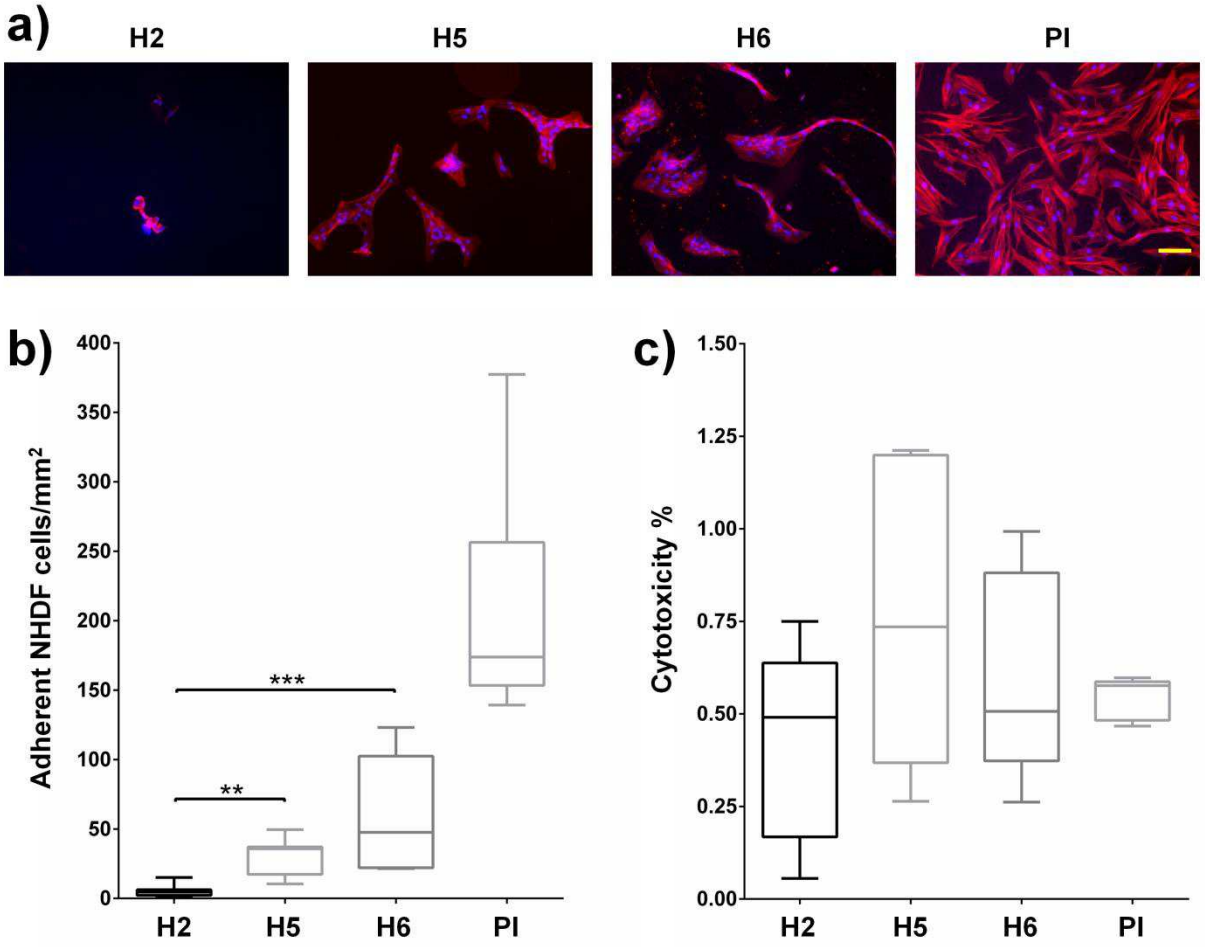


**Figure 38. In vitro evaluation of zwitterionic hydrogels on fibroblast cells. a) Fluorescence images at 10x magnification of nHDF cells on zwitterionic hydrogels H2, H5, H6 and on PI samples, showing nuclei stained in blue and actin in red (scale bar = 100 µm). b) Quantification of the adhesion of nHDF fibroblasts on zwitterionic hydrogels and on PI samples after 24 h culture. The box and whisker plots represent the median values and interquartile ranges of the number of adherent cells per cm$^2$ (whiskers represent the maximum and minimum values obtained). ** = $p < 0.01$, *** = $p < 0.001$. c) Quantification of the cytotoxicity percentage of zwitterionic hydrogels and PI by LDH cytotoxicity assay measured using nHDF fibroblasts after 24 h culture on substrates. The box and whisker plots represent the median values and interquartile ranges (whiskers represent the maximum and minimum values obtained).**

The obtained results are in a good agreement with previously published data. Stach *et al.* described significant reduction of RAT-2 fibroblasts adhesion on poly(sulfobetaine) modified conductive surfaces using electrografting method.[207] Significant reduction of RAT-2 fibroblasts adhesion was observed also in the case of zwitterionic hydrogels spin-coated on glass coverslips.[208] Similarly, the photoimmobilized sulfobetaine and carboxybetaine-based

polymeric films significantly inhibited the non-specific adhesion of fibroblast-like STO mammalian cells in comparison with non-modified substrates.[191] In the work of Chien *et al*., L929 cells well adhered on the non-modified poly(styrene) surface while cell adhesion was inhibited almost completely on the poly(carboxybetaine)-modified surfaces.[188] All these data, including those obtained in this work, indicate that immobilization of either sulfo- or carboxybetaine zwitterionic polymers on different surfaces enables to reduce cell adhesion in a significant way. Concerning neural electrode coatings featured by tuned mechanical properties, the sole recent study we can refer to is the work of Spencer *et al.*[178] Here, the authors demonstrated that PEG-based hydrogels with a Young's modulus of ~ 10 kPa significantly reduced the scarring process *in vivo* with respect to stiffer implants (glass capillaries, with a Young's modulus of ~ 70 kPa). The scarring process involves several events, included the adhesion of fibroblasts on the implant surface. Thus, although with several differences, *i.e. in vitro vs in vivo* data, different materials involved, different stiffness values investigated, our results can be considered in line with those reported by Spencer *et al*.[178] It is worth mentioning that in our work we further clarified the role of stiffness in this process, showing that values well below 10 kPa (almost one order of magnitude smaller) prevent fibroblast adhesion more efficiently.

Cytotoxicity of the different substrates was evaluated using nHDFs fibroblasts by quantifying the LDH release; results are reported in Figure 38c. Almost no cytotoxicity was observed for all the samples (the highest median value was 0.7%, found for the **H5** sample), in agreement with previous studies performed with NIH-3T3 fibroblasts on zwitterionic hydrogels.[209, 210] No statistical difference was found between the different hydrogels and the PI samples.

As for fibroblasts, macrophages adhesion and morphology was evaluated by fluorescence imaging of both living and fixed RAW 264.7 cells cultured on **H2**, **H5** and **H6** hydrogels and on PI controls. Fluorescence images of actin (stained in red) and nuclei (stained in blue) of cells attached on different substrates are shown in Figure 39a. Macrophages reflected the fibroblasts behavior: almost no adhesion was observed on **H2** samples and cells formed few clusters in scattered areas of **H5** and **H6** samples, while well spread cells were found on the PI samples, without cluster formation. A large reduction of cell adhesion was observed in the

samples covered with zwitterionic hydrogels with respect to PI samples (median value reduction: **H2** = 98.9%, **H5** = 93.2% and **H6** = 90.8%), see Figure 39b. This cell behavior is in agreement with the one observed in the study of Khandwekar *et al*., where sulfobetaine molecules were entrapped on poly(methyl methacrylate) surfaces leading to a reduction of RAW 264.7 cells adhesion.[211] Comparing adhesion of macrophages on the three different hydrogels, a statistical difference was found between sample **H2** and **H5** ($p$ = 0.0247) and between **H2** and **H6** ($p$ = 0.0019). The lower adhesion of macrophages on **H2** samples may be again explained by its low Young's modulus value. In the literature, a stiffness-based influence on macrophages adhesion has been reported, although on another cell line, THP-1.[212] Differently, Blakney *et al*. indicated that substrate stiffness did not play a role in RAW 264.7 cell attachment. However, in this case, the investigated Young's moduli were in the range of hundreds of kPa.[175]

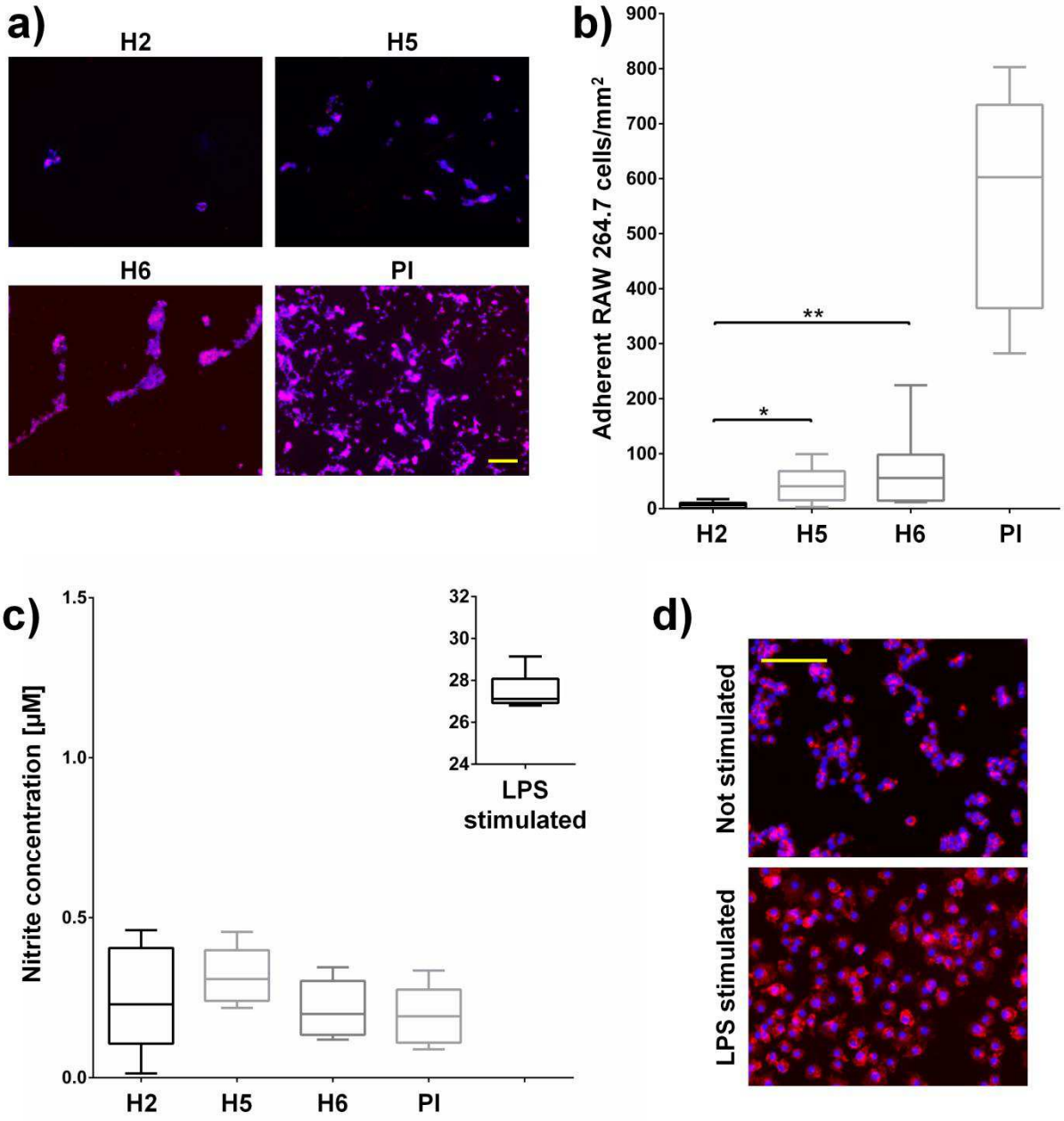


**Figure 39. In vitro evaluation of zwitterionic hydrogels on macrophage cells. a) Fluorescence images at 10x magnification of RAW 264.7 cells on zwitterionic hydrogels and on PI samples, showing nuclei in blue and actin in red (scale bar = 100 µm). b) Quantification of the adhesion of RAW 264.7 macrophages on zwitterionic hydrogels H2, H5, H6 and on PI samples after 24h of culture. Box and whisker plots represent the median values and interquartile ranges of the number of adherent cells per cm2 (whiskers represent the maximum and minimum values obtained). * = $p < 0.05$, ** = $p < 0.01$. c) Spontaneous nitric oxide production of cells seeded on zwitterionic hydrogels and PI samples for 24 h. Box and whisker plots represent the median values and interquartile ranges of the concentration of nitric oxide produced (whiskers represent the maximum and minimum values obtained). d) Morphological difference between non-stimulated and LPS-stimulated macrophages seeded on polystyrene. LPS-stimulated macrophages show activation-dependent morphology, with higher adhesion and spreading, compared to non-stimulated ones. Nuclei are stained in blue and actin in red (scale bar = 100 µm).**

Macrophages activation was evaluated by assessing nitric oxide (NO) production, in particular by measurement of nitrite release in the supernatant. NO is a physiological messenger and effector molecule involved in several biological processes. It is released in excess during host response and it contributes to pathogenic conditions by promoting oxidative stress. The nitrite concentrations are reported in Figure 39c. There was no statistical difference between the samples exhibiting very low absolute concentration for each hydrogel type (the highest median value was found for **H5** = 0.3 μM), especially when these data are compared with the amount of nitrite released by LPS-activated macrophages used as control (Figure 39c). This was confirmed by morphological evaluation: on each sample, the cells that attached maintained a round shape (Figure 39a), a morphology that is typical of non-activated cells (Figure 39d, top image), whereas LPS-stimulated cells tend to spread on the surface and thus increase their adhesion surface (Figure 39d, bottom image).

***Preliminary optimization of electrodes coverage and ex vivo insertion tests***

As stated in the Methods subsection, after the achievement of zwitterionic hydrogel based PI-coatings with the young modulus in the range of neural tissue one, and having understood their *in vitro* response, we started to optimize the hydrogel integration in the electrodes production process. The hydrogel layer had to be deposited on top of the electrodes which are fabricated by lithography technique, and be patterned by UV-masking in order to expose the electrode active sites and to facilitate electrodes peel off from Si wafers. For these reasons the photolabile azidophenyl group content in the poly(carboxybetaine methacrylamide) was modified (3.3 mol.%) and optimized as well as the coating deposition method in order to be included in the production process of thin film PI intraneural interfaces. PI-based interfaces produced by SMANIA S.r.l were coated with the modified zwitterionic hydrogel adopting the procedure described in details in the Methods subsection.

For these preliminary tests the hydrogel was not patterned, hence also the active sites were covered by the soft layer. As envisioned in future *in vivo* application, the hydrogel was inserted in a dry state to reduce the probability of hydrogel detachment. Figure 40 shows the manual insertion procedure in calf sciatic nerve.

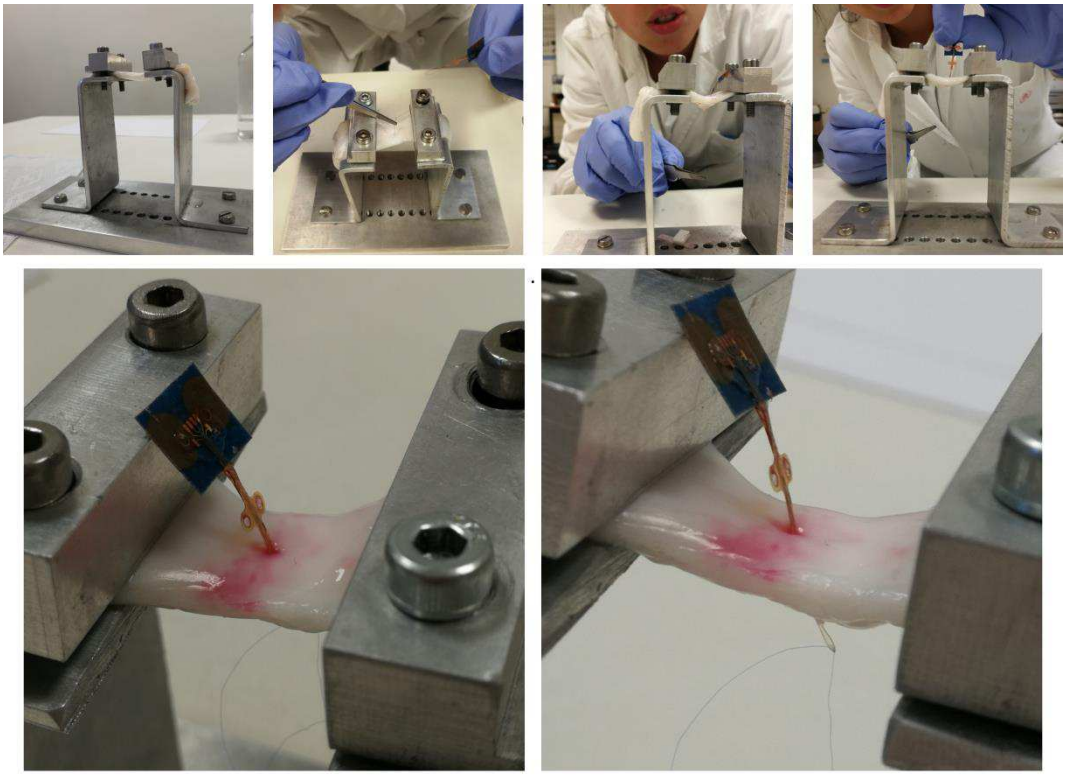

**Figure 40. Manual procedures of intraneural interface insertion**

The coating deposited on intraneural interface showed quite good stability during the insertion in the sciatic nerve. This was better demonstrated by controlled insertion tests performed on six different interfaces. The images obtained before and after the insertion were analyzed by eye and also by comparing the colour histogram of the red component. Just on two out of six interfaces, a detachment of the coating was noticed. Figure 41 represents the dyed coated electrodes before (a and c) and after (b and d) the insertion. In particular Figures 41 a and b show a case in which the coating detached from the interface surface, leaving the bare PI exposed, while Figures 41 c and d show a case in which the coating remained well attached on the surface, except for some little parts at the external borders of the interfaces, maybe due to the fact that the hydrogel was not patterned and hence it was ripped off during the peeling of the electrode from the Si wafer. Figure 42 shows the red colour histograms of the images acquired before (red) and after (green) the insertion in the nerve tissue.

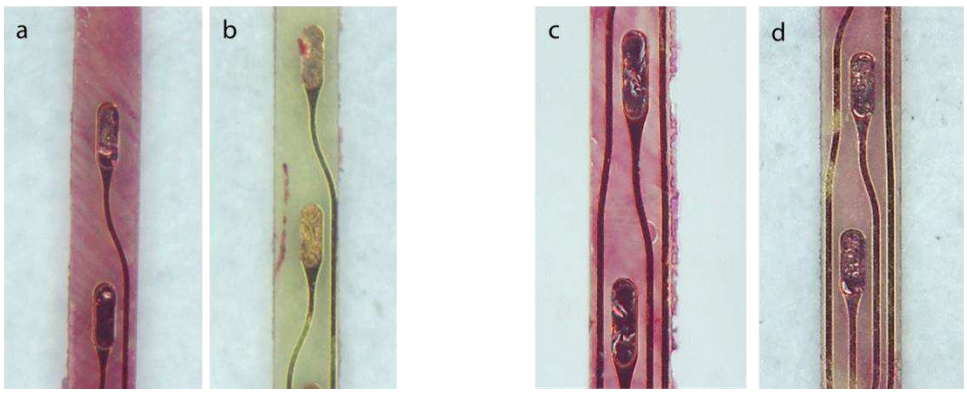


**Figure 41. Qualitative images of intraneural interfaces coated with zwitterionic hydrogel taken with a Hirox digital microscope before a) and c), and after b) and d) the insertion in a sciatic nerve, to verify coating stability. To ease the visualization, the hydrogel was stained by using a red dye. b) shows a case in which the coating was removed by the insertion procedure, thus leaving the bare PI.**

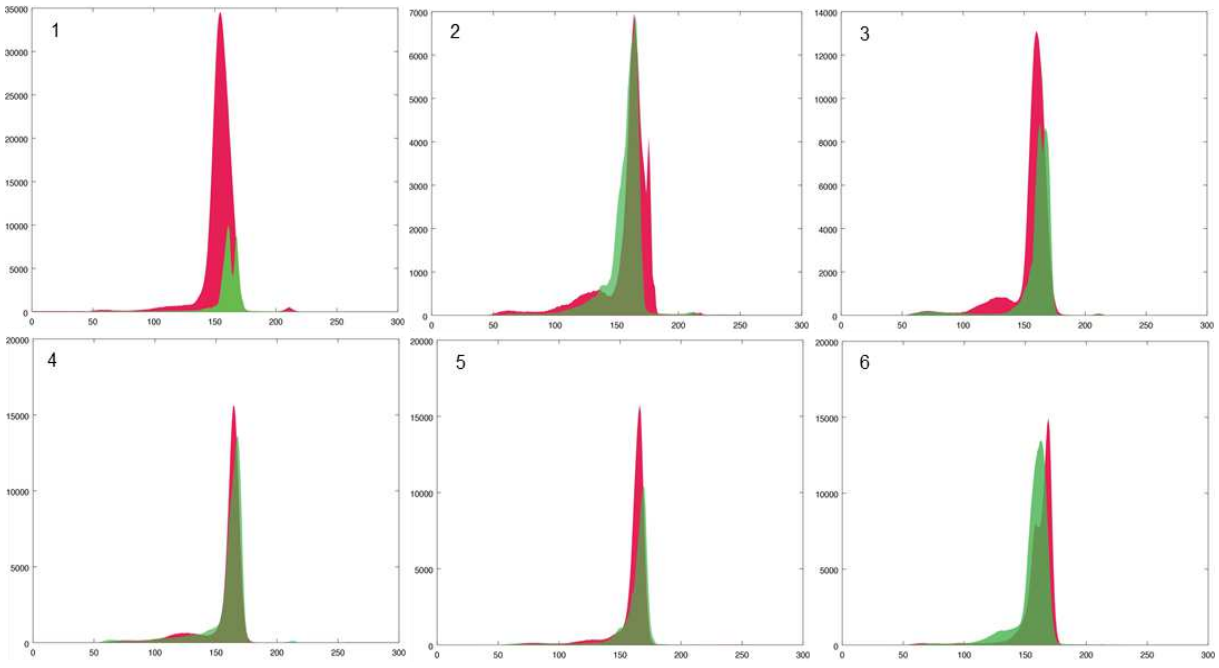


**Figure 42. Red colour histograms of the images obtained before (red) and after (green) the electrodes insertion in the nerve for all the 6 tested electrodes. The coordinates of the peaks were compared, showing that electrode 1 and 3 underwent coating detachment.**

Moreover few preliminary tests were performed to assess the possibility of patterning the hydrogel by UV-masking during the crosslinking process. The modified zwitterionic copolymer and the changed concentration and deposition method show promise for the future implementation in PI based intraneural electrodes, as showed in Figure 43.

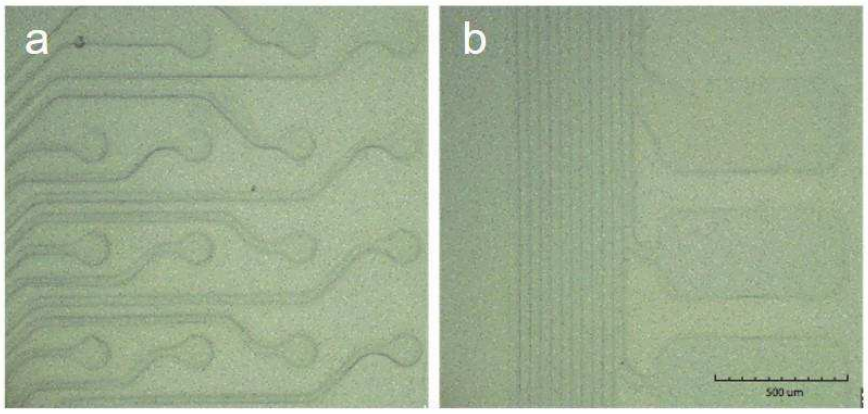


**Figure 43. Zwitterionic hydrogel deposited in PI surface and patterned by UV masking technique, normally used in lithography.**

This optimization process to obtain a fully covered PI interface has just begun and is still in progress. A considerable amount of work has to be carried out in order to characterize this obtained coating.

***In summary***

Due to their biocompatibility, flexibility and patternability with lithographic and dry etching techniques, polyimides (PI) are widely used both as implant encapsulation materials and as substrates for implanted neural interfaces. Despite these promising properties, they cannot prevent the formation of a fibrotic capsule. Several approaches have been reported aiming at reducing the formation of a scar-like tissue around the implant. The inhibition of protein and cell adhesion by means of non-biofouling coatings is one of these strategies. Moreover, it has been shown that the undesired host response to implants is also determined by the mechanical mismatch between the implant and the surrounding tissue. To this aim, in this Section we presented a strategy for covalently attaching carboxybetaine polyzwitterionic

hydrogel coatings to PI substrates, obtained by means of a photoactivated process. These coatings were featured by low stiffness values in the range of the neural tissues, for their possible future application as coatings for neural interfaces. Modified PI plates were characterized by a set of physico-chemical methods to evidence the presence of coatings, to visualize the completeness of the surface coverage by hydrogels, and to characterize the layer thickness and Young's modulus. The *in vitro* response of both fibroblasts and macrophages (the main cell types involved in the foreign body response) was assessed. The zwitterionic hydrogel coatings reduced the adhesion of both cell lines respect to PI control, showing almost no cytotoxicity and a clear correlation with the hydrogel stiffness. Moreover, the hydrogel layers did not induce macrophages activation, evaluated through the quantification of nitric oxide production. These results demonstrate the non-biofouling properties, low stiffness and UV patternability of zwitterionic hydrogels and thus establish the foundation for their possible *in vivo* investigation as coatings for PI-based neural interfaces.

### 3.1.2 Low intensity pulsed ultrasound stimulation (LIPUS) on muscle cells

## *Framework*

As already mentioned, soft tissue regeneration is one of the main goals of tissue engineering and regenerative medicine. Such disciplines combine engineering and life sciences to restore, maintain, replace and improve the functions of tissues and organs that are lost, due to injuries or diseases [8, 213]. In particular, skeletal muscle regeneration represents an interesting research domain. Thanks to resident stem cells and precursor cells, skeletal muscle is constantly renewed in response to injury, damage or aging[214]. According to Musarò[215], muscle injury and regeneration processes can undergo five interrelated and time-dependent phases, the first of which is degeneration (necrosis); then, inflammation, regeneration, remodeling, and maturation/functional repair occur. After the intervention of macrophages for the removal of necrotic cellular debris, the satellite cells (particular stem cells localized between the basal lamina and the muscle fiber membrane) and other myogenic progenitors are activated and undergo proliferation, differentiation and fusion to one another or to undamaged portions of the fibers, thus forming new myofibers or myofiber segments [216]. Some of these processes reiterate the sequence of events observed during embryonic myogenesis [215]. Severe damages due to diseases such as muscular dystrophies, or traumatic lesions such as contusions and strains (that are common in sports medicine), cause necrosis of myofibers, stimulate the inflammatory response and trigger the consequent regeneration process[216]. Several approaches have been proposed to improve and accelerate muscle regeneration. In the most critical cases, the self-repairing capability of skeletal muscle can be seriously impaired due to subject ageing, severe muscle diseases such as different types of congenital myopathies featured by progressive muscle wasting and weakness or large mass loss following trauma, aggressive tumor removal and prolonged denervation. In these cases bio/non-bio interfaces play an important role; invasive regenerative medicine approaches can be pursued and new genetic and cell therapy strategies have been proposed. For example, myogenic cells from embryonic stem cells and

induced pluripotent stem cells have been considered for the reconstruction of whole muscle tissue parts, by engineering functional three-dimensional skeletal muscle tissues using biocompatible smart materials [217-219]. Along this research line, several efforts have focused both on the direct stimulation of biological components thanks to surface properties such as surface topography [220-222], material stiffness [223], surface electrical properties [224] as well as the effects of external physical stimuli such as electro-mechanical inputs [225]on myogenesis.

Considering less severe muscle injuries, typical of sport activities, less invasive strategies have been suggested to improve tissue healing and regeneration. First of all, immediate treatment of an injured skeletal muscle usually follows the 'RICE' principle (Rest, Ice, Compression and Elevation) with the aim to minimize bleeding into the injury site. Then, different therapies can be exploited, such as rehabilitation exercises, use of non-steroidal anti-inflammatory drugs or glucocorticoids and hyperbaric oxygen therapy [226, 227]. It has been shown that microcurrent electrical neuromuscular stimulation can reduce signs and symptoms of muscle damage, thus strongly suggesting that it can facilitate the regeneration of injured skeletal muscles [228]. Moreover, it is known that skeletal muscle is sensitive to mechanical stimulation, that can be provided by means of massages and exercises, by using smart materials or by exploiting therapeutic ultrasound [226, 227, 229, 230].

Ultrasound is commonly used for imaging and diagnostic applications and has the advantage over other imaging modalities of being non-ionizing. It has been shown that ultrasound can be used also for therapeutic purposes, both in low and high intensity ranges. Several bioeffects due to ultrasound exposure have been observed in the literature at a tissue, cellular and protein level [231-233]. Healing properties have been assigned in particular to Low Intensity Pulsed Ultrasound (LIPUS) stimulation [231]. At a cellular level, LIPUS has been observed to increase proliferation and migration of aortic endothelial cells, and increase proliferation of fibroblasts, Schwann cells and other cell types [233].

Therapeutic ultrasound produces a combination of non-thermal effects (acoustic streaming and cavitation) that are difficult to isolate. Acoustic streaming is defined as the physical forces of the sound waves that provide a driving force capable of displacing ions and small molecules.[234] At the cellular level, organelles and molecules of different molecular weight

exist. While many of these structures are stationary, many are free floating and may be driven to move around more stationary structures. This mechanical pressure applied by the wave produces unidirectional movement of fluid along and around cell membranes.[235] Cavitation is defined as the physical forces of the sound waves on microenvironmental gases within fluid. As the sound waves propagate through the medium, the characteristic compression and rarefaction causes microscopic gas bubbles to contract and expand, in the tissue fluid.[236] It is generally thought that the rapid changes in pressure occur both in and around the cell. Substantial injury to the cell can occur when microscopic gas bubbles expand and then collapse. In the case of low intensity ultrasound (30–1000 mW/cm$^2$), it is possible that the mechanisms are non-cavitational, and the processes involved are not well understood.[233]

What is known is that LIPUS is able to induce micromotion on the extra cellular matrix (ECM) and that the process of signal transduction starts at the cell membrane. These strains are transduced by the cell membrane and coupled into the cell cytoskeleton and cytoplasm, where they initiate intracellular signalling cascades.[233] Additional reports suggest that ultrasound alters cellular membrane properties (cellular adhesion, membrane permeability, calcium flux, and proliferation), activating signal-transduction pathways that lead to proteomes regulation [237, 238]. Importantly, exposure to ultrasound causes an increase in intracellular calcium in many cells types, such as fibroblast, monocyte and mesenchymal stem cells. Cells employ calcium as a cofactor in regulating the activity of enzymes, many of which are associated with signal-transduction pathways and relative proteomes modulation.[239]

We mentioned in the Introduction section that in the field of bio/non-bio interfaces it is very important to know which are the bioeffects that can be generated by the external stimulus itself so to provide an augmented beneficial effect to the regeneration process. For this reason, a deep analysis of the literature has been done on the effect of LIPUS on muscle tissues, in this case.

Considering muscle regeneration, as reported by Abrunhosa et al.[240], therapeutic applications of ultrasound have been used in physiotherapy and rehabilitative settings since

the 1950s in order to induce both thermal and mechanical bioeffects. Despite the wide use of this instrument in the clinical practice, in vitro and in vivo studies aimed at evaluating the bioeffects triggered by ultrasound led to rather divergent results.

Concerning *in vivo* tests, Wilkin *et al.* [241] and Markert *et al.* [242] found no evidences that LIPUS was able to enhance and accelerate skeletal muscle regeneration after contusion injury. In these studies, the authors stimulated rats at different intensities and in a pulsed mode at a frequency of 3.3 MHz and continuously at a frequency of 3 MHz. In contrast, Fisher *et al.* [243] proved that rat muscles receiving pulsed ultrasound at a frequency of 870 kHz responded in a positive way in comparison with continuous stimulation and non-stimulated controls, with a significant production of contractile proteins. Chan *et al.* [244] found an enhancement in regenerative myofiber formation after injury, when mice muscles were stimulated by LIPUS at a frequency of 1.5 MHz, while Matsumoto *et al.* [245] suggested that pulsed ultrasound irradiation can inhibit the development of disuse muscle atrophy in rats (partly via activation of satellite cells), by stimulating muscles in a continuous mode at 1 MHz. Nagata *et al.* [246] found a reduction of the inflammatory infiltrate cell number and an increase of the regenerating myofiber size in the experimental group of C57BL/6 mices that were treated with pulsed ultrasound at 1 MHz, in comparison with the control group.

Considering *in vitro* tests, Chan *et al.* [244] performed differentiation experiments on C2C12, a murine skeletal muscle cell line, showing an increase of the myogenin protein during differentiation, due to LIPUS treatment at a frequency of 1.5 MHz. Nagata *et al.* [246] observed an enhancement of myogenin mRNA expression in the same cell line due to LIPUS treatment at a frequency of 3 MHz, simulating an inflammatory environment. Abrunhosa *et al.* (2014) [240] compared the effects of continuous and pulsed ultrasound treatment at a frequency of 1 MHz on primary cultures of chick skeletal muscle cells, determining in both cases an increase of differentiation due to stimulation with respect to the non-stimulated controls and showing better results in the case of continuous stimulation. Ikeda *et al.* [247] demonstrated that LIPUS pushes the differentiation pathway of C2C12 cells more in the osteoblast and/or chondroblast lineage than in the myoblast one, by activating the phosphorylation of ERK1/2 and p38 MAPK.

The wide range of exposure parameters and metrics used in the studies discussed here makes it difficult to observe clear correlations between ultrasound exposure conditions and the muscle regeneration efficacy. This is mainly due to the lack of standardization of stimulation protocols and to the lack of systematic investigations that compare different exposure conditions. In addition, the different biological models used and the different types of injuries analyzed contribute to a scarce coherence of the results. As reported by Abrunhosa *et al.* [240](2014), ultrasound are broadly used in the frequency range 0.5 - 5.0 MHz, but the typical equipment used can be set only at 1 or 3 MHz. The most common intensities range from few tens of $mW/cm^2$ up to 1 $W/cm^2$. The treatment duration also varies among studies, making comparison of the results difficult. Moreover, in many cases, poorly controlled cell exposure conditions are used. A full list of employed exposure parameters is often not provided and the lack of standardized dose concepts for ultrasound[248] makes difficult the comparison between studies. Most stimulation set-ups do not consider undesired artifacts such as standing waves, ring interferences, temperature elevations and cross-stimulation of adjacent wells. In many cases, ultrasound transducers are directly placed at the bottom of standard cell culture plates. Although gels or water-filled gaps can help to improve the acoustic coupling between transducer and plate, attenuation and reflection of ultrasound cannot be avoided with this approach [249]. Puts *et al.* [250, 251] suggested a solution to overcome these issues, providing a focused low-intensity pulsed ultrasound (FLIPUS) stimulation set-up. They stimulated C2C12 cells, taking into account the possible attenuation of the ultrasound by the polystyrene wells and the spatial variations of intensities across them. They found pronounced transmission losses at the frequencies of 3 MHz, 4.5 MHz, 5 MHz, while maximum transmission was found at 3.3, 4.2 and 4.9 MHz. The authors limited the stimulation protocol to only one frequency, 3.6 MHz, which was not the one showing the maximum transmission, but it allowed to minimize spatial variations across cell chambers. Table 4 and Table 5 summarize the *in vivo* and *in vitro* evidences reported in the state-of-the-art described above.

To the best of our knowledge, no studies report an *in vitro* systematic investigation of the effects of LIPUS exposures at different frequencies and intensities. This was done by exploiting a proper fully tunable stimulation system with an ultrasound-transparent cell

culture well, thus enabling correlation between the ultrasound delivered and the triggered bioeffects, and it is presented in this Section. In particular, we performed highly controlled LIPUS on C2C12 cells, by comparing 4 different selected frequencies (500 kHz, 1 MHz, 3 MHz and 5 MHz) and 3 different selected intensities (250, 500 and 1000 mW/cm$^2$) and quantifying the triggered bioeffects for the different conditions, in terms of cell proliferation and differentiation.

The work reported in this Section is published in:

**Salgarella A.R.**, Cafarelli A.., Ricotti L., Capineri L., Dario P., Menciassi A. (2017). "Optimal Ultrasound Exposure Conditions for Maximizing C2C12 Muscle Cell Proliferation and Differentiation". Ultrasound in Medicine & Biology, 43(7), pp.1452-1465.[252]

**In vivo**

| Reference | US frequency | Treatment duration | US Intensity | Mode | Animal model | Bioeffects |
|---|---|---|---|---|---|---|
| Wilkin *et al.* 2004 | 3.3 MHz | 5 min daily for 7 days | 1 W/cm$^2$ | Pulsed (duty cycle 20%) | Wistar rats | No influence of the treatment on the markers of skeletal regeneration such as muscle mass, total protein concentration, myonuclear number and density, respect to the controls. |
| Markert *et al.* 2005 | 3 MHz | 5 min daily for 4 days | 100 mW/cm$^2$ | Continuous | Wistar rats | No significant effect on muscle mass, mean cross-sectional area, number of nuclei per cell, myonuclear density and concentration of contractile protein, respect to the controls. |
| Fisher *et al.* 2003 | 870 kHz | 5 min daily for 6 days | 1 W/cm$^2$ | Continuous or Pulsed (duty cycle not available) | Sprague-Dawley rats | Increment in the production of proteins responsible for the contractile machinery due to Pulsed US, with respect to both non-stimulated controls and continuous US treatment. |
| Chan *et al.* 2010 | 1.5 MHz | 20 min daily for 28 days | 30 mW/cm$^2$ | Pulsed (duty cycle 20%) | C57BL10J+/+ mices | Increase of the regeneration of myofibers, fast-twitch and tetanus of LIPUS-treated muscles. No major strength difference between the normal non-injured muscle and the group treated with LIPUS. |
| Matsumoto *et al.* 2013 | 1 MHz | 15 min daily, for 4 weeks (6 days/week) | 1 W/cm$^2$ | Pulsed (duty cycle 20%) | Wistar rats | Inhibition of the development of disuse muscle atrophy by means of pulsed US. Increase of diameter of all types of muscle fibers and activation of satellite cells (BrdU-positive muscle nuclei), respect to the controls. |
| Nagata *et al.* 2013 | 1 MHz | 15 min daily, for 7 days | 150 mW/cm$^2$ | Pulsed (duty cycle 20%) | C57BL/6 mices | Reduction of the number of inflammatory infiltrate cells and increase of the size of regenerating myofibers and of Pax7-positive cells in the US treated group. |

**Table 4. *In vivo* studies on ultrasound stimulations of muscles. ("US" = ultrasound)[252]**

**In vitro**

| Reference | US frequency | Treatment duration | US Intensity | Mode | Cell Line | Bioeffects |
|---|---|---|---|---|---|---|
| Chan *et al.* 2010 | 1.5 MHz | 20 min daily for 8 days | 30 mW/cm$^2$ | Pulsed (duty cycle 20%) | C2C12 | Significantly higher proliferative rate and cell number, increase in myogenin and actin proteins in the experimental group treated with LIPUS |
| Nagata *et al.* 2013 | 3 MHz | 15 min single exposure | 30 mW/cm$^2$ | Pulsed (duty cycle 20% | C2C12 stimulated by TNF-α or IL-1β to simulate inflammation | Significant down-regulation of COX-2 mRNA expression and up-regulation of myogenin mRNA expression and protein synthesis in C2C12 cells stimulated by TNF-α or IL-1β and treated with ultrasound, respect to the controls only provided with the chemical compounds. |
| Abrunhosa *et al.* 2014 | 1 MHz | 5 or 10 min single exposure | 500 mW/cm$^2$ or 1 W/cm$^2$ | Continuous or Pulsed (duty cycle not available) | Myogenic cells from chick embryos | Significant differences in myotube thickness between treatments in continuous mode at 0.5 W/cm$^2$ for 5 or 10 min, in continuous mode at 1.0 W/cm$^2$ for 5 min, and in pulsed mode at 1.0 W/cm$^2$ for 5min, compared with non-stimulated samples. The treatment in continuous mode at 0.5 W/cm$^2$ for 5 min induced the higher increase in desmin protein, myotube thickness, number of nuclei per image field and number of nuclei per myotube, compared with non-treated samples |
| Ikeda *et al.* 2006 | 1.5 MHz | 20 min single exposure | 70 mW/cm$^2$ | Pulsed (duty cycle not available) | C2C12 | Increase of Runx2, Msx2, Dlx5, AJ18, and Sox9 gene expression, Runx2 protein expression and ERK1/2 and p38 MAPK phosphorylation in the US stimulated samples compared with non-stimulated controls. US treatment pushed the differentiation pathway of C2C12 cells into the osteoblast and/or chondroblast lineage instead of the myogenic one. |
| Puts *et al.* 2015, 2016 | 3.6 MHz | 5 min or 30 min or 1h single exposure | 29.4 mW/cm$^2$ (2015) 44.5 mW/cm$^2$ (2016) | Pulsed (duty cycle 27.8%) | C2C12 | Focused LIPUS increases C2C12 proliferation and activates mechanosensitive transcription factors such as TEAD, AP-1 and Sp1. US stimulation also affects the expression of mechanosensitive genes such as c-fos, c-jun, HB-Gam and Cyr61. |

**Table 5. In vitro studies on ultrasound stimulations of muscle cells. ("US" = ultrasound)[252]**

# *Methods*

***LIPUS stimulation set-up***

The ultrasonic set-up for cell stimulation (shown in Figure 44a) was composed of a programmable wave generator (33220A, Agilent technologies, Santa Clara, California, USA) connected in series with a power amplifier and an immersion ultrasound transducer (WS75-0.5, WS75-2 and WS75-5, Ultran Group, State College, Pennsylvania, USA) with an active diameter of 19 mm. Three different transducers were used for exploring four different stimulation frequencies: WS75-0.5 for 500 kHz, WS75-2 for 1 and 3 MHz and WS75-5 for 5 MHz. For the WS75-0.5 and the WS75-2 transducers, a radio frequency (RF) power amplifier (50 dB gain, 240L, Electronics & Innovation, Rochester, New York, USA) was used. Due to the very low electrical impedance (Z) of the WS75-5 transducer (|Z| = 3.5 Ω @ 5 MHz, measured with a vector network analyzer, DG8SAQ, SDR-Kits, Trowbridge, Wilts, UK), a linear 15 MHz bandwidth power amplifier was used instead of the broadband RF amplifier in order to maximize the power transfer to the ultrasonic transducer[253]. The latter amplifier was designed with very low output impedance and low distortion for power ultrasonic applications. For the experiments at 500 kHz a low pass impedance matching electric circuit, with an inductance of 122 µH and a capacitance of 443 pF, was designed and interposed between the RF amplifier and the WS75-0.5 transducer (Re(Z) = 64 Ω and Im(Z) = -813 Ω @500 kHz) in order to maximize the power transferred to the transducer and to minimize the reflected signal.

The transducer and the sample were coaxially aligned in a tank of deionized and degassed water (Figure 44a). A linear rail allowed movement of the sample along the beam axis of the transducer to enable alignment of the cells at the location of the axial maximum of the pressure field. In order to determine the geometry of the acoustic field generated by each transducer, the acoustic pressure was measured under free field conditions using a hydrophone mounted on a 3 axis step-by-step motorized positioning frame (XYZ BiSlide, Velmex Inc, Bloomfield, New York, USA), immersed in a dedicated calibration tank and connected to an oscilloscope (7034B, InfiniiVision, Agilent Technologies, Santa Clara, California, USA). A 0.2 mm PVDF needle hydrophone (calibrated from 1-30 MHz, Precision

Acoustics Ltd, Dorchester, Dorset, UK) was used for the characterization of transducers in the MHz range and an ITC-6128 hydrophone (100-600 kHz, International Transducer Corporation, Santa Barbara, California, USA) was used for characterization in the kHz range. A dedicated LabVIEW program (National Instruments Corporation, Austin, Texas, USA) allowed the synchronization between the motors, the wave generator and the signal acquired by the oscilloscope. Pressure field maps (normalized to the maximum pressure) in the axial planes of each of the transducers are reported in Figure 44b, for each frequency investigated in this study.

Each transducer was characterized also in terms of intensity *vs* driven voltage. For each frequency, the Spatial Peak Pulse Average Intensity (SPPA intensity) was evaluated at the point of maximum amplitude and it was computed as

$$SPPA\ intensity = p^2 / (\rho \cdot c)$$

where $p$ denotes the root mean squared acoustic pressure detected by the hydrophone, $\rho$ the density of water and $c$ the speed of sound in water, while the driven voltage was measured at the output of the power amplifier. To enhance the reliability of the study, all cell stimulation experiments were performed in deionized and degassed water with samples positioned in the point of maximum pressure (dashed vertical red lines, in Figure 44b). The water in the stimulation tank was kept at room temperature (~ 28°C); all samples were immersed in the tank for the duration of the stimulation task (5 min). Control samples were also immersed for 5 min, although not stimulated, so to exclude possible manipulation- and temperature-dependent effects on the final results.

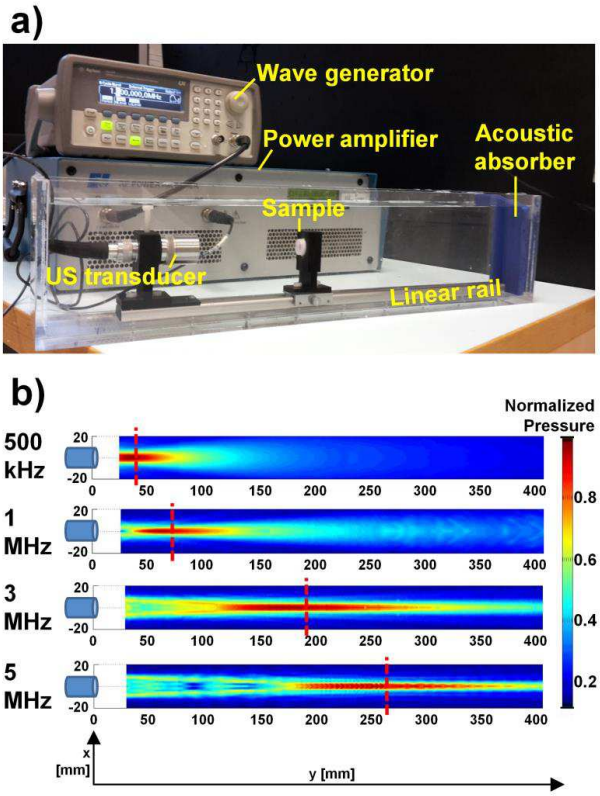


**Figure 44. Custom ultrasound stimulation set-up. a) Ultrasound stimulation set-up and its components. b) Normalized pressure field maps for each frequency under investigation, obtained during the transducer characterization phase. Dashed vertical red lines highlight the highest pressure field conditions for each frequency, which correspond to the positions in which the samples were placed during stimulation. (from Salgarella *et al.*, 2017[252])**

***Temperature measurements***

Temperature rising inside the cell culture well due to ultrasound stimulation was evaluated by means of a fine wire thermocouple (COCO-001, OMEGA, Stamford, Connecticut, USA), positioned inside the well for each ultrasound stimulation condition. A type T thermocouple (resolution of 0.1 C°) with a diameter of 25 µm was selected in order to minimize scattering and reflections of the ultrasound wave and to minimize the consequent errors in temperature measurements, which could occur using probes with typical dimensions equal to or greater than 1/2 of the square root of the wavelength (Hynynen and Edwards 1989). Temperature data were acquired at 1 Hz of sampling frequency by means of a thermocouple measurement device (USB-TC01, National Instruments Corporation, Austin, Texas, USA). Tests were performed at room temperature (~ 28 °C).

***Ultrasound-transparent wells***

An ultrasound transparent cell culture well was needed in order to guarantee a known and reproducible ultrasound cell exposure. To this purpose, a multilayered structure for cell cultures was designed (Figure 45). It consisted of a thin polystyrene membrane (25 µm thickness, Goodfellow, Huntington, Cambridge, UK) secured within a cylindrical well (1 cm in diameter) made of polytetrafluoroethylene and containing the cell culture medium. Secure mounting of the structure was guaranteed by a custom perforated cup produced by 3D printing (Projet HD 3000, 3D Systems, Rock Hill, South Carolina, USA) that allowed ultrasound waves to directly reach the membrane. Moreover, the cup houses an agarose disk during the culture, which was used to provide cells with a uniform support. The disk was removed during ultrasound stimulation.

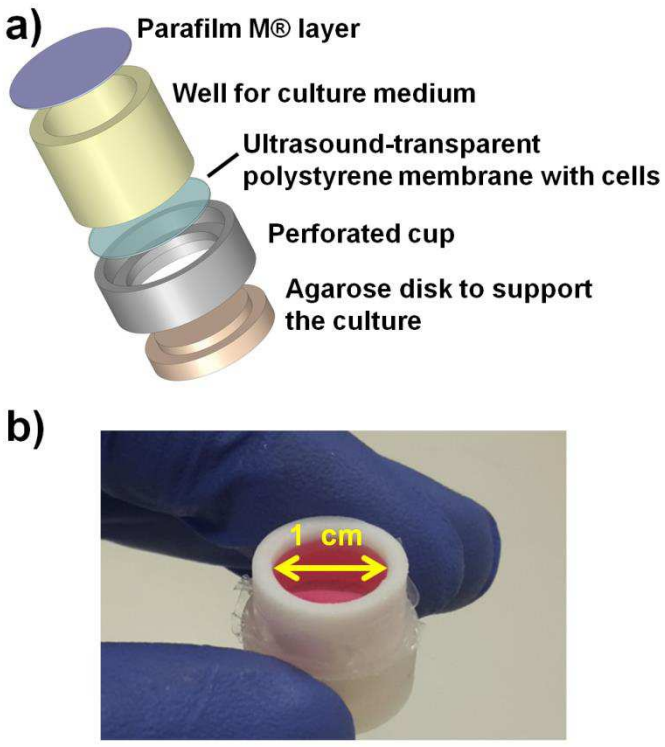


**Figure 45. Ultrasound-transparent cell culture well. a) Exploded representation of the culture well, showing its components. The polystyrene membrane is featured by a thickness of 25 µm, thus resulting transparent to ultrasound waves. b) Picture of a fully assembled well, filled with cell culture medium. (from Salgarella *et al.*, 2017[252])**

Thanks to its small thickness (much smaller than the ultrasound wavelengths, which range from 2.96 mm to 0.3 mm), the polystyrene membrane did not attenuate ultrasound waves. The transmission through the membrane was measured by using a through-transmission technique in which the signal was acquired in absence and in presence of the membrane interposed between the emitting transducer and the hydrophone [254]. The transmission values for the different frequencies resulted as follows: (1) f = 500 kHz, transmission: 99.86%; (2) f = 1 MHz, transmission: 99.74%; (3) f = 3 MHz, transmission: 99.36%; (4) f = 5 MHz, transmission: 99.10%. For these measurements, the transducers were driven with a sinusoidal tone burst of 40 cycles at frequency f, in presence and absence of the sample. Then, the root mean squares of the two corresponding signals acquired were calculated and divided each other. For all measurements, signals were averaged 10 times in order to significantly reduce the noise.

Before use, all parts of the wells were washed with Ethanol 70% (Sigma Aldrich® Corporation, St. Louis, Missouri, USA) and ultrapure MilliQ® water (Merck Millipore, Darmstadt, Assia, Germany) and exposed to UV light for 30 min; then all components were assembled under sterile conditions. In order to avoid liquid leakage, UV sterilized Parafilm M® (Bemis Company, Neenah, Wisconsin USA) was used as a gasket to be placed on the opposite side of the well, to close it during stimulation. Sterile agarose disks (2% wt/vol, Sigma Aldrich® Corporation, St. Louis, Missouri, USA) were prepared in the autoclave. Once removed from the autoclave, the solution was allowed to cool down to 45 ºC, when Penicillin/Streptomycin (PEN/STREP, Gibco™ - Thermo Fisher Scientific, Waltham, Massachusetts, USA) and Amphotericin B (Sigma Aldrich® Corporation, St. Louis, Missouri, USA) were added to the agarose solution, to a final concentration of 1% each. The solution was then cast into a disk and left to set.

The polystyrene membrane, within the assembled wells, was then treated with oxygen plasma (Colibrì, Gambetti Kenologia S.r.l., Binasco, Milan, Italy; parameters: 100% O2, 50 s at 50 W and 0.5 mBar), to make it hydrophilic and to promote the formation of a stable protein coating. The membrane was incubated for 6 h at 37 °C with 100 µL of a Collagen Type I solution from rat tail (Sigma Aldrich® Corporation, St. Louis, Missouri, USA), diluted in sterile

water (100 µg/mL). After the incubation period, the liquid was removed and the membrane was left to dry overnight. Just before cell seeding, the wells were exposed again to UV light for 30 min. This protein coating was performed to improve cell attachment to the polystyrene membrane and to help the formation of multinucleated myotubes avoiding their detachment from the surface.

***Cell cultures and biological assays***

The C2C12 cell line (ATCC® CRL1772™, ATCC®, Manassas, Virginia, USA) was used in this study. It is a subclone of the mouse myoblast cell line established by D. Yaffe and O. Saxel (Yaffe and Saxel 1977) which can differentiate, forming contractile myotubes and producing characteristic muscle proteins. C2C12 cells were cultured and propagated in vented flasks to near 80% confluence. The proliferation medium was composed of high-glucose Dulbecco's Modified Eagle's Medium (DMEM, Gibco™ - Thermo Fisher Scientific, Waltham, Massachusetts, USA) added with Fetal Bovine Serum (FBS, Gibco™- Thermo Fisher Scientific, Waltham, Massachusetts, USA) to a final concentration of 10%, and PEN/STREP, to a final concentration of 1%. To harvest cells, the medium was removed and the cells were washed twice with PBS (Gibco™- Thermo Fisher Scientific, Waltham, Massachusetts, USA) and trypsinized for 2-3 min at 37 °C (trypsin solution: 0.25% w/v Trypsin - 0.53 mM EDTA, Gibco™ - Thermo Fisher Scientific, Waltham, Massachusetts, USA). Trypsin was inhibited by adding complete medium, and removed by centrifuging cells (2500 rpm, 7 min, EBA 20 centrifuge, Hettich Lab Technology, Tuttlingen, Germany). Then cells were re-suspended and seeded in the wells for experiments at the desired density.

For proliferation tests, cells were seeded at a density of 10,000 cells/cm$^2$ and kept in culture for 24 h. 12 h post ultrasound treatment, cells were harvested using trypsin and centrifuged to form a cell aggregate (pellet). Then the liquid above the pellet (surnatant) was removed and the pellet was washed twice with PBS. Finally, sterile milliQ water was added and cells underwent two freeze-thaw cycles to lyse cell membranes. The lysates were analyzed using the Quant-iT™ PicoGreen® dsDNA Assay (Invitrogen™ - Thermo Thermo Fisher Scientific, Waltham, Massachusetts, USA) to quantify double-stranded DNA (dsDNA).

For differentiation tests, cells were seeded at a density of 50,000 cells/cm$^2$ and kept in culture for 24 h, after which they reached confluence. Then cells were switched to differentiation medium, composed of high-glucose DMEM added with FBS to a final concentration of 1%, PEN/STREP to a final concentration of 1% and 1% of Insulin-transferrin-sodium selenite media supplement (ITS, Sigma Aldrich® Corporation, St. Louis, Missouri, USA). The medium was changed once per day for 7 days. 24 h after the last stimulation, cells were fixed with a paraformaldehyde (Sigma Aldrich® Corporation, St. Louis, Missouri, USA) solution in PBS (4% w/v) for 15 min, then permeabilized with 0.1% Triton X-100 (Sigma Aldrich® Corporation, St. Louis, Missouri, USA) in PBS for 15 min. The cells were then stained for actin fibers with Tetramethylrhodamine B Isothiocyanate Labeled Phalloidin (Sigma Aldrich® Corporation, St. Louis, Missouri, USA) and for nuclei with Hoechst 33342 (Molecular Probes™ - Thermo Fisher Scientific, Waltham, Massachusetts, USA) for further 15 min. Fluorescence images were obtained by means of a UV-VIS microscopy analysis (ECLIPSE Ti-E, Nikon Corporation, Minato-ku, Tokyo, Japan). Images of the blue channel (nuclei) and the red channel (actin) were acquired for each sample at 10X magnification in 5 different areas of the well. Differentiation was evaluated by quantifying length and width of the myotubes formed, by means of the ImageJ® software (National Institutes of Health, Bethesda, Maryland, USA) and by computing the fusion index. This, for each image, was calculated as the number of nuclei in multinucleated structures divided by the total number of nuclei in the image (Figure 46).

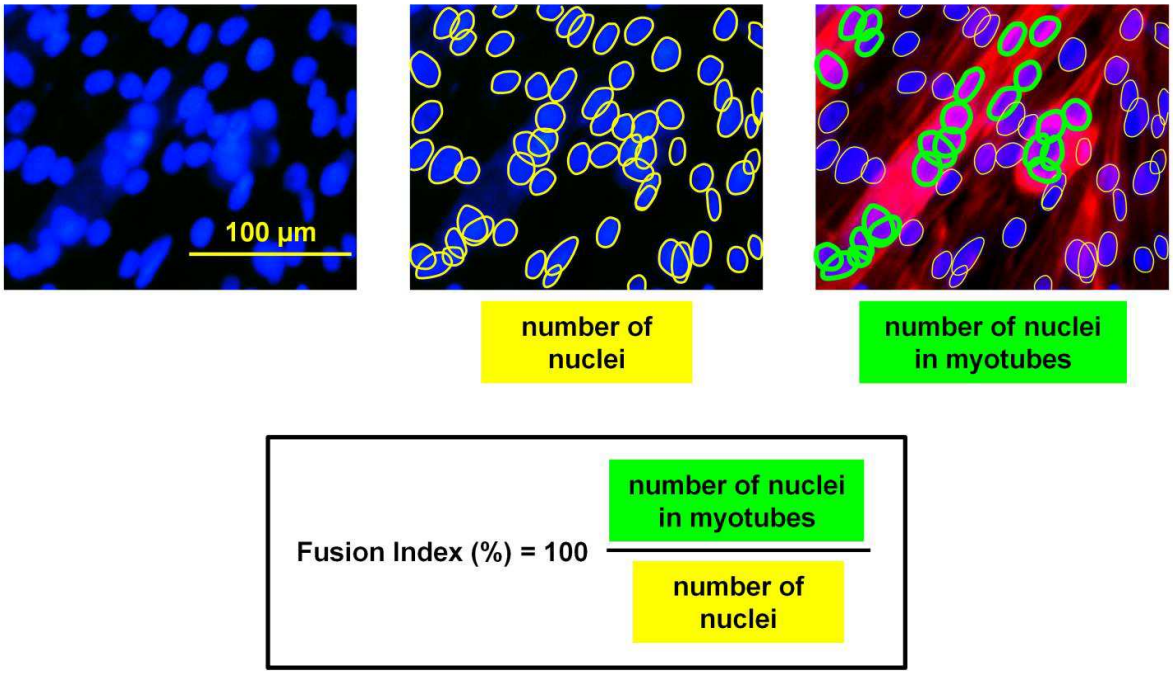


**Figure 46. Depiction of the fusion index calculation procedure. Fluorescence images show cell nuclei in blue, F-actin in red. Yellow lines indicate nuclei, green lines indicate nuclei embedded in myotubes (elongated multinucleated structures). (from Salgarella *et al.*, 2017[252])**

Moreover, images at 4X magnification of the red channel (actin) were taken for each sample, in order to have an overall low-magnification qualitative view of the different sample types.

***Stimulation protocol***

The protocol for proliferation tests consisted of a single LIPUS stimulation performed 24 h after cell seeding; the evaluation of the effects produced was carried out 12 h after such single ultrasound exposure (Figure 47a). The protocol for differentiation tests, instead, consisted of LIPUS exposures repeated daily for 7 days, associated with medium renewals for 7 days, starting 24 h after cell seeding. The effects of the treatment were evaluated 24 h after the last ultrasound stimulation (Figure 47b).

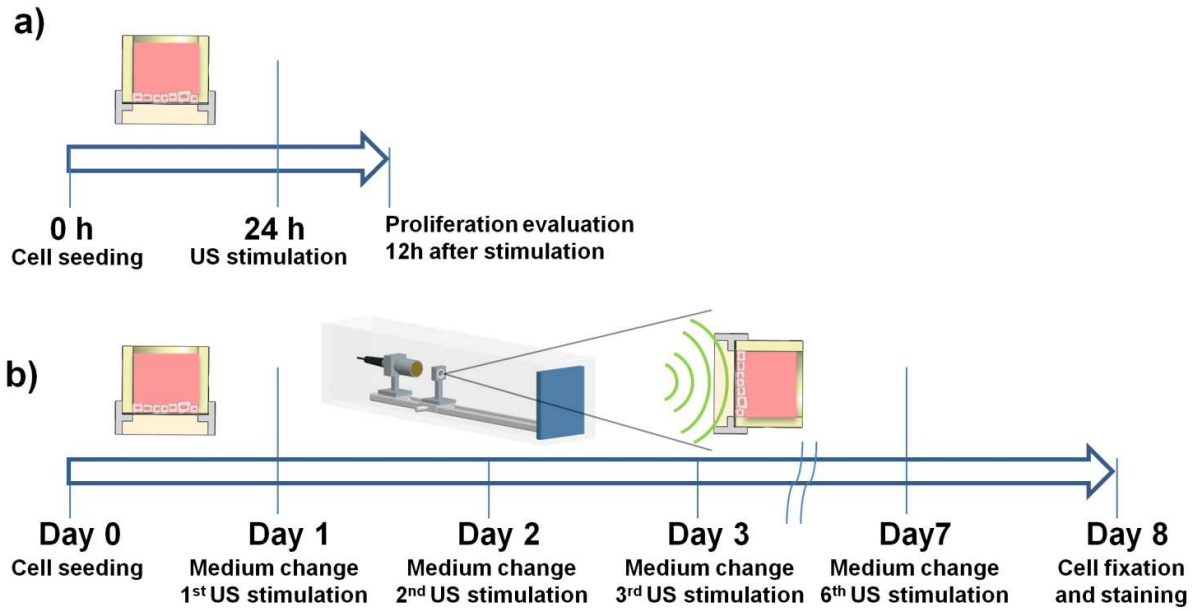


**Figure 47. Stimulation protocols for C2C12 cells. LIPUS stimulation protocol depiction for proliferation (a) and differentiation (b) tests. (from Salgarella *et al.*, 2017[252])**

In both proliferation and differentiation tests, each LIPUS exposure lasted for 5 min, with a pulse repetition frequency of 1 kHz and a duty cycle of 20%. As a first trial, the following exposure conditions were tested: (1) f = 500 kHz, SPPA intensity = 500 mW/cm$^2$ (peak negative pressure, Pn= 122 kPa); (2) f = 1 MHz, SPPA intensity = 500 mW/cm$^2$ (Pn= 122 kPa); (3) f = 3 MHz, SPPA intensity = 500 mW/cm$^2$ (Pn= 122 kPa); (4) f = 5 MHz, SPPA intensity = 500 mW/cm$^2$ (Pn= 122 kPa); (5) control without stimulation.

The control wells were placed in the stimulation tank for 5 min, similarly to the other samples, but without switching on the generator.

After evaluating the optimal frequencies for maximum cell proliferation and differentiation, the same protocols were repeated at those frequencies at each of the following SPPA intensities: (1) 250 mW/cm$^2$ (Pn= 86 kPa) (2) 500 mW/cm$^2$ (Pn= 122 kPa) and (3) 1 W/cm$^2$ (Pn= 172 kPa)

Three and four independent samples per exposure condition were analyzed for proliferation and differentiation tests, respectively.

***Statistical analyses***

The data obtained in proliferation tests (dsDNA concentration in the cell lysate) and in differentiation tests (myotube length, myotube width and fusion index), for the different ultrasound exposure conditions, underwent a non-parametric statistical analysis using the Kruskal-Wallis post-hoc test and the Dunn's multiple comparison test in order to evaluate significant differences among the samples. Results were considered statistically different for $p$-values $\leq 0.05$.

# *Results and discussion*

## ***C2C12 proliferation***

As previously mentioned, in order to assess the bioeffects triggered by different ultrasound exposure conditions on C2C12 cell proliferation, the quantification of dsDNA was performed 12 h after ultrasound stimulation. The aim of the first set of experiments was to identify the ultrasonic frequency that maximized this cellular process. Thus, 4 different ultrasound frequencies were tested, at a constant intensity of 500 mW/cm$^2$. Non stimulated control samples have been also added. As shown in Figure 48a, an increase of dsDNA (and consequently of cell proliferation) was found in all samples treated with ultrasound with respect to the non stimulated ones. Such differences were statistically significant for exposures at 500 kHz ($p$ = 0.0097), 1 MHz ($p$ = 0.0274), 3 MHz ($p$ < 0.0001), but not for 5 MHz. Moreover, a significant difference was observed between samples treated with ultrasound at 3 MHz and at 5 MHz, ($p$ = 0.0080). Samples stimulated at 3 MHz showed an amount of dsDNA that appeared higher in comparison with samples stimulated at 500 kHz and 1 MHz. However, the differences with such sample types were not statistically significant: the p value between 3 MHz and 500 kHz samples was 0.1265, while the one between 3 MHz and 1 MHz samples was 0.0514.

However, data suggested quite clearly that 3 MHz was the stimulation frequency that maximized cell proliferation; for this reason, it was selected for the following experiments, in which the frequency was kept constant at 3 MHz and different SPPA intensity values were evaluated, so to identify the optimal LIPUS exposure to maximize proliferation. Figure 48b shows the obtained results. The sample stimulated at the highest intensity (1 W/cm$^2$) showed a significant increment in the dsDNA with respect to both samples stimulated at 250 mW/cm$^2$ and at 500 mW/cm$^2$ ($p$ = 0.0081 and $p$ = 0.0168, respectively).

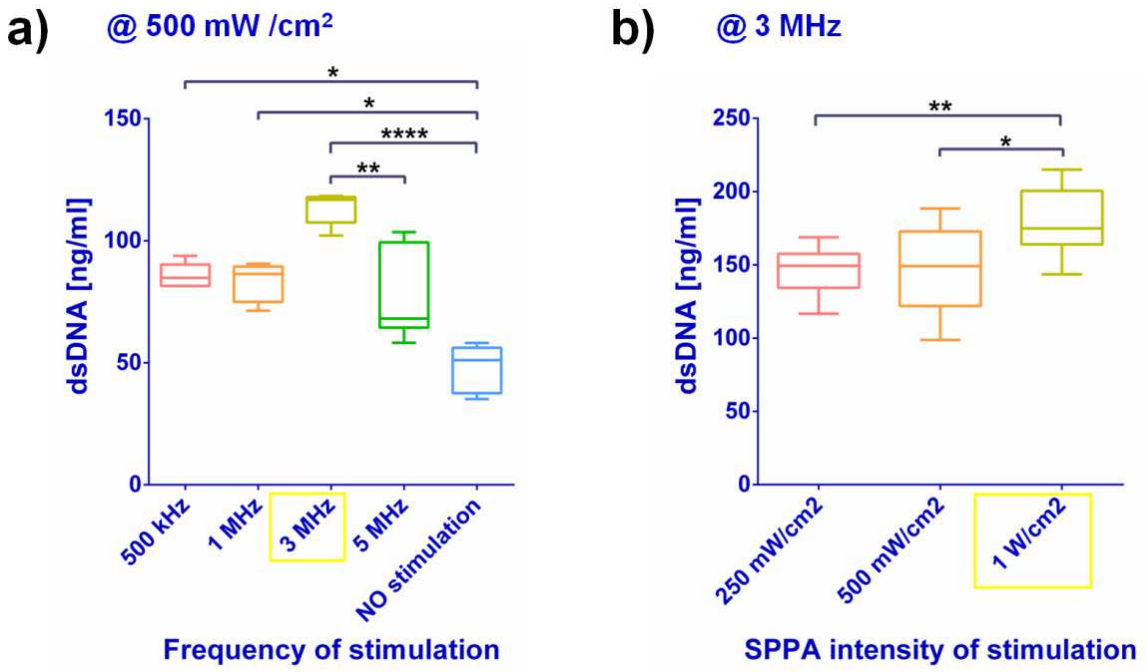


**Figure 48. Proliferation tests. a) Box and whiskers plots representing the median values and interquartile ranges of the dsDNA concentrations found in the cell lysates of samples subjected to LIPUS treatment at an SPPA intensity of 500 mW/cm$^2$ and at different frequencies, and non-stimulated samples (whiskers represent the maximum and minimum values obtained). b) Box and whiskers plots of the dsDNA concentrations found in samples subjected to LIPUS treatment at the fixed frequency of 3 MHz and at different SPPA intensities. In proliferation experiments, three independent samples were analyzed for each sample type. * = $p < 0.05$, ** = $p < 0.01$, **** = $p < 0.0001$. (from Salgarella *et al.*, 2017[252])**

From these results, it appears that the optimal LIPUS exposure conditions, among those tested, which maximize proliferation are 3 MHz and 1 W/cm$^2$. Although it is rather difficult to compare results obtained with different stimulation set-ups, it must be mentioned that Puts *et al.* [250, 251] demonstrated that stimulation at 3.6 MHz, although at lower intensities than the ones tested in this study, led to an increase in the activator protein-1 (AP-1) with respect to non-stimulated C2C12 cells. AP-1 is a heterodimeric protein activated by the mechanical tension applied to cells, which has a pro-mitogenic function. Thus, we may hypothesize that the optimal exposure conditions found in our study maximized the activity of this protein, probably in synergy with other extracellular and intracellular mechanisms, such as the Rho A, ROCK and ERK pathways[255].

***C2C12 differentiation***

The effects of LIPUS at different frequencies on C2C12 cell differentiation were evaluated after 7 days of stimulation in differentiation medium. First, 4 different ultrasound frequencies were tested, by keeping the same intensity of 500 mW/cm$^2$, in addition to non-stimulated control samples. Figure 49a,b show fluorescence images of the myotubes formed. In particular, Figure 49a shows low-magnification (4X) images of actin, stained in red for each stimulation condition, while Figure 49b shows images at 10X magnification for each stimulation conditions with nuclei stained in blue and actin in red. Figure 49c shows the results of a quantitative morphological analysis of myotube width i) and length ii) and of the cell fusion index iii). A statistically significant enhancement of myotube length (Figure 49c ii)) and width (Figure 49c i)) was found in samples treated with ultrasound at a frequency of 1 MHz with respect to all other treatments and to non-stimulated controls ($p < 0.0001$). No significant differences were found in myotube width (Figure 49c i)) between 500 kHz, 3 MHz, 5 MHz treatments and non-stimulated samples, while for myotube length (Figure 49c ii)) a difference was observed by comparing 5 MHz samples with control samples and also with 500 kHz samples ($p = 0.0364$ and $p = 0.0019$, respectively). 500 kHz samples and 3 MHz samples also slightly differed ($p = 0.0208$).

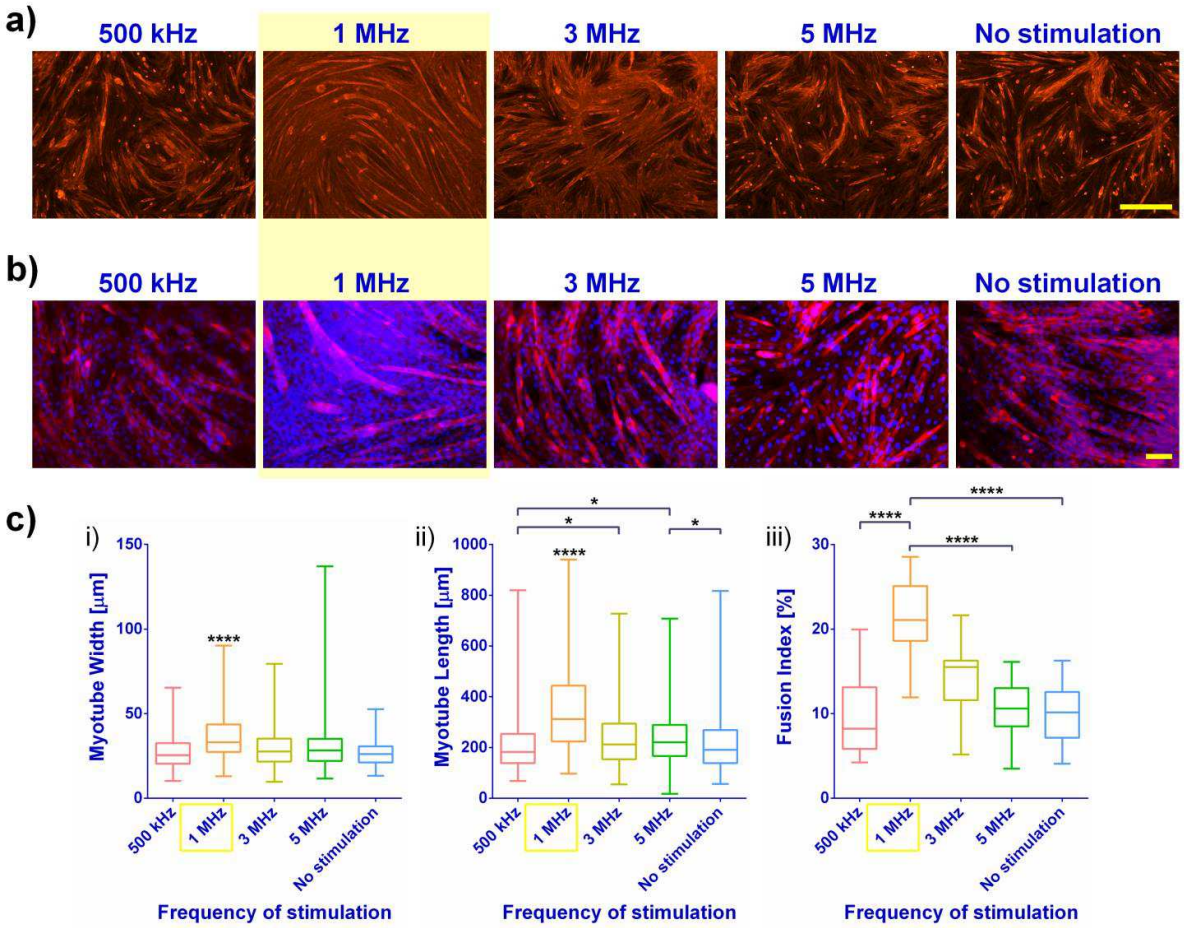


**Figure 49. Differentiation tests - different frequencies. a) Fluorescence images at 4X magnification of differentiated C2C12 cells after 7 days of daily LIPUS stimulation and differentiation medium renewal. Control samples underwent only medium renewal. Different stimulation frequencies were tested, at a fixed SPPA intensity of 500 mW/cm$^2$. Actin filaments are shown in red (scale bar = 500 µm). b) Fluorescence images at 10X magnification of differentiated C2C12 in the same stimulation conditions of point a), showing nuclei in blue and actin in red (scale bar = 100 µm). c) Box and whiskers plots representing the median values and interquartile ranges of the 3 parameters used to quantify cell differentiation, namely myotube width i), myotube length ii) and fusion index iii), obtained for the different stimulation frequencies tested, at a fixed SPPA intensity of 500 mW/cm$^2$ (whiskers represent the maximum and minimum values obtained). In differentiation experiments, four independent samples were analyzed for each sample type. * = $p < 0.05$, **** = $p < 0.0001$. (from Salgarella *et al.*, 2017[252])**

Analysis of the fusion index (Figure 49c iii)) revealed an increase of this parameter in the samples treated at a frequency of 1 MHz. This increment was statistically significant in comparison with the samples stimulated at 500 kHz and 5 MHz and with control (non-stimulated) samples ($p < 0.0001$). The difference between samples stimulated at 1 MHz and

those stimulated at 3 MHz was not statistically significant ($p$ = 0.0814), although samples stimulated at 1 MHz showed a clear tendency to develop myotubes with higher fusion index levels.

Overall, the absolute fusion index values obtained (maximum median value obtained for 1 MHz = 21.07%) are in general smaller respect to the ones that can be found in some literature examples. This can be due to the sub-optimal culture conditions, in terms of substrate and extracellular environment features, used in this study. Our culture well was in fact designed with the main aim to provide an ultrasound-transparent interface, so to properly correlate the bioeffects to the actual ultrasound delivered. To improve skeletal muscle differentiation, a variety of stimuli are needed, such as chemical [256], topographical [222], mechanical [257], electrical [258] and intracellular ones [259]. The scope of this scientific research was to study the effects of ultrasound stimulation on muscle development, thus a multi-stimulation platform would be out of the scope of this work.

Overall, the LIPUS treatment at a frequency of 1 MHz showed an enhancement in myotube development in comparison with the other conditions. Thus, it was identified as the optimal frequency to induce skeletal muscle differentiation. The following tests were thus based on 3 different SPPA intensities values (250 mW/cm$^2$, 500 mW/cm$^2$ and 1 W/cm$^2$) at a constant frequency of 1 MHz.

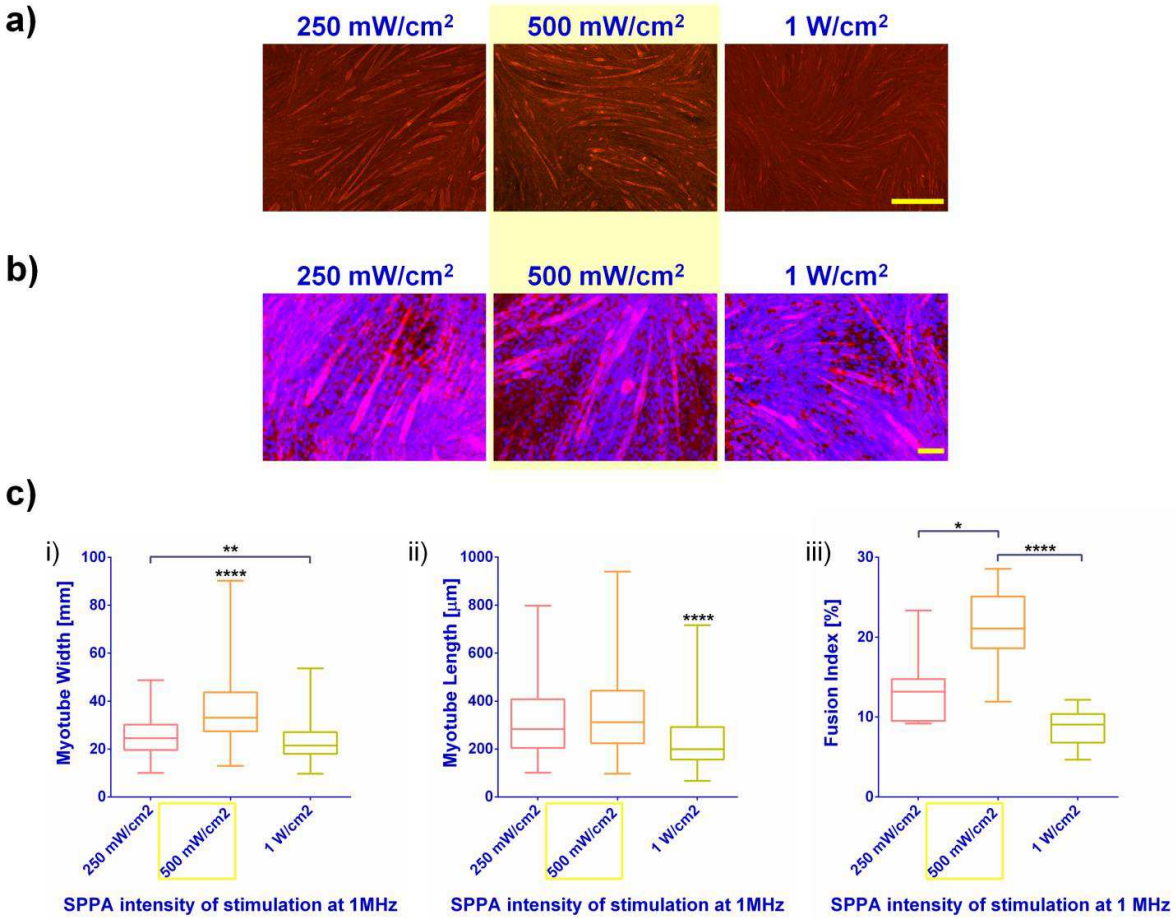


**Figure 50. Differentiation tests - different intensities. a) Fluorescence images at 4X magnification of differentiated C2C12 cells after 7 days of daily LIPUS stimulation and differentiation medium renewal. Stimulation was performed at the fixed frequency of 1 MHz and at different SPPA intensities (scale bar = 500 µm). b) Fluorescence images at 10X magnification of differentiated C2C12 in the same stimulation conditions of point a), showing nuclei in blue and actin in red (scale bar = 100 µm). c) Box and whiskers plots representing the median and interquartile ranges of myotube width i), myotube length ii) and fusion index iii), obtained for the treatments at the fixed frequency of 1 MHz and at different SPPA intensities (whiskers represent the maximum and minimum values obtained). In differentiation experiments, four independent samples were analyzed for each sample type. * = p < 0.05, ** = p < 0.01, **** = p < 0.0001. (from Salgarella *et al.*, 2017[252])**

As shown in the fluorescence images of Figure 50a,b and in the quantitative analysis of Figure 50c, the SPPA intensity of 500 mW/cm$^2$ appeared to increase all the 3 differentiation parameters (Figure 50c i), ii), iii)) with respect to the other two intensities tested. Such differences were significant, for all parameters, in the case of comparisons between 500 mW/cm$^2$ samples and 1 W/cm$^2$ samples ($p$ < 0.0001). Significant differences were also found

between 500 mW/cm$^2$ samples and 250 mW/cm$^2$ samples concerning myotube width (Figure 50c i)) and fusion index (Figure 50c iii)) ($p < 0.0001$ and $p = 0.0134$, respectively), but not concerning myotube length (Figure 50c ii)) ($p = 0.2000$). Finally, a significant difference was also found by comparing myotube width (Figure 50c i)) between 250 mW/cm$^2$ samples and 1 W/cm$^2$ samples ($p = 0.0097$). Overall, these results suggest that 1 MHz and 500 mW/cm$^2$ are the optimal LIPUS exposure conditions, among the ones tested, to maximize C2C12 cell differentiation.

Considering the different *in vitro* studies on cell differentiation and ultrasound stimulation (reported in Table 5), some of them showed an increase in term of myogenin or desmin protein content and gene expression, that is representative of an increase of differentiation. Among these studies, Abrunhosa *et al.* [240] reported an analysis of the myotube morphology that is similar to the one presented in this study, although with a different cell line. The bioeffects obtained in this work, in terms of fusion index and myotube width, are higher than the ones achieved by Abrunhosa *et al.* [240]. This group used similar ultrasound stimulation parameters, although they found better results in continuous than in pulsed mode. This discrepancy could be due to the different ultrasound stimulation set-ups used; thus, a direct comparison is difficult.

There are different cellular pathways involved in the enhanced muscle differentiation due to ultrasound exposure. Ikeda *et al.* [247] showed that ultrasound activates phosphorylation of p38 MAPK. Despite they demonstrated that the ultrasound stimulation of C2C12 cells pushes their differentiation towards an osteoblast and/or chondroblast lineage, it is well known that phosphorylation and activity of the α and β isoforms of p38 MAPK is gradually induced during the differentiation of myoblast [260]. Moreover, a change in its activity affects the transcriptional pattern of muscle-specific genes, indicating that it may modulate transcriptions factors involved in the differentiation process [260-262]. Calcium ions may also have an important role: they are in fact essential for muscle cell contraction and differentiation. These ions can enter cells through stretch-activated channels, which are strictly connected to the cell stress fibers. Porter *et al.* [263] reported that calcium channel

blockade decrease both the number and the size of differentiated myotubes. Ultrasound may be a trigger for an increased activation of such channels.

C2C12 cell line consists of murine myoblast cells derived from satellite cells, whose behavior corresponds to the one of the progenitor lineage. It is considered a good model of skeletal muscle development and it is widely used to this purpose [264]. C2C12 cells are indeed a subclone of C2 myoblasts that can differentiate in culture, and it is known that they reproduce a number of skeletal muscle features [265], representing a reliable model for the study of muscle tissue in a variety of normal and pathological conditions. For these reasons the results obtained could partly clarifies why some *in vivo* ultrasound-based experiments reported in the literature showed significant muscle regeneration, while others did not. In fact, a significant improvement of muscle regeneration after injuries was observed in some studies featured by a stimulation frequency around 1 MHz [243, 245, 246]. Other studies that did not report significant bioeffects on muscles due to ultrasound stimulation, were based on stimulation frequencies around 3 MHz [242] [241]. It is obviously premature to affirm that a strong correlation can be drawn between our findings and these previous studies, because *in vivo* stimulation conditions varied between studies in terms of intensity and duration and it is also well known that attenuation in tissues is frequency-dependent and it also varies between tissues [266]. Since the same free field intensity may result in different conditions at the target tissue, further investigation is needed to translate the results obtained in this study to in vivo settings, with the aim of evaluating the bioeffects triggered by ultrasound on muscle tissues.

Overall, our results showed that two different frequencies allow to maximize the proliferation and the differentiation processes in myoblasts. This is coherent with the fact that these processes are governed by completely different and often mutually exclusive cellular pathways [267]. In fact, myoblast must exit the proliferation cycle in order to differentiate and to fuse in multinucleated myotubes. Additional investigations could further clarify the cellular pathways activated by the different ultrasound exposures, e.g. by means of gene expression microarrays. Since literature findings suggest that therapeutic ultrasound can modulate signal-transduction pathways (leading to regulation of gene expression and/or

the modulation of RNA translation to a protein product), we have proposed some possible activated pathways that bring to LIPUS induced proliferation (increase in AP-1[250, 268] protein which is activated by the mechanical tension applied to cells and has a pro-mitogenic function) and differentiation (activation of MAPK p38 phosphorylation[247], increase of calcium ions[239]). The frequency resonance hypothesis proposed by John (2002)[269] could support our findings. The central premise of the frequency resonance hypothesis is that the mechanical energy within the ultrasound wave is absorbed by proteins, altering their single structural conformation of or the function of a multimolecular complex. Moreover, the ultrasound wave may induce resonant activity in the protein, modulating the molecule's or multimolecular complex's effector function. Considering enzymatic proteins as a molecular model, he suggested that the energy provided to the enzyme by the ultrasound wave may induce transient conformational shifts, altering the enzyme's activity (i.e., kinases or phosphatases) and the overall function of the cell. Alternatively, ultrasound's resonating force may result in the dissociation of functional multimolecular complexes or in the release of a sequestered molecule (dislodging an inhibitor molecule from the multimolecular complex). Hypothetically, frequency resonance may imply that different frequencies establish different resonant forces. Hence, various frequencies may affect combinations of proteins or multimolecular complexes in different ways, lending to the possibility of targeted effects at the cellular and molecular levels.[269]

***Temperature measurements***

As mentioned, few works associate temperature measurements to the ultrasound stimulation regimes used, but this is crucial to discriminate between thermal and mechanical bioeffects. The results of temperature measurements in our case are reported in Figure 51.

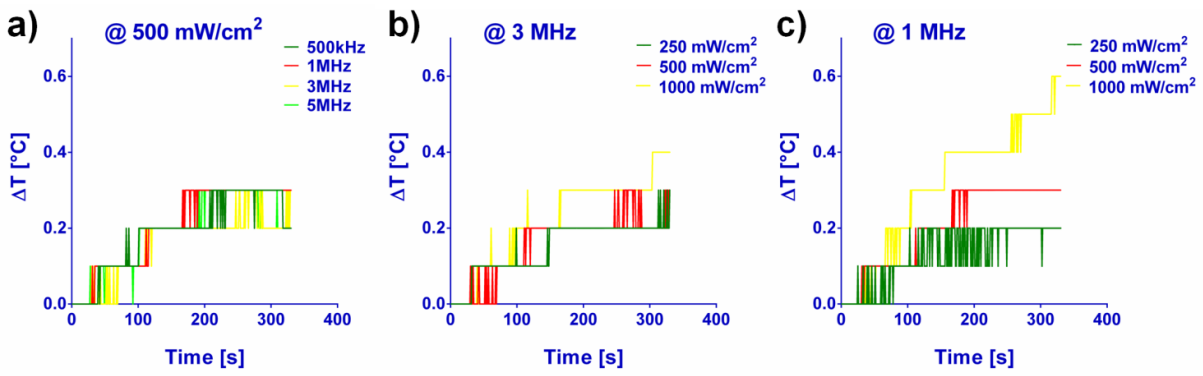


**Figure 51. Temperature measurements. a) Graph representing the temperature variations inside the cell culture well for the following stimulation conditions: 500 kHz, 1 MHz, 3 MHz, 5 MHz, at an SPPA intensity of 500 mW/cm$^2$. b) Graph representing the temperature variations due to LIPUS stimulation at 3 MHz (the optimal one in proliferation tests) and 250 mW/cm$^2$, 500 mW/cm$^2$ and 1 W/cm$^2$. c) Temperature variations measured during LIPUS stimulation at 1 MHz (for the optimal one in differentiation tests) and 250 mW/cm$^2$, 500 mW/cm$^2$ and 1 W/cm$^2$. (from Salgarella *et al.*, 2017[252])**

Results show that for the different conditions tested (intensity fixed at 500 mW/cm$^2$ and different frequencies - Figure 51a, frequency fixed at 3 MHz and different intensities – Figure 51b, frequency fixed at 1 MHz and different intensities – Figure 51c, all temperature rises were equal to or lower than 0.6 °C. These findings are in line with the typical temperature rise reported in LIPUS stimulation (< 1 °C) [270]. Thus, our experimental conditions can be classified as non-thermal ultrasound exposures [271]. Moreover, it must be pointed out that a contribution of this temperature increase could be due in part to viscous heating artefacts. In fact, we did not use viscous-free sensors, such as thin film termocouples, for these measurements [272]. This probably led to an overestimation of the real temperature rise within the culture wells, due to ultrasound stimulation. Since the temperature increase was almost the same for all the different frequencies tested (Figure 51a), it can be affirmed that the different results obtained concerning proliferation and differentiation at diverse stimulation frequencies are surely due only to non-thermal bioeffects.

***I***

***In summary***

Skeletal muscle tissue possesses an intrinsic regeneration capability, but this self-repairing property can be seriously impaired in certain conditions, due to ageing, severe muscle diseases or loss of large muscle mass; patients would thus strongly benefit from external inputs promoting muscle regeneration. In other cases, the damage is less severe, but it would be highly desirable to hasten the regeneration process. For example this could be needed for physiotherapy purposes to get in shape professional athletes, bringing them to the best performances after injuries as quick as possible. Therapeutic ultrasound, in particular LIPUS stimulation, have been proposed for this purpose and show promises in these domains. In this study we overcame the limitations of previous state-of-the-art evidences, which showed rather incoherent results in terms of LIPUS treatment efficacy on muscle regeneration. For this purpose, a systematic *in vitro* investigation and comparison of the effects triggered by controlled LIPUS exposures at different frequencies and intensities was performed. To this aim, an ad hoc tunable stimulation system and an ultrasound-transparent cell culture well were used. Results allowed identification of the most effective parameters to maximize proliferation, which were 3 MHz and 1 $W/cm^2$, and differentiation, which were 1 MHz and 500 $mW/cm^2$. Results also demonstrated that only mechanical effects play in this process, while thermal effects are negligible. The outcomes of this work shed light on the optimal ultrasound stimulation parameters for muscle regeneration *in vitro* and show promises for a future *in vivo* translation of these findings.

# 3.2 Indirect stimulation

## Ultrasound-responsive micelles for dexamethasone release

### *Framework*

Triggerable drug release systems based on stimuli-responsive polymers are emerging platforms aiming at increasing the effectiveness and reducing the side effects of traditional therapies.[273] This on-demand targeted therapy is based on nanocarriers,[274] thin films and hydrogels,[275] nanogels,[276] and other miniaturized systems applied for several pathological conditions. Such pathologies include nervous system disorders, bone inflammation and infections, chronic pain, oncological diseases, and diabetes.[277, 278] As for all the bio/non-bio interfaces, also polymeric carriers can be designed in order to respond to different stimuli (chemical and physical ones), so to deliver the desired drug dose at the site of interest. Such stimuli can be internal to the body, such as pH changes, redox gradients, enzymes action, temperature changes.[279] In this case, the triggering action is determined by local alterations of the diseased tissues with respect to the healthy ones. As stated in the Introduction section, stimuli can be also external to the body: this makes a remote triggering possible, thus adding a degree of controllability to the therapy. The remote drug release triggering can be based on different driving physical inputs, including electric and magnetic fields, light and ultrasound.[280]

We have already mentioned that, among these external stimuli, ultrasound (US) has a high potential. In fact, US possesses several advantages[281, 282]: (1) penetrates through a number of different tissues, especially the soft ones, in a safe and reliable way without a dramatic attenuation of the wave energy, (2) is a versatile tool able to trigger both mechanical and thermal phenomena, and (3) has promising theragnostic abilities, being an effective tool for enhancing a drug release and visualizing the target during the therapeutic action. Consequently, the US stimulation raises an interest in the biomedical community, especially

in the need to understand the mechanism of US waves interaction with nanocarriers for a controlled delivery of therapeutic agents.[283]

Nanocapsules, microbubbles liposomes and micelles are typical carriers developed for this purpose.[282] In all these systems, the polymeric structure is permanently or temporarily perturbed by mechanical and/or thermal action of US, resulting in a modulated drug delivery.[284] Micelles are particularly interesting since they can be easily prepared by self-assembling of block copolymers.[285] Their small size (diameter between 10 and 100 nm) enhances the penetration into the target tissue and decreases the renal excretion.[284] Some examples of US-triggered micelles used for drug release have been recently reviewed.[282, 286, 287] The US mediates release of drug from a micellar core proceeds (1) irreversibly via ester hydrolysis induced typically by high intensity focused ultrasound (HIFU, 1.1 MHz)[288, 289] or (2) reversibly via transient cavitation effect of low-frequency ultrasound (20 - 90 kHz).[290] The impact of chemical structure of copolymers on the degradation and release was studied to some extent by Zhao *et al.* for irreversible degradation by HIFU.[288] In contrast, in case of reversible perturbation/disruption of polymeric micelles, the drug release experiments are typically performed on one selected type of copolymer. The most commonly examined parameters are frequency, power density, pulse duration of US, concentration of polymer and drug, especially in the case of Pluronic P-105 micelles.[291, 292] More versatile materials with tunable hydrophobicity, higher drug loading capacity and stealth properties would be desirable, in this field. A promising polymer family showing these features is the one of poly(2-oxazoline)s.

Poly(2-oxazoline)s (POx) are synthetic polymers that can be prepared by living cationic polymerization of 2-oxazolines. The living nature of the polymerization process enables to control molar mass, dispersity and overall architecture of resulting polymers.[293] Moreover, it allows to prepare well-defined block copolymers by a simple subsequent addition of properly selected monomers.[294] A large library of 2-oxazoline monomers, including hydrophilic, thermoresponsive and hydrophobic ones, allows for forming versatile POx structures that exhibit significantly different chemical and physical characteristics. POx exhibit stealth behaviour[295, 296] and have been found to be non-toxic both *in vitro*[297, 298] and

*in vivo*[299, 300]. For these reasons, they are attracting an increasing attention in different biomedical fields, including the preparation of drug and protein conjugates[301], anti-fouling[302] and thermoresponsive[303] membranes, hydrogels[304, 305], and vectors for gene[306] and radionuclide[307] delivery.

It has been reported that amphiphilic block and gradient copolymers of (2-oxazoline)s self-assemble in aqueous solution, resulting in polymeric micelles[308, 309], polymersomes[310], and vesicles[311] formation. The hydrophobic core of such self-assembled aggregates can be used for a confinement of hydrophobic drugs. As recently demonstrated[312-314], triblock copoly(2-oxazoline)s containing a 2-butyl-2-oxazoline monomer are able to solubilize large amounts, more than 40 wt%, of anticancer drugs. The performance of POx-based drug delivery systems, including micelles, is highly dependent on the chemical composition of both the copolymer and the drug.[315-317] Thus, a systematic investigation of different POx types, based on different comonomers and chain lengths, is crucial for well-tuned drug delivery applications. This potential is mostly under-investigated, since most of studies in this field focus on a single condition used for micelle formulation in combination with a specific drug.

This Section focuses on a systematic analysis of the drug release profiles from POx-based polymeric micelles with and without low-frequency ultrasound stimulation. No study investigated US as a possible means to modulate drug release from POx-based micelles, so far. We have selected POx-based copolymers especially for their chemical versatility with well tunable hydrophilic-lipophilic balance and outstanding drug loading capacity. Moreover this polymer family shows good stealth properties[295, 296] and no toxicity[297-300]. To this purpose, five different copoly(2-oxazoline)s were prepared and characterized. Two diblock copolymers and one triblock copolymer composed of 2-n-propyl-2-oxazoline and two diblock terpolymers containing 2-butyl-2-oxazoline-co-2-(3-butenyl)-2-oxazoline as hydrophobic part. Their ability to encapsulate dexamethasone, an anti-infammatory drug, was assessed by means of high performance liquid chromatography and the stability of such prepared micelles in PBS was studied by dynamic light scattering. Drug release measurement were performed with and without US stimulation and the variation in the release profiles after US was computed. Finally, delivery profiles were fitted by means of different mathematical

models. This analysis aims at filling a knowledge gap in the current state-of-the-art, concerning the responsiveness of POx-based micelles to ultrasound waves.

Also this work has been done in strict collaboration with the Department for Biomaterials Research of the Polymer Institute of the Slovak Academy of Sciences thanks to their deep knowledge on POx synthesis and chemical characterization.

The work reported in this Section has been recently accepted for publication in ACS Langmuir journal:

Treľova D.#, **Salgarella A.R.#**, Ricotti L., Giudetti G., Cutrone A., Šrámková P., Zahoranová A., Chorvát Jr. D., Haško D., Canale C., Micera S., Kronek J., Menciassi A., Lacík I. "Soft hydrogel zwitterionic coatings minimize fibroblast and macrophage adhesion on polyimide substrates" accepted in ACS Langmuir.

# *Methods*

## ***Synthesis of monomers***

Monomers were synthesized by adapting known procedures, as reported in detail in the following part. The purity of the synthesized monomers was verified by HPLC measurement using Agilent 1200 Series HPLC System (UV detection at 210 nm, Zorbax Eclipse Plus column C18, 4.6*250 mm, 5 µm, eluent methanol/water 90/10).

*2-n-Propyl-2-oxazoline*

2-n-Propyl-2-oxazoline (nPropOx) was prepared according to the procedure for the first time reported by Witte and Seeliger[318] adopted with slight modifications. In a round bottom flask, butyronitrile (55.6 g, 0.805 mol) and zinc acetate (2.68 g, 0.015 mol) were heated to 100 °C. Next, 2-aminoethanol (44.7 g, 0.731 mol) was added *dropwise* into the reaction mixture. The reaction mixture was stirred at 130 °C for 48h to yield dark brown liquid. The colourless nPropOx was obtained from the reaction mixture by fraction distillation. The third fraction of the product was dried over KOH and $CaH_2$ and distilled prior to use (25.6 g, yield 31%, $bp^{30mBar}$ =55 °C, lit. $bp^{40mBar}$ = 68 °C [319]).

$^1$H NMR (400 MHz, $CDCl_3$, δ) 0.97 (t, 3H; $CH_3$-$CH_2$-$CH_2$), 1.65 (m, 2H; $CH_3$-$CH_2$-$CH_2$), 2.25 (m, 2H; $CH_3$-$CH_2$-$CH_2$), 3.82 (t, 2H; $CH_2$-N), 4.21 (t, 2H; $CH_2$-O).

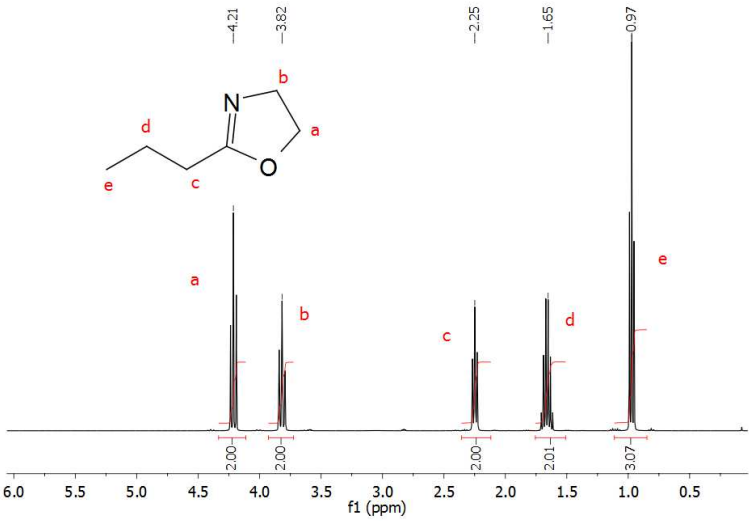


**Figure 52. 1H NMR spectrum of 2-n-propyl-2-oxazoline in $CDCl_3$.**

*2-Butyl-2-oxazoline*

2-Butyl-2-oxazoline (ButOx) was prepared according to the procedure for the first time reported by Witte and Seeliger[318] adopted with slight modifications. Briefly, in a round bottom flask the valeronitrile (23.85 g, 0.287 mol) and zinc acetate (0.96 g, 0.005 mol) were heated to 130°C. 2-Aminoethanol (16 g, 0.262 mol) was subsequently added dropwise into the reaction mixture. Reaction was stirred under the argon atmosphere at 130°C for 20h followed by addition of dichloromethane (50 ml). After the washing with brine and water, the organic layer was dried over anhydrous sodium sulfate. Sodium sulfate was filtered off and solvent was evaporated. Brownish liquid was dried over KOH for two days and distilled over $CaH_2$ to yield ButOx as colourless liquid (17.22 g, yield 47%, $bp^{14mbar}$= 57 °C, lit. $bp^{16\ mbar.}$= 61 °C [312]).

$^1$H NMR (400 MHz, $CDCl_3$, δ) 0.85 (t, 3H, *$CH_3$*-$CH_2$-$CH_2$-$CH_2$-), 1.3 (m, 2H; $CH_3$-*$CH_2$*-$CH_2$-$CH_2$-), 1.54 (m, 2H; $CH_3$-$CH_2$-*$CH_2$*-$CH_2$-), 2.19 (t, 2H; $CH_3$-$CH_2$-$CH_2$-*$CH_2$*-), 3.74 (t, 2H; $CH_2$-N), 4.13 (t, 2H; $CH_2$-O).

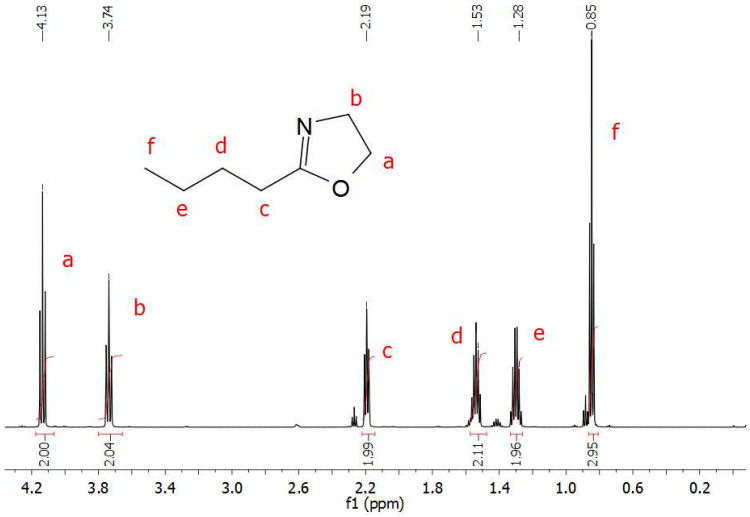


**Figure 53. 1H NMR spectrum of 2-butyl-2-oxazoline in $CDCl_3$.**

*2-(3-Butenyl)-2-oxazoline*

2-(3-Butenyl)-2-oxazoline (EnOx) was synthesized in two steps according to a procedure described previously for bis(2-oxazolines)[320]. First, 4-pentenoyl chloride (26.85 g, 0.226 mol) dissolved in dichloromethane (300 mL) was added dropwise to aqueous KOH (38.12 g, 0.679 mol) with 2-chloroethylamine hydrochloride (31.52 g, 0.272 mol) cooled in ice bath. After addition of 4-pentenoyl chloride solution, the reaction mixture was stirred overnight at room temperature. Organic layer was separated, washed with brine and water and dried over anhydrous sodium sulfate. Dichloromethane was evaporated and the obtained liquid yellowish *N*-(2-chloroethyl)pent-4-enamide (yield 33.68 g, 92%) was used for second step without purification. The intermediate product was dissolved in 0.1 M methanolic KOH (250 mL) and refluxed for 6h. Product was dissolved in chloroform and residual KCl was filtered off. Chloroform was evaporated and yellowish product was distilled over $CaH_2$ and stabilized with 2,6-di-*tert*-butyl-4-methoxyphenol to give a EnOx as a colourless liquid (yield 13.64 g, 52%, $bp^{8mbar}$= 47 °C, lit. $bp^{20mBar}$= 67 °C [321]).

$^1$H NMR (400 MHz, $CDCl_3$, δ, ppm): 2.38 (s, 4H, $CH_2$=CH-*$CH_2$*-*$CH_2$*-), 3.82 (t, 2H; $CH_2$-O), 4.22 (t, 2H; $CH_2$-N), 5.00-5.09 (m, 2H, *$CH_2$*=CH-), 5.80-5.89 (m, 1H, $CH_2$=*CH*-).

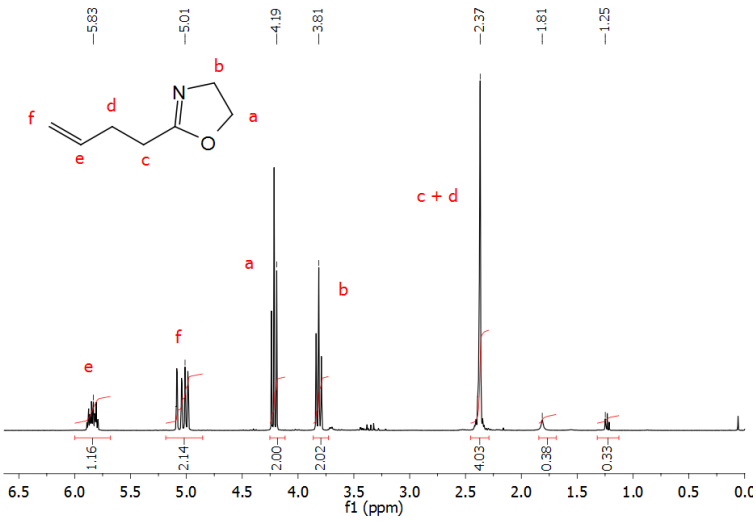


**Figure 54. 1H NMR spectrum of 2-(3-butenyl)-2-oxazoline in $CDCl_3$.**

***Synthesis of copolymers $MeOx_n$-b-$nPropOx_m$ (P1, P2)***

Two diblock copolymers from 2-methyl-2-oxazoline and 2-n-propyl-2-oxazoline differing in chain length and ratio of blocks were prepared. As an example, the synthesis of **P1** was performed as follows. The initiator methyl 4-nitrobenzene sulfonate (71.9 mg, 0.331 mmol) was dried in a Schlenk flask under reduced pressure for 1 h. Subsequently, benzonitrile (12 mL) and 2-methyl-2-oxazoline (4.7 g, 55.2 mmol) were injected into the flask. The polymerization of the first copolymer block proceeded under stirring in oil bath at 100°C for 24 h. Then, 2-n-propyl-2-oxazoline (1.5 g, 13.3 mmol) and benzonitrile (10 mL) were added into the reaction mixture, which was polymerized at 100°C for further 24 h until full conversion was achieved, as confirmed by ATR-FTIR measurement. Termination was performed by treatment of the cooled polymerization mixture with 1 M methanolic KOH (1 mL) for further 3 h. Resulting diblock copolymer was precipitated into cold diethylether. Dried copolymer was dissolved in distilled water and purified by dialysis against distilled water (SpectraPor® of 1 kDa molecular weight cut-off, Spectrum Laboratories, Inc., USA) for 72 h and freeze-dried. Resulting diblock copolymers were achieved as white powder (yield P1 = 5.0 g, 81%).

Copolymer **P2** was prepared accordingly, using 72.3 mg (0.333 mmol) of methyl 4-nitrobenzene sulfonate and 1.09 g (12.8 mmol) of 2-methyl-2-oxazoline in 4 mL of benzonitrile for the first step, and 1.9 g (16.8 mmol) of 2-n-propyl-2-oxazoline in 5.5 mL of benzonitrile for the second step. Following the same work-up procedure as for **P1**, the product was obtained as yellow powder with the yield 74% (2.16 g).

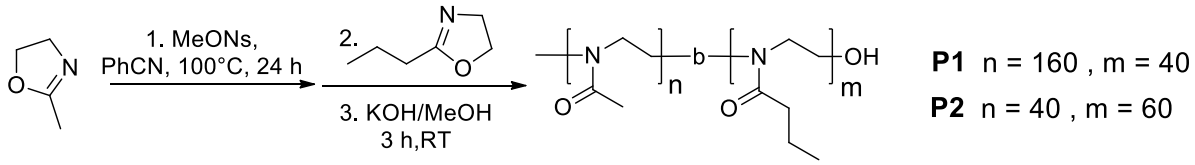


**Figure 55. Polymerization reaction scheme of diblock copolymer P1 and P2.**

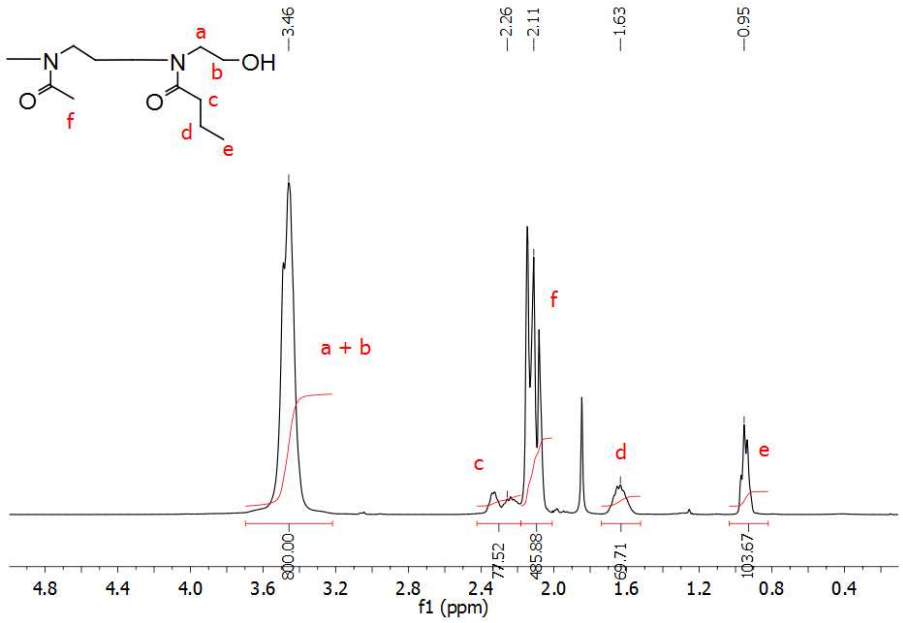


**Figure 56. $^{1}$H NMR spectrum of polymer P1 in $CDCl_3$.**

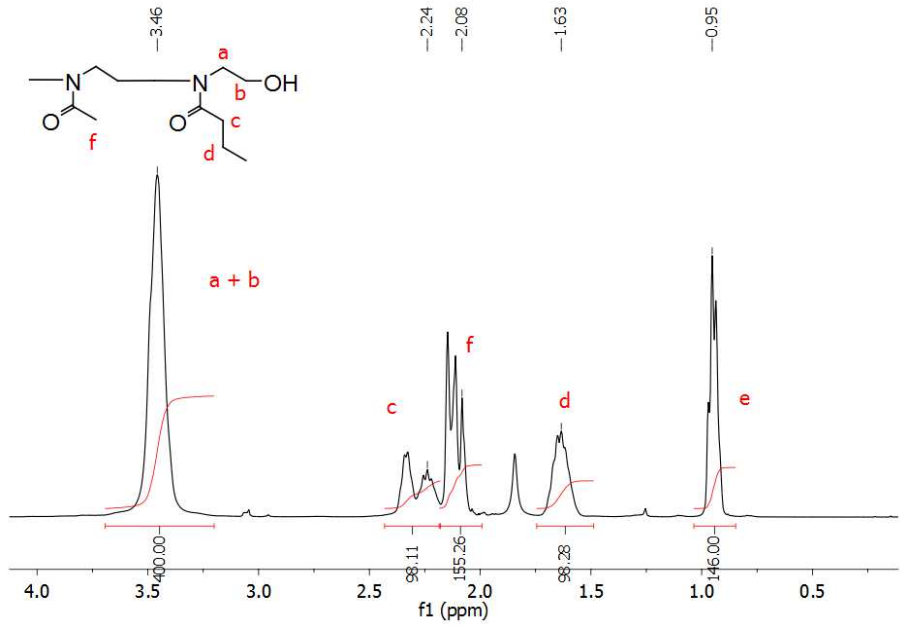


**Figure 57. $^{1}$H NMR spectrum of polymer P2 in $CDCl_3$.**

***Synthesis of copolymers $MeOx_m$-b-$(ButOx_{n1}$-$EnOx_{n2})_{stat}$ (P3, P4)***

Diblock copolymers containing double bonds were prepared in two sequential steps starting from hydrophobic block based on 2-butyl-2-oxazoline (ButOx) and 2-butenyl-2-oxazoline (EnOx) in statistical arrangement. The preparation of block copolymer **P3** with composition MeOx/ButOx/EnOx = 40/20/10 was performed as follows. The initiator methyl 4-nitrobenzenesulfonate (MeONs, 0.134 g, 0.62 mmol) was dried in a Schlenk flask under reduced pressure for 1 h. Subsequently, acetonitrile (4 mL), ButOx (1.57 g, 12.34 mmol) and EnOx (0.77 g, 6.15 mmol) were injected into the flask and solution was degassed by three freeze-thaw cycles. The reaction mixture was stirred in oil bath at 80°C for 24 h, until the full conversion was achieved, as confirmed by ATR-FTIR. Subsequently, the MeOx (2 mL, 23.62 mmol) and additional acetonitrile (4 mL) were added into the reaction mixture, which was polymerized for further 24 h at the same temperature until full conversion was achieved. Termination was performed by treatment of the cooled polymerization mixture with methanolic KOH for further 3 h. Resulting diblock copolymer was precipitated into cold diethylether. Dried copolymer was purified by dialysis against distilled water (MWCO: 1 kDa; Spectrum Laboratories, Inc., USA) for 72 h and freeze-dried. Resulting diblock copolymer were obtained as white powders (yields P3 = 2.3 g, 53%).

Copolymer **P4** was prepared accordingly, starting with 53 mg of MeONs (0.244 mmol), 0.87 g of ButOx (6.84 mmol), 0.3 g of ButEnOx (2.4 mmol) in 2.4 mL of acetonitrile as a first step. As a second step, 2 g of MeOx (23.5 mmol) in 4 mL of acetonitrile was added. Following the same work-up procedure as **P3**, the product was obtained as white powder (yield 1.45 g, 46%).

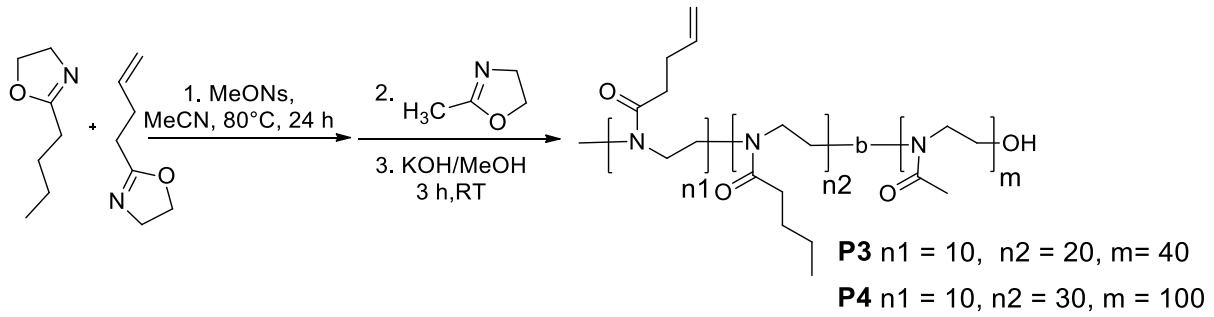


**Figure 58. Polymerization reaction scheme of diblock copolymer P3 and P4**

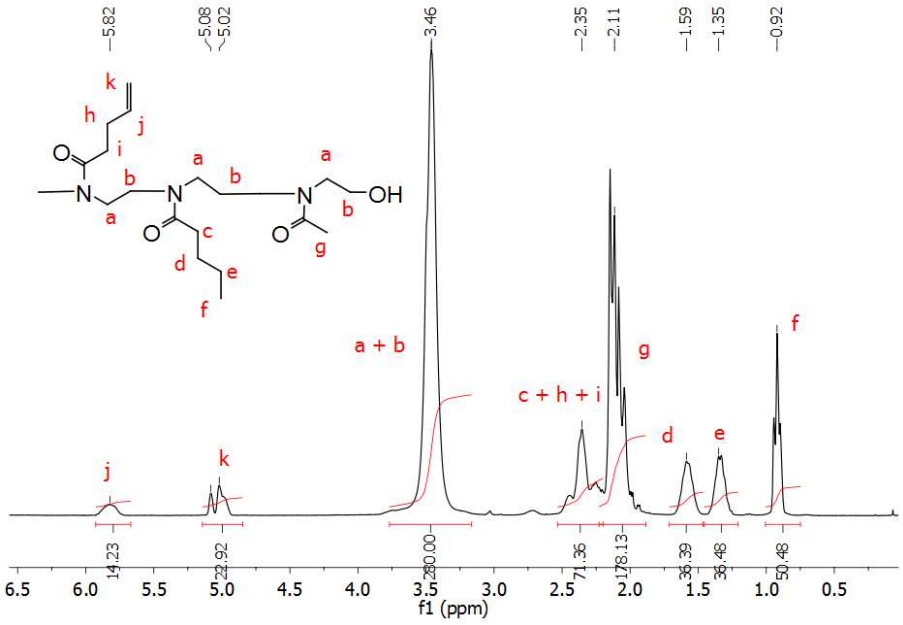


**Figure 59. $^{1}$H NMR spectrum of polymer P3 in $CDCl_3$.**

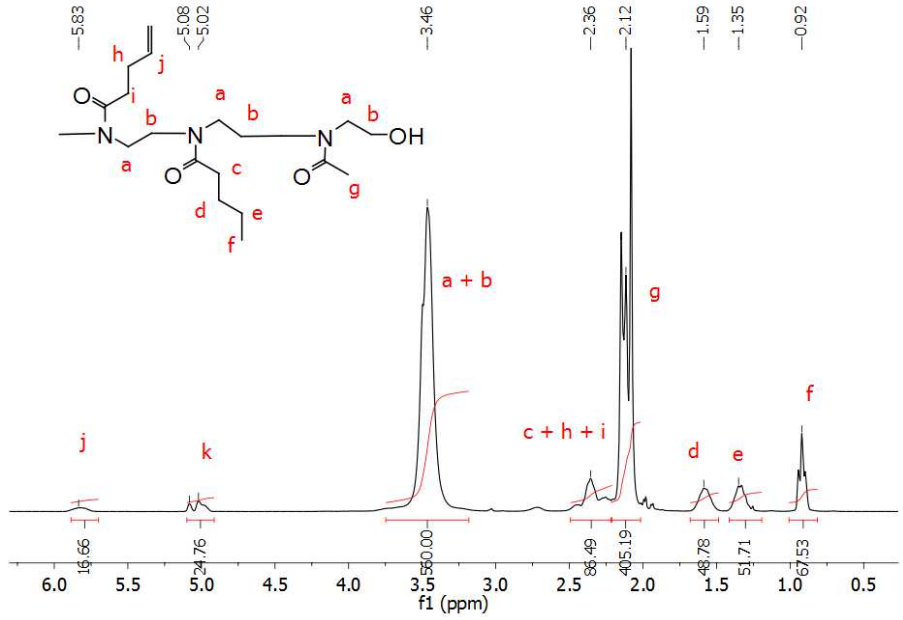


**Figure 60. $^{1}$H NMR spectrum of polymer P4 in $CDCl_3$.**

***Synthesis of copolymers MeOx$_{25}$-b-nPropOx$_{145}$-b-MeOx$_{25}$ (P5)***

Triblock copolymer consisting of 2-methyl-2-oxazoline and 2-n-propyl-2-oxazoline was synthesized as previously described.[322] To a pre-dried Schlenk flask initiator 1,3-propanediol di-p-tosylate (193 mg, 0.5 mmol), dissolved in benzonitrile (25 mL), was added. Subsequently, 2-n-propyl-2-oxazoline (8.21 g, 72.6 mmol) was added. The reaction mixture was stirred in an oil bath at 100 °C until the full conversion was achieved as verified by 1H-NMR. The polymerization mixture was then cooled with an ice bath and 2-methyl-2-oxazoline (2.13 g, 25.0 mmol) and benzonitrile (8 mL) were added under inert atmosphere. The mixture was then stirred at 100 °C until the full conversion of the second monomer was achieved. The polymerization was terminated by adding an excess of piperidine (0.76 g). After several hours of stirring at room temperature (RT), an excess of K2CO3 was added. The product was purified by repeated precipitation in cold diethyl ether followed by dialysis against distilled water (MWCO: 1 kDa; Spectrum Laboratories, Inc., USA) and freeze-dried. The polymer was obtained as a white powder (yield 45%).

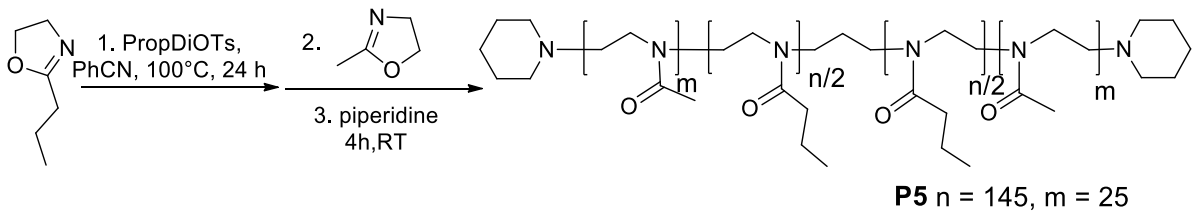


**Figure 61. Polymerization reaction scheme of triblock copolymer P5.**

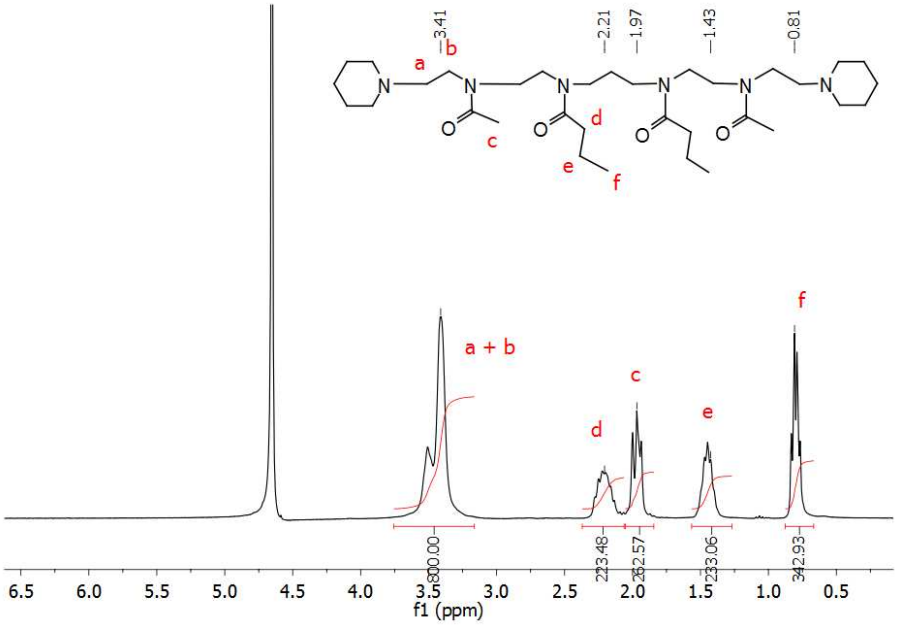


**Figure 62. $^{1}$H NMR spectrum of polymer P5 in methanol-$d_4$.**

***$^{1}$H NMR***

$^{1}$H NMR spectra of all compounds were recorded at room temperature on a Varian VXR-400 (Varian, USA) in $CDCl_3$ and methanol-$d_4$ solutions using tetramethylsilane (TMS) as an internal standard.

***Size exclusion chromatography(SEC)***

The size exclusion chromatography (SEC) characterization was performed using a P102 pump (Watrex, Czech Republic) and an evaporative light scattering detector ELS–1000 (PL-Agilent Technologies, Stretton, UK) with the temperature set to 180 °C and the gas flow rate of 1.5 mL/min. The TSK gel GMH hr - M, 300 x 7.5 mm (TosoHaas Bioscience) SEC column was used for separation. The SEC analysis was performed at ambient temperature. The mixture of 50 wt.% N,N-dimethylformamide (HPLC grade 99.7%, Alfa Aesar) and 50 wt.% chloroform (HPLC grade 99.8%, amylene stabilized, Sigma-Aldrich) was used as SEC eluent at the flow rate of 1 mL/min. The calibration was based on narrow polystyrene standards (580 - 100 000 g·mol$^{-1}$, Pressure Chemical Company, Pittsburgh, US) providing the molar mass data for synthesized

copolymers relative to polystyrene standards. Data were collected and processed using the Clarity software (DataApex, Czech Republic).

***Preparation of dexamethasone (Dex) loaded micelles***

POx-based micelles were prepared according to the thin film hydration method described elsewhere.[313] Stock solutions of copolymers and Dex in ethanol were prepared (usually 100 $g \cdot L^{-1}$ and 10 $g \cdot L^{-1}$, respectively). The stock solutions were then pipetted into glass vials to obtain desired ratios of polymer to Dex. Ethanol was subsequently evaporated using a heat gun to obtain a thin film on the glass surface. The vials were dried at 60 °C in vacuum oven. Prior to experiment, polymer layers were re-hydrated using appropriate amounts of distilled water or PBS (200 µL for HPLC measurements, 1 mL for DLS measurements, 100 µL for drug release study). The resulting solutions were resuspended by vortexing, centrifuged (3,000 rpm for 10 min) in order to remove non-loaded Dex and the supernatant was used in further experiments immediately after the preparation.

***High performance liquid chromatography (HPLC)***

The purity of synthesized monomers was verified by HPLC measurements and the amount of Dex loaded in micelles was measured using Agilent 1200 Series HPLC System (UV detection at 240 nm, Zorbax Eclipse Plus column C18, 4.6*250 mm, 5 µm, eluent methanol/water 90/10). For these measurements, the layer containing a copolymer and Dex was re-hydrated by adding of 200 µl of distilled water to obtain final concentration 10 $g \cdot L^{-1}$ of a copolymer and 0.5 – 10 $g \cdot L^{-1}$ of Dex. The loading efficiency was calculated as the weight percentage of loaded Dex, $m_{Dex}$, from the original Dex feed, $m_{Dex,0}$:

$$LE = (m_{Dex}/m_{Dex,0}) \cdot 100$$

The loading capacity was calculated as the percentage of loaded Dex with respect to the total weight of the formulation:

$$LC = \left( m_{Dex}/(m_{Dex,0} + m_{copolymer}) \right) \cdot 100$$

where $m_{copolymer}$ is the weight of copolymer in the formulation. The amounts of loaded Dex were calculated from calibration against free Dex dissolved in HPLC eluent (methanol:water

90:10) in the concentration range from 0.01 to 0.1 $g \cdot L^{-1}$. The experiment was performed in quadruplicates.

***Dynamic light scattering (DLS)***

Dynamic light scattering (DLS) measurements were performed using Zetasizer Nano-ZS (Malvern Instruments, UK) equipped with a 4 mW helium/neon laser (λ = 633nm) and thermo-electric temperature controller, with the following parameters set for poly(2-ethyl-2-oxazoline): refractive index = 1.520, absorbance = 0.001. All measurements were performed at 28 °C in measurement angle 173°. The micelles for this analysis were prepared to obtain final concentration 10 $g \cdot L^{-1}$ of copolymer and 1 $g \cdot L^{-1}$ or 2 $g \cdot L^{-1}$ of Dex in PBS. The diameter ($D_{mode}$) of the polymeric micelles was expressed as the peak maximum from the intensity size distribution. The stability measurements of the micelles were performed immediately after the preparation in the time interval 24h. Typically, 200 - 400 measurements were done for each sample and averaged value of the diameter ($D_{mode}$) from these measurements was compared.

***Dexamethasone release study***

Immediately after micelles preparation, the surnatants containing micelles (100 µL) were inserted in dialysis devices (Slide A-Lyzer® MINI Dialysis Units, 3,500 MWCO - Thermo Fisher Scientific). The devices were then placed in centrifuge tubes (2 mL volume) containing PBS at the initial time point (See Figure 63 for the drug release protocols schemes). For spontaneous release protocol, the dialysis device was moved from one centrifuge tube to another at each time point (5 min, 15 min, 30 min, 1 h, 3 h, 6 h, 10 h and 24h). The Dex release from micelles was measured through absorbance readings (λ = 243 nm) of the PBS contained in each centrifuge tube (1.5 mL). After 24 h the micelles were exposed to 2 h sonication provided with the ultrasound water bath and absorbance measures were performed in order to evaluate the maximum Dex release (considered as 100%). Four different samples were analyzed for each micelle type (**P1**-**P5**) and for each of the Dex concentrations (1 and 2 $g \cdot L^{-1}$). The US-mediated protocol was the same of the spontaneous one except for US stimulation, which was provided to the micelles over 10 min with a water bath, by setting it at a 20 W power and a 40 kHz frequency, for three time-points (17 min, 2

h and 8 h). Also in this case four different samples were analyzed for each micelle type (**P1**-**P5**) and for each Dex concentration (1 and 2 $g \cdot L^{-1}$).

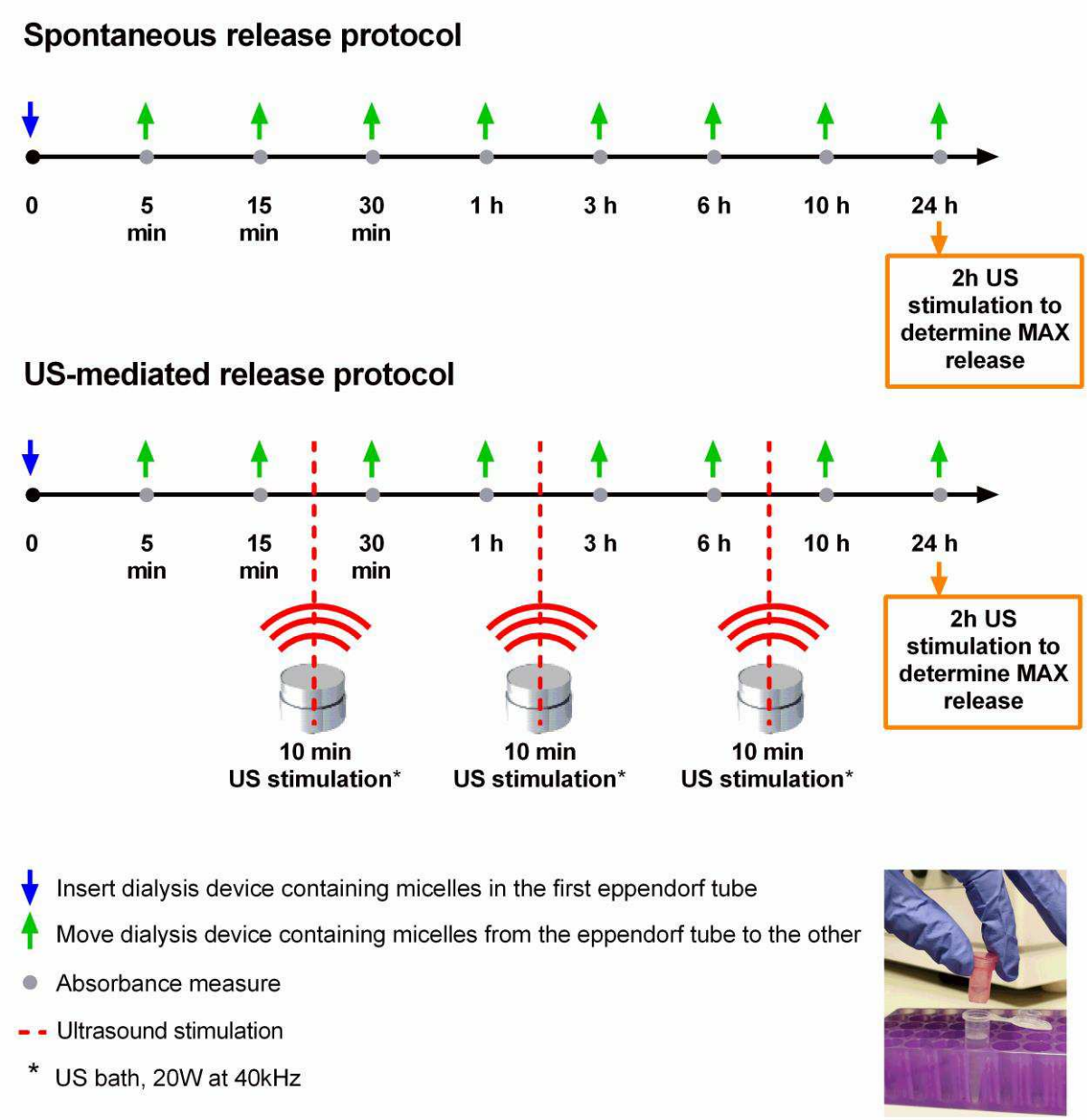


**Figure 63. Drug release protocols.**

Both the US mediated and the spontaneous Dex release profiles are reported as the percentage cumulative Dex release respect to the maximum release. Differences between the spontaneous and the US-triggered drug release extent were evaluated at the time points

after US stimulation and reported as respective increases, *Δ Release* and *Δ Slope*, for each copolymer and each Dex concentration. *Δ Release* was computed at 3 different time points (30 min, 3 h and 10 h) as the percentage variation of the cumulative release due to US, that is

$$\Delta\, Release = \frac{(US_{PCR}(t) - S_{PCR}(t))}{S_{PCR}(t)} \cdot 100$$

where $US_{PCR}\ (t)$ and $S_{PCR}\ (t)$ are respectively the US mediated and spontaneous percentage cumulative release at the time point t after US stimulation, respect to the maximum release achieved after 2 h US stimulation. *Δ Slope* was calculated for 3 different time intervals (from 15 min to 30 min, from 1 h to 3 h, and from 6 h to 10h) as the percentage variation of the slope of the cumulative release profiles due to US, that is

$$\Delta\, Slope\ (t_{1-2}) = \frac{US_{slope}(t_{1-2}) - S_{slope}(t_{1-2})}{S_{slope}(t_{1-2})} \cdot 100$$

where $US_{slope}$ ($t_{1\text{-}2}$) and $S_{slope}$ ($t_{1\text{-}2}$) are respectively US mediated and spontaneous slope of the percentage cumulative release profiles in the US stimulation containing time interval $t_{1\text{-}2}$. For better clarification on computation of *Δ Release* and *Δ Slope*, please refer to Figure 64.

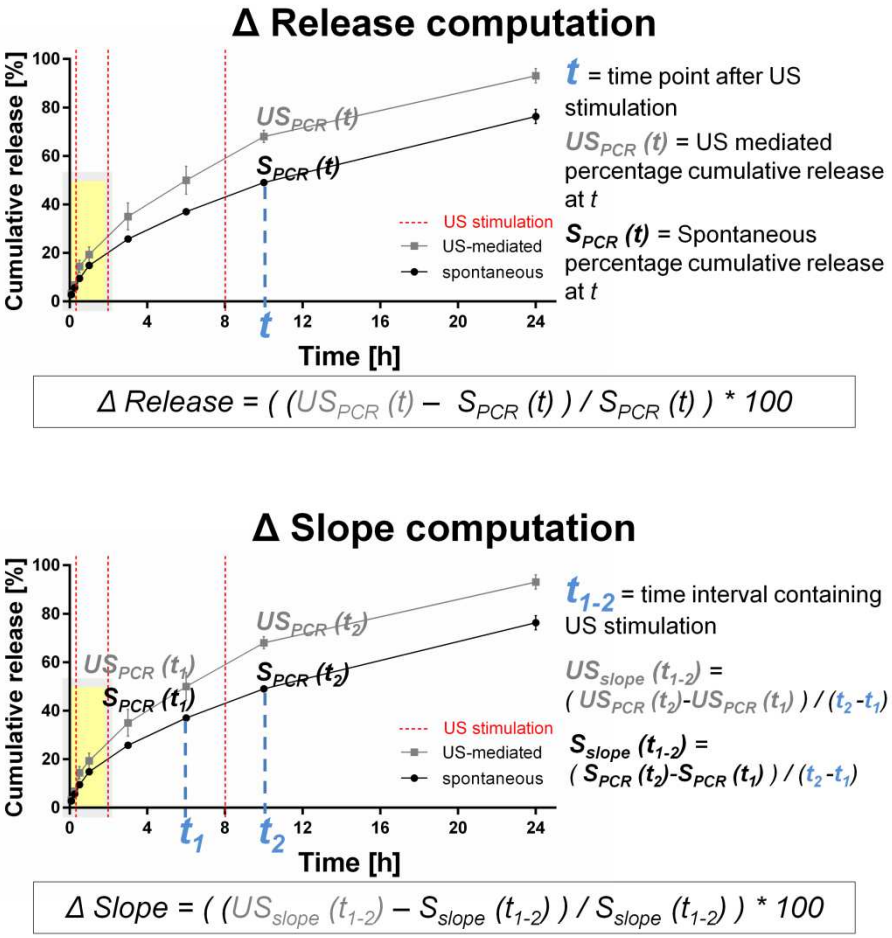


**Figure 64. Δ Release and Δ Slope computation**

Data of the percentage cumulative release profiles were fitted with the zero order model and with Ritger-Peppas model by means of a MATLAB® toolbox (cftool) for curve fitting.

***Statistical Analysis***

The percentage cumulative release values from US-mediated and spontaneous release experiments were compared at the time points immediately after the US stimulation (30 min, 3 h and 10 h) by using a non-parametric statistical analysis: a two-sample Kolmogorov-Smirnovn test was performed in order to evaluate significant differences. Results were considered statistically different for *p*-values ≤ 0.05.

## *Results and discussion*

For the study of spontaneous and ultrasound-mediated release of dexamethasone model hydrophobic drug, we prepared five different poly(2-oxazoline)-based amphiphilic block copolymers shown in Figure 65a.

**P1** (nPropOx$_{40}$-MetOx$_{160}$) and **P2** (nPropOx$_{60}$-MetOx$_{40}$) are diblock copolymers consisting of 2-methyl-2-oxazoline and 2-n-propyl-2-oxazoline, which differ in the blocks ratio and in their chain length.

**P3** ((EnOx$_{10}$-ButOx$_{20}$)$_{stat}$-b-MetOx$_{40}$) and **P4** ((EnOx$_{10}$-ButOx$_{30}$)$_{stat}$-b-MetOx$_{100}$) are diblock terpolymers, with a hydrophobic part containing 2-butyl-2-oxazoline and unsaturated 2-(3-butenyl)-2-oxazoline components. It is known that such 2-oxazoline monomers containing double bonds are incorporated into a micellar structure and allow further modifications via radical reactions, *e.g.*, incorporation of drugs or targeting moieties, [323] and crosslinking of micellar core.[324]

Finally, **P5** (MetOx25-nPropOx145-MetOx25) is a triblock copolymer consisting of an outer hydrophilic 2-methyl-2-oxazoline and an inner 2-n-propyl-2-oxazoline part. This architecture is inspired by the one of Pluronics, well-known triblock copolymers, extensively explored in the US-mediated drug delivery.[286, 325] Pluronics are composed of thermoresponsive poly(propylene glycol) inner block and two outer hydrophilic poly(ethylene glycol) blocks.

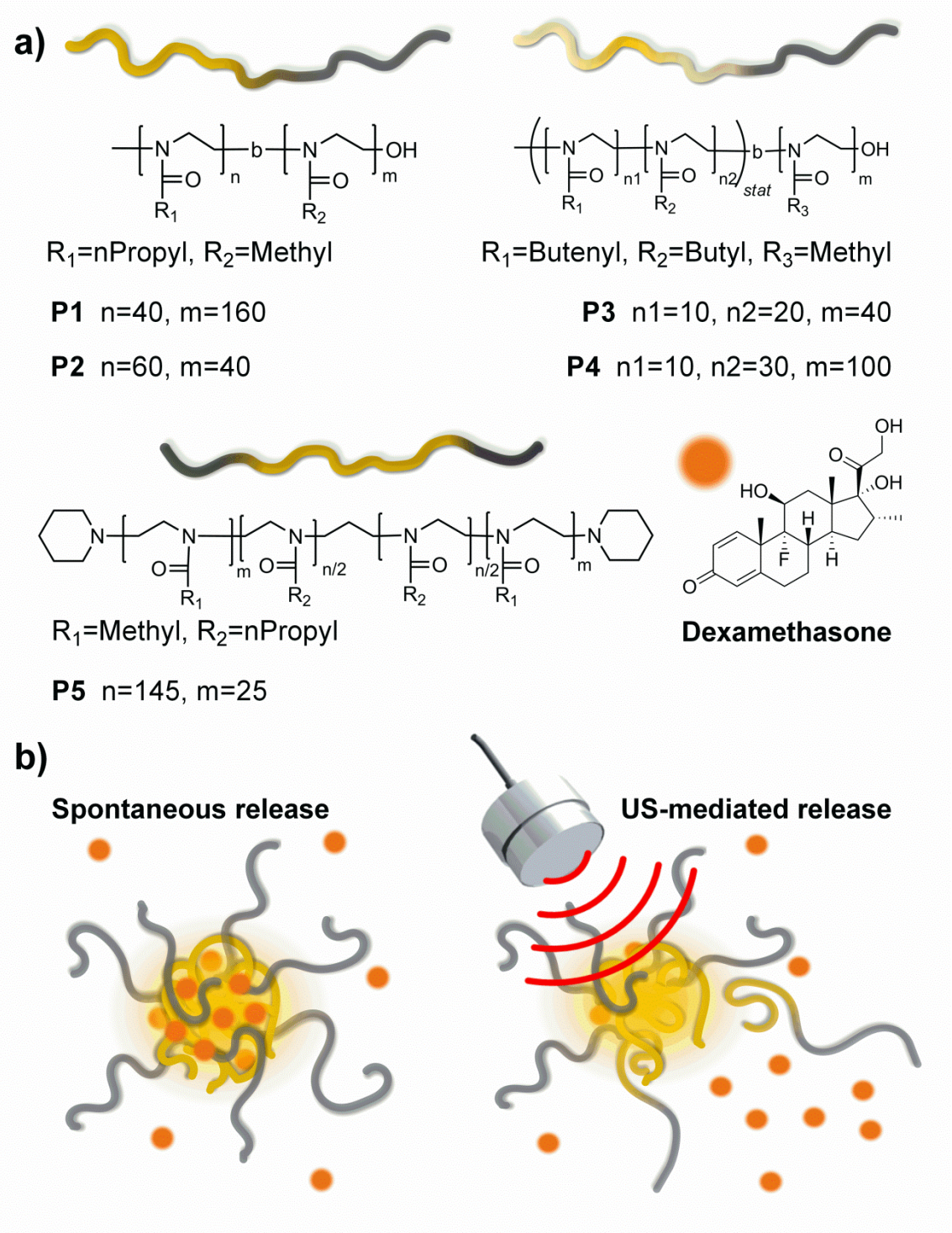


**Figure 65. Representation of ultrasound triggered release from different POx micelle types. a) Chemical structures and illustrative images of the diblock and triblock copolymers P1 – P5 synthesized and analyzed in this section (yellow: hydrophobic copolymer parts, grey: hydrophilic copolymer parts) and of dexamethasone, the steroid anti-inflammatory drug, used for drug release studies. b) Depiction of the two experimental conditions studied: spontaneous release (left) and ultrasonic-mediated release (right) from POx micelles.**

The purity of synthesized monomers was measured by HPLC (see Figure 66), demonstrating 96%, 93% and 97% purity for nPropOx, ButOx and EnOx, respectively.

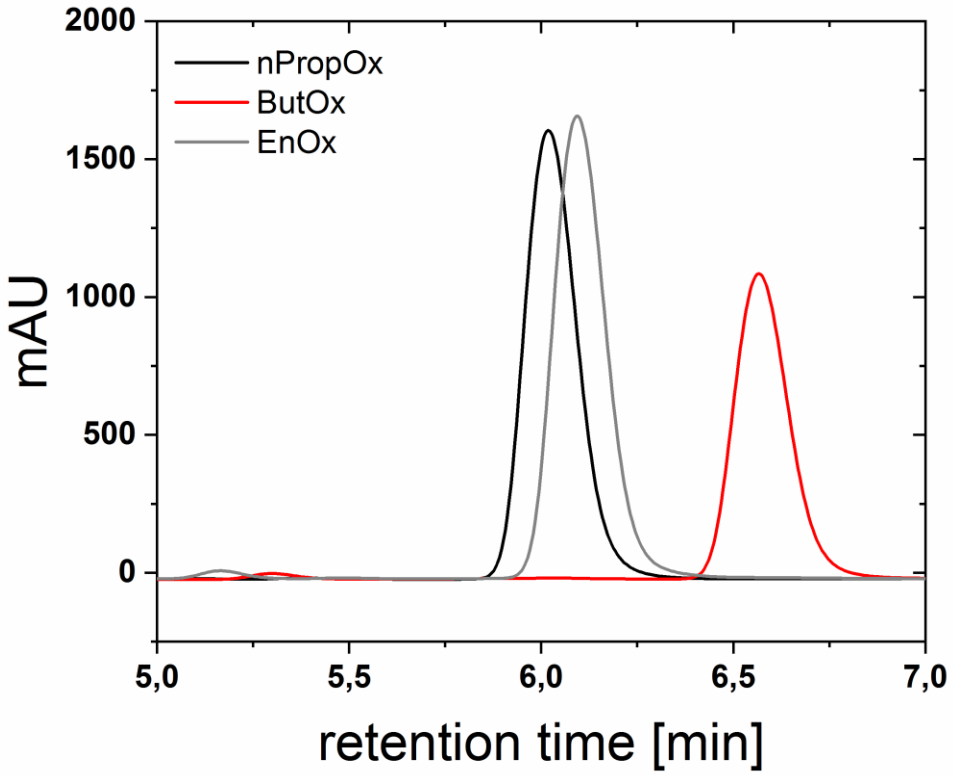


**Figure 66. HPLC elugrams of synthesized monomers. The monomers were measured using Agilent 1200 Series HPLC System (UV detection at 210 nm, Zorbax Eclipse Plus column C18, 4.6*250 mm, 5 µm, eluent methanol/water 90/10).**

The block copolymers structure were studied by means of nuclear magnetic resonance (NMR) spectroscopy and size exclusion chromatography (SEC). The results are summarized in the following Table.

| Sample | Theoretical composition | $M_{n,theor}$ [kDa] | $M_n$ [kDa] | Đ | $F_{theor}$ [%] | F [%] | Yield [%] | $D_{mode,1}$ [nm] | $D_{mode,2}$ [nm] |
|---|---|---|---|---|---|---|---|---|---|
| **P1** | $MetOx_{160}$-b-$nPropOx_{40}$ | 18.2 | 13.1 | 1.44 | 80 | 82 | 81 | 158 ± 11 | 129 ± 28 |
| **P2** | $MetOx_{40}$-b-$nPropOx_{60}$ | 10.2 | 11.5 | 1.27 | 40 | 51 | 74 | 33 ± 1 | 33 ± 0.0 |
| **P3** | $MetOx_{40}$-b-$(ButOx_{20}$-$EnOx_{10})_{stat}$ | 7.2 | 7.8 | 1.22 | 57 | 68 | 53 | 193 ± 15 | 134 ± 34 |
| **P4** | $MetOx_{100}$-b-$(ButOx_{30}$-$EnOx_{10})_{stat}$ | 13.6 | 10.5 | 1.32 | 71 | 79 | 46 | 667 ± 122<br>113 ± 51 | 372 ± 178<br>115 ± 30 |
| **P5** | $MetOx_{25}$-b-$nPropOx_{145}$-b-$MetOx_{25}$ | 20.9 | 9.9 | 1.33 | 26 | 43 | 45 | 51 ± 3 | 55 ± 13 |

**Table 6. Theoretical number average molar mass ($M_{n,theor}$) and theoretical molar hydrophilic fraction ($F_{theor}$) calculated from the feed, $M_n$ and dispersity (Đ) measured by SEC, hydrophilic molar fraction (F) calculated from $^1$H NMR spectra, $D_{mode,1}$, $D_{mode,2}$ diameters calculated from DLS measurements in PBS, for dexamethasone concentrations 1 and 2 g·L$^{-1}$, respectively (mean ± SD from 200 - 700 measurements performed from preparation up to 24h).**

In all cases, except for the copolymer **P1** that showed the highest hydrophilic fraction, we observed an increase of the hydrophilic molar fraction F in comparison to theoretical values. This observation is in agreement with recent results,[322] in which a discrepancy between theoretical and experimental composition of triblock copolymers from 2-methyl-2-oxazoline and 2-n-propyl-2-oxazoline was found. Such discrepancy was explained by an inefficient precipitation of copolymers in diethyl ether during a cleaning step, as proven by the presence of a high 2-n-propyl-2-oxazoline copolymer fraction dissolved in diethyl ether. An inefficient precipitation is proposed to be also responsible for obtained low yields, since, in general, the living cationic polymerization of 2-oxazolines reaches a quantitative monomer conversion, resulting in high yields (>95%). [326] Molar masses measured by SEC were in good agreement with theoretical values for copolymers possessing shorter chain lengths (**P2** and **P3**). For the copolymers with longer chains above 10 $kg \cdot mol^{-1}$ (**P1**, **P4** and **P5**), the values obtained from SEC measurements were lower than theoretical ones. However, it should be taken into account that for such wide spectrum of different chemical compositions and the ratios of the blocks, the results from SEC can be considered only as relative values. The dispersities of prepared copolymers were below 1.45, which indicates relatively narrow molar mass distributions.

The prepared block copolymers were then used for encapsulation of dexamethasone (Dex), an anti-inflammatory steroid drug, with a limited water-solubility (0.089 $g \cdot L^{-1}$ at 25 °C)[327]. The polymeric micelles with encapsulated Dex were prepared by fast and simple thin film re-hydration method described by Luxenhofer *et al.* for encapsulation of anticancer drugs in poly(2-oxazoline) micelles.[312, 313, 317] Please refer to Figure 67 for a representative Cryo Scanning Electron Microscopy (Cryo-SEM) image of the micelles formed by the afore mentioned technique (in this case **P2** micellar system).

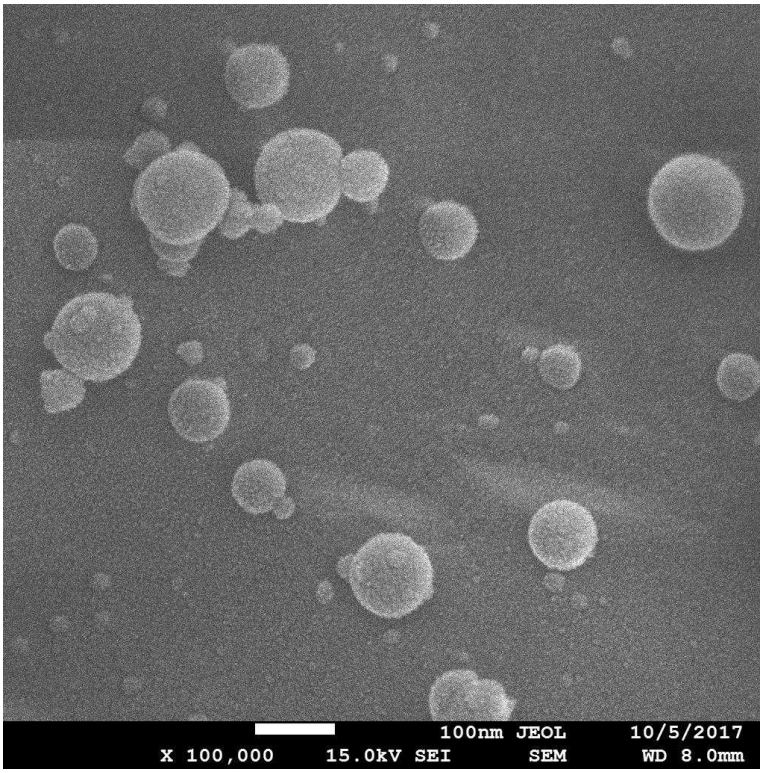


**Figure 67. Cryo-SEM image of P2 Dex-loaded micelles. The morphology of the aggregates was studied using scanning electron microscope JEOL 7500 F (JEOL, Japan) equipped with cryomode system from Quorum, UK. First, cold aqueous solutions of selected micelles were prepared. The samples were transferred to an holder containing 3 mm high copper rivets. The holder was immediately inserted into liquid nitrogen. Frozen samples were transferred into preparation chamber and fractured with scalpel-bladed probe. Surface layer of water was sublimated for 10 min at -90 °C. The samples were subsequently coated with platinum/palladium conductive layer (60 s) and mounted on the SEM stage cooled to -140 °C. The samples were examined using secondary electron imaging (SEI) detector, microscope was operating at accelerating voltage of 15 keV. Working distance was fixed to 8 mm.**

Figure 68 shows the Dex loading data for the different polymeric micelles, expressed as loaded mass and loading efficiency, obtained by HPLC.

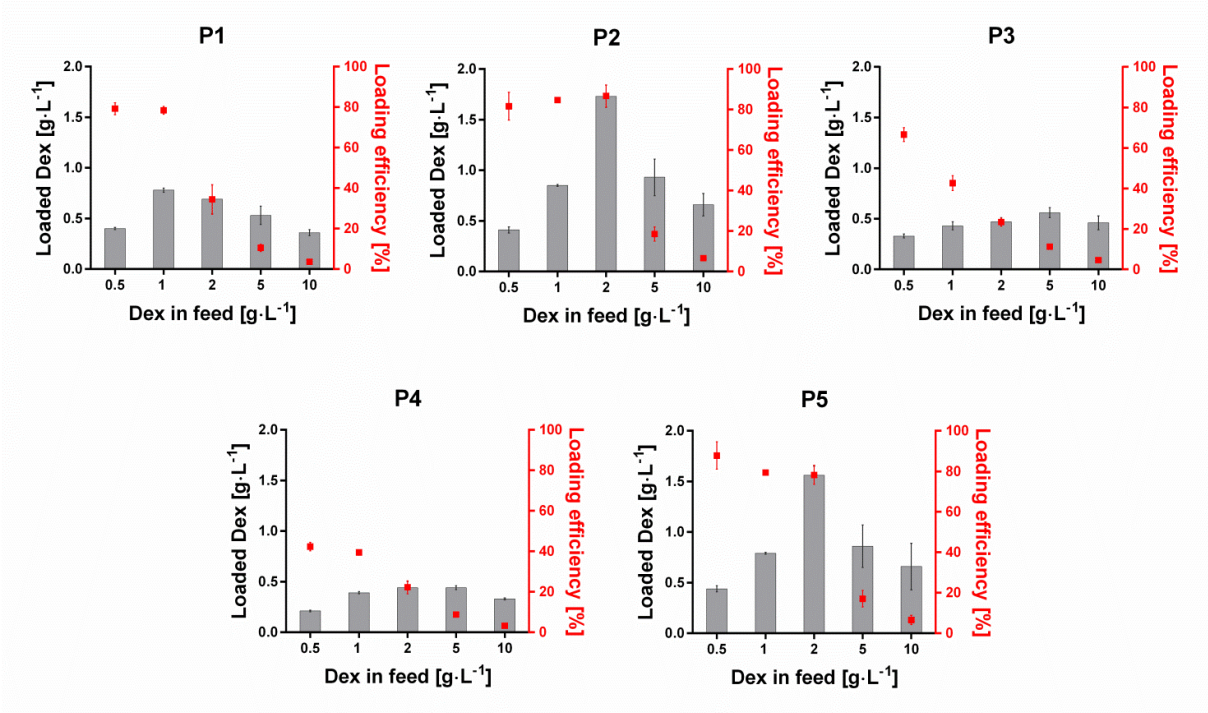


**Figure 68. Loading of Dex in micelles expressed as loaded mass and loading efficiency. Double scaled plots representing the loaded Dex in poly(2-oxazoline)-based micelles with grey columns (mean value and standard deviation from 4 measurements), and corresponding loading efficiency with red dots (mean value and standard deviation, from 4 measurements). P1 (nPropOx$_{40}$-MetOx$_{160}$); P2 (nPropOx$_{60}$-MetOx$_{40}$); P3 (EnOx$_{10}$-ButOx$_{20}$)stat-b-MetOx$_{40}$); P4 (EnOx$_{10}$-ButOx$_{30}$)$_{stat}$-b-MetOx$_{100}$); P5 (MetOx$_{25}$-nPropOx$_{145}$-MetOx$_{25}$). The loading was measured in water by high performance liquid chromatography, using a constant copolymer concentration of 10 g·L$^{-1}$.**

The micelles exhibited large variations in loading efficiency depending on their chemical structure. Diblock copolymers composed of 2-n-propyl-2-oxazoline exhibited loading efficiencies around 80% up to 1 g·L$^{-1}$ (**P1**) and 2 g·L$^{-1}$ (**P2**). Diblock copolymers containing double bonds were featured by a considerably lower loading efficiency in the whole range of Dex concentrations. In particular, for the lowest studied feed concentration of Dex, *i.e.*, 0.5 g·L$^{-1}$, the measured loading efficiency for **P3** was 67%, while for **P4** it was just 42%. The triblock copolymer **P5** exhibited relatively high loading efficiencies up to a Dex concentration of 2 g·L$^{-1}$, comparable with the results obtained for the copolymer **P2**. Both copolymers with highest loading efficiencies also exhibit lowest hydrophilic fractions F (51 and 43% for **P2** and **P5**, respectively), respect to the other copolymers. However, the loading efficiency does not depend solely on the hydrophilic fraction, but also on the chemical structure of hydrophobic

comonomer. In general, two copolymers comprising double bonds (**P3**, **P4**) exhibit inferior loading for all the Dex concetrations. Recently, Raveendran *et al.* described the preparation of curcumin-loaded micelles composed of 2-(3-butenyl)-2-oxazoline and 2-ethyl-2-oxazoline. In accordance with our results, such prepared micelles exhibited encapsulation efficiencies 52 and 83% (with more hydrophobic copolymer featured by higher loading efficiency).[328]

The loading capacity is another characteristic of micellar systems used as drug carriers, expressed as the ratio between the weight of loaded drug and the total weight of the drug carrier, including the loaded drug. The maximal loading capacities of the prepared polymeric micelles **P1**-**P5**, as well as other micellar formulations reported in the literature, are shown in Figure 69.

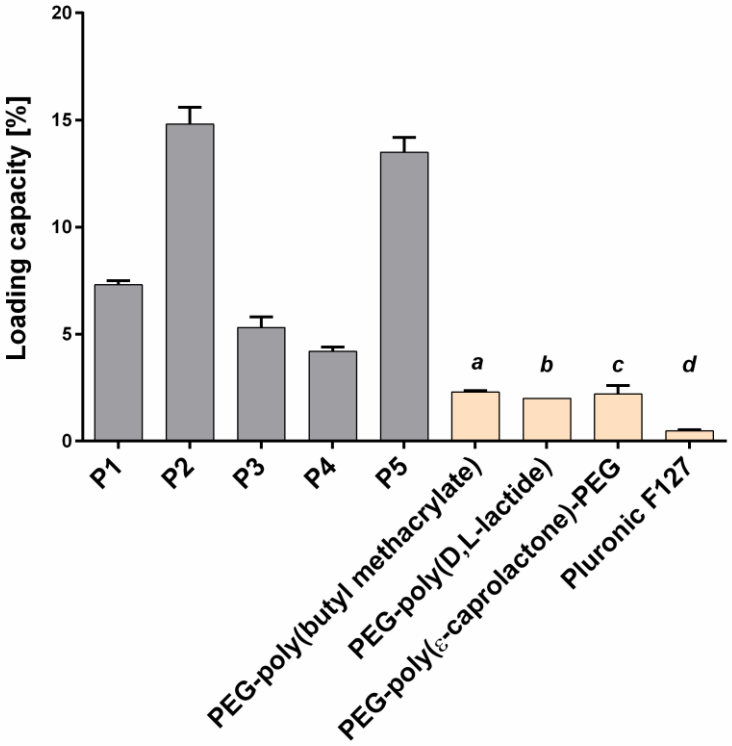


**Figure 69. Loading capacity of different micellar formulations. Maximal loading capacity for POx-based P1-P5 formulations compared to the loading capacity of various Dex-loaded micelles (a = Janas *et al.*[329], b = Yang *et al.*[330], c = Wang *et al.*[331], and d = Nidhi *et al.*[332]) reported in the literature. Loading capacity is calculated as reported in the Methods subsection.**

They ranged from 4.2% for **P4** to 14.7% for **P2**. It is worth mentioning that other polymeric micelles recently used for Dex encapsulation exhibited comparable or much lower loading capacities with respect to **P1**-**P5** formulations. Typically, a loading capacity in the range 0.5 - 3% was observed for Dex-loaded micelles composed of poly(ethylene glycol) (PEG) as a hydrophilic corona and butyl methacrylate[329], D,L-lactide[330], polycaprolactone (PCL)[331, 333] and poly(propylene glycol)[332], respectively, as a hydrophobic core. Slightly higher loading capacities (from 7 to 12%) were reported for PEG-PCL micelles loaded with dexamethasone acetate. However, such micelles remained stable in saline for less than 2 h.[334]

The **P1**-**P5** formulations have to be stable in the physiologically-related environment in order to be considered as potential drug nanocarriers. The instability results in an uncontrolled product due to aggregation and precipitation that would completely hamper obtaining of reliable biological data. The stability and size of Dex-loaded micelles was determined by means of DLS in PBS by monitoring the size of micelles for 24 h. This time range was selected based on the work of Luxenhofer *et al.*[313], where the authors described almost total (> 80%) release of loaded drug from POx micelles after 24h. We thus considered this time range to be relevant for our further studies. We selected two drug concentrations, namely 1 and 2 $g \cdot L^{-1}$, to investigate the micelle stability. In the concentration of Dex $2 \cdot g \cdot L^{-1}$, our micellar formulation exhibits the maximum loading capacity. For the comparison, we selected one lower concentration ($1\ g \cdot L^{-1}$). The copolymer concentration was kept $10 \cdot g \cdot L^{-1}$ in all cases, typically used in drug encapsulation studies on POx micelles.[312, 313] The results for $1\ g \cdot L^{-1}$ Dex concentration are shown in Figure 70 and Table 6. The size is expressed as a peak maximum derived from intensity size distribution ($D_{mode}$). For **P1**-**P3** and **P5** micellar systems, the intensity size distributions were monomodal and the constant values during 24 h of analysis demonstrated their stability. During 24h, the **P4** system exhibited a stable bimodal distribution with peak maxima at 113 nm and 667 nm, respectively. This copolymer also exhibited the lowest loading capacity (Figure 69), which may be associated with a rather unstable formulation.

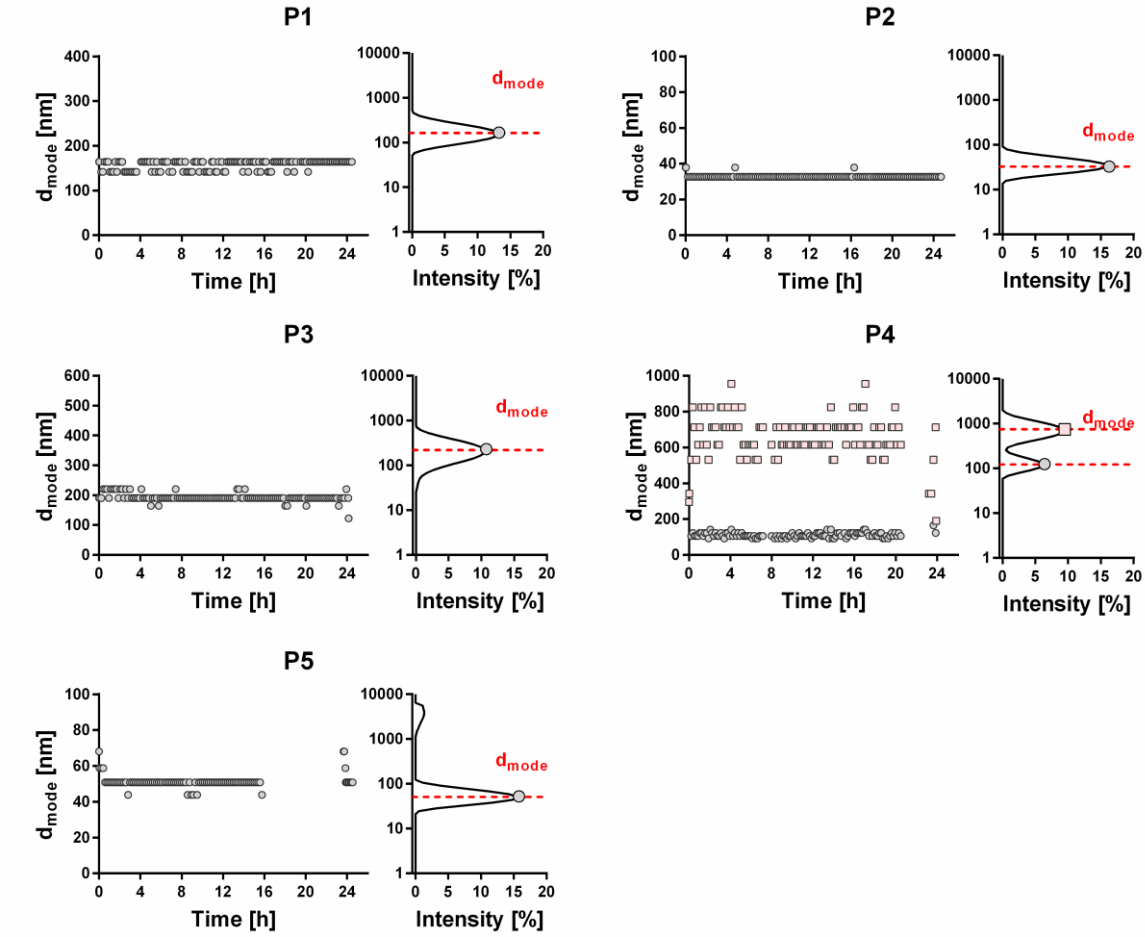


**Figure 70. Stability test of micelles loaded with 1 g·L$^{-1}$. Dex. Dynamic light scattering measurements to assess micelle stability over 24 h in PBS. For each micelle type, the left plot represents the diameter of particles at different time-points expressed as a peak maximum from intensity size distribution ($D_{mode}$), and the right plot shows a representative intensity size distribution, 12h after the preparation.**

The DLS results concerning a 2 g·L$^{-1}$ Dex concentration are summarized in Table 6 and Figure 71. Overall, the results were comparable with the 1 g·L$^{-1}$ Dex concentration apart from a slight reduction of stability in the 24 h observation window showed for all the micellar systems except for **P2**. This is also reflected in observed increase of the standard deviations provided for the diameters in Table 6. Moreover, in some cases a slight decrease in particle size was observed (for copolymers **P1**, **P3** and **P4**). In addition, the **P4** copolymer exhibited a bimodal size distribution for the first 10 h, but afterwards the sample became polydisperse and unstable.

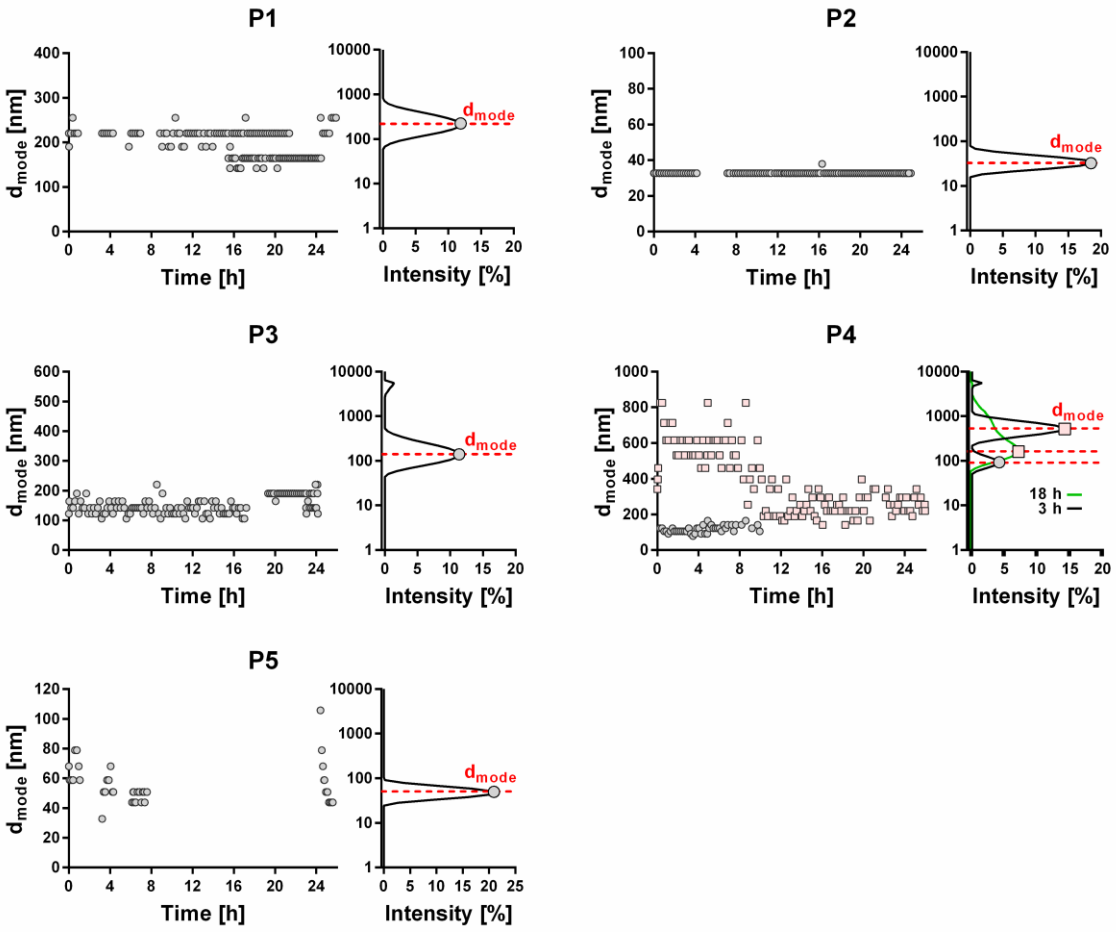


**Figure 71. Stability test of micelles loaded with 2 g·L$^{-1}$. Dynamic light scattering measurements to assess micelle stability over 24 h in PBS. For each micelle type, the left plot represents the diameter of particles at different time-points expressed as a peak maximum from intensity size distribution ($D_{mode}$), and the right plot shows a representative intensity size distribution, 3h after the preparation. P4 Dex-loaded micelles exhibiting bimodal size distribution for the first 10h (black line), then the sample became polydisperse and unstable (grey green line). All other micellar systems were monodisperse and stable.**

**P2** and **P5** Dex-loaded micelles were of a diameter smaller than 100 nm. These sizes are in the typical range of other POx-based micelles.[313] Pluronic micelles typically display even smaller diameter of around 10 nm.[335] This may be attributed to generally smaller molar masses of Pluronic copolymers. Copolymers **P1** and **P3**, featured by a higher hydrophilic fraction, formed micelles with diameters between 100 and 200 nm. These dimensions exceed the typical polymeric micelles size, suggesting that the formed particles may represent polymersomes, worm-like micelles or micelle aggregates. Block copolymers with

high hydrophilic fraction (80 - 90 mol%) may form spherical aggregates composed of tens of micelles with the diameter above 100 nm.[336] Similar aggregates were observed by Hruby *et al.*[307] and Trzebicka *et al.*[309] for thermoresponsive POx copolymers. In general, the hydrophilic fraction of copolymers in the range from 10 to 40 mol% favors the formation of polymersomes or worm-like micelles.[337] Krumm *et al.*[338] reported formation of polymersomes from triblock copolymers with 2-phenyl-2-oxazoline as a middle part, with the hydrophilic fraction around 50 mol%. Our results suggest that POx copolymers with a lower molar hydrophilic fraction (**P2** and **P5**) formed smaller and more stable micelles. The same trend was observed by Trzebicka *et al.*[309] for diblock copolymers composed of 2-ethyl-2-oxazoline and 2-phenyl-2-oxazoline. On the other hand, our copolymers which exhibit larger aggregates (**P1**, **P3** and **P4**) possess high molar hydrophilic fraction (70 - 80%), we thus do not expect the formation of polymersomes, although the formation of micellar aggregates.

We investigated US as a possible modulating input by measuring Dex release from **P1**-**P5** micelles both spontaneously and following US stimulation (see Figure 65b). Figure 63 shows a depiction of the experimental protocol used, detailed described in the Methods subsection. US stimulation (40 KHz, 20 W – 10 min duration) was provided with a US water bath at three time-points over the 24 h release experiment, namely: $t_1$ = 17 min, $t_2$ = 2 h and $t_3$ = 8 h. Figure 72, Figure 73 and Figure 74 show the Dex release data obtained for all the micelle types and both Dex loadings. The release profiles are reported as the cumulative percentage release at different time-points (5 min, 15 min, 30 min, 1 h, 3 h, 6 h, 10 h and 24 h).

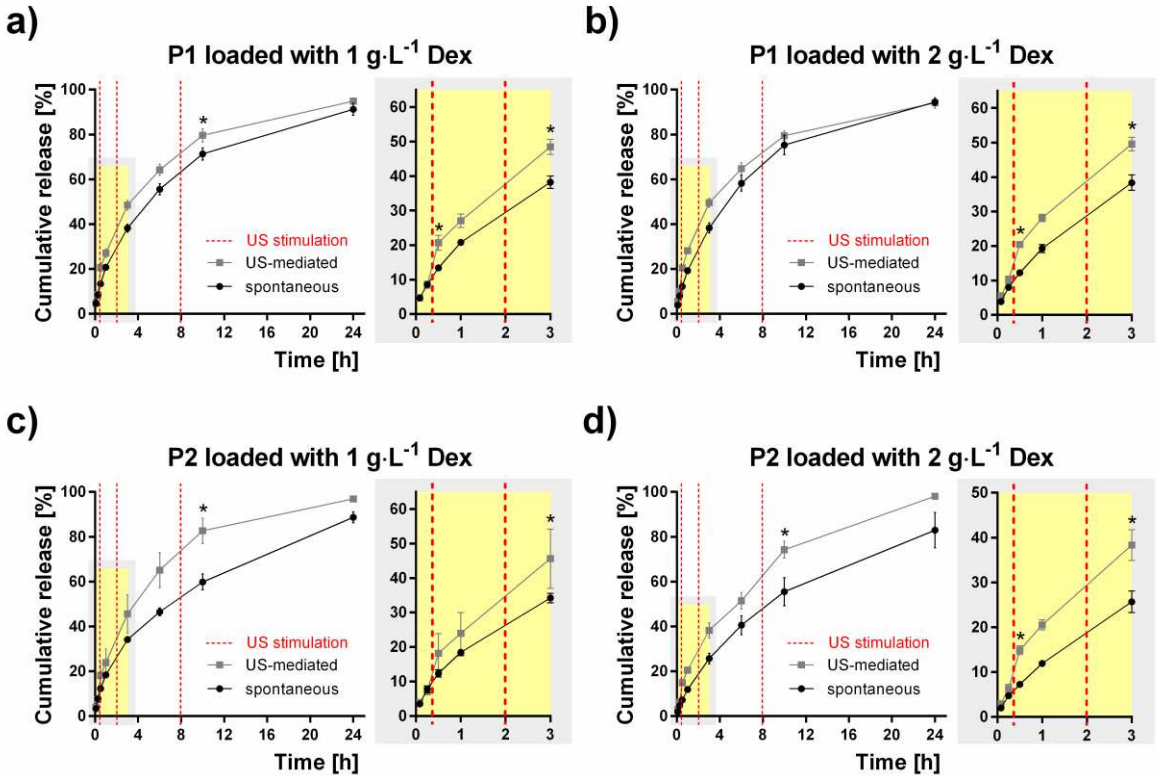


**Figure 72. Dex release profiles for P1 and P2 Dex-loaded micelles. Spontaneous (black round points) and US-mediated (grey square points) for micelles based on POx diblock copolymers, namely P1 and P2, loaded with 1 and 2 g·L$^{-1}$ Dex, respectively. The release data are expressed as the percentage cumulative Dex release with respect to the maximum release for a given micelle type. Each point shows the mean value and the standard deviation obtained from 4 measurements. Red dashed lines represent the time-points when the ultrasound stimulation was provided. The zoomed plots highlight the first 3 h of the release experiment. Asterisk indicates a statistically significant difference between US-mediated and spontaneous release values ($p < 0.05$, two sample Kolmogorov-Smirnov test).**

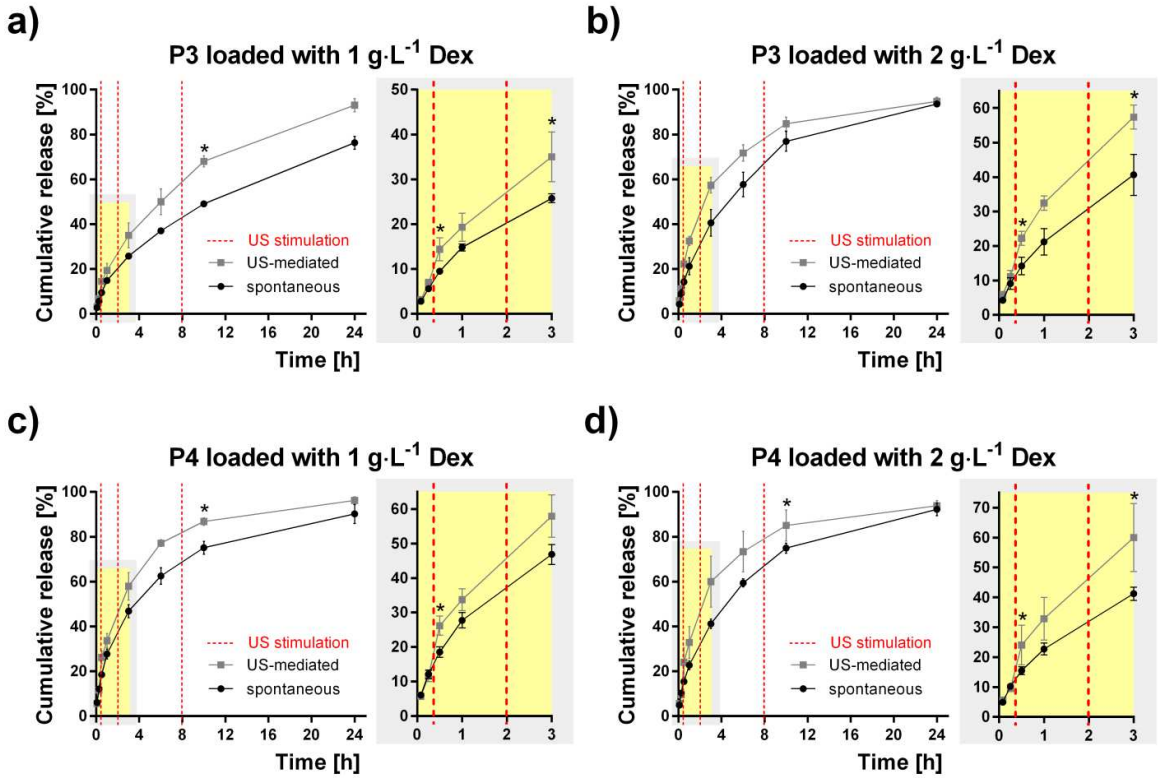


**Figure 73. Dex release kinetics from P3 and P4 micelles. Spontaneous (black round points) and US-mediated (grey square points) for micelles based on POx diblock terpolymers, namely P3 and P4, loaded with 1 and 2 g·L$^{-1}$ Dex, respectively. Red dashed lines represent the time-points when the ultrasound stimulation was provided. The zoomed plots highlight the first 3 h of the release experiment. Asterisk indicates a statistically significant difference between US-mediated and spontaneous release values ($p$ < 0.05, two sample Kolmogorov-Smirnov test).**

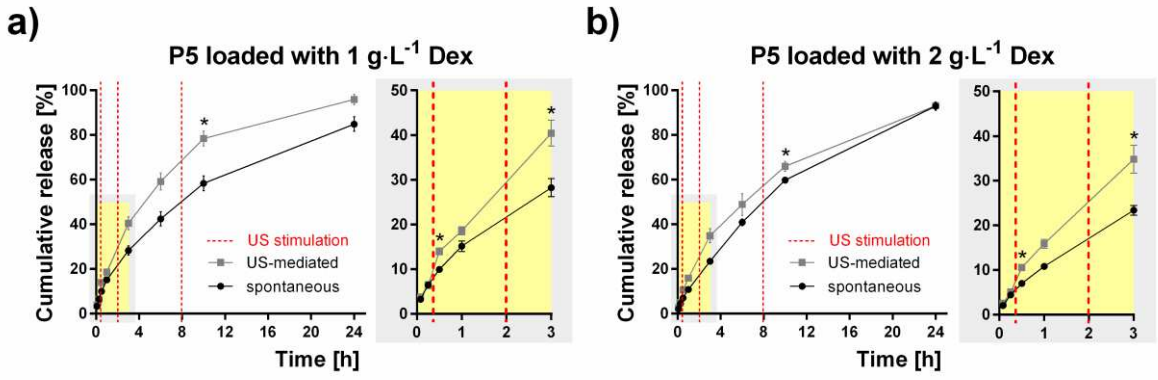


**Figure 74. Dex release kinetics from P5 micelles. Spontaneous (black round points) and US-mediated (grey square points) for micelles based on POx triblock copolymer P5, loaded with 1 and 2 g·L$^{-1}$ Dex, respectively. Red dashed lines represent the time-points when the ultrasound stimulation was provided. The zoomed plots highlight the first 3 h of the release experiment. Asterisk indicates a statistically significant difference between US-mediated and spontaneous release values (p < 0.05, two sample Kolmogorov-Smirnov test).**

In all cases, the US-mediated Dex release (grey square points) was faster than the spontaneous release (black round points) that is highlighted by zooming into the first three measurement time points. Immediately after the first US stimulation at 17 min (first red dashed line, highlighted in the zooming areas in Figures 72 - 74), a statistically significant increase of the cumulative release (grey square points) was observed for almost all sample types, except for **P2** micelles loaded with 1 $g \cdot L^{-1}$ Dex (Figure 72c). Also after the second US stimulation at 2 h (second red dashed line, highlighted in the zooming areas in Figures 72 - 74), a statistically significant difference was found between US-stimulated and non-stimulated Dex release for all micelle types, with the exception of **P4** micelles loaded with 1 $g \cdot L^{-1}$ Dex (Figure 73c). The third US stimulation at 8 h (third red dashed line in Figures 72 - 74) resulted in significant enhancement of the US-triggered release (grey square points) compare to spontaneous release (black round points) for all micelle types, except for **P1** micelles loaded with 2 $g \cdot L^{-1}$ Dex (Figure 72b) and for **P3** micelles loaded with 2 $g \cdot L^{-1}$ Dex (Figure 73b). These results suggest that US can effectively modulate Dex release from POx-based micelles.

Micelles possessing lower hydrophilic fraction (**P3**, **P2**, **P5**) exhibit slower spontaneous release rates, in comparison to their counterparts with higher hydrophilic fraction, as visible especially for the concentration 1 $g \cdot L^{-1}$ Dex (see Figures 72 - 74). Despite this fact, at the final time-point (24 h) of the release tests, both US-stimulated and spontaneous release converged to the same release value in most cases. This is due to the relatively fast-releasing nature of these nanocarriers, which show almost 100% release of the drug after 1 day. However, the ability to modulate drug release kinetics through ultrasound at shorter time-points in an effective way, for certain POx formulations, has interesting applications. Once administered systemically in the bloodstream, in fact, micelles travel quite quickly towards the target: for a human subject, the cardiac output is 5 L/min with a 5 L blood volume, indicating that the blood circulates on average once per minute.[339] Thus, having an outer tool (an ultrasound probe) able to locally trigger the release kinetics in a localized body/tissue portion, even if for few minutes/hours, may have a high clinical relevance.

Considering the micellar systems loaded with 1 g·L$^{-1}$, both in the case of diblock copolymers (Figure 72 a and c) and of diblock terpolymers (Figure 73 a and c), the copolymers featured by the lower hydrophilic fractions, that are **P2** (Figure 72a) and **P3** (Figure 73c) respectively, showed a faster cumulative release profile due to US, respect to the others that have a higher hydrophilic fraction, that are respectively **P1** (Figure 72c) and **P4** (Figure 73a), providing a stronger enhancement of Dex release due to ultrasound respect to the spontaneous one. Also **P5** (Figure 74a) showed the same behaviour. Hence, among all the five different micellar systems, **P2**, **P3**, and **P5**, which are the ones featured with the lowest hydrophilic fractions, are also the ones on which US provides the highest effect on Dex cumulative release profiles. This is also highlighted by the fact that the US mediated release profiles and the respective spontaneous ones continued to differ also at the final time-point (24 h), thus providing some suggestions that a better US modulation can be achieved with systems composed of more hydrophobic copolymers.

Considering the micellar systems loaded with 2 g·L$^{-1}$, instead, the behavior reported before was not confirmed except for the case of the diblock copolymers (Figure 72 b and d), in which **P2** continued to show a faster cumulative release profile due to US respect to **P1**. One should notice that as we mentioned before a slight reduction of stability in the 24 h observation window was shown for all the micellar systems except for **P2**, which remained stable within the 24 h also for the micellar system loaded with 2 g·L$^{-1}$ (see Figure 71 and Table 6).

Another option to capture the differences between US-mediated and spontaneous release is shown in Table 7 with the *Δ release* [%] computed at the time points immediately after US stimulation events and the *Δ slope* [%] in the "US-containing" time intervals (detailed in the Methods subsection). For all the samples, an increase in the release due to the US stimulation was observed. The maximum *Δ release* (+ 105.4%) was found for **P2** micelles loaded with 2 g·L$^{-1}$ Dex, after the first US stimulation. The slope of the cumulative release also increased for all the samples after the first and the second US stimulation (*Δ slope* positive values), while a reduction of the slope was observed after the third US stimulation (*Δ slope* negative values). This can be attributed to an almost complete release of Dex for

US-stimulated systems at this time-point. Some exceptions were provided by **P2** micelles with 1 g·L$^{-1}$ Dex, **P2** micelles with 2 g·L$^{-1}$ Dex, **P3** micelles with 1 g·L$^{-1}$ Dex and **P5** micelles with 1 g·L$^{-1}$ Dex, for which the slope continued to increase. Such latter samples were, as stated before, the ones featured by both the highest hydrophobic fractions and stability.

| Micelles | 1st US stimulation | | 2nd US stimulation | | 3rd US stimulation | |
|---|---|---|---|---|---|---|
| | Δ Release [%] | Δ Slope [%] | Δ Release [%] | Δ Slope [%] | Δ Release [%] | Δ Slope [%] |
| **P1** 1 g.L$^{-1}$ Dex | 54.0 | 150.1 | 26.9 | 22.8 | 11.8 | -1.8 |
| **P1** 2 g.L$^{-1}$ Dex | 67.4 | 143.7 | 29.5 | 12.7 | 5.8 | -13.8 |
| **P2** 1 g.L$^{-1}$ Dex | 48.2 | 135.9 | 33.7 | 38.1 | 38.5 | 36.1 |
| **P2** 2 g.L$^{-1}$ Dex | 105.4 | 243.0 | 50,1 | 31.5 | 35.2 | 58.0 |
| **P3** 1 g.L$^{-1}$ Dex | 52.4 | 98.2 | 36.1 | 43.7 | 38.6 | 49.4 |
| **P3** 2 g.L$^{-1}$ Dex | 60.5 | 123.1 | 43.8 | 29.8 | 10.5 | -31.2 |
| **P4** 1 g.L$^{-1}$ Dex | 42.0 | 129.1 | 24.0 | 27.0 | 15.7 | -23.3 |
| **P4** 2 g.L$^{-1}$ Dex | 56.1 | 183.3 | 45.8 | 46.5 | 13.5 | -23.0 |
| **P5** 1 g.L$^{-1}$ Dex | 41.0 | 117.0 | 43.7 | 67.1 | 34.8 | 22.0 |
| **P5** 2 g.L$^{-1}$ Dex | 51.5 | 120.6 | 49.3 | 51.0 | 10.4 | -9.5 |

**Table 7. Percentage variation of cumulative drug release and difference in the curve slope between US-stimulated samples and samples featured by spontaneous release. *Δ release* values and *Δ slope* values were reported for the different time-points after each US stimulation. Positive *Δ slope* values indicate an increase of the slope while negative ones stand for a reduction respect to spontaneous release kinetics.**

US can produce both mechanical and thermal effects in interaction with a target.[340] In our case, the temperature of the water bath was measured before and after the 10 min US stimulation in order to determine if thermal effects contributed to the augmented release observed for the US-stimulated samples. The measured temperature raise was 1.4 ± 0.5 °C. Although some of the copolymers comprise the thermoresponsive (2-n-propyl-2-oxazoline) blocks (**P1**, **P2**, **P5**), they also differ in hydrophilic fraction. The different hydrophilic fraction leads to the differences in cloud point temperature for these copolymers. As was previously described for a series of triblock copolymers composed of MetOx and nPropOx, the copolymers with hydrophilic fraction from 50 to 88% exhibit a difference in the cloud point temperature of 9 °C.[322] We can state that the overall temperature change of the water bath due to the 10 min US stimulation did not affected the Dex release. Hence, the enhancement in the Dex release is probably not due to the so called "thermal effects of US" but more likely due to the mechanical effects, *e.g.* transient cavitation.

Additionally, the release profiles were fitted with one mechanistic realistic and one empirical/semiempirical model, namely the zero-order model and the Ritger-Peppas model.[341] In particular mechanistic realistic mathematical models are based on equations that describe real phenomena, *i.e.* mass transport by diffusion or dissolution of drug, while the empirical/semiempirical model are purely descriptive and not based on real physical, chemical and/or biological phenomena but can be useful for a comparison of different drug release profiles. The parameters found are reported in Table 8. Zero-order model is proper for drug reservoir systems in which the initial drug concentration exceeds the drug solubility, with constant reservoir properties (*i.e,.* thickness and permeability for the drug). In this case the fitting was rather poor: the maximum $R^2$ value was equal to 0.89 obtained for the spontaneous release of **P5** micelles with 2 $g \cdot L^{-1}$ Dex. A much better fitting was observed with the Ritger-Peppas model. For most of the samples, the $R^2$ values were slightly higher for the spontaneous release than for the US-mediated one, while the release rate constants K were always higher for the case of US-mediated release profiles. The n exponents of the Ritger-Peppas model instead fell in the range typical for a drug release mechanism of anomalous transport, which for a spherical drug carrier system is 0.43 and 0.85.[341] This happened for both US-mediated drug release profiles as well as spontaneous ones, indicating that in both

cases different overlapping phenomena occur in the drug release mechanism, *e.g.* drug diffusion and polymer swelling and perturbation.

| Micelles | Release | Zero-order | | Ritger-Peppas | | |
|---|---|---|---|---|---|---|
| | | K ($h^{-1}$) | $R^2$ | K ($h^{-1}$) | n | $R^2$ |
| **P1** 1 $g.L^{-1}$ Dex | spontaneous | 0.00320 | 0.6030 | 0.20220 | 0.5838 | 0.9992 |
| | US mediated | 0.00329 | 0.4108 | 0.26100 | 0.5759 | 0.9804 |
| **P1** 2 $g.L^{-1}$ Dex | spontaneous | 0.00271 | 0.6341 | 0.19160 | 0.6321 | 1.0000 |
| | US mediated | 0.00302 | 0.3643 | 0.27110 | 0.5592 | 0.9899 |
| **P2** 1 $g.L^{-1}$ Dex | spontaneous | 0.00336 | 0.7192 | 0.18040 | 0.5865 | 0.9986 |
| | US mediated | 0.00401 | 0.5088 | 0.23520 | 0.6122 | 0.9845 |
| **P2** 2 $g.L^{-1}$ Dex | spontaneous | 0.00487 | 0.8326 | 0.11940 | 0.6969 | 0.9999 |
| | US mediated | 0.00544 | 0.6971 | 0.19740 | 0.6150 | 0.9862 |
| **P3** 1 $g.L^{-1}$ Dex | spontaneous | 0.00257 | 0.7918 | 0.13910 | 0.5725 | 0.9950 |
| | US mediated | 0.00305 | 0.7064 | 0.18780 | 0.5782 | 0.9875 |
| **P3** 2 $g.L^{-1}$ Dex | spontaneous | 0.00211 | 0.5953 | 0.21120 | 0.5974 | 0.9997 |
| | US mediated | 0.00215 | 0.1964 | 0.30740 | 0.5799 | 0.9912 |
| **P4** 1 $g.L^{-1}$ Dex | spontaneous | 0.00205 | 0.3431 | 0.26490 | 0.5283 | 0.9961 |
| | US mediated | 0.00215 | 0.1354 | 0.32340 | 0.5461 | 0.9775 |
| **P4** 2 $g.L^{-1}$ Dex | spontaneous | 0.00180 | 0.5258 | 0.22430 | 0.5575 | 0.9994 |
| | US mediated | 0.00206 | 0.1486 | 0.31430 | 0.6006 | 0.9828 |
| **P5** 1 $g.L^{-1}$ Dex | spontaneous | 0.00339 | 0.7838 | 0.14880 | 0.5860 | 0.9997 |
| | US mediated | 0.00396 | 0.6234 | 0.19360 | 0.6685 | 0.9936 |
| **P5** 2 $g.L^{-1}$ Dex | spontaneous | 0.00520 | 0.8921 | 0.11050 | 0.6797 | 0.9997 |
| | US mediated | 0.00521 | 0.7617 | 0.15920 | 0.7141 | 0.9976 |

**Table 8. Drug release model parameters for both spontaneous and US-mediated release. Drug release profiles were fitted with three different drug release models: the Zero order model, and the Ritger-Peppas model. The parameters obtained are reported in the table as well as the $R^2$ values, representing the quality of the fitting.**

The evidences showing the efficacy of US stimulation in producing an increase of Dex release represent a proof of concept that POx micelles can work as US mediated drug delivery systems. For the comparison, Husseini *et al.*[291] reported on ultrasonic triggered release of doxorubicin from Pluronic P105 micelles caused by transient cavitation effect. In that case, the increased concentration of drug in micelles led to the increased amount of drug upon US stimulation. The authors explained the effect by increased hydrophobic interactions between the drug and hydrophobic core of the micelle. Oppositely, in our case, more hydrophobic micelles exhibit increased release when stimulated. The latter study focused on the investigation of the release mechanism by real time fluorescence measurements over a 3 min time scale. In this Section instead, we described how the release profiles were affected over time for multiple ultrasound stimulation and for a longer time scale (24 h).

As stated before, two different approaches to induce drug release from polymeric micelles using ultrasound are described in the literature. In the works of Rapoport and Husseini [286, 291] an increase of doxorubicin release from Pluronic P105 micelles by the application of low-frequency US was described. Authors claim that micelles are physically disrupted during the application of US. This change is however reversible and the micelles re-assemble when the US is switched off. The second approach is described in the works of Xuan and Zhang [288, 342]. High-intensity focused ultrasound was used to induce release of Nile Red from polymeric micelles containing hydrolyzable ester groups. In this case, the changes in polymer structure were irreversible and were attributed to the degradation of polymer chains induced by ultrasound. This was proved by observed decrease of molecular weight of used polymers.

We did not expect the degradation of the copolymers used in our work, since they do not contain any weak bond which is expected to be broken upon not focused ultrasound. To prove this assumption, we performed an experiment in order to compare molecular weights of prepared copolymers before and after application of US. We prepared polymer micelles, the samples were divided into controls without application of US, and micelles which underwent 30 min of ultrasonication. Then we freeze-dried the micelle solution and we measured the molecular weights of polymers by SEC. We added representative elugrams of **P2** in Figure 75. We did not observe any changes in elugrams after the application of

ultrasound. This observation evidenced that the release of defamethasone from the polymeric micelles is not caused by the degradation of polymer chains, rather by reversible physical disintegration of the micelles.

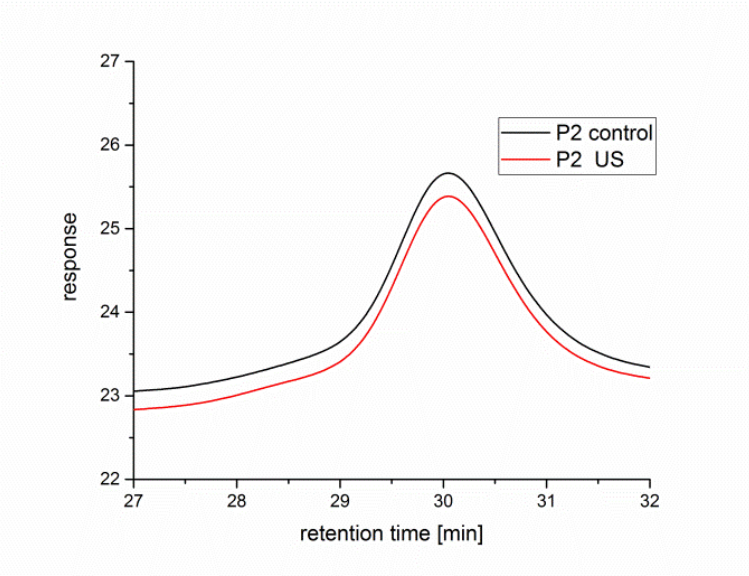


**Figure 75. Representative SEC elugrams of copolymers with and without application of US. Representative SEC elugrams of copolymer P2 , with (red line) and without (black line) ultrasonication of 30 min in form of micelles with dexamethasone in water ($c_{polymer}$ = 10 g·L$^{-1}$, $c_{dexa}$ = 1 g·L$^{-1}$). Elugrams shows no evidence of degradation of polymer chains.**

Hence these findings support the fact that upon US stimulation, POx based micelles can perturb their structure and possibly re-arrange it after stimulation interruption. Most of the US-mediated release systems are designed for delivery of anticancer drugs and are mainly based on Pluronic.[284] In particular the aim is to apply the release of the chemotherapy drug only in the vicinity of the targeted site upon mechanical stimulation provided by US. They showed good effects both in vitro and in vivo, which are reviewed in [284], suggesting that there is synergism between US stimulation and administration of loaded micelle: in fact micelles protect cells from free drug counter effects while US mediates the release as well as the increase of cellular uptake. In our case we are focusing on a class of material which show great promise: POx exhibit stealth behaviour[295, 296] and have been found to be non-toxic both *in vitro*[297, 298] and *in vivo*[299, 300]. They are stable in vivo, they are excreted unchanged in urine with no accumulation, they do not show immunogenicity in animal models and there

no known anti-POx antibodies in human population.[343] Moreover a clinical study is ongoing on SER-214 is a poly (2-ethyl-2oxazoline) polymer conjugate of rotigotine, a potent dopamine agonist that has high affinity for the subclass of dopamine receptors in the brain that mediate dopamine signaling, for the treatment of early, stable or untreated Parkinson's disease and are still experiencing motor fluctuations (https://clinicaltrials.gov/ct2/show/NCT02579473). Considering the loading of dexamethasone, a glucocorticoid, that is used in the clinics as anti-inflammatory and immunosuppressive agent, we showed in Figure 69 that the loding capacitiy achieved by our POx micelles are higher than the one proposed in the literature. As a matter of fact these nanostructures could even be included in matrix for anti-inflammatory purposes such as hydrogels[172].

***In summary***

At present, most of the US-mediated release systems are designed for delivery of anticancer drugs.[284] In this work, we analyzed POx-based micelles loaded by dexamethasone, a glucocorticoid, that is used in the clinics as anti-inflammatory and immunosuppressive agent. The action of this drug can be relevant for several biomedical applications: dexamethasone-loaded micelles administered systemically in the bloodstream have demonstrated an effective antitumor activity[344] but have been also used for the treatment of rheumatoid arthritis[345], ocular diseases[346] and other pathologies dealing with inflammatory states. In this context, the responsiveness of POx micelles to ultrasound, with the ability of tuning their release kinetics at short time-points may have a high clinical relevance, as previously discussed. Further biomedical applications can be devised: the implant of neural interfaces, for example, allows to connect the patient's nervous system with an external device, such as a prosthesis.[81] However as already mentioned in previous Sections, the long-term stability and efficacy of neural interfaces is hampered by inflammatory and fibrotic events.[150] Thus, a technology allowing a precise modulation of Dex release, enhanced through the US waves, would allow to tune/minimize such undesired body reactions. This would be beneficial, in general, for modulating the fibrotic reactions to

implanted artificial organs[347], biomaterials[348] and other medical devices. In these domains, in which there is the need of a temporized drug delivery for several days or weeks, plain POx micelles could be hardly used, but they could be combined with additional elements, further modulating (*e.g.* slowing down) the release rate, for example matrices based on properly designed hydrogels, encapsulating the micelles.

# 4. General discussion and conclusion

Whenever a "natural" component, comes in contact with an artificial one, it generates a bio/non-bio interface, leading to a mutual action of one component on the other. This determines various effects, sometimes undesired ones. Whether it is a human-machine collaboration, or a biomedical device in the human body, as well as a neural interface, in all these "hybrid" conditions there is a profound synergy and interaction between different and heterogeneous elements. This allows, for example, a damaged body to restore its vital function, an amputee to be able to fill again a glass of water, a worker to carry out his task more safely and easily, a surgeon to remotely operate in a mini-invasive way. These are just some of the examples that can be reported. Models of such heterogeneous interactions can be found especially in the biomedical field, in which there is a growing need to replace and repair soft and hard tissues or even entire organs, as well as to develop advanced therapeutic strategies for age-related chronic illnesses.

As already stated, biomaterials and medical devices undoubtedly improve the quality of life of an increasing number of people each year and one of the key factors in their success is their ability to optimize the so called “bio/non-bio interfaces”. Hence these interfaces are crucial for a considerable number of applications, in fields such as implantable biomedical devices, biomechatronics, tissue engineering and regenerative medicine, involving multi-disciplinary knowledge between life science, biomedical engineering, biomaterial science, biotechnology.

In the introduction we attempted to classify bio/non-bio interfaces, following the scheme proposed by Dhowre *et al.*[5]. We identified the three main players in a bio/non-bio interface that are (1) the biological component the material is in contact with, (2) the man-made material/biomaterial and (3) the external environment/stimuli. We also stated that the role each component plays, determines the interfaces classification, and that each component must be deeply studied in order to design and optimize their interaction.

For this purpose, we have presented in this thesis work an attempt to face different aspects of bio/non-bio interfaces, with the scope to find novel solutions going beyond the state-of-the-art. In particular, the thesis contributes to the fields of neural interfaces, bio-hybrid tactile sensors, triggerable drug delivery system and remote cell/tissue stimulation by means of ultrasound.

The possibility to exploit bio/non-bio interfaces for sensing applications from biological components, and the fact that such sensing properties can be combined with responsive ones so to achieve a desired body response, have been faced. Concerning sensing bio-interfaces, a bio-hybrid mechanotransduction system has been presented. The developed system and its preliminary experimental evaluation demonstrated the possibility to integrate Madin Darby Canine Kidney cells as the core sensing element of a bio-hybrid mechanotransduction system. The novel technology presented in this study integrates fluidic filling material and living cellular transducers with promising future applications in prosthetics and other bio-applied domains, envisioning an always deeper interrelation between artifacts and biocomponents. This would allow to fully exploit the intriguing advantages of the bio-hybrid paradigm with respect to synthetic ones, such as intrinsic compliance and self-healing capabilities. Derived from this technology, we developed a fluidic mechanotransducer that exploits measurement of electrochemical impedance changes due to mechanical stimulation, following the recent trend of creating flexible force sensors by using non toxic filling material, such as deionised water and PBS. This system is far away from being considered a fully functioning force sensor, but can be used as a platform for the test of different filling materials and their application for electrochemical impedance based force sensing.

Moreover the M2Neural project concept was explained with the aim to obtain an advanced coating for bi-directional responsive peripheral nerve interface. Although the complete multifunctional coating, targeted by the project, was not achieved in this thesis work, several strategies has been developed to face the different requirements regarding low stiffness, ultrasound external stimulation and a possible way to achieve controlled release of anti-inflammatory factors, that will be discussed below.

In fact, we mentioned that bio/non-bio interfaces are often exploited to achieve a targeted body response or bioeffects thanks to a proper stimulation. This direct stimulation of biological components can be provided with particular physical and chemical surface properties. This issue was faced with the *in vitro* characterization of novel soft coatings for polyimide substrate, based on zwitterionic hydrogels that showed non-biofouling properties and low stiffness, approaching the one of nervous tissues. Due to their biocompatibility, flexibility and patternability with lithographic and dry etching techniques, polyimides (PI) are widely used both as implant encapsulation materials and as substrates for implanted neural interfaces. Despite these promising properties, they cannot prevent the formation of a fibrotic capsule. As already stated, it has been shown that the undesired host response to implants is also determined by the mechanical mismatch between the implant and the surrounding tissue. Hence we presented a strategy for covalently attaching carboxybetaine polyzwitterionic hydrogel coatings to PI substrates, obtained by means of a photoactivated process. The zwitterionic hydrogel coatings reduced the adhesion of both fibroblasts and macrophages (the main cell types involved in the foreign body response) respect to PI control, showing almost no cytotoxicity and a clear correlation with the hydrogel stiffness. Moreover, the hydrogel layers did not induce macrophages activation, evaluated through the quantification of nitric oxide production, providing good foundation for their possible future application as coatings for neural interfaces.

Then we focused on the study of the bioeffects of one of the most attractive external stimulus, *i.e.* ultrasound, in this case applied to muscle cells, thanks to an *ad hoc* tunable ultrasound platform and an ultrasound transparent cell culture well. In fact skeletal muscle tissue possesses an intrinsic regeneration capability, but this self-repairing property can be seriously impaired. Therapeutic ultrasound and in particular LIPUS themselves show promise. The limitations of previous state-of-the-art evidences, which showed rather incoherent results in terms of LIPUS treatment efficacy on muscle regeneration, were overcome by a systematic *in vitro* investigation of the effects triggered by controlled LIPUS exposures at different frequencies and intensities. Results allowed identification of the most effective parameters to maximize proliferation, which were 3 MHz and 1 W/cm$^2$, and differentiation, which were 1 MHz and 500 mW/cm$^2$. The outcomes of this work support

even more the fact that in a bio/non-bio interface also the external stimulus must be deeply known and studied.

Finally an externally triggered drug release system was presented in order to achieve an indirect stimulation of the biological component. In particular we tested responsiveness of dexamethasone loaded POx micelles to ultrasound. This drug can be relevant for several biomedical applications dealing with inflammatory states. Dexamethasone-loaded micelles administered systemically in the bloodstream have demonstrated an effective antitumor activity[344] but have also been used for the treatment of rheumatoid arthritis[345], ocular diseases[346] and other pathologies. In this context, the responsiveness of POx micelles to ultrasound, with the ability of tuning their release kinetics at short time-points may have a high clinical relevance, as previously discussed. Further biomedical applications can be devised, for example the implant of neural interfaces, where a technology allowing a precise modulation of Dex release, enhanced through the US waves, would allow to tune/minimize such undesired body reactions. This would be beneficial, in general, for modulating the fibrotic reactions to implanted artificial organs[347], biomaterials[348] and other medical devices.

The findings described in this thesis, constitute a promising basis for the development of furtherly evolved interfaces (*e.g.* combining together some of the described technologies), thus to allow, in the future, an ever more deep interaction between the human body/tissues and artificial devices/artifacts. We believe that, although to a minor extent, the different aspects treated in this manuscript tried to overcome some limitations that are presented in the literature, especially referring to the general lack of systematic evaluations (referring to US stimulation, US triggered drug release from different POx micelles, for example). We also have shown that all the components of a bio/non-bio interface play an essential role to obtain a desired biological response and deep investigation must be performed to engineer them.

Moreover, during this research study we realized that a strong interrelation between different background and knowhow must be achieved, collaborating also with several research groups in order to obtain consistent results in the bio/non-bio interface field.

# Scientific production

## *Papers published on ISI Journals*

**Salgarella A.R.**, Cafarelli A.., Ricotti L., Capineri L., Dario P., Menciassi A. (2017). "Optimal Ultrasound Exposure Conditions for Maximizing C2C12 Muscle Cell Proliferation and Differentiation". Ultrasound in Medicine & Biology, 43(7), pp.1452-1465.

**Salgarella A.R.**, Giudetti G., Ricotti L., Camboni D., Puleo G.L., Ruini F., Tonda-Turo C., Chiono V., Ciardelli G., Micera S., Menciassi A., Oddo C.M. (2015). "A bio-hybrid mechanotransduction system based on ciliate cells". Microelectronic Engineering, 144, pp.51-56.

Russo L.O., Airò Farulla G., Pianu D., **Salgarella A.R.**, Controzzi M., Cipriani C., Oddo C.M., Geraci C., Rosa S., Indaco M. (2015). "PARLOMA - A Novel Human-Robot Interaction System for Deaf-blind Remote Communication". International Journal Of Advanced Robotic Systems, ISSN 1729-8806.

## *Papers submitted to ISI Journals*

Treľova D.#, **Salgarella A.R.#**, Ricotti L., Giudetti G., Cutrone A., Šrámková P., Zahoranová A., Chorvát Jr. D., Haško D., Canale C., Micera S., Kronek J., Menciassi A., Lacík I. "Soft hydrogel zwitterionic coatings minimize fibroblast and macrophage adhesion on polyimide substrates" submitted to ACS Langmuir (8$^{th}$ March 2018, accepted after major revision).

**Salgarella A.R.#**, Zahoranová A.#, Šrámková P., Majerčíková M., Luxenhofer R., Kronek J., Lacík I., Ricotti L. "Investigation of drug release modulation from poly(2-oxazoline) micelles through ultrasound" submitted to Scientific Reports (20$^{th}$ March 2018, resubmitted after major revisions 1$^{st}$ June 2018).

# *Conference Abstracts*

Ricotti L., Cafarelli A., Vannozzi L., **Salgarella A.R.**, Menciassi A. (2018). "Ultrasound-responsive nanomaterials for biomedical applications" in 3rd International Symposium on Nanoparticles/Nanomaterials and Applications (ISN$^2$A 2018).

**Salgarella A.R.**, Šrámková P., Zahoranová A., Kronek J., Menciassi A., Lacík I., Ricotti L. (2017). "Ultrasound-mediated drug release from micelles based on poly(2-oxazoline) terpolymers and triblock copolymer", in 28th Annual Meeting of the European Society for Biomaterials (ESB 2017).

Zahoranová A., Treľová D. **Salgarella A.R.**, Ricotti L., Giudetti G., Cutrone A:, Šramková P., Chorvát Jr. D., Haško D., Canale C., Micera S., Kronek J., Menciassi A., Lacík I. (2017). "Soft and non-fouling polyzwitterionic coatings for neural interfaces", in Danube Vltava Sava Polymer Meeting (DVSPM 2017).

Genchi G.G., **Salgarella A.R.**, Pezzini I., Marino A., Ciofani G. (2017). "Cerium Oxide Nanoparticles For Skeletal Muscle Cell Protection Against Oxidative Stress In Space", in 68th International Astronautical Congress (IAC 2017).

Ricotti L., Di Cioccio I., **Salgarella A.R.**, Cafarelli A., Losi P., Barsotti M.C., Foffa I., Dario P., Menciassi A., Soldani G. (2017). "Nanocomposite small diameter vascular graft stimulated by ultrasound waves" in Material Research Society Fall Meeting & Exhibit 2017 (MRS 2017).

**Salgarella A.R.**, Ricotti L., Giudetti G., Kronek J., Righi M., Cutrone A., Cafarelli A., Zahoranová A., Šramková P., Treľová D., Bossi S., Micera S., Lacík I., Menciassi A. (2015). “Advanced nano-doped materials for long-term neural interfaces”, in IEEE 15th International Conference on Nanotechnologies (IEEE Nano 2015).

# References


1. BCC Research group. Medical Devices: Technologies and Global Markets, 2017.

2. Markets and Markets. Biomaterials Market by Type of Materials (Metallic, Ceramic, Polymers, Natural) & Application (Cardiovascular, Orthopedic, Dental, Plastic Surgery, Wound Healing, Neurology, Tissue Engineering, Ophthalmology) - Global Forecast to 2021, 2017.

3. Wilson CJ, Clegg RE, Leavesley DI, Pearcy MJ. Mediation of biomaterial–cell interactions by adsorbed proteins: a review. *Tissue Eng* 2005; **11**(1-2): 1-18.

4. Custódio CA, Reis RL, Mano JF. Engineering biomolecular microenvironments for cell instructive biomaterials. *Advanced healthcare materials* 2014; **3**(6): 797-810.

5. Dhowre HS, Rajput S, Russell NA, Zelzer M. Responsive cell–material interfaces. *Nanomedicine* 2015; **10**(5): 849-71.

6. Chapekar MS. Tissue engineering: challenges and opportunities. *Journal of Biomedical Materials Research Part A* 2000; **53**(6): 617-20.

7. Cheung H-Y, Lau K-T, Lu T-P, Hui D. A critical review on polymer-based bio-engineered materials for scaffold development. *Composites Part B: Engineering* 2007; **38**(3): 291-300.

8. Langer R, Vacanti JP. Tissue engineering. *Science* 1993; **260**(5110): 920-6.

9. Genchi GG, Marino A, Tapeinos C, Ciofani G. Smart materials meet multifunctional biomedical devices: Current and prospective implications for nanomedicine. *Frontiers in Bioengineering and Biotechnology* 2017; **5**: 80.

10. Xia F, Jiang L. Bio-inspired, smart, multiscale interfacial materials. *Adv Mater* 2008; **20**(15): 2842-58.

11. Holzapfel BM, Reichert JC, Schantz J-T, et al. How smart do biomaterials need to be? A translational science and clinical point of view. *Adv Drug Del Rev* 2013; **65**(4): 581-603.

12. Hench LL. Biomaterials: a forecast for the future. *Biomaterials* 1998; **19**(16): 1419-23.

13. Hench LL, Thompson I. Twenty-first century challenges for biomaterials. *Journal of The Royal Society Interface* 2010; **7**(Suppl 4): S379-S91.

14. Hench LL. Bioactive materials: the potential for tissue regeneration. *Journal of Biomedical Materials Research Part A* 1998; **41**(4): 511-8.

15. Orme C, Noy A, Wierzbicki A, et al. Formation of chiral morphologies through selective binding of amino acids to calcite surface steps. *Nature* 2001; **411**(6839): 775-9.

16. Hosoda N, Kato T. Thin-film formation of calcium carbonate crystals: effects of functional groups of matrix polymers. *Chem Mater* 2001; **13**(2): 688-93.

17. Niemeyer CM. Nanoparticles, proteins, and nucleic acids: biotechnology meets materials science. *Angew Chem Int Ed* 2001; **40**(22): 4128-58.

18. Tomsia AP, Saiz E, Song J, Bertozzi CR. Biomimetic bonelike composites and novel bioactive glass coatings. *Adv Eng Mater* 2005; **7**(11): 999-1004.

19. Lu Y, Liu J. Smart nanomaterials inspired by biology: dynamic assembly of error-free nanomaterials in response to multiple chemical and biological stimuli. *Acc Chem Res* 2007; **40**(5): 315-23.

20. Kinbara K, Aida T. Toward intelligent molecular machines: directed motions of biological and artificial molecules and assemblies. *Chem Rev* 2005; **105**(4): 1377-400.

21. Service R. Bioelectronics. The cyborg era begins. *Science (New York, NY)* 2013; **340**(6137): 1162.

22. Nguyen TD, Timko BP. Bionics in Tissue Engineering. *Tissue Engineering for Artificial Organs: Regenerative Medicine, Smart Diagnostics and Personalized Medicine* 2017: 677-99.

23. Wei Q, He J, Zhao W, Chen Y. Functional Polymers for Biointerface Engineering. *International Journal of Polymer Science* 2017; **2017**.

24. Hackett AJ, Malmström J, Travas-Sejdic J. FUNCTIONALIZATION OF CONDUCTING POLYMERS FOR BIOINTERFACE APPLICATIONS. *Progress in Polymer Science* 2017.

25. Kiick KL. Materials science. Polymer therapeutics. *Science (New York, NY)* 2007; **317**(5842): 1182.

26. Wang C, Dong L. Exploring 'new'bioactivities of polymers at the nano–bio interface. *Trends Biotechnol* 2015; **33**(1): 10-4.

27. Hench L. Biomaterials. *Science* 1980; **208**(4446): 826-31.

28. Ventre M, Causa F, Netti PA. Determinants of cell–material crosstalk at the interface: towards engineering of cell instructive materials. *Journal of the Royal Society Interface* 2012: rsif20120308.

29. Ratner BD, Bryant SJ. Biomaterials: where we have been and where we are going. *Annu Rev Biomed Eng* 2004; **6**: 41-75.

30. Daley WP, Peters SB, Larsen M. Extracellular matrix dynamics in development and regenerative medicine. *J Cell Sci* 2008; **121**(3): 255-64.

31. Cavalcanti-Adam EA, Volberg T, Micoulet A, Kessler H, Geiger B, Spatz JP. Cell spreading and focal adhesion dynamics are regulated by spacing of integrin ligands. *Biophys J* 2007; **92**(8): 2964-74.

32. Santos E, Orive G, Hernández RM, Pedraz JL. Cell-biomaterial interaction: strategies to mimic the extracellular matrix. On Biomimetics: InTech; 2011.

33. Nagase H, Visse R, Murphy G. Structure and function of matrix metalloproteinases and TIMPs. *Cardiovasc Res* 2006; **69**(3): 562-73.

34. Frantz C, Stewart KM, Weaver VM. The extracellular matrix at a glance. *J Cell Sci* 2010; **123**(24): 4195-200.

35. Gutowski SM, Shoemaker JT, Templeman KL, et al. Protease-degradable PEG-maleimide coating with on-demand release of IL-1Ra to improve tissue response to neural electrodes. *Biomaterials* 2015; **44**: 55-70.

36. Tang L, Thevenot P, Hu W. Surface chemistry influences implant biocompatibility. *Curr Top Med Chem* 2008; **8**(4): 270-80.

37. Roach P, Farrar D, Perry CC. Surface tailoring for controlled protein adsorption: effect of topography at the nanometer scale and chemistry. *J Am Chem Soc* 2006; **128**(12): 3939-45.

38. Zelzer M, Majani R, Bradley JW, Rose FR, Davies MC, Alexander MR. Investigation of cell–surface interactions using chemical gradients formed from plasma polymers. *Biomaterials* 2008; **29**(2): 172-84.

39. Murphy WL, McDevitt TC, Engler AJ. Materials as stem cell regulators. *Nature materials* 2014; **13**(6): 547-57.

40. Chan A, Orme RP, Fricker RA, Roach P. Remote and local control of stimuli responsive materials for therapeutic applications. *Adv Drug Del Rev* 2013; **65**(4): 497-514.

41. Mendes PM. Cellular nanotechnology: making biological interfaces smarter. *Chem Soc Rev* 2013; **42**(24): 9207-18.

42. Mendes PM. Stimuli-responsive surfaces for bio-applications. *Chem Soc Rev* 2008; **37**(11): 2512-29.

43. Auernheimer J, Dahmen C, Hersel U, Bausch A, Kessler H. Photoswitched cell adhesion on surfaces with RGD peptides. *J Am Chem Soc* 2005; **127**(46): 16107-10.

44. Gong Y-H, Li C, Yang J, Wang H-Y, Zhuo R-X, Zhang X-Z. Photoresponsive “smart template” via host–guest interaction for reversible cell adhesion. *Macromolecules* 2011; **44**(19): 7499-502.

45. Liu D, Xie Y, Shao H, Jiang X. Using Azobenzene-Embedded Self-Assembled Monolayers To Photochemically Control Cell Adhesion Reversibly. *Angew Chem Int Ed* 2009; **48**(24): 4406-8.

46. Pranzetti A, Mieszkin S, Iqbal P, et al. An Electrically Reversible Switchable Surface to Control and Study Early Bacterial Adhesion Dynamics in Real-Time. *Adv Mater* 2013; **25**(15): 2181-5.

47. Yeung CL, Iqbal P, Allan M, Lashkor M, Preece JA, Mendes PM. Tuning Specific Biomolecular Interactions Using Electro-Switchable Oligopeptide Surfaces. *Adv Funct Mater* 2010; **20**(16): 2657-63.

48. Ng CCA, Magenau A, Ngalim SH, et al. Using an electrical potential to reversibly switch surfaces between two states for dynamically controlling cell adhesion. *Angew Chem Int Ed* 2012; **51**(31): 7706-10.

49. Yeo W-S, Mrksich M. Electroactive self-assembled monolayers that permit orthogonal control over the adhesion of cells to patterned substrates. *Langmuir* 2006; **22**(25): 10816-20.

50. Yeo W-S, Yousaf MN, Mrksich M. Dynamic interfaces between cells and surfaces: electroactive substrates that sequentially release and attach cells. *J Am Chem Soc* 2003; **125**(49): 14994-5.

51. Yousaf MN, Houseman BT, Mrksich M. Turning on cell migration with electroactive substrates. *Angew Chem* 2001; **113**(6): 1127-30.

52. Zarzar LD, Kim P, Kolle M, Brinker CJ, Aizenberg J, Kaehr B. Direct Writing and Actuation of Three-Dimensionally Patterned Hydrogel Pads on Micropillar Supports. *Angew Chem Int Ed* 2011; **50**(40): 9356-60.

53. Xia F, Feng L, Wang S, et al. Dual-Responsive Surfaces That Switch between Superhydrophilicity and Superhydrophobicity. *Adv Mater* 2006; **18**(4): 432-6.

54. Rahane SB, Floyd JA, Metters AT, Kilbey SM. Swelling Behavior of Multiresponsive Poly (methacrylic acid)-block--poly (N-isopropylacrylamide) Brushes Synthesized Using

Surface-Initiated Photoiniferter-Mediated Photopolymerization. *Adv Funct Mater* 2008; **18**(8): 1232-40.

55. Ward MA, Georgiou TK. Thermoresponsive polymers for biomedical applications. *Polymers* 2011; **3**(3): 1215-42.

56. Tekin H, Sanchez JG, Tsinman T, Langer R, Khademhosseini A. Thermoresponsive platforms for tissue engineering and regenerative medicine. *AICHE J* 2011; **57**(12): 3249-58.

57. Rimmer S, Soutar I, Swanson L. Switching the conformational behaviour of poly (N-isopropyl acrylamide). *Polym Int* 2009; **58**(3): 273-8.

58. Ionov L. Hydrogel-based actuators: possibilities and limitations. *Mater Today* 2014; **17**(10): 494-503.

59. Fuhrer R, Hofmann S, Hild N, et al. Pressureless mechanical induction of stem cell differentiation is dose and frequency dependent. *PLoS One* 2013; **8**(11): e81362.

60. Mertz D, Vogt C, Hemmerlé J, et al. Mechanotransductive surfaces for reversible biocatalysis activation. *Nature materials* 2009; **8**(9): 731-5.

61. Lam MT, Clem WC, Takayama S. Reversible on-demand cell alignment using reconfigurable microtopography. *Biomaterials* 2008; **29**(11): 1705-12.

62. Marino A, Genchi GG, Sinibaldi E, Ciofani G. Piezoelectric Effects of Materials on Biointerfaces. *ACS Applied Materials & Interfaces* 2017.

63. Wilson GS, Gifford R. Biosensors for real-time in vivo measurements. *Biosensors Bioelectron* 2005; **20**(12): 2388-403.

64. Vaddiraju S, Tomazos I, Burgess DJ, Jain FC, Papadimitrakopoulos F. Emerging synergy between nanotechnology and implantable biosensors: a review. *Biosensors Bioelectron* 2010; **25**(7): 1553-65.

65. Siontorou CG, Nikoleli G-PD, Nikolelis DP, Karapetis S, Tzamtzis N, Bratakou S. Point-of-Care and Implantable Biosensors in Cancer Research and Diagnosis. Next Generation Point-of-care Biomedical Sensors Technologies for Cancer Diagnosis: Springer; 2017: 115-32.

66. de Puig H, Bosch I, Gehrke L, Hamad-Schifferli K. Challenges of the Nano–Bio Interface in Lateral Flow and Dipstick Immunoassays. *Trends Biotechnol* 2017.

67. Fu YQ, Luo J, Nguyen N-T, et al. Advances in piezoelectric thin films for acoustic biosensors, acoustofluidics and lab-on-chip applications. *Prog Mater Sci* 2017.

68. Zhang Y, Wang X, Pong M, Chen L, Ye Z. Application of Bioreactor in Stem Cell Culture. *Journal of Biomedical Science and Engineering* 2017; **10**(11): 485.

69. Greenman J. Looking to the future of organs-on-chip. Future Science; 2017.

70. Luni C, Serena E, Elvassore N. Human-on-chip for therapy development and fundamental science. *Curr Opin Biotechnol* 2014; **25**: 45-50.

71. Beißner N, Lorenz T, Reichl S. Organ on chip. Microsystems for Pharmatechnology: Springer; 2016: 299-339.

72. Wellman SM, Eles JR, Ludwig KA, et al. A materials roadmap to functional neural interface design. *Adv Funct Mater* 2017.

73. Cheneler D, Buselli E, Camboni D, et al. A Bio-Hybrid Tactile Sensor Incorporating Living Artificial Skin and an Impedance Sensing Array. *Sensors* 2014; **14**(12): 23781-802.

74. Tibbitt MW, Langer R. Living Biomaterials. *Acc Chem Res* 2017; **50**(3): 508-13.

75. Salinas CN, Anseth KS. The enhancement of chondrogenic differentiation of human mesenchymal stem cells by enzymatically regulated RGD functionalities. *Biomaterials* 2008; **29**(15): 2370-7.

76. Yu J, Zhang Y, Ye Y, et al. Microneedle-array patches loaded with hypoxia-sensitive vesicles provide fast glucose-responsive insulin delivery. *Proceedings of the National Academy of Sciences* 2015; **112**(27): 8260-5.

77. Chortos A, Liu J, Bao Z. Pursuing prosthetic electronic skin. *Nature materials* 2016.

78. Adamala K, Szostak JW. Nonenzymatic template-directed RNA synthesis inside model protocells. *Science* 2013; **342**(6162): 1098-100.

79. Ricotti L, Menciassi A, Morishima K. Guest editorial introduction to the Special Issue on bio-hybrid systems and living machines. *Biomed Microdevices* 2012: 1-3.

80. Ricotti L, Menciassi A. Bio-hybrid muscle cell-based actuators. *Biomed Microdevices* 2012; **14**(6): 987-98.

81. Raspopovic S, Capogrosso M, Petrini FM, et al. Restoring Natural Sensory Feedback in Real-Time Bidirectional Hand Prostheses. *Science Translational Medicine* 2014; **6**(222): 222ra19.

82. Dahiya RS, Metta G, Valle M, Sandini G. Tactile Sensing: From Humans to Humanoids. *IEEE Transactions on Robotics* 2010; **26**(1): 1-20.

83. Lucarotti C, Oddo CM, Vitiello N, Carrozza MC. Synthetic and bio-artificial tactile sensing: A review. *Sensors* 2013; **13**(2): 1435-66.

84. Tiwana MI, Redmond SJ, Lovell NH. A review of tactile sensing technologies with applications in biomedical engineering. *Sensor Actuat a-Phys* 2012; **179**: 17-31.

85. Tran R, Dey J, Gyawali D, et al. Biodegradable elastomeric polymers and MEMS in tissue engineering. Pan Stanford Publishing Pte Ltd.: Singapore, Singapore; 2010. p. 1-32.

86. Muhammad HB, Hunt NC, Shelton RM, et al. Incorporation of Novel MEMS Tactile Sensors into Tissue Engineered Skin. Bioinformatics and Biomedical Engineering (iCBBE), 2010 4th International Conference on; 2010 18-20 June 2010; 2010. p. 1-4.

87. Cheneler D, Ward M, Anthony C. Bio-hybrid tactile sensor for the study of the role of mechanoreceptors in human tactile perception. *Microelectron Eng* 2012; **97**: 297-300.

88. Cheneler D, Buselli E, Oddo C, et al. Bio-hybrid tactile sensor and experimental set-up for investigating and mimicking the human sense of touch. *HRI 2012* 2012.

89. Adamatzky A. Slime mould tactile sensor. *Sensors Actuators B: Chem* 2013; **188**: 38-44.

90. Ingber DE. Cellular mechanotransduction: putting all the pieces together again. *The FASEB journal* 2006; **20**(7): 811-27.

91. Salgarella AR, Giudetti G, Ricotti L, et al. A bio-hybrid mechanotransduction system based on ciliate cells. *Microelectron Eng* 2015; **144**: 51-6.

92. Praetorius H, Spring KR. Bending the MDCK cell primary cilium increases intracellular calcium. *The Journal of membrane biology* 2001; **184**(1): 71-9.

93. Prasad RM, Jin X, Nauli SM. Sensing a Sensor: Identifying the Mechanosensory Function of Primary Cilia. *Biosensors* 2014; **4**(1): 47-62.

94. Praetorius H, Frøkiær J, Leipziger J. Transepithelial pressure pulses induce nucleotide release in polarized MDCK cells. *American Journal of Physiology-Renal Physiology* 2005; **288**(1): F133-F41.

95. Rodat-Despoix L, Hao J, Dandonneau M, Delmas P. Shear stress-induced Ca2+ mobilization in MDCK cells is ATP dependent, no matter the primary cilium. *Cell Calcium* 2013; **53**(5-6): 327-37.

96. Praetorius H, Leipziger J. Released nucleotides amplify the cilium-dependent, flow-induced [Ca2+] i response in MDCK cells. *Acta physiologica* 2009; **197**(3): 241-51.

97. Praetorius HA. The primary cilium as sensor of fluid flow: new building blocks to the model. A review in the theme: cell signaling: proteins, pathways and mechanisms. *American Journal of Physiology-Cell Physiology* 2014; **308**(3): C198-C208.

98. Delling M, Indzhykulian A, Liu X, et al. Primary cilia are not calcium-responsive mechanosensors. *Nature* 2016; **531**(7596): 656.

99. Delling M, DeCaen PG, Doerner JF, Febvay S, Clapham DE. Primary cilia are specialized calcium signalling organelles. *Nature* 2013; **504**(7479): 311.

100. Patel A. The primary cilium calcium channels and their role in flow sensing. *Pflügers Archiv-European Journal of Physiology* 2015; **467**(1): 157-65.

101. Delmas P, Nauli SM, Li X, et al. Gating of the polycystin ion channel signaling complex in neurons and kidney cells. *The FASEB journal* 2004; **18**(6): 740-2.

102. Dukes JD, Whitley P, Chalmers AD. The MDCK variety pack: choosing the right strain. *BMC Cell Biol* 2011; **12**(1): 43.

103. Tonda-Turo C, Gnavi S, Ruini F, et al. Development and characterization of novel agar and gelatin injectable hydrogel as filler for peripheral nerve guidance channels. *Journal of Tissue Engineering and Regenerative Medicine* 2014.

104. Pearce TM, Wilson JA, Oakes SG, Chiu S-Y, Williams JC. Integrated microelectrode array and microfluidics for temperature clamp of sensory neurons in culture. *Lab on a Chip* 2005; **5**(1): 97-101.

105. El-Ali J, Sorger PK, Jensen KF. Cells on chips. *Nature* 2006; **442**(7101): 403-11.

106. Gnavi S, di Blasio L, Tonda-Turo C, et al. Gelatin-based hydrogel for vascular endothelial growth factor release in peripheral nerve tissue engineering. *Journal of tissue engineering and regenerative medicine* 2014.

107. Liang X, Boppart SA. Biomechanical properties of in vivo human skin from dynamic optical coherence elastography. *Biomedical Engineering, IEEE Transactions on* 2010; **57**(4): 953-9.

108. Szulcek R, Bogaard HJ, van Nieuw Amerongen GP. Electric cell-substrate impedance sensing for the quantification of endothelial proliferation, barrier function, and motility. *Journal of visualized experiments: JoVE* 2014; (85).

109. Ghosh PM, Keese CR, Giaever I. Morphological response of mammalian cells to pulsed ac fields. *Bioelectrochem Bioenerget* 1994; **33**(2): 121-33.

110. Grinsted A, Moore JC, Jevrejeva S. Application of the cross wavelet transform and wavelet coherence to geophysical time series. *Nonlinear processes in geophysics* 2004; **11**(5/6): 561-6.

111. Yousef H, Boukallel M, Althoefer K. Tactile sensing for dexterous in-hand manipulation in robotics—A review. *Sensor Actuat a-Phys* 2011; **167**(2): 171-87.

112. Li H, Lai F, Luo R. Analysis of responsive characteristics of ionic-strength-sensitive hydrogel with consideration of effect of equilibrium constant by a chemo-electro-mechanical model. *Langmuir* 2009; **25**(22): 13142-50.

113. Wettels N, Santos VJ, Johansson RS, Loeb GE. Biomimetic Tactile Sensor Array. *Adv Robot* 2008; **22**(8): 829-49.

114. Fishel JA, Loeb GE. Bayesian exploration for intelligent identification of textures. *Frontiers in neurorobotics* 2012; **6**: 1-20.

115. Park Y-L, Majidi C, Kramer R, Bérard P, Wood RJ. Hyperelastic pressure sensing with a liquid-embedded elastomer. *Journal of Micromechanics and Microengineering* 2010; **20**(12): 125029.

116. Yin J, Santos VJ, Posner JD. Bioinspired flexible microfluidic shear force sensor skin. *Sensors and Actuators A: Physical* 2017; **264**: 289-97.

117. Wong RDP, Posner JD, Santos VJ. Flexible microfluidic normal force sensor skin for tactile feedback. *Sensors and Actuators A: Physical* 2012; **179**: 62-9.

118. Gao Y, Ota H, Schaler EW, et al. Wearable Microfluidic Diaphragm Pressure Sensor for Health and Tactile Touch Monitoring. *Adv Mater* 2017; **29**(39).

119. Fishel JA, Loeb GE. Sensing tactile microvibrations with the BioTac—Comparison with human sensitivity. Biomedical Robotics and Biomechatronics (BioRob), 2012 4th IEEE RAS & EMBS International Conference on; 2012: IEEE; 2012. p. 1122-7.

120. Nie B, Li R, Brandt JD, Pan T. Microfluidic tactile sensors for three-dimensional contact force measurements. *Lab on a Chip* 2014; **14**(22): 4344-53.

121. Eltaib M, Hewit J. Tactile sensing technology for minimal access surgery—a review. *Mechatronics* 2003; **13**(10): 1163-77.

122. Weiland JD, Liu W, Humayun MS. Retinal prosthesis. *Annu Rev Biomed Eng* 2005; **7**: 361-401.

123. Berger TW, Glanzman D. Toward replacement parts for the brain: implantable biomimetic electronics as neural prostheses: MIT Press; 2005.

124. Han L, Noble JA, Burcher M. A novel ultrasound indentation system for measuring biomechanical properties of in vivo soft tissue. *Ultrasound Med Biol* 2003; **29**(6): 813-23.

125. Gutierrez CA, Meng E. Impedance-based force transduction within fluid-filled parylene microstructures. *Journal of Microelectromechanical Systems* 2011; **20**(5): 1098-108.

126. Gutierrez C, Meng E. A dual function Parylene-based biomimetic tactile sensor and actuator for next generation mechanically responsive microelectrode arrays. Solid-State Sensors, Actuators and Microsystems Conference, 2009 TRANSDUCERS 2009 International; 2009: IEEE; 2009. p. 2194-7.

127. Gutierrez CA, Meng E. A subnanowatt microbubble pressure sensor based on electrochemical impedance transduction in a flexible all-parylene package. Micro Electro Mechanical Systems (MEMS), 2011 IEEE 24th International Conference on; 2011: IEEE; 2011. p. 549-52.

128. Rockwood DN, Preda RC, Yücel T, Wang X, Lovett ML, Kaplan DL. Materials fabrication from Bombyx mori silk fibroin. *Nat Protoc* 2011; **6**(10): 1612.

129. Yucel T, Cebe P, Kaplan DL. Vortex-induced injectable silk fibroin hydrogels. *Biophys J* 2009; **97**(7): 2044-50.

130. Dargahi J, Najarian S, Liu B. Sensitivity analysis of a novel tactile probe for measurement of tissue softness with applications in biomedical robotics. *J Mater Process Technol* 2007; **183**(2-3): 176-82.

131. Cavuoto J. The market for neurotechnology. *Journal of Medical Marketing* 2002; **2**(3): 263-74.

132. Neurotech Reports. The Market for Neurotechnology: 2016-2020, 2016.

133. SharpBrains. Market Report on Pervasive Neurotechnology: A Groundbreaking Analysis of 10,000+ Patent Filings Transforming Medicine, Health, Entertainment and Business. California, USA; 2015.

134. Lago N, Yoshida K, Koch KP, Navarro X. Assessment of biocompatibility of chronically implanted polyimide and platinum intrafascicular electrodes. *Biomedical Engineering, IEEE Transactions on* 2007; **54**(2): 281-90.

135. Grill WM, Norman SE, Bellamkonda RV. Implanted neural interfaces: biochallenges and engineered solutions. *Annu Rev Biomed Eng* 2009; **11**: 1-24.

136. Hilborn J, Bjursten LM. A new and evolving paradigm for biocompatibility. *J Tissue Eng Regen Med* 2007; **1**(2): 110-9.

137. Righi M, Puleo GL, Tonazzini I, Giudetti G, Cecchini M, Micera S. Peptide-based coatings for flexible implantable neural interfaces. *Sci Rep* 2018; **8**(1): 502.

138. Rao SS, Han N, Winter JO. Polylysine-modified PEG-based hydrogels to enhance the neuro–electrode interface. *J Biomater Sci Polym Ed* 2011; **22**(4-6): 611-25.

139. Cutrone A, Del Valle J, Santos D, et al. A three-dimensional self-opening intraneural peripheral interface (SELINE). *Journal of neural engineering* 2015; **12**(1): 016016.

140. Ciofani G, Danti S, D'Alessandro D, et al. Enhancement of neurite outgrowth in neuronal-like cells following boron nitride nanotube-mediated stimulation. *ACS nano* 2010; **4**(10): 6267-77.

141. Marino A, Arai S, Hou Y, et al. Piezoelectric Nanoparticle-Assisted Wireless Neuronal Stimulation. *ACS nano* 2015; **9**(7): 7678-89.

142. Rothschild RM. Neuroengineering tools/applications for bidirectional interfaces, brain–computer interfaces, and neuroprosthetic implants–a review of recent progress. *Front Neuroeng* 2010; **3**: 112.

143. Raspopovic S, Capogrosso M, Petrini FM, et al. Restoring natural sensory feedback in real-time bidirectional hand prostheses. *Sci Transl Med* 2014; **6**(222): 222ra19-ra19.

144. Hochberg LR, Bacher D, Jarosiewicz B, et al. Reach and grasp by people with tetraplegia using a neurally controlled robotic arm. *Nature* 2012; **485**(7398): 372-5.

145. Mercanzini A, Cheung K, Buhl DL, et al. Demonstration of cortical recording using novel flexible polymer neural probes. *Sensors and Actuators A: Physical* 2008; **143**(1): 90-6.

146. Cheung KC, Renaud P, Tanila H, Djupsund K. Flexible polyimide microelectrode array for in vivo recordings and current source density analysis. *Biosensors Bioelectron* 2007; **22**(8): 1783-90.

147. Hollenberg BA, Richards CD, Richards R, Bahr DF, Rector DM. A MEMS fabricated flexible electrode array for recording surface field potentials. *J Neurosci Methods* 2006; **153**(1): 147-53.

148. Birla R. Introduction to Tissue Engineering: Applications and Challenges: U of Nebraska Press; 2013.

149. Onuki Y, Bhardwaj U, Papadimitrakopoulos F, Burgess DJ. A review of the biocompatibility of implantable devices: current challenges to overcome foreign body response. *Journal of diabetes science and technology* 2008; **2**(6): 1003-15.

150. Wurth S, Capogrosso M, Raspopovic S, et al. Long-term usability and bio-integration of polyimide-based intra-neural stimulating electrodes. *Biomaterials* 2017; **122**: 114-29.

151. Grill WM, Mortimer JT. Stability of the input-output properties of chronically implanted multiple contact nerve cuff stimulating electrodes. *IEEE Trans Rehabil Eng* 1998; **6**(4): 364-73.

152. Tyler DJ, Durand DM. A slowly penetrating interfascicular nerve electrode for selective activation of peripheral nerves. *IEEE Trans Rehabil Eng* 1997; **5**(1): 51-61.

153. Lago N, Yoshida K, Koch KP, Navarro X. Assessment of biocompatibility of chronically implanted polyimide and platinum intrafascicular electrodes. *IEEE Trans Biomed Eng* 2007; **54**(2): 281-90.

154. Boretius T, Badia J, Pascual-Font A, et al. A transverse intrafascicular multichannel electrode (TIME) to interface with the peripheral nerve. *Biosensors Bioelectron* 2010; **26**(1): 62-9.

155. Lago N, Ceballos D, Rodríguez FJ, Stieglitz T, Navarro X. Long term assessment of axonal regeneration through polyimide regenerative electrodes to interface the peripheral nerve. *Biomaterials* 2005; **26**(14): 2021-31.

156. Giselbrecht S, Rapp BE, Niemeyer CM. The chemistry of cyborgs—interfacing technical devices with organisms. *Angew Chem Int Ed* 2013; **52**(52): 13942-57.

157. Navarro X, Krueger TB, Lago N, Micera S, Stieglitz T, Dario P. A critical review of interfaces with the peripheral nervous system for the control of neuroprostheses and hybrid bionic systems. *J Peripher Nerv Syst* 2005; **10**(3): 229-58.

158. Fekete Z, Pongrácz A. Multifunctional soft implants to monitor and control neural activity in the central and peripheral nervous system: A review. *Sensors Actuators B: Chem* 2017; **243**: 1214-23.

159. Myllymaa S, Myllymaa K, Korhonen H, Lammi MJ, Tiitu V, Lappalainen R. Surface characterization and in vitro biocompatibility assessment of photosensitive polyimide films. *Colloids Surf B Biointerfaces* 2010; **76**(2): 505-11.

160. Sun Y, Lacour S, Brooks R, Rushton N, Fawcett J, Cameron R. Assessment of the biocompatibility of photosensitive polyimide for implantable medical device use. *Journal of Biomedical Materials Research Part A* 2009; **90**(3): 648-55.

161. Birla R. Introduction to tissue engineering: applications and challenges: John Wiley & Sons; 2014.

162. Rao SS, Winter J. Adhesion molecule-modified biomaterials for neural tissue engineering. *Front Neuroeng* 2009; **2**: 6.

163. Ahmed I, Liu HY, Mamiya PC, et al. Three-dimensional nanofibrillar surfaces covalently modified with tenascin-C-derived peptides enhance neuronal growth in vitro. *Journal of Biomedical Materials Research Part A* 2006; **76**(4): 851-60.

164. Righi M, Bossi S, Puleo G, et al. Surface Modification of Polyimide Thin Films for Peripheral Invasive Neural Interfaces. *J Med Device* 2013; **7**(2): 020937.

165. He W, McConnell GC, Schneider TM, Bellamkonda RV. A novel anti-inflammatory surface for neural electrodes. *Adv Mater* 2007; **19**(21): 3529-33.

166. Straley KS, Heilshorn SC. Design and adsorption of modular engineered proteins to prepare customized, neuron-compatible coatings. *Front Neuroeng* 2009; **2**: 9.

167. Abidian MR, Martin DC. Multifunctional nanobiomaterials for neural interfaces. *Adv Funct Mater* 2009; **19**(4): 573-85.

168. Moxon KA, Kalkhoran NM, Markert M, Sambito MA, McKenzie J, Webster JT. Nanostructured surface modification of ceramic-based microelectrodes to enhance biocompatibility for a direct brain-machine interface. *IEEE Trans Biomed Eng* 2004; **51**(6): 881-9.

169. Moxon K, Hallman S, Aslani A, Kalkhoran N, Lelkes P. Bioactive properties of nanostructured porous silicon for enhancing electrode to neuron interfaces. *J Biomater Sci Polym Ed* 2007; **18**(10): 1263-81.

170. Lu Y, Wang D, Li T, et al. Poly (vinyl alcohol)/poly (acrylic acid) hydrogel coatings for improving electrode–neural tissue interface. *Biomaterials* 2009; **30**(25): 4143-51.

171. Heo D, Song S, Kim H, et al. Multifunctional hydrogel coatings on the surface of implantable cuff electrode for improving electrode-peripheral nerve tissue interfaces. *Acta Biomater* 2016.

172. Kim D-H, Martin DC. Sustained release of dexamethasone from hydrophilic matrices using PLGA nanoparticles for neural drug delivery. *Biomaterials* 2006; **27**(15): 3031-7.

173. Minev IR, Musienko P, Hirsch A, et al. Electronic dura mater for long-term multimodal neural interfaces. *Science* 2015; **347**(6218): 159-63.

174. Lacour SP, Courtine G, Guck J. Materials and technologies for soft implantable neuroprostheses. *Nature Reviews Materials* 2016; **1**: 16063.

175. Blakney AK, Swartzlander MD, Bryant SJ. The effects of substrate stiffness on the in vitro activation of macrophages and in vivo host response to poly (ethylene glycol)-based hydrogels. *Journal of biomedical materials research Part A* 2012; **100**(6): 1375.

176. Okay O. General properties of hydrogels. Hydrogel sensors and actuators: Springer; 2009: 1-14.

177. Park SJ, Lee YJ, Heo DN, et al. Functional nerve cuff electrode with controllable anti-inflammatory drug loading and release by biodegradable nanofibers and hydrogel deposition. *Sensors Actuators B: Chem* 2015; **215**: 133-41.

178. Spencer KC, Sy JC, Ramadi KB, Graybiel AM, Langer R, Cima MJ. Characterization of Mechanically Matched Hydrogel Coatings to Improve the Biocompatibility of Neural Implants. *Sci Rep* 2017; **7**.

179. Barz M, Luxenhofer R, Zentel R, Vicent MJ. Overcoming the PEG-addiction: well-defined alternatives to PEG, from structure-property relationships to better defined therapeutics. *Polymer Chemistry* 2011; **2**(9): 1900-18.

180. Li L, Chen S, Jiang S. Protein interactions with oligo(ethylene glycol) (OEG) self-assembled monolayers: OEG stability, surface packing density and protein adsorption. *J Biomater Sci Polym Ed* 2007; **18**(11): 1415-27.

181. Knop K, Hoogenboom R, Fischer D, Schubert US. Poly(ethylene glycol) in Drug Delivery: Pros and Cons as Well as Potential Alternatives. *Angew Chem Int Ed* 2010; **49**(36): 6288-308.

182. Jiang S, Cao Z. Ultralow-Fouling, Functionalizable, and Hydrolyzable Zwitterionic Materials and Their Derivatives for Biological Applications. *Adv Mater* 2010; **22**(9): 920-32.

183. Chen S, Zheng J, Li L, Jiang S. Strong Resistance of Phosphorylcholine Self-Assembled Monolayers to Protein Adsorption: Insights into Nonfouling Properties of Zwitterionic Materials. *J Am Chem Soc* 2005; **127**(41): 14473-8.

184. Sin M-C, Chen S-H, Chang Y. Hemocompatibility of zwitterionic interfaces and membranes. *Polym J* 2014; **46**(8): 436-43.

185. Shao Q, He Y, White AD, Jiang S. Difference in Hydration between Carboxybetaine and Sulfobetaine. *The Journal of Physical Chemistry B* 2010; **114**(49): 16625-31.

186. Wu J, Lin W, Wang Z, Chen S, Chang Y. Investigation of the hydration of nonfouling material poly(sulfobetaine methacrylate) by low-field nuclear magnetic resonance. *Langmuir* 2012; **28**(19): 7436-41.

187. Liu P, Huang T, Liu P, et al. Zwitterionic modification of polyurethane membranes for enhancing the anti-fouling property. *J Colloid Interface Sci* 2016; **480**: 91-101.

188. Chien HW, Cheng PH, Chen SY, Yu J, Tsai WB. Low-fouling and functional poly(carboxybetaine) coating via a photo-crosslinking process. *Biomater Sci* 2017; **5**(3): 523-31.

189. Lin X, Fukazawa K, Ishihara K. Photoreactive Polymers Bearing a Zwitterionic Phosphorylcholine Group for Surface Modification of Biomaterials. *ACS Applied Materials & Interfaces* 2015; **7**(31): 17489-98.

190. Konno T, Hasuda H, Ishihara K, Ito Y. Photo-immobilization of a phospholipid polymer for surface modification. *Biomaterials* 2005; **26**(12): 1381-8.

191. Sakuragi M, Tsuzuki S, Obuse S, et al. A photoimmobilizable sulfobetaine-based polymer for a nonbiofouling surface. *Materials Science and Engineering: C* 2010; **30**(2): 316-22.

192. Sobolčiak P, Popelka A, Mičušík M, et al. Photoimmobilization of zwitterionic polymers on surfaces to reduce cell adhesion. *J Colloid Interface Sci* 2017; **500**: 294-303.

193. Abraham S, Unsworth LD. Multi-functional initiator and poly (carboxybetaine methacrylamides) for building biocompatible surfaces using "nitroxide mediated free radical polymerization" strategies. *J Polym Sci, Part A: Polym Chem* 2011; **49**(5): 1051-60.

194. Ito Y, Hasuda H, Sakuragi M, Tsuzuki S. Surface modification of plastic, glass and titanium by photoimmobilization of polyethylene glycol for antibiofouling. *Acta Biomater* 2007; **3**(6): 1024-32.

195. Cross SE, Jin Y-S, Rao J, Gimzewski JK. Nanomechanical analysis of cells from cancer patients. *Nature nanotechnology* 2007; **2**(12): 780-3.

196. Matzke R, Jacobson K, Radmacher M. Direct, high-resolution measurement of furrow stiffening during division of adherent cells. *Nat Cell Biol* 2001; **3**(6): 607-10.

197. Hutter JL, Bechhoefer J. Calibration of atomic-force microscope tips. *Rev Sci Instrum* 1993; **64**(7): 1868-73.

198. Ferrera D, Canale C, Marotta R, et al. Lamin B1 overexpression increases nuclear rigidity in autosomal dominant leukodystrophy fibroblasts. *The FASEB Journal* 2014; **28**(9): 3906-18.

199. Bilodeau G. Regular pyramid punch problem. *Journal of applied mechanics* 1992; **59**(3): 519-23.

200. Mrsevic M, Düsselberg D, Staudt C. Synthesis and characterization of a novel carboxyl group containing (co)polyimide with sulfur in the polymer backbone. *Beilstein J Org Chem* 2012; **8**: 776-86.

201. Vigano C, Ruysschaert J-M, Goormaghtigh E. Sensor applications of attenuated total reflection infrared spectroscopy. *Talanta* 2005; **65**(5): 1132-42.

202. Khattak SF, Bhatia SR, Roberts SC. Pluronic F127 as a cell encapsulation material: utilization of membrane-stabilizing agents. *Tissue Eng* 2005; **11**(5-6): 974-83.

203. Zhang W, Gilstrap K, Wu L, et al. Synthesis and characterization of thermally responsive pluronic F127− chitosan nanocapsules for controlled release and intracellular delivery of small molecules. *ACS nano* 2010; **4**(11): 6747-59.

204. Cho S-J, Nguyen T, Boo J-H. Polyimide Surface Modification by Using Microwave Plasma for Adhesion Enhancement of Cu Electroless Plating. *Journal of Nanoscience and Nanotechnology* 2011; **11**(6): 5328-33.

205. Lieu Le N, Quilitzsch M, Cheng H, et al. Hollow fiber membrane lumen modified by polyzwitterionic grafting. *J Membr Sci* 2017; **522**: 1-11.

206. Inoue Y, Ishihara K. Reduction of protein adsorption on well-characterized polymer brush layers with varying chemical structures. *Colloids Surf B Biointerfaces* 2010; **81**(1): 350-7.

207. Stach M, Kroneková Z, Kasák P, et al. Polysulfobetaine films prepared by electrografting technique for reduction of biofouling on electroconductive surfaces. *Appl Surf Sci* 2011; **257**(24): 10795-801.

208. Kasák P, Kroneková Z, Krupa I, Lacík I. Zwitterionic hydrogels crosslinked with novel zwitterionic crosslinkers: Synthesis and characterization. *Polymer* 2011; **52**(14): 3011-20.

209. Zhang Z, Chao T, Liu L, Cheng G, Ratner BD, Jiang S. Zwitterionic hydrogels: an in vivo implantation study. *J Biomater Sci Polym Ed* 2009; **20**(13): 1845-59.

210. Zhang L, Cao Z, Bai T, et al. Zwitterionic hydrogels implanted in mice resist the foreign-body reaction. *Nat Biotechnol* 2013; **31**(6): 553-6.

211. Khandwekar AP, Patil DP, Shouche YS, Doble M. The biocompatibility of sulfobetaine engineered polymethylmethacrylate by surface entrapment technique. *J Mater Sci Mater Med* 2010; **21**(2): 635-46.

212. Irwin E, Saha K, Rosenbluth M, Gamble L, Castner D, Healy K. Modulus-dependent macrophage adhesion and behavior. *J Biomater Sci Polym Ed* 2008; **19**(10): 1363-82.

213. Wobma H, Vunjak-Novakovic G. Tissue engineering and regenerative medicine 2015: a year in review. *Tissue Engineering Part B: Reviews* 2016; **22**(2): 101-13.

214. Zouraq FA, Stölting M, Eberli D. Skeletal muscle regeneration for clinical application. *Regenerative Medicine and Tissue Engineering, ed JA Andrades* 2013.

215. Musarò A. The basis of muscle regeneration. *Advances in Biology* 2014; **2014**.

216. Ciciliot S, Schiaffino S. Regeneration of mammalian skeletal muscle: basic mechanisms and clinical implications. *Curr Pharm Des* 2010; **16**(8): 906-14.

217. Bach A, Beier J, Stern-Staeter J, Horch R. Skeletal muscle tissue engineering. *J Cell Mol Med* 2004; **8**(4): 413-22.

218. Juhas M, Ye J, Bursac N. Design, evaluation, and application of engineered skeletal muscle. *Methods* 2016; **99**: 81-90.

219. Tedesco FS, Dellavalle A, Diaz-Manera J, Messina G, Cossu G. Repairing skeletal muscle: regenerative potential of skeletal muscle stem cells. *The Journal of clinical investigation* 2010; **120**(1): 11-9.

220. Altomare L, Gadegaard N, Visai L, Tanzi M, Fare S. Biodegradable microgrooved polymeric surfaces obtained by photolithography for skeletal muscle cell orientation and myotube development. *Acta Biomater* 2010; **6**(6): 1948-57.

221. Bajaj P, Reddy B, Millet L, et al. Patterning the differentiation of C2C12 skeletal myoblasts. *Integrative Biology* 2011; **3**(9): 897-909.

222. Ricotti L, Polini A, Genchi GG, et al. Proliferation and skeletal myotube formation capability of C2C12 and H9c2 cells on isotropic and anisotropic electrospun nanofibrous PHB scaffolds. *Biomedical Materials* 2012; **7**(3): 035010.

223. Engler AJ, Griffin MA, Sen S, Bönnemann CG, Sweeney HL, Discher DE. Myotubes differentiate optimally on substrates with tissue-like stiffness pathological implications for soft or stiff microenvironments. *The Journal of cell biology* 2004; **166**(6): 877-87.

224. Ricotti L, Taccola S, Bernardeschi I, Pensabene V, Dario P, Menciassi A. Quantification of growth and differentiation of C2C12 skeletal muscle cells on PSS–PAH-based polyelectrolyte layer-by-layer nanofilms. *Biomedical Materials* 2011; **6**(3): 031001.

225. van der Schaft DW, van Spreeuwel AC, Boonen KJ, Langelaan ML, Bouten CV, Baaijens FP. Engineering skeletal muscle tissues from murine myoblast progenitor cells and application of electrical stimulation. *JoVE (Journal of Visualized Experiments)* 2013; (73): e4267-e.

226. Cheung K, Hume PA, Maxwell L. Delayed onset muscle soreness. *Sports Med* 2003; **33**(2): 145-64.

227. Järvinen TA, Järvinen TL, Kääriäinen M, et al. Muscle injuries: optimising recovery. *Best Practice & Research Clinical Rheumatology* 2007; **21**(2): 317-31.

228. Fujiya H, Goto K. New aspects of microcurrent electrical neuromuscular stimulation in sports medicine. *The Journal of Physical Fitness and Sports Medicine* 2016; **5**(1): 69-72.

229. Cezar CA, Roche ET, Vandenburgh HH, Duda GN, Walsh CJ, Mooney DJ. Biologic-free mechanically induced muscle regeneration. *Proceedings of the National Academy of Sciences* 2016; **113**(6): 1534-9.

230. Teixeira E, Duarte JA. Skeletal Muscle Loading Changes its Regenerative Capacity. *Sports Med* 2016: 1-10.

231. Khanna A, Nelmes RT, Gougoulias N, Maffulli N, Gray J. The effects of LIPUS on soft-tissue healing: a review of literature. *Br Med Bull* 2009; **89**(1): 169-82.

232. Marchioni C, Riccardi E, Spinelli S, et al. Structural changes induced in proteins by therapeutic ultrasounds. *Ultrasonics* 2009; **49**(6): 569-76.

233. Martin E. The Cellular Bioeffects of Low Intensity Ultrasound. *Ultrasound* 2009; **17**(4): 214-9.

234. Edmonds PD. Physical mechanisms for biological effects of ultrasound: By WL Nyborg. DHEW Publication (FDA) 78-8062, 59 pp., available without charge from BRH Technical Information Staff (HFX-25), 5600 Fishers Lane, Rockville, MD 20857 (Limited distribution). *Ultrasound Med Biol* 1978; **4**(4): 414.

235. Nyborg W. Ultrasonic microstreaming and related phenomena. *The British journal of cancer Supplement* 1982; **5**: 156.

236. O'Brien Jr WD. Ultrasound–biophysics mechanisms. *Prog Biophys Mol Biol* 2007; **93**(1-3): 212-55.

237. Fischell TA, Abbas MA, Grant GW, Siegel RJ. Ultrasonic energy. Effects on vascular function and integrity. *Circulation* 1991; **84**(4): 1783-95.

238. Maxwell L, Collecutt T, Gledhill M, Sharma S, Edgar S, Gavin J. The augmentation of leucocyte adhesion to endothelium by therapeutic ultrasound. *Ultrasound Med Biol* 1994; **20**(4): 383-90.

239. Hassan MA, Campbell P, Kondo T. The role of Ca2+ in ultrasound-elicited bioeffects: progress, perspectives and prospects. *Drug Discov Today* 2010; **15**(21-22): 892-906.

240. Abrunhosa VM, Soares CP, Possidonio ACB, et al. Induction of Skeletal Muscle Differentiation In Vitro by Therapeutic Ultrasound. *Ultrasound Med Biol* 2014; **40**(3): 504-12.

241. Wilkin L, Merrick M, Kirby T, Devor S. Influence of therapeutic ultrasound on skeletal muscle regeneration following blunt contusion. *Int J Sports Med* 2004; **25**(01): 73-7.

242. Markert CD, Merrick MA, Kirby TE, Devor ST. Nonthermal ultrasound and exercise in skeletal muscle regeneration. *Arch Phys Med Rehabil* 2005; **86**(7): 1304-10.

243. Fisher BD, Hiller CM, Rennie SG. A comparison of continuous ultrasound and pulsed ultrasound on soft tissue injury markers in the rat. *Journal of Physical Therapy Science* 2003; **15**(2): 65-70.

244. Chan Y-S, Hsu K-Y, Kuo C-H, et al. Using low-intensity pulsed ultrasound to improve muscle healing after laceration injury: an in vitro and in vivo study. *Ultrasound Med Biol* 2010; **36**(5): 743-51.

245. Matsumoto Y, Nakano J, Oga S, et al. The non-thermal effects of pulsed ultrasound irradiation on the development of disuse muscle atrophy in rat gastrocnemius muscle. *Ultrasound Med Biol* 2014; **40**(7): 1578-86.

246. Nagata K, Nakamura T, Fujihara S, Tanaka E. Ultrasound modulates the inflammatory response and promotes muscle regeneration in injured muscles. *Ann Biomed Eng* 2013; **41**(6): 1095-105.

247. Ikeda K, Takayama T, Suzuki N, Shimada K, Otsuka K, Ito K. Effects of low-intensity pulsed ultrasound on the differentiation of C2C12 cells. *Life Sci* 2006; **79**(20): 1936-43.

248. Shaw A, ter Haar G, Haller J, Wilkens V. Towards a dosimetric framework for therapeutic ultrasound. *Int J Hyperthermia* 2015; **31**(2): 182-92.

249. Leskinen JJ, Hynynen K. Study of factors affecting the magnitude and nature of ultrasound exposure with in vitro set-ups. *Ultrasound Med Biol* 2012; **38**(5): 777-94.

250. Puts R, Ruschke K, Kadow-Romacker A, et al. Mechanosensitive response of murine C2C12 myoblasts to focused Low-Intensity Pulsed Ultrasound (FLIPUS) stimulation. Ultrasonic Characterization of Bone (ESUCB), 2015 6th European Symposium on; 2015: IEEE; 2015. p. 1-4.

251. Puts R, Rikeit P, Ruschke K, et al. Activation of Mechanosensitive Transcription Factors in Murine C2C12 Mesenchymal Precursors by Focused Low-Intensity Pulsed Ultrasound (FLIPUS). 2016.

252. Salgarella AR, Cafarelli A, Ricotti L, Capineri L, Dario P, Menciassi A. Optimal ultrasound exposure conditions for maximizing C2C12 muscle cell proliferation and differentiation. *Ultrasound Med Biol* 2017; **43**(7): 1452-65.

253. Capineri L. A 15 MHz bandwidth, 60 Vpp, low distortion power amplifier for driving high power piezoelectric transducers. *Rev Sci Instrum* 2014; **85**(10): 104701.

254. Cafarelli A, Verbeni A, Poliziani A, Dario P, Menciassi A, Ricotti L. Tuning acoustic and mechanical properties of materials for ultrasound phantoms and smart substrates for cell cultures. *Acta Biomater* 2016.

255. Lin G, Reed-Maldonado AB, Lin M, Xin Z, Lue TF. Effects and Mechanisms of Low-Intensity Pulsed Ultrasound for Chronic Prostatitis and Chronic Pelvic Pain Syndrome. *International Journal of Molecular Sciences* 2016; **17**(7): 1057.

256. Duffy RM, Sun Y, Feinberg AW. Understanding the role of ECM protein composition and geometric micropatterning for engineering human skeletal muscle. *Ann Biomed Eng* 2016: 1-14.

257. Boonen KJ, Langelaan ML, Polak RB, van der Schaft DW, Baaijens FP, Post MJ. Effects of a combined mechanical stimulation protocol: value for skeletal muscle tissue engineering. *J Biomech* 2010; **43**(8): 1514-21.

258. Fujita H, Nedachi T, Kanzaki M. Accelerated de novo sarcomere assembly by electric pulse stimulation in C2C12 myotubes. *Exp Cell Res* 2007; **313**(9): 1853-65.

259. Ricotti L, Fujie T, Vazão H, et al. Boron nitride nanotube-mediated stimulation of cell co-culture on micro-engineered hydrogels. *PLoS One* 2013; **8**(8): e71707.

260. Wu Z, Woodring PJ, Bhakta KS, et al. p38 and extracellular signal-regulated kinases regulate the myogenic program at multiple steps. *Mol Cell Biol* 2000; **20**(11): 3951-64.

261. Zetser A, Gredinger E, Bengal E. p38 mitogen-activated protein kinase pathway promotes skeletal muscle differentiation participation of the MEF2C transcription factor. *J Biol Chem* 1999; **274**(8): 5193-200.

262. Penn BH, Bergstrom DA, Dilworth FJ, Bengal E, Tapscott SJ. A MyoD-generated feed-forward circuit temporally patterns gene expression during skeletal muscle differentiation. *Genes Dev* 2004; **18**(19): 2348-53.

263. Porter GA, Makuck RF, Rivkees SA. Reduction in intracellular calcium levels inhibits myoblast differentiation. *J Biol Chem* 2002; **277**(32): 28942-7.

264. Nedachi T, Fujita H, Kanzaki M. Contractile C2C12 myotube model for studying exercise-inducible responses in skeletal muscle. *American Journal of Physiology-Endocrinology and Metabolism* 2008; **295**(5): E1191-E204.

265. Burattini S, Ferri P, Battistelli M, Curci R, Luchetti F, Falcieri E. C2C12 murine myoblasts as a model of skeletal muscle development: morpho-functional characterization. *European journal of histochemistry: EJH* 2004; **48**(3): 223.

266. Duck F. Acoustic properties of tissue at ultrasonic frequencies. *Physical Properties of Tissue: A Comprehensive Reference Book* 1990: 73-124.

267. Charge SB, Rudnicki MA. Cellular and molecular regulation of muscle regeneration. *Physiol Rev* 2004; **84**(1): 209-38.

268. Puts R, Rikeit P, Ruschke K, et al. Activation of mechanosensitive transcription factors in murine C2C12 mesenchymal precursors by focused low-intensity pulsed ultrasound (FLIPUS). *IEEE transactions on ultrasonics, ferroelectrics, and frequency control* 2016; **63**(10): 1505-13.

269. Johns LD. Nonthermal effects of therapeutic ultrasound: the frequency resonance hypothesis. *Journal of athletic training* 2002; **37**(3): 293.

270. Feril LB, Kondo T. Biological effects of low intensity ultrasound: the mechanism involved, and its implications on therapy and on biosafety of ultrasound. *J Radiat Res (Tokyo)* 2004; **45**(4): 479-89.

271. Ter Haar G. Ultrasound bioeffects and safety. *Proceedings of the Institution of Mechanical Engineers, Part H: Journal of Engineering in Medicine* 2010; **224**(2): 363-73.

272. Morris H, Rivens I, Shaw A, ter Haar G. Investigation of the viscous heating artefact arising from the use of thermocouples in a focused ultrasound field. *Phys Med Biol* 2008; **53**(17): 4759.

273. Timko BP, Dvir T, Kohane DS. Remotely triggerable drug delivery systems. *Adv Mater* 2010; **22**(44): 4925-43.

274. Ganta S, Devalapally H, Shahiwala A, Amiji M. A review of stimuli-responsive nanocarriers for drug and gene delivery. *J Control Release* 2008; **126**(3): 187-204.

275. Tokarev I, Minko S. Stimuli-responsive hydrogel thin films. *Soft Matter* 2009; **5**(3): 511-24.

276. Zha L, Banik B, Alexis F. Stimulus responsive nanogels for drug delivery. *Soft Matter* 2011; **7**(13): 5908-16.

277. Karimi M, Ghasemi A, Zangabad PS, et al. Smart micro/nanoparticles in stimulus-responsive drug/gene delivery systems. *Chem Soc Rev* 2016; **45**(5): 1457-501.

278. Wang Y, Kohane DS. External triggering and triggered targeting strategies for drug delivery. *Nature Reviews Materials* 2017; **2**(6): 17020.

279. Ricotti L, Cafarelli A, Iacovacci V, Vannozzi L, Menciassi A. Advanced micro-nano-bio systems for future targeted therapies. *Current Nanoscience* 2015; **11**(2): 144-60.

280. Mura S, Nicolas J, Couvreur P. Stimuli-responsive nanocarriers for drug delivery. *Nature materials* 2013; **12**(11): 991.

281. Deckers R, Moonen CT. Ultrasound triggered, image guided, local drug delivery. *J Control Release* 2010; **148**(1): 25-33.

282. Sirsi SR, Borden MA. State-of-the-art materials for ultrasound-triggered drug delivery. *Adv Drug Del Rev* 2014; **72**: 3-14.

283. Mitragotri S. Healing sound: the use of ultrasound in drug delivery and other therapeutic applications. *Nature Reviews Drug Discovery* 2005; **4**(3): 255-60.

284. Ahmed SE, Martins AM, Husseini GA. The use of ultrasound to release chemotherapeutic drugs from micelles and liposomes. *J Drug Target* 2015; **23**(1): 16-42.

285. Husseini GA, Pitt WG. Micelles and nanoparticles for ultrasonic drug and gene delivery. *Adv Drug Del Rev* 2008; **60**(10): 1137-52.

286. Rapoport N. Ultrasound-mediated micellar drug delivery. *Int J Hyperthermia* 2012; **28**(4): 374-85.

287. Xia H, Zhao Y, Tong R. Ultrasound-mediated polymeric micelle drug delivery. Therapeutic Ultrasound: Springer; 2016: 365-84.

288. Xuan J, Pelletier M, Xia H, Zhao Y. Ultrasound-Induced Disruption of Amphiphilic Block Copolymer Micelles. *Macromol Chem Phys* 2011; **212**(5): 498-506.

289. Li Y, Tong R, Xia H, Zhang H, Xuan J. High intensity focused ultrasound and redox dual responsive polymer micelles. *Chem Commun* 2010; **46**(41): 7739-41.

290. Husseini GA, Pitt WG, Martins AM. Ultrasonically triggered drug delivery: breaking the barrier. *Colloids Surf B Biointerfaces* 2014; **123**: 364-86.

291. Husseini GA, Myrup GD, Pitt WG, Christensen DA, Rapoport NY. Factors affecting acoustically triggered release of drugs from polymeric micelles. *J Control Release* 2000; **69**(1): 43-52.

292. Tanbour R, M Martins A, G Pitt W, A Husseini G. Drug delivery systems based on polymeric micelles and ultrasound: a review. *Curr Pharm Des* 2016; **22**(19): 2796-807.

293. Hoogenboom R, Schlaad H. Bioinspired poly (2-oxazoline) s. *Polymers* 2011; **3**(1): 467-88.

294. Luxenhofer R, Han Y, Schulz A, et al. Poly (2-oxazoline) s as Polymer Therapeutics. *Macromol Rapid Commun* 2012; **33**(19): 1613-31.

295. Pidhatika B, Rodenstein M, Chen Y, et al. Comparative stability studies of poly (2-methyl-2-oxazoline) and poly (ethylene glycol) brush coatings. *Biointerphases* 2012; **7**(1-4): 1.

296. Zhang N, Pompe T, Amin I, Luxenhofer R, Werner C, Jordan R. Tailored Poly (2-oxazoline) Polymer Brushes to Control Protein Adsorption and Cell Adhesion. *Macromol Biosci* 2012; **12**(7): 926-36.

297. Kronek J, Kroneková Z, Lustoň J, Paulovičová E, Paulovičová L, Mendrek B. In vitro bio-immunological and cytotoxicity studies of poly (2-oxazolines). *J Mater Sci Mater Med* 2011; **22**(7): 1725-34.

298. Luxenhofer R, Sahay G, Schulz A, et al. Structure-property relationship in cytotoxicity and cell uptake of poly (2-oxazoline) amphiphiles. *J Control Release* 2011; **153**(1): 73-82.

299. Gaertner FC, Luxenhofer R, Blechert B, Jordan R, Essler M. Synthesis, biodistribution and excretion of radiolabeled poly (2-alkyl-2-oxazoline) s. *J Control Release* 2007; **119**(3): 291-300.

300. Wyffels L, Verbrugghen T, Monnery BD, et al. μPET imaging of the pharmacokinetic behavior of medium and high molar mass 89Zr-labeled poly (2-ethyl-2-oxazoline) in comparison to poly (ethylene glycol). *J Control Release* 2016; **235**: 63-71.

301. Farkaš P, Korcová J, Kronek J, Bystrický S. Preparation of synthetic polyoxazoline based carrier and Vibrio cholerae O-specific polysaccharide conjugate vaccine. *Eur J Med Chem* 2010; **45**(2): 795-9.

302. Konradi R, Acikgoz C, Textor M. Polyoxazolines for Nonfouling Surface Coatings — A Direct Comparison to the Gold Standard PEG. *Macromol Rapid Commun* 2012; **33**(19): 1663-76.

303. Dworak A, Utrata-Wesołek A, Oleszko N, et al. Poly (2-substituted-2-oxazoline) surfaces for dermal fibroblasts adhesion and detachment. *J Mater Sci Mater Med* 2014; **25**(4): 1149-63.

304. Zahoranová A, Kroneková Z, Zahoran M, Chorvát D, Janigová I, Kronek J. Poly (2-oxazoline) hydrogels crosslinked with aliphatic bis (2-oxazoline) s: Properties, cytotoxicity, and cell cultivation. *J Polym Sci, Part A: Polym Chem* 2016; **54**(11): 1548-59.

305. Farrugia BL, Kempe K, Schubert US, Hoogenboom R, Dargaville TR. Poly (2-oxazoline) hydrogels for controlled fibroblast attachment. *Biomacromolecules* 2013; **14**(8): 2724-32.

306. Hsiue G-H, Chiang H-Z, Wang C-H, Juang T-M. Nonviral gene carriers based on diblock copolymers of poly (2-ethyl-2-oxazoline) and linear polyethylenimine. *Bioconj Chem* 2006; **17**(3): 781-6.

307. Hruby M, Filippov SK, Panek J, et al. Polyoxazoline thermoresponsive micelles as radionuclide delivery systems. *Macromol Biosci* 2010; **10**(8): 916-24.

308. Bonné TB, Lüdtke K, Jordan R, Štěpánek P, Papadakis CM. Aggregation behavior of amphiphilic poly (2-alkyl-2-oxazoline) diblock copolymers in aqueous solution studied by fluorescence correlation spectroscopy. *Colloid Polym Sci* 2004; **282**(8): 833-43.

309. Trzebicka B, Koseva N, Mitova V, Dworak A. Organization of poly (2-ethyl-2-oxazoline)-block-poly (2-phenyl-2-oxazoline) copolymers in water solution. *Polymer* 2010; **51**(12): 2486-93.

310. Krumm C, Konieczny S, Dropalla GJ, Milbradt M, Tiller JC. Amphiphilic polymer conetworks based on end group cross-linked poly (2-oxazoline) homo-and triblock copolymers. *Macromolecules* 2013; **46**(9): 3234-45.

311. Stoenescu R, Meier W. Asymmetric membranes from amphiphilic ABC triblock copolymers. *Mol Cryst Liq Cryst* 2004; **417**(1): 185-91.

312. Seo Y, Schulz A, Han Y, et al. Poly (2-oxazoline) block copolymer based formulations of taxanes: effect of copolymer and drug structure, concentration, and environmental factors. *Polym Adv Technol* 2015; **26**(7): 837-50.

313. He Z, Schulz A, Wan X, et al. Poly (2-oxazoline) based micelles with high capacity for 3rd generation taxoids: Preparation, in vitro and in vivo evaluation. *J Control Release* 2015; **208**: 67-75.

314. Luxenhofer R, Schulz A, Roques C, et al. Doubly amphiphilic poly (2-oxazoline) s as high-capacity delivery systems for hydrophobic drugs. *Biomaterials* 2010; **31**(18): 4972-9.

315. Milonaki Y, Kaditi E, Pispas S, Demetzos C. Amphiphilic gradient copolymers of 2-methyl-and 2-phenyl-2-oxazoline: self-organization in aqueous media and drug encapsulation. *J Polym Sci, Part A: Polym Chem* 2012; **50**(6): 1226-37.

316. Lübtow MM, Hahn L, Haider MS, Luxenhofer R. Drug Specificity, Synergy and Antagonism in Ultrahigh Capacity Poly (2-oxazoline)/Poly (2-oxazine) based Formulations. *J Am Chem Soc* 2017; **139**(32): 10980-3.

317. Schulz A, Jaksch S, Schubel R, et al. Drug-induced morphology switch in drug delivery systems based on poly (2-oxazoline) s. *ACS nano* 2014; **8**(3): 2686-96.

318. Witte H, Seeliger W. Cyclische imidsäureester aus nitrilen und aminoalkoholen. *European J Org Chem* 1974; **1974**(6): 996-1009.

319. Salzinger S, Huber S, Jaksch S, Busch P, Jordan R, Papadakis CM. Aggregation behavior of thermo-responsive poly (2-oxazoline) s at the cloud point investigated by FCS and SANS. *Colloid Polym Sci* 2012; **290**(5): 385-400.

320. Nery L, Lefebvre H, Fradet A. Kinetic and Mechanistic Studies of Carboxylic Acid–Bisoxazoline Chain-Coupling Reactions. *Macromol Chem Phys* 2003; **204**(14): 1755-64.

321. Gress A, Völkel A, Schlaad H. Thio-click modification of poly [2-(3-butenyl)-2-oxazoline]. *Macromolecules* 2007; **40**(22): 7928-33.

322. Zahoranová A, Mrlík M, Tomanová K, Kronek J, Luxenhofer R. ABA and BAB Triblock Copolymers Based on 2-Methyl-2-oxazoline and 2-n-Propyl-2-oxazoline: Synthesis and Thermoresponsive Behavior in Water. *Macromol Chem Phys* 2017; **218**(13).

323. Kempe K, Vollrath A, Schaefer HW, et al. Multifunctional Poly (2-oxazoline) Nanoparticles for Biological Applications. *Macromol Rapid Commun* 2010; **31**(21): 1869-73.

324. Hartlieb M, Kempe K, Schubert US. Covalently cross-linked poly (2-oxazoline) materials for biomedical applications–from hydrogels to self-assembled and templated structures. *Journal of Materials Chemistry B* 2015; **3**(4): 526-38.

325. Marin A, Sun H, Husseini GA, Pitt WG, Christensen DA, Rapoport NY. Drug delivery in pluronic micelles: effect of high-frequency ultrasound on drug release from micelles and intracellular uptake. *J Control Release* 2002; **84**(1-2): 39-47.

326. Hoogenboom R. Poly (2-oxazoline) s: a polymer class with numerous potential applications. *Angew Chem Int Ed* 2009; **48**(43): 7978-94.

327. Yalkowsky SH, He Y, Jain P. Handbook of aqueous solubility data: CRC press; 2016.

328. Raveendran R, Mullen KM, Wellard RM, Sharma CP, Hoogenboom R, Dargaville TR. Poly (2-oxazoline) block copolymer nanoparticles for curcumin loading and delivery to cancer cells. *Eur Polym J* 2017; **93**: 682-94.

329. Janas C, Mostaphaoui Z, Schmiederer L, Bauer J, Wacker MG. Novel polymeric micelles for drug delivery: Material characterization and formulation screening. *Int J Pharm* 2016; **509**(1-2): 197-207.

330. Yang J, Yan J, Zhou Z, Amsden BG. Dithiol-PEG-PDLLA micelles: preparation and evaluation as potential topical ocular delivery vehicle. *Biomacromolecules* 2014; **15**(4): 1346-54.

331. Wang Q, Jiang J, Chen W, Jiang H, Zhang Z, Sun X. Targeted delivery of low-dose dexamethasone using PCL–PEG micelles for effective treatment of rheumatoid arthritis. *J Control Release* 2016; **230**: 64-72.

332. Nidhi K, Indrajeet S, Khushboo M, Gauri K, Sen DJ. Hydrotropy: A promising tool for solubility enhancement: A review. *International Journal of Drug Development and Research* 2011; **3**(2).

333. Wu Q, Wang N, He T, et al. Thermosensitive hydrogel containing dexamethasone micelles for preventing postsurgical adhesion in a repeated-injury model. *Sci Rep* 2015; **5**: 13553.

334. Wang Y, Wu M, Gu L, et al. Effective improvement of the neuroprotective activity after spinal cord injury by synergistic effect of glucocorticoid with biodegradable amphipathic nanomicelles. *Drug Deliv* 2017; **24**(1): 391-401.

335. Kumi BC, Hammouda B, Greer SC. Self-assembly of the triblock copolymer 17R4 poly (propylene oxide) 14–poly (ethylene oxide) 24–poly (propylene oxide) 14 in D2O. *J Colloid Interface Sci* 2014; **434**: 201-7.

336. Xu R, Winnik MA, Hallett F, Riess G, Croucher MD. Light-scattering study of the association behavior of styrene-ethylene oxide block copolymers in aqueous solution. *Macromolecules* 1991; **24**(1): 87-93.

337. Fetsch C, Gaitzsch J, Messager L, Battaglia G, Luxenhofer R. Self-Assembly of Amphiphilic Block Copolypeptoids–Micelles, Worms and Polymersomes. *Sci Rep* 2016; **6**: 33491.

338. Krumm C, Fik CP, Meuris M, et al. Well-Defined Amphiphilic Poly (2-oxazoline) ABA-Triblock Copolymers and Their Aggregation Behavior in Aqueous Solution. *Macromol Rapid Commun* 2012; **33**(19): 1677-82.

339. Nichols JW, Bae YH. Odyssey of a cancer nanoparticle: from injection site to site of action. *Nano today* 2012; **7**(6): 606-18.

340. Gourevich D, Dogadkin O, Volovick A, et al. Ultrasound-mediated targeted drug delivery with a novel cyclodextrin-based drug carrier by mechanical and thermal mechanisms. *J Control Release* 2013; **170**(3): 316-24.

341. Siepmann J, Siepmann F. Mathematical modeling of drug delivery. *Int J Pharm* 2008; **364**(2): 328-43.

342. Zhang H, Xia H, Wang J, Li Y. High intensity focused ultrasound-responsive release behavior of PLA-b-PEG copolymer micelles. *J Control Release* 2009; **139**(1): 31-9.

343. Moreadith RW, Viegas TX, Bentley MD, et al. Clinical development of a poly (2-oxazoline)(POZ) polymer therapeutic for the treatment of Parkinson's disease–Proof of concept of POZ as a versatile polymer platform for drug development in multiple therapeutic indications. *Eur Polym J* 2017; **88**: 524-52.

344. Coimbra M, Rijcken CJ, Stigter M, Hennink WE, Storm G, Schiffelers RM. Antitumor efficacy of dexamethasone-loaded core-crosslinked polymeric micelles. *J Control Release* 2012; **163**(3): 361-7.

345. Crielaard BJ, Rijcken CJ, Quan L, et al. Glucocorticoid-Loaded Core-Cross-Linked Polymeric Micelles with Tailorable Release Kinetics for Targeted Therapy of Rheumatoid Arthritis. *Angew Chem Int Ed* 2012; **51**(29): 7254-8.

346. Liu S, Jones L, Gu FX. Nanomaterials for ocular drug delivery. *Macromol Biosci* 2012; **12**(5): 608-20.

347. Ricotti L, Assaf T, Dario P, Menciassi A. Wearable and implantable pancreas substitutes. *J Artificial Organs* 2013; **16**(1): 9-22.

348. Morais JM, Papadimitrakopoulos F, Burgess DJ. Biomaterials/tissue interactions: possible solutions to overcome foreign body response. *The AAPS journal* 2010; **12**(2): 188-96.